



HAL
open science

New nanoparticles for electrocatalysis applied to energy conversion : synthesis and operando X-ray absorption analysis

Madeleine Han

► **To cite this version:**

Madeleine Han. New nanoparticles for electrocatalysis applied to energy conversion : synthesis and operando X-ray absorption analysis. Material chemistry. Sorbonne Université, 2020. English. NNT : 2020SORUS101 . tel-03825752

HAL Id: tel-03825752

<https://theses.hal.science/tel-03825752>

Submitted on 23 Oct 2022

HAL is a multi-disciplinary open access archive for the deposit and dissemination of scientific research documents, whether they are published or not. The documents may come from teaching and research institutions in France or abroad, or from public or private research centers.

L'archive ouverte pluridisciplinaire **HAL**, est destinée au dépôt et à la diffusion de documents scientifiques de niveau recherche, publiés ou non, émanant des établissements d'enseignement et de recherche français ou étrangers, des laboratoires publics ou privés.



Sorbonne Université

École doctorale 397 – Physique et Chimie des Matériaux

Laboratoire Chimie de la Matière Condensée de Paris – Synchrotron SOLEIL

New nanoparticles for electrocatalysis applied to energy conversion: synthesis and operando X-ray absorption analysis

Par Madeleine HAN

Thèse de doctorat de Chimie des Matériaux

Dirigée par Christel Laberty-Robert, David Portehault et Benedikt Lassalle-Kaiser

Présentée et soutenue publiquement le 21 octobre 2020

Devant un jury composé de :

Pr. Elena SAVINOVA	Professeur de l'Université de Strasbourg	Rapporteur
Dr. Manuel GAUDON	Maître de conférences à l'Université de Bordeaux	Rapporteur
Dr. Frédéric JAOUEN	Chargé de Recherche CNRS	Examineur
Pr. Mathieu SALANNE	Professeur de Sorbonne Université	Examineur
Dr. Benedikt LASSALLE-KAISER	Scientifique de ligne au synchrotron SOLEIL	Co-directeur de thèse
Dr. David PORTEHAULT	Chargé de Recherche CNRS	Co-directeur de thèse
Pr. Christel LABERTY-ROBERT	Professeur de Sorbonne Université	Directrice de thèse



Except where otherwise noted, this work is licensed under <http://creativecommons.org/licenses/by-nc-nd/3.0/>

Acknowledgements

I would like to acknowledge Florence Babonneau for allowing me to do my thesis at the Laboratoire Chimie de la Matière Condensée de Paris, and Christian Bonhomme who took up the torch. Even with a busy schedule, he could always find time to discuss on any topic.

I give many thanks to Delphine Vantelon for her warm welcome on the LUCIA beamline. Her help and understanding appeased my concerns many times.

I thank Christel Laberty-Robert for the patience and the adaptability she showed during the supervision of my PhD. I thank David Portehault for his dedication to train his PhD students because indeed, we are still students. I thank Benedikt Lassalle-Kaiser for introducing me to the synchrotrons and keeping me company during the beamtimes. I want to thank again these three people for the supervision of my PhD. While each of them has their area of expertise, they showed great interest in learning from the field of one another and most of the topics were discussed and decided between the four of us.

I thank Nathaly Ortiz Peña for her kindness and for introducing me to *operando* TEM. It was always a pleasure to see her, whether in Paris or in Strasbourg. We struggled together in this unexpected hard study of Co_3O_4 .

I thank all the members of the Insichem ANR: Ovidiu Ersen and Dris Ihiwakrim for their expertise in *in situ* TEM and their warm welcome when we come to Strasbourg, Sophie Carencio for her dynamic and positive personality and all the advices she gave me, Clément Sanchez for the counselling he offered, and finally Andrea Zitolo for welcoming us on SAMBA beamline.

I thank the local contacts who welcomed us on their beamlines: Christoph Salhe (ID20, ESRF) and Veronica Celorrio (B18, DIAMOND). I also thank the beamline managers Emiliano Fonda (SAMBA, SOLEIL) and Giannantonio Cibin (B18, DIAMOND) who also helped and gave us advices during our beamtimes.

I thank the students of the former Nanobreakfast team: Tsou-Hsi Camille, Jérôme, Clément, Nadège, Simon, Anh-Minh, Binghua, Kim-Chi, Guillaume Crochet, Yang,

Antoine, Rémi, Fernando, Edouard, Cyprien, Océane, Alexandre, Francisco, Ram, Isabel, Xavier, Florian and Alexis. These gourmet meetings were always a pleasure to attend thanks to their caring and friendly atmosphere.

I also thank the microfluidics/electrocatalysis team at SOLEIL for their kindness and their mind open to subjects that are far from theirs: Yuanyuan, Tiphaine, Daniela, Thanh, Baptiste and Stéphane. I also acknowledge Anthony and Gildas, especially for the organization of the “petit-déjeuner scientifique”.

Finally, I am grateful to my family, the Yozz and my friends, who supported me during these three years. Thank you all.

Summary

Acknowledgements	1
Abbreviations	8
French resume	9
General introduction	14
Chapter I:	17
State of the art	17
1. Introduction	18
1.1. Global energy context.....	18
1.2. Batteries, electrolyzers and fuel cells	18
2. Oxygen evolution reaction (OER) and oxygen reduction reaction (ORR) ...	20
2.1. The mechanisms of OER and ORR	20
2.2. Defining the electrocatalytic activity	21
2.2.1. The overpotential and the current	21
2.2.2. The Tafel slope.....	21
2.2.3. Normalized current	22
2.2.4. Turnover frequency.....	22
2.3. Common electrocatalysts and current research trends.....	22
3. <i>Operando</i> X-ray Absorption Spectroscopy	24
3.1. Fundamentals of XAS.....	24
3.1.1. The XANES	25
3.1.2. The EXAFS.....	26
3.1.3. Spectrum collection.....	27
3.2. Historical background of <i>in situ</i> XAS.....	28
3.3. Information provided by XAS on materials	29
3.3.1. Oxidation state and local structure.....	29
3.3.2. Site occupancy	29

3.3.3.	Nanoparticle size.....	30
3.3.4.	Surface sensitivity.....	30
4.	Other <i>in situ</i> studies for electrocatalysis	32
4.1.	Time resolution.....	32
4.2.	Surface state.....	33
4.3.	Phase evolution.....	34
4.4.	Morphology insights.....	34
5.	Conclusion.....	35
	Chapter II:	37
	Electrocatalytic properties of Ni_xB_y nanoparticles for water splitting	37
1.	Ni _x B _y presentation	40
2.	XAS analysis technique	42
2.1.	Linear combination fitting	42
2.1.1.	Principle	42
2.1.2.	Methodological limitations	43
2.2.	EXAFS fits	44
2.2.1.	Principle	44
2.2.2.	Reference crystal data.....	47
3.	Results	48
3.1.	Solid samples overview	48
3.2.	Nickel oxide references	49
3.3.	Nickel boride-based nanoelectrocatalysts	51
3.3.1.	Metallic nickel	51
3.3.2.	Ni ₃ B	62
3.3.3.	Ni ₄ B ₃	72
4.	Discussion	81
4.1.	Methodology.....	81

4.2.	Evolution of the electrocatalysts	82
5.	Conclusion	84
Chapter III:		87
Evolution of Mn and Co-based perovskites during the OER and the ORR ...		87
1.	Introduction	88
2.	Model materials: LaMnO_3 and $\text{La}_{0.67}\text{Sr}_{0.33}\text{MnO}_3$	90
2.1.	An overview of the synthesis of perovskites	90
2.2.	Molten salt synthesis of LaMnO_3 (LMO) and $\text{La}_{0.67}\text{Sr}_{0.33}\text{MnO}_3$ (LSMO)	91
2.3.	Material characterization	92
2.4.	Electrocatalytic properties	94
2.4.1.	Electrochemical set-up	94
2.4.2.	Results	94
3.	Manganese partial substitution in $\text{LaMn}_{1-x}\text{Co}_x\text{O}_3$	96
3.1.	Synthesis	96
3.2.	Characterization	96
4.	Synthesis of $\text{La}_{0.67}\text{Sr}_{0.33}\text{CoO}_3$	98
5.	Electrocatalytic properties of $\text{La}_{1-x}\text{Sr}_x\text{CoO}_3$ and $\text{LaMn}_{1-x}\text{Co}_x\text{O}_3$	104
6.	XAS analysis	108
6.1.	Pristine compounds	108
6.2.	In situ characterization	112
6.2.1.	LaMnO_3	112
6.2.2.	$\text{La}_{0.67}\text{Sr}_{0.33}\text{MnO}_3$	115
6.2.3.	$\text{La}_{0.75}\text{Sr}_{0.25}\text{CoO}_3$	117
6.2.4.	$\text{LaMn}_{0.6}\text{Co}_{0.4}\text{O}_3$	120
7.	Discussion	123
7.1.	Synthesis and <i>ex situ</i> electrochemical characterization	123
7.2.	Operando XAS technique	124

7.3.	Observations on the electrocatalysts.....	126
8.	Conclusion.....	128
Chapter IV:		131
An <i>in situ</i> XAS and TEM study of Co₃O₄, a model system for the OER.....		131
1.	Introduction	132
2.	Co ₃ O ₄ nanoparticles synthesis and characterization	134
3.	XAS at the Co L-edge	138
3.1.	<i>Ex situ</i> analysis of reference compounds.....	138
3.2.	Co L-edge XAS spectra of Co ₃ O ₄ electrodes before and after OER.....	140
4.	<i>In situ</i> TEM experiment	142
4.1.	<i>Post mortem</i> Co K-edge XAS spectra of Co ₃ O ₄ in the TEM cell	143
4.2.	<i>In situ</i> Co K-edge XAS spectra of Co ₃ O ₄ in the TEM cell.....	144
5.	Discussion	146
5.1.	<i>In situ</i> techniques	146
5.2.	Insights on Co ₃ O ₄ behavior during OER.....	147
6.	Conclusion.....	148
General conclusion		150
Appendix		153
1.	Methods.....	154
1.1.	Material synthesis	154
1.1.1.	Synthesis of perovskites in molten salts	154
1.1.2.	Synthesis of spinel nanoparticles by microwave-assisted heating....	156
1.2.	<i>Ex situ</i> electrochemical measurements.....	156
1.2.1.	Setup preparation	156
1.2.2.	Cyclic voltammetry.....	157
1.3.	Techniques of characterization.....	157
1.3.1.	X-ray diffraction	157

1.3.2.	Transmission electron microscopy.....	157
1.3.3.	Elemental mapping	157
1.3.4.	Wavelength-dispersive X-ray fluorescence	157
2.	Material characterization	158
2.1.	Elemental distribution inside $\text{LaMn}_{0.70}\text{Co}_{0.30}\text{O}_3$ nanoparticles	158
2.2.	Characterization of the $\text{La}_{1-x}\text{Sr}_x\text{CoO}_3$ perovskite.....	158
3.	XAS measurements	160
3.1.	Beamline settings	160
3.1.1.	SAMBA beamline.....	160
3.1.2.	B18 beamline	160
3.1.3.	LUCIA beamline.....	160
3.2.	Cell description	162
3.2.1.	In situ cell for K-edge	162
3.2.2.	In situ cell for L-edge.....	164
3.3.	Operando experiments	166
3.3.1.	Cyclic voltammograms of in situ experiments	166
3.3.2.	Scan history of the operando experiments	169
3.3.3.	XANES corresponding to the linear combination fitting.....	171
3.3.4.	Chronoamperometry of some <i>operando</i> experiments.....	180
3.3.5.	Operando XAS of Co_3O_4 from a classical ink	181
3.3.6.	Supplementary FT-EXAFS fits without paths from nickel oxides... ..	182
4.	Discussion.....	183
4.1.	Calculation of the nickel oxide content and layer thickness.....	183
4.2.	Evaluation of the uncertainty of linear combination fitting.....	183
4.3.	Impact of the nature of the crucible on the synthesis of $\text{La}_{1-x}\text{Sr}_x\text{CoO}_3$	185
4.4.	Stability of the electrocatalyst by the intensity of the raw XAS.....	187
	References	191

Abbreviations

(N)AP	(Near) Ambient Pressure
DFT	Density Functional Theory
EDX	Energy Dispersive X-ray analysis
(FT-)EXAFS	(Fourier Transform) Extended X-ray Absorption Fine Structure
FY	Fluorescence Yield
GC	Glassy Carbon
HER	Hydrogen Evolution Reaction
HOR	Hydrogen Oxidation Reaction
LCF	Linear Combination Fitting
NPs	Nanoparticles
OCV	Open Circuit Voltage
OER	Oxygen Evolution Reaction
ORR	Oxygen Reduction Reaction
RHE	Reversible Hydrogen Electrode
SCE	Saturated Calomel Electrode
(HR)TEM	(High-Resolution) Transmission Electron Microscopy
TEY	Total Electron Yield
TOF	TurnOver Frequency
WDXRF	Wavelength Dispersive X-Ray Fluorescence
XANES	X-ray Absorption Near Edge Structure
XAS	X-ray Absorption Spectroscopy/Spectrum
XPS	X-ray Photoelectron Spectroscopy
XRD	X-Ray Diffraction

French resume

La prochaine évolution majeure dans la transition énergétique devrait comprendre une économie basée sur le dihydrogène. Le dihydrogène peut être utilisé de différentes manières en tant que matière première, combustible, vecteur énergétique ou système de stockage dont l'utilisation n'est pas source d'émission de CO₂. Il offre ainsi une solution pour décarboner les procédés industriels et les secteurs économiques où la réduction des émissions de carbone est à la fois urgente et difficile à mettre en place.

L'Union Européenne a fait du développement du dihydrogène renouvelable une priorité à travers l'électrolyse de l'eau, dont l'électricité serait produite à partir de sources renouvelables telles que l'énergie solaire ou éolienne. Son coût doit pouvoir concurrencer celui de l'hydrogène produit à partir des énergies fossiles, qui est aux alentours de 1,5 euros kg⁻¹. Cela est possible dans des régions où l'électricité renouvelable est bon marché et en réduisant de moitié le coût des électrolyseurs actuels, notamment à travers le développement de nouveaux électrocatalyseurs dépourvus de platinoïdes, en particulier pour l'oxydation de l'eau. Parallèlement, l'étude des mécanismes de formation de l'oxygène (OER) sur ces « nouveaux » catalyseurs est vitale pour résoudre la faible cinétique de cette réaction.

La recherche sur le développement d'électrocatalyseurs performants en OER a mené à beaucoup d'études sur les mécanismes de cette réaction. Ces travaux ont souvent associé les performances électrocatalytiques des électrocatalyseurs à leur structure. En particulier, le développement de techniques *operando* permettant d'analyser les électrocatalyseurs pendant leur activité électrocatalytique a apporté de nouveaux éclairages dans l'identification du « site » actif ou de « l'espèce » active, dont la stabilité est souvent faible lorsque l'électrocatalyseur est au repos à l'intérieur (*in situ*) ou à l'extérieur (*ex situ*) de l'environnement électrochimique. Depuis la découverte de ces espèces actives instables, l'analyse *operando* est devenue indispensable pour la description complète de l'activité d'un électrocatalyseur.

L'une des techniques *operando* les plus utilisées est la spectroscopie d'absorption des rayons-X (XAS) car elle donne des renseignements à la fois sur le degré d'oxydation des métaux et sur leur environnement local. Le XAS est une technique qui sonde le volume d'un matériau, ce qui permet de suivre l'évolution globale de l'électrocatalyseur pendant

l'électrocatalyse, mais peut aussi paraître limité, en particulier pour suivre l'évolution des espèces en surface. Heureusement, le développement de nouveaux procédés de synthèse, dicté par le besoin d'une augmentation du rapport surface/volume des électrocatalyseurs pour améliorer l'activité massique, a permis la fabrication d'électrocatalyseurs à l'échelle nanométrique. Ces électrocatalyseurs présentent des surfaces spécifiques suffisamment élevées pour que la proportion d'atomes à la surface soit suffisamment importante par rapport à celle du cœur, rendant ainsi le XAS sensible aux phénomènes localisés à la surface de ces nanomatériaux.

Bien que l'efficacité du XAS ait été prouvée maintes fois lors de la caractérisation *ex situ* de divers électrocatalyseurs, l'utilisation de XAS *operando* dans l'électrocatalyse est pour l'instant principalement limitée à l'observation de l'évolution du degré d'oxydation des éléments ou à l'identification de distances interatomiques caractéristiques

Dans ce contexte, l'objectif de cette thèse est d'approfondir le développement du XAS *operando* en transposant les traitements de données usuellement utilisés en XAS *ex situ* aux expériences *operando*. En utilisant des nanomatériaux qui présentent des surfaces spécifiques élevées, nous examinons les espèces électroactives situées en surface et suivons leur évolution en fonction du potentiel appliqué et du temps. Pour finir, le couplage XAS avec des techniques *operando* complémentaires, comme la microscopie, permet une description multi-échelle de l'électrocatalyseur. Ces sujets sont illustrés dans ce travail de thèse à travers l'analyse de trois familles de matériaux : les borures de nickel, les oxydes à structure pérovskite et les spinelles à travers Co_3O_4 . L'objectif du travail est de comprendre l'activité électrocatalytique de ces différents matériaux à partir des résultats obtenus par XAS *operando* qui permettent de décrire le site électrocatalytique.

Le premier chapitre présente les bases de la spectroscopie d'absorption des rayons-X, et en particulier les informations qui peuvent être extraites des spectres d'absorption des rayons-X. Il discute aussi des limites de la technique, démontrant ainsi la nécessité de coupler cette étude à d'autres approches faisant intervenir des techniques *operando* « plus locales » pour décrire intégralement le fonctionnement de l'électrocatalyseur.

Dans le second chapitre, nous étudions des nanoparticules de borure de nickel Ni_3B et Ni_4B_3 qui sont des électrocatalyseurs pour la formation du dihydrogène (HER) à pH acide, et pour la formation de l'oxygène (OER) à pH basique. Leur structure cristalline contient

une quantité excessive de courtes distances interatomiques, ce qui rend leur caractérisation par XAS difficile. De plus, nous avons étudié le rôle du bore dans l'activité électrocatalytique, jusqu'ici peu étudié dans la littérature. Dans un premier temps, nous montrons qu'il est possible d'obtenir par XAS *operando* des données quantitatives, en utilisant la combinaison linéaire (LCF) de spectres XAS de composés définis et du fit de la transformée de Fourier de spectres EXAFS (FT-EXAFS) obtenus expérimentalement. Nous démontrons que la phase électroactive de Ni₃B est la même que celle observée pour le nickel métallique : il s'agit de Ni^{III}OOH durant l'OER et la phase non oxydée durant l'HER. Cependant, nous observons que Ni₃B contient une plus faible proportion de Ni^{III}OOH en OER, bien qu'il soit plus actif que le Ni métal. L'activité stable et élevée de Ni₃B en OER s'explique par un modèle cœur-coquille où une fine couche de NiOOH très électroactive se forme à l'interface avec l'électrolyte, tout en préservant un cœur, Ni₃B, conducteur. Dans cette description, le bore limite l'oxydation du nickel. À l'inverse, dans le cas de Ni₄B₃, les fits EXAFS et la LCF n'ont pas donné de résultats concluants, montrant que notre modèle n'est pas adapté à la description de l'électroactivité de ce composé. Ici, la formation d'une phase supplémentaire telle qu'un borate de nickel a été proposée pour expliquer son comportement, bien qu'une étude plus poussée soit nécessaire pour confirmer cette hypothèse. Ces résultats mettent en évidence l'apport de la LCF, en particulier, dans l'estimation de la proportion d'oxyde de nickel dans les nanoparticules de nickel et de borure de nickel. Cette quantification a rarement été réalisée dans les expériences *operando* reportées dans la littérature. Ces dernières suivent, en général, seulement le degré d'oxydation du métal de transition via le déplacement de l'énergie à mi-seuil. Enfin, le couplage de la LCF et du fit EXAFS permet d'estimer l'épaisseur de la couche d'oxyde de nickel formée à la surface des nanoparticules de borure de nickel pendant l'électrocatalyse.

Dans le troisième chapitre, nous étudions les oxydes pérovskites, les manganites, les cobaltites et les pérovskites mixtes manganèse-cobalt, dont les activités en OER et ORR (réduction de l'oxygène) en milieu basique sont directement liées à la nature du (ou des) métal(aux) de transition en site B. Les quelques articles dans la littérature sur l'analyse *operando* de ces matériaux ne relient pas l'activité électrocatalytique à la nature même du métal de transition. Notre méthodologie a consisté à analyser les spectres XAS des pérovskites de manganèse et/ou de cobalt aux seuils K du manganèse et du cobalt puis, à suivre l'évolution temporelle du degré d'oxydation du Mn et du Co pendant l'OER et l'ORR. Nous montrons que l'activité électrocatalytique des manganites et des cobaltites est liée à la

présence respective du Mn et du Co en ORR et en OER. Dans le cas des oxydes mixtes, la description de l'activité électrocatalytique en fonction du rapport Mn/Co est plus complexe. En particulier, nous remarquons que l'activité en ORR/OER ne varie pas de façon linéaire avec le rapport Mn/Co. Cette observation met en évidence un effet de synergie possible entre les deux métaux de transition. Dans le cas du XAS *operando* sur les pérovskites contenant un seul métal de transition, LaMnO_3 ou $\text{La}_{0.67}\text{Sr}_{0.33}\text{CoO}_3$, le degré d'oxydation du métal de transition augmente pendant l'OER et diminue pendant l'ORR. En revanche, le degré d'oxydation de ces mêmes métaux de transition est très stable dans les pérovskites mixtes $\text{LaMn}_{0.7}\text{Co}_{0.3}\text{O}_3$ et $\text{LaMn}_{0.6}\text{Co}_{0.4}\text{O}_3$. L'énergie du seuil à mi-hauteur indique que les pérovskites mixtes contiennent du Mn^{4+} et du Co^{2+} , ce qui suggère que les rôles prédominants de Mn et Co en ORR et OER sont inversés : le Mn^{4+} serait l'espèce active en OER et le Co^{2+} l'espèce active en ORR.

Dans le dernier chapitre, nous utilisons un électrocatalyseur modèle, Co_3O_4 , bien connu pour son activité en OER, de façon à comparer les résultats obtenus par deux techniques *operando*: le XAS et la microscopie électronique à transmission (TEM). La réversibilité de l'oxydation de Co_3O_4 en OER a été affirmée dans la littérature. Nos travaux montrent bien l'oxydation du matériau en OER, mais les résultats obtenus dans le cadre de l'évolution du degré d'oxydation du cobalt après l'OER sont différents de ceux attendus : une réversibilité seulement partielle est observée. Cette conclusion s'appuie sur les résultats de XAS obtenus aux seuils L et K du cobalt et les résultats TEM (imagerie et spectroscopie EELS). Les résultats contradictoires obtenus entre les différentes techniques peuvent provenir de conditions d'analyse différentes, inhérentes aux techniques utilisées. Par exemple, nous pouvons nous interroger sur l'influence des conditions d'analyse de l'échantillon, notamment à l'exposition au vide nécessaire à l'analyse par XAS au seuil L du Co et par EELS, qui peut réduire les métaux de transition. Parallèlement à ceci, les conditions expérimentales d'étude des échantillons doivent être considérées en fonction des techniques d'analyse utilisées : l'électrode est toujours en contact avec l'électrolyte, au contraire de l'état *post-mortem*, où le matériau est complètement retiré de la cellule électrochimique et séché. Dans ce dernier cas, l'analyse de l'échantillon peut se dérouler durant plusieurs heures, voire plusieurs jours, après l'expérience électrochimique (i.e. XAS au seuil L du cobalt et EELS), pouvant entraîner une modification de l'échantillon. Ainsi, les résultats divergents obtenus par ces différentes techniques montrent que nous ne caractérisons pas l'électrocatalyseur dans le « même état ». Parallèlement, nous suspectons

que les chemins réactionnels peuvent être influencés par les conditions d'analyse : quel est l'impact du faisceau de rayons X du XAS ou du faisceau d'électrons du TEM sur l'électrocatalyse ? Ces interrogations nous mènent à nous demander laquelle de ces techniques est la plus adaptée pour décrire l'activité électrocatalytique.

Toutes ces observations mettent en lumière la difficulté de développer des techniques *operando* en électrocatalyse du fait des conditions d'analyse (interface solide/liquide, formulation d'électrode complexe (polymère, carbone/électrocatalyseur)) peu compatibles avec les conditions d'observation optimales en XAS ou microscopie, des temps de vie des espèces électroactives parfois incompatibles avec les techniques d'observation pouvant conduire à des conclusions non représentatives des conditions d'électrocatalyse. Des compromis (préparation d'électrode adaptée à la technique d'observation, conditions d'observation particulières) sont souvent adoptés, mais ils peuvent impacter le cycle électrocatalytique et *in fine* les conclusions de l'étude. La vérification en aval de la fidélité des expériences électrochimiques *operando* par rapport à celles *ex situ* est nécessaire, bien que souvent délicate. La comparaison des résultats obtenus entre plusieurs techniques *operando* (ce que nous avons fait dans le cadre de cette thèse, avec le XAS et le TEM), semble donc être une approche intéressante pour limiter les conclusions hâtives qui peuvent s'avérer parfois inexactes.

General introduction

The next significant transformation in the energy transition is likely to include hydrogen economy. Hydrogen can be used in different ways as a feedstock, a fuel or an energy carrier and storage and it does not emit CO₂ when used¹. It thus offers a solution to decarbonize industrial processes and economic sectors where reducing carbon emissions is both urgent and hard to achieve. Interest in hydrogen is growing in Europe and all around the world, with a demand increasing rapidly.

The priority for the EU² is then the development of renewable hydrogen, produced through the electrolysis of water, with electricity stemming from renewable sources including solar energy and wind. It needs to be cost-competitive against fossil-based hydrogen around 1.5 euros kg⁻¹.³ This is possible in regions where renewable electricity is cheap and by a reduction by half of the cost of the actual electrolyzers. This calls to the development of new electrocatalysts exempt of platinoids in particular for the oxidation of water. In parallel, an understanding of the oxygen evolution reaction mechanism (OER) on these “new” catalysts is highly needed in order to overcome the sluggish kinetics of this reaction.

The quest of developing “efficient” OER electrocatalysts has led to many investigations of the OER mechanisms. These studies linked often the electrocatalytic performances of the electrocatalysts to their structure⁴. The development of *operando* techniques, which can analyze electrocatalysts while they operate during electrocatalysis, has in particular brought new insights in the identification of the active “site” or “species” as the stability of these species are often poor when the electrocatalyst is at a resting state inside (*in situ*) or outside (*ex situ*) the electrochemical environment. Since the discovery of these unstable and active species, *operando* analysis has become indispensable to fully describe the activity of an electrocatalyst.

One of the most commonly employed *operando* techniques is the X-ray absorption spectroscopy (XAS) because it provides information on both the oxidation state of the metals and their local environment. XAS is a technique that probes the entire volume of a material and is therefore sensitive to “bulk” transformations, which might appear poorly suited to assess surface events occurring during electrocatalysis. Fortunately, the development of new synthesis processes, driven by the need to increase the surface-to-volume ratio for enhancing

General introduction

the mass activity of electrocatalysts, has allowed the fabrication of nanoscaled electrocatalysts exhibiting high specific surface area, where the significant portion of surface atoms versus the overall volume renders XAS able to probe events occurring at this surface.

However, while the efficiency of XAS in the *ex situ* characterization of various electrocatalysts has been proven many times, the use of *operando* XAS in electrocatalysis is currently merely limited to the observation of the evolution of the oxidation state of the constituent elements⁵, or the identification of characteristic interatomic distances under electrocatalytic conditions⁶.

In this context, the aim of this PhD thesis is to go further in the development of *operando* XAS by extending *ex situ* XAS data treatment to *operando* experiments. By using nanomaterials with high specific area, we probe the electroactive species and follow their evolution in regards of the applied potentials and of the duration of the experiment. Finally, coupling XAS with complementary *operando* techniques such as surface specific analysis or microscopies allows a multiscale description of the electro catalyst. These topics will be illustrated through the analysis of three family of materials, on which our current level of understanding varies.

The first chapter will present the basics of X-ray absorption spectroscopy, the information that can be extracted from X-ray absorption spectra, but also the grey area that can remain on the understanding of the electrocatalyst behavior after the interpretation of the spectra, therefore highlighting the complementarity of XAS and other *operando* techniques to fully describe an electrocatalyst.

In the second chapter, we analyze nickel boride nanoparticles, which are electrocatalysts of the hydrogen evolution reaction (HER) at acidic pH and of the oxygen evolution reaction (OER) at basic pH. Because of their complex crystal structure, metal borides have rarely been accurately characterized by XAS in their pristine form and the role of boron on the electroactivity is not clearly established. By using linear combination fitting (LCF) and Fourier transform EXAFS (FT-EXAFS) fitting, we will show that such challenging materials can be monitored by *operando* XAS and that even quantitative information can also be extracted.

In the third chapter, we study perovskite oxides, whose activities in OER and ORR (oxygen reduction reaction) at high pH are correlated to the nature of the transition metal(s)

General introduction

inside the perovskite. The scarce reports on *operando* analysis of these materials did not tackle how the presence of two transition metals together inside one perovskite may impact electroactivities usually independently related to each metal. We will analyze the XAS of manganese cobaltite perovskite on Mn and Co K-edges and monitor the temporal evolution of the oxidation state of Mn and Co during OER and ORR.

In the fourth chapter, we will use Co_3O_4 spinel, a deeply investigated OER electrocatalyst, as a model. The objective is to compare the conclusions of two different *operando* studies: XAS and transmission electron microscopy (TEM). We will then discuss the divergence of the results and assess to what extent we can combine the results of *operando* experiments between different techniques.

Chapter I:
State of the art

1. Introduction

1.1. Global energy context

The global energy demand is constantly increasing and should reach 30 000 TWh in 2030 (Figure I - 1 Global energy demand (in TWh) by region⁷.Figure I - 1). To meet this urging demand, the diversification of energy sources, adding to the will to progressively reduce the contribution of fossil energies, promotes the development of renewable energies (solar, wind, hydro...). However, the intermittent energy production of these alternative sources requires devices that can store energy, whether as electricity (batteries) or as chemical bonds (electrolyzers and fuel cells).

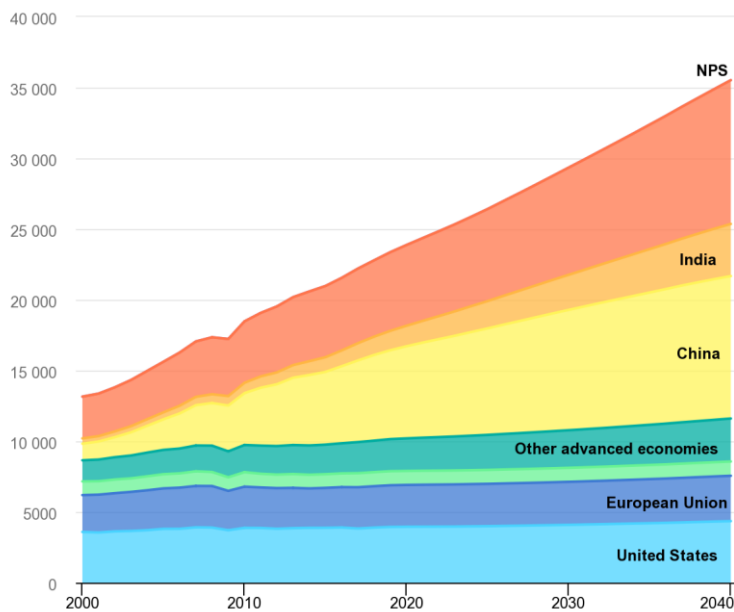


Figure I - 1 Global energy demand (in TWh) by region⁷.

1.2. Batteries, electrolyzers and fuel cells

Batteries are widely used for the storage of electricity. Lithium-based battery is one of the most advanced technologies in this field with many applications in vehicles, electronics, etc. New lithium battery concepts such as lithium-metal, lithium-oxygen and lithium-sulfur batteries are being studied⁸, which would provide better performance while avoiding the use of expensive transition metals. Lithium-oxygen batteries raise attention because their theoretical specific energy is high compared to the conventional lithium-ion batteries (2000 vs. 600 W h kg⁻¹)⁹. Another advantage is that it uses air as a cost-effective

Chapter I: State of the art

and light reagent: during the discharge, oxygen is reduced at the positive electrode by electrons and combines with lithium ions that are supplied from the negative electrode (metal lithium) to form Li_2O_2 . However, the current densities of Li- O_2 cells hardly reach 1 mA cm^{-2} while lithium-ion batteries usually reach currents around 30 mA cm^{-2} . A better understanding of the oxygen reduction reaction (ORR) at the positive electrode and of its counterpart oxygen evolution reaction (OER) involved during charge should help improve the performances of lithium-air batteries.

Dihydrogen is a medium that can store energy in its chemical bond with a specific energy of 142.2 MJ kg^{-1} .¹ However, this gas is currently produced from the combustion of fossil fuels¹⁰ which is responsible for CO_2 emissions of more than 800 million tons per year¹⁰. The electrolysis of water into dihydrogen and oxygen is a very promising technology to store electrical energy into chemical bonds without CO_2 emissions. The energy required for this reaction can be obtained by many energy sources, the most attractive ones being renewable energies, such as wind-turbines or photovoltaics. In solar water-splitting cells, the electrolysis of water can be coupled with photoelectrodes to store solar energy and therefore provide a carbon-free dihydrogen source. Conversely, fuel cells can be designed with H_2 and O_2 as fuels, and water and electricity as the products of the reaction. Electrolyzers and fuel cells rely on the OER and ORR, respectively, on the oxygen electrode, while, on the hydrogen electrode, the reactions are the reduction of water into hydrogen (HER) and the oxidation of hydrogen into water (HOR). The reactions at the oxygen electrode are much slower than the reactions at the hydrogen electrode. As for the case of lithium-air batteries, OER and ORR are major bottlenecks to the development of water-splitting devices and advances in the understanding and the improvement of the performances of these reactions shall highly impact the efficiency of these devices.

2. Oxygen evolution reaction (OER) and oxygen reduction reaction (ORR)

2.1. The mechanisms of OER and ORR

At basic pH, the oxygen evolution reaction is: $4HO^- \rightarrow O_2 + 2H_2O + 4e^-$. Since the electrons are transferred one at a time, this is a multistep reaction that generates several intermediates at the surface of the electrode.

While various mechanisms have been proposed in the literature¹¹⁻¹⁵, most of them initiate the OER by the adsorption of a HO^- ion to form the hydroxide intermediate MOH on a catalytically active surface site, M. The equilibrium potential voltage of the OER is 1.23 V/SHE. However, the kinetic barrier of this reaction requires an additional overpotential that needs to be overcome. Following the mechanism displayed in Figure I - 2, Rossmeisl et al.¹⁶ used theoretical calculations of the free energies of adsorption of each intermediates of the OER reaction to highlight that the rate-determining step is the formation of MOOH from MO (ΔG_3). Consequently, stabilizing the intermediate MOOH intermediate should reduce the overpotential of the reaction.

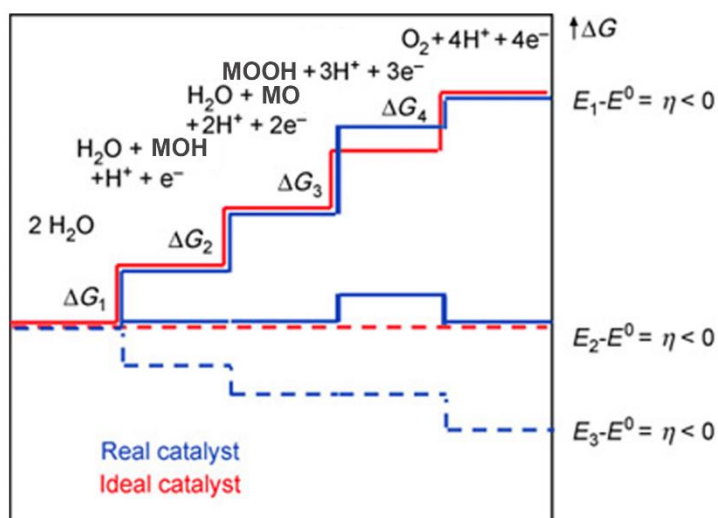


Figure I - 2 Gibbs free energy of adsorption of reactive species and intermediates of the OER in acidic medium. Inspired from Dau et al.¹⁷.

Chapter I: State of the art

The oxygen reduction reaction is the reverse reaction of the OER. Hence, it is also a multistep reaction, which either follows an associative mechanism (O_2 is adsorbed on the catalytic site before breaking of the O-O bond) or a dissociative mechanism (The O-O bond is first broken, yielding MO species, followed by reduction of oxygen on two separate catalytic sites). Rossmeisl et al.¹⁸ also used DFT calculations to identify the rate-determining step of the ORR. They concluded that the high stability of adsorbed oxygen MO prevents the transfer of proton and electron at high potential during the step $MO + H^+ + e^- \rightarrow MOH$, which explains why an overpotential is required to destabilize oxygen. The authors also highlighted that both associative and dissociative mechanisms can contribute to the ORR, depending on the catalytic metal and the applied potential.

Overall, both OER and ORR are slow because of the high stability of the intermediates. Increasing the overpotential or modifying the catalytic site can destabilize these intermediates and fasten the reactions. The energetic cost-efficiency of the modification of the catalytic site has led to the development of electrocatalysts to reduce the overpotential required to activate the reactions.

2.2. Defining the electrocatalytic activity

A good electrocatalyst must be highly active, stable and efficient on a long time-scale in order to be employed in the targeted devices. These characteristics are quantified through several descriptors.

2.2.1. The overpotential and the current

The simplest way to analyze the electrocatalysts activity is to compare their overpotentials, required to produce the same current. The overpotential is defined as the difference between the thermodynamic potential of an electrochemical half-reaction and the experimental potential. The most efficient electrocatalyst is then the one with the lowest overpotential because it is the one that needs the less energy to be activated. Likewise, the most active electrocatalysts show the highest currents at a given overpotential.

2.2.2. The Tafel slope

The relationship between the current I and the overpotential η can be described by the Tafel relationship: $\eta = b * \log(I/I_0)$ where b is the Tafel slope and I_0 is the exchange current, which is the intercept at $\eta = 0$, extrapolated from a linear portion of the plot of η versus $\log(I)$. The Tafel slope, b , quantifies the amount of energy necessary for the

Chapter I: State of the art

electrocatalyst to trigger a current increase. Consequently, a low Tafel slope reflects an electrocatalyst that requires little energy intake to become more active. Some reaction mechanisms can also be determined by further investigation of the Tafel plot^{19,20}.

2.2.3. Normalized current

Because electrocatalysis –and more generally catalysis– is a surface process, two materials of the same composition with different specific areas have different mass-normalized electroactivities. The electrocatalyst with the highest specific area is the most active, because of its higher surface-to-volume ratio, hence its higher amount of surface catalytic sites per volume unit. To calculate the intrinsic activity of the material, the current is normalized to the specific surface area of the electrocatalyst.

2.2.4. Turnover frequency

The turnover frequency (TOF) is the number of catalytic cycles occurring at an active site per time unit and is calculated following the relation: $TOF = \frac{I}{nFm}$, where I is the current, n is the number of electrons exchanged in one cycle, F is the Faraday constant and m is the number of active sites. The TOF enables to assess the intrinsic activity of catalytic sites.

This variety of descriptors illustrates that the performances of an electrocatalyst result from the convergence of different properties of the materials, such as the intrinsic activity or the specific surface area and that the efficiency of an electrocatalyst may depend on the considered descriptor.

2.3. Common electrocatalysts and current research trends

Currently, noble metal–based materials are the benchmark in electrocatalysis at low pH. Platinum is the most active and stable pure metal electrocatalyst for HER and ORR in acidic medium^{21,22}, with an ORR overpotential around 0.4 V for a current density of 1.5 A cm⁻².²³ However, it is less efficient in OER as it undergoes oxidation^{24,25}. Rutile IrO₂ and RuO₂ are the gold standards of OER catalysts²⁶ as they have sustained OER activity in low pH solutions. The TOF of iridium oxide can reach 10 s⁻¹ at an overpotential of 250 mV²⁷. However, IrO₂ is not completely stable under high oxidative potentials^{21,28,29}.

Because of the scarcity and high cost of noble metals³⁰, alternatives are sought out, especially among transition metal-based materials³¹. They can be applied for different electrocatalytic reactions thanks to the various oxidation states that transition metals can

Chapter I: State of the art

bear. For instance, Co^{2+} exhibits a high ORR electrocatalytic activity because it favors O_2 adsorption, whereas $\text{Co}^{3+/4+}$ facilitates OH^- anion adsorption, giving these cations a high OER activity³². In alkaline solutions, several non-precious metal oxides are reported to have higher OER activity than IrO_x , like NiFeO_x ¹³.

The cost can also be lowered by reducing the amount of electrocatalyst required for a similar electrocatalytic activity, namely by increasing the surface-to-volume ratio of the material or its intrinsic activity⁴. Nanostructuring has brought nanoelectrocatalysts with high specific surface area, whose activity is enhanced thanks to the high number of active sites^{33,34}, but also to a higher doping of oxygen vacancies or charge carriers created at the surface of the electrocatalyst that increases the conductivity of the material³⁵.

The intrinsic activity of the electrocatalyst is highly dependent on the chemical composition. In their studies on transition metal-based perovskite oxides, Shao-Horn et al. correlated the OER and ORR activities of these materials to the occupation of the e_g orbitals of the transition metal.³⁶ If the e_g occupancy is lower than 1, the rate-determining step is the deprotonation of the oxyhydroxide group (ΔG_4 on Figure I-2), while if the e_g occupancy is higher than 1, the rate-determining step is the formation of the O-O bond (ΔG_3 on Figure I-2). They concluded that an e_g occupancy slightly higher than 1 provides the highest activity in OER³⁶, while an e_g occupancy lower than 1 favors the activity in ORR³⁷. According to their model, they identified $\text{Ba}_{0.5}\text{Sr}_{0.5}\text{Co}_{0.8}\text{Fe}_{0.2}\text{O}_3$ as the perovskite that has the highest activity in OER³⁶. Metal-heteroatom bonds can also modify the activity of the active site and many families of compounds have been studied since then, including metal borides^{38,39}, phosphides³⁸, and fluorides⁴⁰. But even with the same composition, the electrocatalytic activity of a material may vary depending on the crystallographic structure⁴¹, the crystallographic orientation²², the defect density or the local surface composition^{42,43}.

In the search for high electrocatalytic performances, the stability of the material during the electrocatalysis is the second main criterion for any viable application. Nowadays, the OER/ORR-based devices are using electrolytes with low pH, where precious metals are currently the only stable electrocatalysts⁴⁴.

Several pathways are explored to increase the cost-effectiveness of OER/ORR electrocatalysts. While a plethora of performant materials are proposed every year, the understanding of the electrocatalytic activity is often limited to the analysis of the pristine

form of the catalyst, before operation. The last decades have seen the emergence of *in situ/operando* techniques that can analyze electrocatalysts inside an electrochemical cell/during electrocatalysis and probe the exact nature of electroactive species. One of the most used techniques is X-ray absorption spectroscopy.

3. *Operando* X-ray Absorption Spectroscopy

3.1. Fundamentals of XAS

X-ray absorption spectroscopy relies on the excitation of core electrons by a photon. Depending on the energy of the photon, different physical processes can occur. If the photon energy, $h\nu$, is higher than the energy of absorption, E_0 , the coefficient of absorption, $\mu(E)$, increases drastically as the photoelectron is emitted to the continuum (Figure I - 3). The ramp of absorption around E_0 , where $\mu(E)$ increases greatly, is called the edge. If the energy is lower than E_0 , the emission does not occur and the $\mu(E)$ is close to 0. If the energy is higher than E_0 , the photoelectron is emitted to the continuum with a kinetic energy $(h\nu - E_0)$. $\mu(E)$ then fluctuates around a constant value, which is fixed to 1 after normalization.

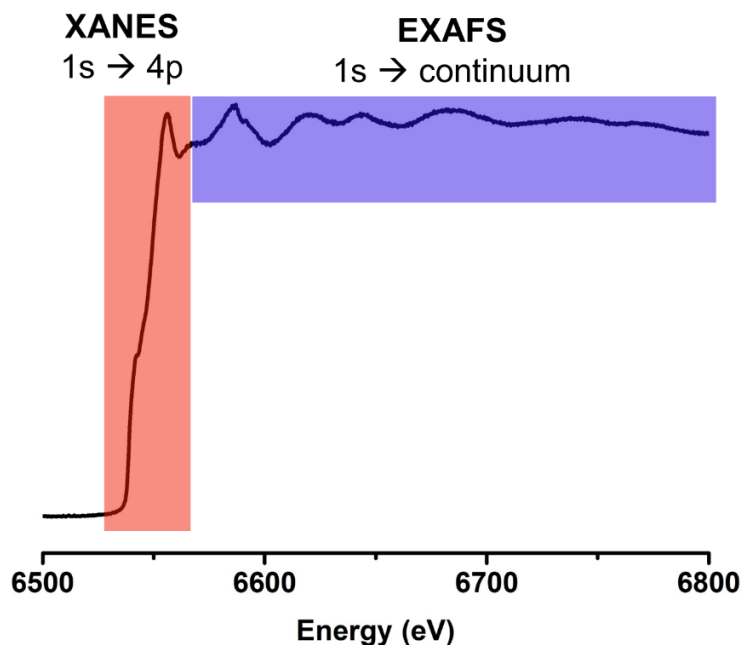


Figure I - 3 Mn K-edge XAS of metal Mn. The XANES area is in red. The EXAFS area is in blue.

Chapter I: State of the art

3.1.1. The XANES

The XANES (X-ray Absorption Near-Edge Structure) spectrum is the area of the spectrum that spreads from a few eV before the edge to around 50 eV after the edge. It contains information about the local environment of the absorbing atom and its electronic structure. If the energy of the photon is high enough to excite an electron, but still lower than E_0 , the electronic transition occurs to the first vacant levels. In the case of transition metals, it is usually the 3d orbitals. In theory, the 1s \rightarrow 3d transition is forbidden. Yet, it is allowed when 4p and 3d orbitals are mixed. This phenomenon results in a low intensity peak before the edge, which is called the pre-edge. The hybridization of 4p and 3d orbitals is the highest in a structure with a tetrahedral geometry, yielding a high pre-edge, and it is the lowest in a structure with an octahedral geometry,⁴⁵ which should give a negligible pre-edge. Consequently, in a K-edge absorption spectrum, the symmetry of the local environment of an atom can be determined by the intensity of the pre-edge (Figure I - 4). The electronic occupancy of a valence band can be determined by the intensity of the transition to its level. In the K-edge of transition metals, only the intensity of the pre-edge informs on the occupation of the 3d⁴⁶ orbitals, whereas the analysis of L_{2,3} edges, which directly probe the 3d levels, gives access to the occupation of 3d levels by comparing their integrated intensities⁴⁷. The energy of ionization E_0 , i.e. the position of the edge, is highly dependent of the oxidation state of the ion. Oxidizing an atom first decreases screening effect and thus stabilizes core levels. Second, it shortens distances and destabilizes antibonding levels. Consequently, transitions are shifted to higher energies (Figure I - 5).

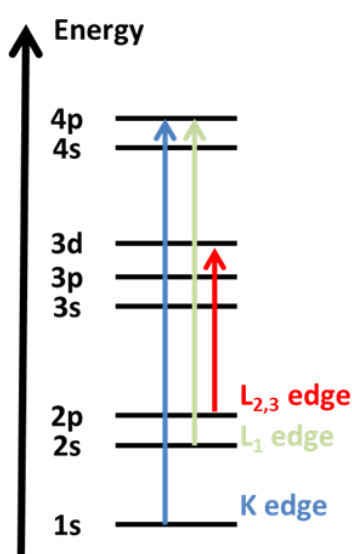


Figure I - 4 Illustration of K-edge (in blue), L₁-edge (in green) and L_{2,3}-edges (in red).

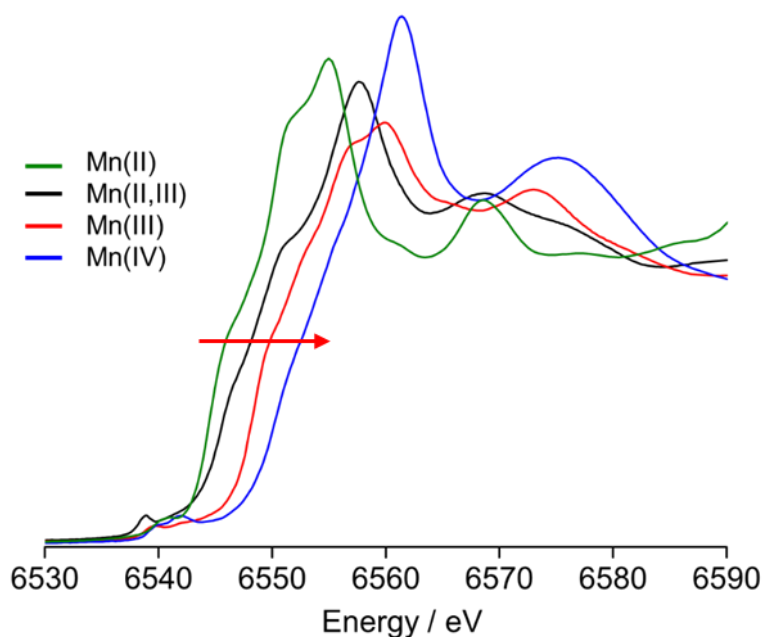


Figure I - 5 Manganese K-edge XAS of different compounds where manganese oxidation state varies from +II to +IV. The red arrow indicates the shift of the edge energy when the oxidation state of Mn increases.

3.1.2. The EXAFS

The area from 50 eV to 1000 eV after the edge is called EXAFS (Extended X-ray Absorption Fine Structure). The electron is ejected with a high kinetic energy and is scattered by the atoms neighboring the absorbing atom. The scattering wave interferes with itself. As this interference at the absorbing atom varies with the energy, the value of the absorption coefficient $\mu(E)$ oscillates as well. The Fourier transform of these oscillations is a convolution of peaks and each of them describes a scattering path (Figure I - 6). Because the elastic mean free path of a photoelectron in the EXAFS domain is short ($\lambda < 10 \text{ \AA}$), the influence of the multiple scattering paths is negligible and usually only the single scattering path is taken into account. Consequently, each peak of the Fourier transform EXAFS characterizes a distance between the absorbing atom and neighboring atoms, based on different parameters: the nature of the neighbor, the distance value, R , the number of neighbors at the same distance, N , and the fluctuations of this distance evaluated by the Debye-Waller factor, σ^2 . The values of these parameters are determined by fitting the whole EXAFS domain.

Chapter I: State of the art

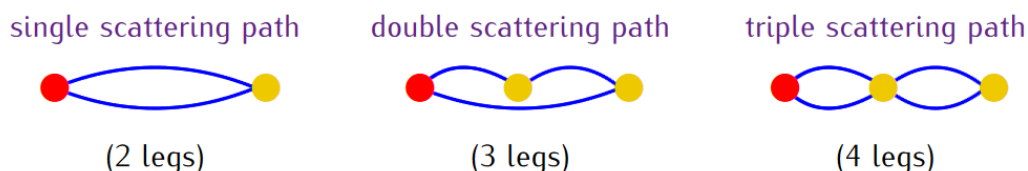


Figure I - 6 Scheme of multiple scattering paths. The absorbing atom is in red. The scattering atoms are in yellow⁴⁸.

X-ray absorption spectroscopy is a powerful tool that provides an in depth analysis of the electronic structure, the local structure and the local environment of an element. The wide range of energies provided by synchrotron radiation allows the measurement of the K- and/or L-edge of nearly hundred elements. Moreover, this spectroscopy is highly selective and rarely suffers from the superposition of edges of different elements. On the range of the K-edges of transition metals, which are at most 1000 eV, the only interfering elements are the K-edges of the following atom in the periodic table and the L-edge of heavy atoms (Table I - 1).

Element	Mn	Fe	Co	Ni
K-edge (eV)	6539.0	7112.0	7708.9	8332.8
1 st interference	Ce	Nd	Sm	Gd

Table I - 1 Energy of the K-edge of some transition metals along with the lightest element whose L-edge is higher than the K-edge of the transition metal⁴⁹.

3.1.3. Spectrum collection

The X-ray absorption spectrum can be collected by three modes of detection: transmission, fluorescence yield and total electron yield.

The transmission mode follows the relation: $I_{tr} = I_0 \exp[-\mu(E)x]$ where I_{tr} is the intensity of the transmitted beam, I_0 is the intensity of the incident beam, $\mu(E)$ is the absorption coefficient and x is the thickness of the sample. Consequently, $\mu(E)$ can be measured through I_{tr} and I_0 . This transmission mode of acquisition is adapted for concentrated systems at energies high enough to penetrate the sample. From a practical point of view, as the transmission beam passes through the whole sample, it is well adapted for isolated materials. However, analyzing a compound on a complex setup may become tricky, as the X-rays can also be absorbed by any other component situated on their path.

Chapter I: State of the art

In the fluorescence yield, we measure the intensity of the fluorescence emitted by the sample after excitation of the core electron by the absorbed X-rays fluorescence. With a penetration depth of around $1 \mu\text{m keV}^{-1}$, this mode is adapted for many materials and especially for diluted samples. Yet, distortions provoked by self-absorption and saturation effects have been reported on the L_3 -edge XAS with different degrees of impact depending on the element.⁵⁰ Advanced fluorescence modes, such as partial-fluorescence yield and inverse partial fluorescence yield, have been investigated to overcome this problem.⁵⁰

Finally, XAS can be performed by measuring the Total Electron Yield (TEY). The absorbed X-rays create photoelectrons through the excitation of core electrons. The created holes are filled by Auger decay that emit Auger electrons. The TEY intensity quantifies the number of Auger electrons and of scattered secondary electrons created by these Auger electrons. Clearly, this mode is only adapted to conductive samples. The probed depth depends on the electron mean free path, which may vary from 10 to 100 nm depending on the energy. It is usually employed for surface analysis. During *operando* electrochemical experiments, this electronic mode of detection may interfere with the current coming from charge transfer during electrocatalytic reactions.

3.2. Historical background of *in situ* XAS

Before being applied to electrocatalysis, XAS was one of the many *in situ* methods employed in the battery research^{51,52} to analyze the electrode during the charge process⁵³ or during its thermal decomposition⁵⁴. For instance, Nam et al. recently studied the $\text{Li}_x\text{Ni}_{0.8}\text{Co}_{0.15}\text{Al}_{0.05}\text{O}_2$ and $\text{Li}_x\text{Ni}_{1/3}\text{Co}_{1/3}\text{Mn}_{1/3}\text{O}_2$ cathodes and the evolution of XAS at the K-edge of the transition metals during heating⁵⁴. From the shifts in the XANES, they highlighted the reduction of the transition metals induced by the release of oxygen. From the EXAFS, the authors detected transition metal-based spinels as the product of the thermal decomposition of the electrodes.

The growing interest dedicated to the electrode/electrolyte interface has led to the application of XAS to thin film electrodes (c.a. 50 nm^{55}), thus proving that this bulk technique can also be employed to analyze surface phenomena such as electrocatalysis. The main difficulty of probing electrocatalysis by XAS is the identification of the active site of the material, which requires studies under *operando* conditions, i.e. when an electrochemical potential is applied. Eventually, the development of *operando* cells adapted to XAS in several synchrotrons has allowed the analysis of electrocatalysts inside an operating

Chapter I: State of the art

electrochemical cell⁵⁶⁻⁵⁸. The next challenges include the advancing of the exploitation of XAS analysis on *operando* experiments and the coupling of XAS with other *operando* techniques to obtain complementary information. This requires the design of *in situ* electrochemical cells adapted for multiple techniques of analysis.

3.3. Information provided by XAS on materials

3.3.1. Oxidation state and local structure

The most important information extracted from XAS is the oxidation state and the local structure of the absorbing element. The oxidation is mostly indicated by a shift of the edge^{56,59,60}, while the local structure is deduced from the pre-edge (for the symmetry) and the EXAFS of the K-edge (for the distances between the absorbing atom and its neighbors). Friebel et al. studied Pt/Au(111) and observed a shift of the Pt L₃-edge to higher energy when a high potential is applied⁵⁹. They attributed this shift to the oxidation of metal Pt⁰ to Pt^{IV} that is induced by the dissolution of the noble metal.

3.3.2. Site occupancy

When the absorbing atom occupies different sites, XAS can determine the occupation of each site. In materials that contain transition metal ions in various crystallographic sites, the site occupancy can have a high impact on the reactivity during electrocatalysis^{61,62}. As the pre-edge of the K-edge is sensitive to the symmetry⁴⁵, if an element occupies two sites with different symmetries, the ratio of each site can be determined by the intensity of the pre-edge. The deconvolution of the L_{2,3}-edges, which are directly impacted by the energy and the occupation of the 3d levels, also informs on the contribution of each site and can also discriminate the oxidation state. Kwon et al. analyzed the Co L₃-edge and the pre-edge of the Co K-edge of amorphous cobalt borate (CoBi) and cobalt phosphate (CoPi)⁶³ (Figure I - 7). They deconvoluted the peaks and observed that in CoBi both Co^{III} and Co^{II} are in octahedral symmetry, whereas the fit of the Co L₃-edge of CoPi requires, in addition to the previous Co^{III} and Co^{II} in octahedral symmetry, another component corresponding to Co^{II} in tetrahedral sites. The existence of Co^{II} in tetrahedral site could explain the higher electron-proton conductivity of CoBi compared to CoPi.

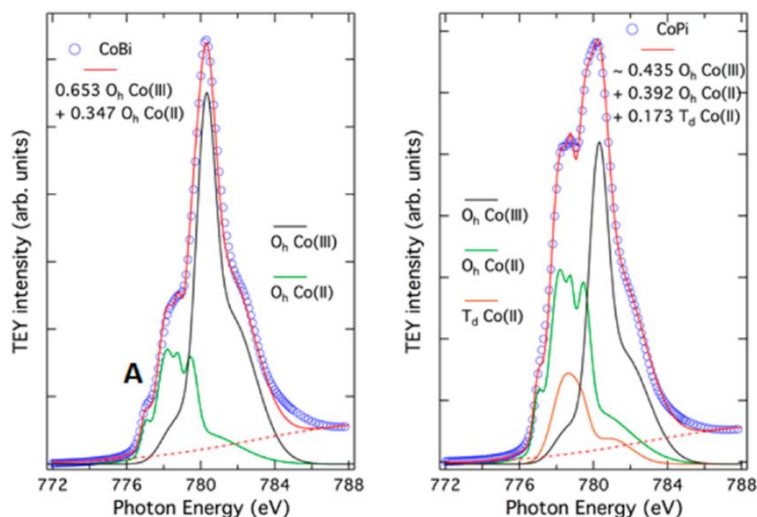


Figure I - 7 XAS at the Co L_3 -edge of CoBi (left) and CoPi (right) with linear combination fittings with the O_h Co^{III} , T_d Co^{II} , O_h Co^{II} reference spectra. Figures extracted from ⁶³.

3.3.3. Nanoparticle size

Quantitative information on nanoparticle size and shape are also provided by XAS, especially by fitting the EXAFS to calculate the number of neighbors of each paths. If the experimental number of neighbor is lower than the theoretical one, it can indicate defects in the structure, a low range order for amorphous materials, a small nanoparticle or cluster size for crystalline compounds. Bediako et al. calculated the size of ordered domains in anodized nickel oxide films from the number of neighbors evaluated by the fit of the EXAFS of the activated material, compared to the reference γ -NiOOH⁶⁴.

3.3.4. Surface sensitivity

Electrocatalysis is a surface phenomenon while XAS is probing the bulk structure. We can ask ourselves whether this spectroscopy is a valuable technique for probing surface phenomena. The answer is highly dependent on the size and the amplitude of the expected surface modification. For instance, a change on a 1 nm layer of a 10 nm thick film will impact 10 % of the XAS signal. On a nanoparticle of 10 nm, a modification on a 1 nm layer would impact 27 % of the XAS signal. On the other hand, the XAS sensitivity varies with the nature of the modification: an increase of the oxidation state from Co^{III} to Co^{IV} implies an energy shift of less than 1 eV⁵⁶ and is less easy to measure than a shift of 2 eV from Pt^0 to Pt^{IV} ⁵⁹. Consequently, it is not trivial to establish a general critical size below which the XAS signal can be significantly impacted by surface states. Furthermore, the definition of a

Chapter I: State of the art

critical size only applies to nanoparticles, while XAS is also suited to nanoporous materials whose specific area can be comparable to nanoparticles.

Conversely, as XAS describes an average state of the material, how can we state that any impact on the XAS signal is due only to a surface modification rather than a bulk phenomenon? The discrimination requires supplementary investigation, the first one being comparing XAS results between bulk samples and thin film or nanostructured materials: Kanan et al. compared the *in situ* XAS of CoPi in thin film and in bulk form⁶⁵. They observed a significant energy shift of the Co-K edge between the activated and the open circuit voltage (OCV) states when CoPi was in the thin film form. This shift was not detected on bulk CoPi, proving that this phenomenon is located at the surface. Another option would be to use complementary techniques of analysis that are specific to the surface, e.g. XPS (Figure I - 8). Eventually, the strength of XAS is that it can detect any significant change whether in the core or on the surface of the material. Determining the localization of this change requires further investigation.

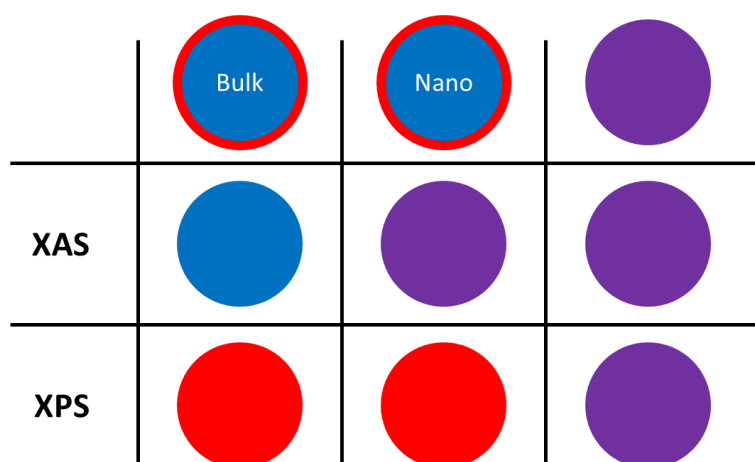


Figure I - 8 Schematic response of XAS and XPS according to the structure of a biphasic material. Phase 1 is in blue. Phase 2 is in red. Mixed phases 1 and 2 is in purple. From left to right: phase 2 is a surface layer on a bulk phase 1, the phase 2 is a surface layer on a nanoscaled phase 1, and the phases 1 and 2 are mixed inside the material.

While XAS can bring such variety of information on materials, *operando* XAS studies rarely fully exploit the potential of this spectroscopy. Most of them only study the qualitative evolution of the oxidation state and the inter-atomic distances⁵⁶. As for the remaining types of information, other *operando* techniques that are more specific to a given piece of information are generally called into to also bring additional insights on elements that are unobtainable from XAS.

4. Other *in situ* studies for electrocatalysis

As stated previously, *in situ* XAS encounters grey areas in the investigation of electrocatalysts and sometimes requires the support of complementary techniques to bring solid conclusions. The most common *in situ* techniques (spectroscopies, microscopies and X-ray diffraction) are summarized in the review of Choi et al.⁶⁶ In this section, we will focus on new insights that these alternative techniques could bring to *in situ* XAS for the study of electrocatalysts.

4.1. Time resolution

Electrocatalysis involves fast reactions that can reach a TOF of 10 s^{-1} ²⁷. Observing the different steps of the mechanism would require instruments with a time resolution below 100 ms, which is not the case of XAS. The scan rate at which the spectra are collected varies from one beamline to another. Some beamlines, such as ROCK at SOLEIL, are equipped with a quick-EXAFS monochromator that allows the collection of a few spectra per second, but they are still not fast enough to decompose the electrocatalytic cycle in a trivial way. Instead of scanning an energy range, X-ray emission spectroscopy uses one single incident X-ray energy to excite the metal above its electron binding energy and uses a wavelength-dispersive spectrometer to collect emission spectra shot by shot. This method allows monitoring several edges at once. For instance, Gul et al. followed the $K\beta_{1,3}$ of Mn and Ni in MnNiO_x and showed that the presence of nickel allowed manganese to reach higher oxidation state during OER⁵⁸ (Figure I - 9). Such technique allows the collection of spectra on a very short time. However, this fast recording speed has consequence on the quality of the data. For instance, the spectra presented in the article were recorded during an hour. There is then a tradeoff between the speed of recording and the signal-to-noise ratio.

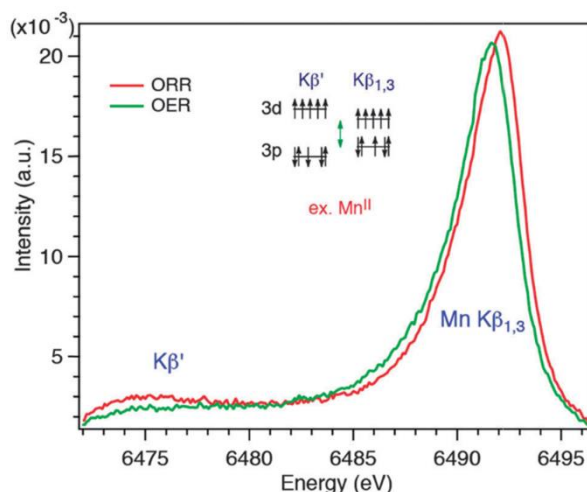


Figure I - 9 Mn $K\beta_{1,3}$ XES spectra of the $MnNiO_x$ catalyst under ORR and OER conditions. Figure taken from ⁵⁸. Acquisition time: 1 h

4.2. Surface state

An accurate description of the surface of the electrocatalyst is key for describing mechanisms occurring during electrocatalysis. X-ray photoelectron spectroscopy (XPS) is the most common method to characterize surface states^{67–73}. The development of *in situ* XPS is confronted to the adaptation of this technique, which is usually carried out under vacuum, to near ambient pressure experiments. Near-ambient-pressure-XPS (NAP-XPS) with pressures up to 10 mbar, enables the presence of a gas reagent near the surface of the electrocatalyst⁷⁴. Electrocatalytic experiments can also be carried out on “ambient pressure” XPS (AP-XPS) at 30 mbar by a “dip and pull” method⁷⁵. In this experiment, the electrode is partly removed from the liquid electrolyte so that the emerged part of the electrode is covered by a thin film of electrolyte. The emerged part of the electrode can then be analyzed by *operando* AP-XPS while it is still in contact with the whole electrochemical setup through the electrolyte film. Eventually, even if great advances have to be highlighted, the low pressure environment (despite the erroneous nomination of “AP-XPS”) is still a bottleneck to *in situ/operando* XPS analysis of electrocatalysts in a liquid electrolyte.

Chapter I: State of the art

4.3. Phase evolution

As XAS describes the environment of the absorbing atom on a short-range, it is not adequate to detect long-range order, which can give insights on the stability of the material or its active phase. *Operando* X-ray diffraction (XRD) is well developed for electrode materials in batteries⁷⁶. Analyzing electrocatalysts through this technique can bring information about phase modification or lattice shrinking or relaxing. Reikowski et al. studied Co_3O_4 (111) epitaxial thin films deposited on gold during OER by *operando* XRD⁷⁷. They observed a decrease of the size of Co_3O_4 domains during OER that they attributed to the formation of a thin CoOOH top layer of up to 4 nm-thickness. As the size of the Co_3O_4 domains is restored when the potential is brought back to low potential, the authors concluded that the formation of the thin layer is reversible. While this study was carried out on an epitaxial thin film with a long-range crystal order and a controlled orientation, we can wonder if such information can be extracted from more disordered or more divided materials such as nanoparticles.

4.4. Morphology insights

On an even larger scale than the crystal domain, the morphology of the electrocatalyst materials can hardly be determined from XAS. Consequently, microscopy techniques can provide substantial information on the morphology and the size of the material, the formation of layers around the electrocatalyst or the active facets during electrocatalysis. While atomic force microscopy⁷⁸ and scanning tunneling microscopy⁷⁹ do not require specific environmental conditions and can easily be adapted to *operando* electrochemical observations, transmission electron microscopy (TEM) experiments are run under ultra-high vacuum. The development of liquid TEM holders has recently enabled such studies. By using such holders, Han et al. observed the formation of O_2 bubbles during OER at the surface of $\text{Ba}_{0.5}\text{Sr}_{0.5}\text{Co}_{0.8}\text{Fe}_{0.2}\text{O}_{3-\delta}$ under H_2O vapour⁸⁰. We have also recently followed Co_3O_4 nanoparticles amorphization during OER in liquid electrolyte⁸¹. This work will be presented in chapter IV.

5. Conclusion

The growing interest to understand the electrocatalytic mechanisms of OER and ORR is motivated by the development of performing devices for energy conversion and storage to cover the increasing energy demand. *In situ* techniques have brought new tools to analyze electrocatalysts during operation and have demonstrated that some active species can only be observed *operando*, i.e. during electrocatalysis. However, none of these techniques is self-sufficient enough to fully describe the electrocatalytic system and it becomes obviously necessary to couple complementary techniques to understand the electrocatalytic reaction.

X-ray absorption spectroscopy is a powerful technique to analyze the local environment of a specific atom in a bulk material. Thanks to high specific area nanomaterials, it is also used to analyze the surface of these compounds, and *operando* XAS is now regularly employed to study surface sensitive phenomena, such as the evolution of electrocatalysts during OER/ORR. However, while XAS can provide various information on the materials, most of the *operando* studies limit the exploitation of *operando* XAS to its basics, namely the evolution of the oxidation state and the inter-atomic distances, and rather look into complementary *in situ/operando* techniques that are more specific to the desired information, even though the *in situ/operando* environment may differ depending on the employed technique.

In contrast to this trend, the goal of this thesis is to extend the contribution of *operando* XAS in the understanding of electrocatalysis. To do so, we will apply *operando* XAS to two families of materials. In chapter II, we will analyze Ni₃B and Ni₄B₃ nickel borides and investigate how the presence of a heteroatom such as boron impacts the electrocatalytic activity of nickel in HER and OER. In chapter III, we will study, LaMn_{1-x}Co_xO₃ perovskites, which contain two transition metals, and try to identify the active site in OER and ORR and look out for any synergy or concurrence between the two transition metals.

Chapter IV will illustrate the complementarity of *operando* techniques by comparing the observations from *operando* XAS and *operando* transmission electron microscopy on Co₃O₄ spinel, which is a model OER electrocatalyst. The *operando* TEM study was carried out by Nathaly Ortiz-Peña, Dris Ihiawakrim and Ovidiu Ersen. They are our collaborators

Chapter I: State of the art

from the ANR InsiChem, which is a project between the Laboratoire Chimie de la Matière Condensée de Paris, SOLEIL Synchrotron and the Institut de Physique et Chimie des Matériaux de Strasbourg. This project seeks to combine *in situ* X-ray absorption spectroscopy and *in situ* transmission electron microscopy to provide a multiscale description of the evolution of electrocatalysts during electrocatalysis.

Chapter II:
Electrocatalytic properties of Ni_xB_y
nanoparticles for water splitting

Chapter II: Electrocatalytic properties of Ni_xB_y nanoparticles for water splitting

Metal borides attract attention for their diverse properties such as magnetism, hardness or electrocatalysis. These characteristics are linked to their uncommon crystal structure that holds metal-boron and boron-boron covalent bonds. In these compounds, besides covalence, strong electron delocalization may also occur in the M-M sublattice³⁸. Recently, transition metal borides have shown high electrocatalytic activity in HER and OER³⁹. In amorphous transition metal borides, electrocatalytic performances were attributed to higher electron density on electrocatalytic sites due to reverse electron transfer from boron to metal centers⁸². In OER, some investigations revealed surface oxidation of metal borides into metal (oxy)hydroxides⁸³. One common hypothesis is the formation of a core-shell structure with a metal boride core and a metal (oxy)hydroxide shell^{67,84}. However, most of these studies were carried out on amorphous metal borides, whose stability over time may be lower compared to more stable crystalline solids. Here, we analyzed Ni_3B and $\text{o-Ni}_4\text{B}_3$ crystalline nickel boride nanoparticles that present high electrocatalytic activity in HER (Ni_3B , $\text{o-Ni}_4\text{B}_3$) and OER (Ni_3B)⁸⁵. These materials compete with reference metal boride performances (Table II - 1; Table II - 2). We used *operando* XAS to probe the electrocatalytically active species within these nanomaterials and to discuss the electrocatalysis mechanisms occurring with these synthesized nanoparticles.

Chapter II: Electrocatalytic properties of Ni_xB_y nanoparticles for water splitting

Catalysts	Electrolyte	Onset potential (V Vs. RHE)	η_{10} (mV)	Tafel slope (mV dec ⁻¹)	References
IrO ₂	1 M KOH		325		86
Co ₂ B/N- graphene	0.1 M KOH	1.51	360	45	67
Co-Mo-B	1 M NaOH		460		87
Co-3Mo-B	1 M KOH	1.50	320	155	88
FeB ₂	1 M KOH	1.48	296	52	83
Amorphous NiB	0.5 M KOH		330		85
Ni _x B	1 M KOH	1.54	380	89	84
NiB _{0.45}	1 M KOH		296		89
Ni(II)borate @Ni ₃ B	1 M KOH	1.48	302	52	89
Ni ₃ B-reduced graphene oxide	1 M KOH	1.43	290	88	90
Ni ₃ B	1 M KOH	1.51	340	81	90
*Ni₃B NPs	0.5 M KOH		300		85
Ni ₃ B NPs	1 M KOH		302		86
*Ni₄B₃ NPs	0.5 M KOH				85

Table II - 1 OER activity of some metal borides and of iridium oxide as reference. The samples studied in this chapter are preceded by *. η_{10} is the overpotential at a current density of 10 mA cm⁻²_{collector}. "NPs" = nanoparticles.

Catalysts	Electrolyte	Onset potential (mV/RHE)	η_{10} (mV)	η_{20} (mV)	References
Pt/C	0.1 M HClO ₄	0		-75	91
Co-B NPs	0.4 M K ₂ HPO ₄	-70	-250		82
FeB ₂	1 M KOH	-20	-61	-82	83
MoB ₂	0.5 M H ₂ SO ₄	-50	$\eta_{2.5} = -180$		92
Amorphous NiB	0.5 M H ₂ SO ₄	-50		-160	85
Amorphous Ni-B NP	0.1 M HClO ₄	-15	-100	-132	91
*Ni₃B NPs	0.5 M H₂SO₄	-40		-145	85
*Ni₄B₃ NPs	0.5 M H₂SO₄	-70		-177	85

Table II - 2 HER activity of some metal borides and platinum deposited on carbon. Compounds studied in this chapter are preceded by *. η_{10} and η_{20} are the overpotentials at a current density of 10 and 20 mA cm⁻²_{collector}.

Chapter II: Electrocatalytic properties of Ni_xB_y nanoparticles for water splitting

1. Ni_xB_y presentation

Nickel boride nanoparticles are obtained by a two-step synthesis process: monodisperse nickel nanoparticles of ca. 20 nm are first synthesized, then boron is incorporated without altering the size distribution by reacting sodium borohydride with nickel the nickel nanoparticles in molten salts (not published yet). The initial polycrystalline nickel (0) nanoparticles are obtained by colloidal synthesis in organic solvents by reduction of nickel (II) acetylacetonate with oleylamine and in the presence of trioctylphosphine as a ligand.^{93,94} The particles are then dispersed into a eutectic mixture of lithium and potassium iodides and further mixed with sodium borohydride. The mixture is heated at 450 °C, while the eutectic mixture melts at 276 °C. Boron is then inserted into the particles by decomposition of NaBH₄ in molten salts, yielding single crystal nickel boride nanoparticles with maintained morphology.

These materials show high activity and stability under electrocatalytic conditions. According to onset potentials in acidic medium, for nanoparticles of the same size, Ni₃B are more active in HER electrocatalysis than Ni₄B₃, which is also much more active than Ni(0) nanoparticles (Figure II - 1). These results indicate an intricate boron effect: while nickel borides are more electrocatalytically active than metallic Ni, adding too much boron up to boron-rich Ni₄B₃ seems detrimental to the activity. In alkaline medium, under OER conditions, while the Ni₃B electrocatalytic activity is higher than Ni(0), Ni₄B₃ performances are insignificant (Figure II - 2). These results bring out that boron can even deactivate the Ni intrinsic electrocatalytic activity. These observations raise a question: what are the actual active species in electrocatalysis, and what is the evolution of the materials under electrocatalysis conditions?

Nickel borides require more investigation to understand the role of boron during electrocatalysis. *Operando* XAS on Ni K-edge could explore the fate of Ni during these reactions. Indeed, the B K-edge energy (<200 eV) is too low to enable *operando* studies under ambient pressure, but the Ni K-edge energy (8333 eV) is high enough to provide more convenient conditions for *operando* measurements. Comparing the Ni K-edge for Ni, Ni₃B and Ni₄B₃ nanoparticles should clarify the effect of boron.

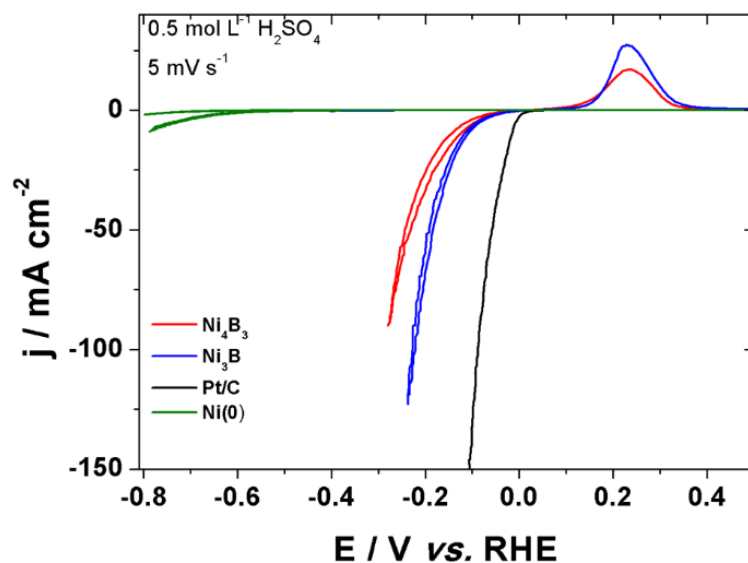


Figure II - 1 Cyclic voltammograms in HER conditions in H_2SO_4 0.5 M: Ni_4B_3 ($40 \mu g \cdot cm^{-2}_{disk}$) (red), Ni_3B ($30 \mu g \cdot cm^{-2}_{disk}$) (blue), Pt/C 10% ($400 \mu g \cdot cm^{-2}_{disk}$) (black), Ni (green).

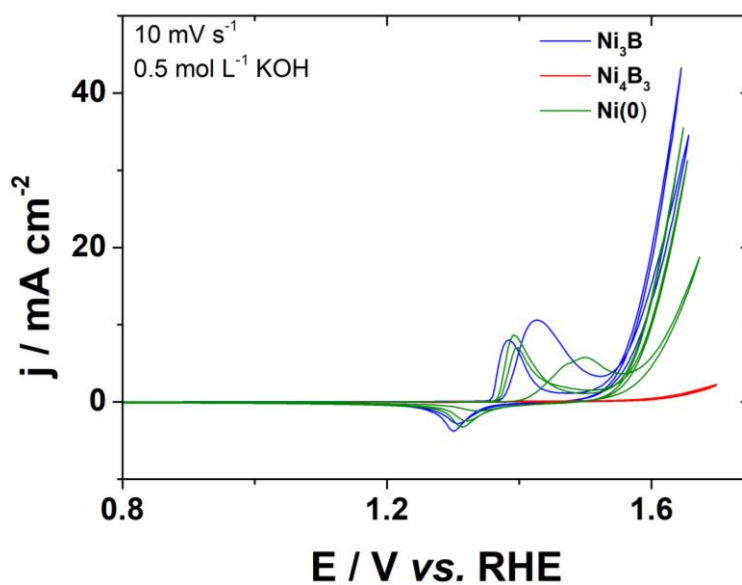


Figure II - 2 Cyclic voltammograms in OER conditions in KOH 0.5 M: Ni_3B ($30 \mu g \cdot cm^{-2}_{disk}$) (blue), Ni_4B_3 ($40 \mu g \cdot cm^{-2}_{disk}$) (red), Ni (green).

2. XAS analysis technique

For each spectrum, XANES and EXAFS regions are treated by linear combination fitting and Fourier transform analysis fitting, respectively.

2.1. Linear combination fitting

2.1.1. Principle

The edge position is highly dependent on the oxidation state. Oxidizing an atom first decreases screening effect and thus stabilizes core levels. Second, it shortens distances and destabilizes antibonding levels. Consequently, transitions are shifted to higher energies. A qualitative evaluation of the oxidation state may then be provided simply by comparing edges. For our study, Ni metal, NiO, Ni(OH)₂ and NiOOH nickel oxide spectra are collected as references.

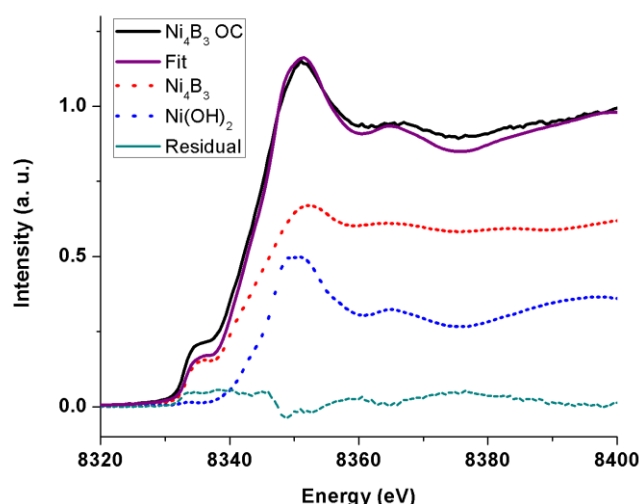


Figure II - 3 Linear combination applied to Ni₄B₃ under resting state. The experimental spectrum (black) is compared to the fit (purple), which is constructed from pristine Ni₄B₃ (dotted red) and nickel hydroxide (dotted blue) reference spectra. The residual difference is also plotted (dotted green).

Quantitative oxidation state determination can be performed by linear combination fitting (LCF), following the Beer-Lambert law (Figure II - 3). Accordingly, the optical absorbance of species can be directly linked to their concentration. If a material is composed of different species with known proportions, its X-ray absorption spectrum is a linear combination of the reference species spectra with the same proportions, where the proportions are weighted by the atomic percentage of the probed element. The residual plot,

Chapter II: Electrocatalytic properties of Ni_xB_y nanoparticles for water splitting

that is the difference between the experimental spectrum and the calculated fit, should be close to zero for a reliable fit.

Even though LCF is valid on the whole spectrum, we only calculate the contribution of each compound based on the narrow part of the spectrum localized in a 50 eV range around the edge (8313-8363 eV), where absorption variations are the highest. The theoretical spectrum is then constructed by applying the obtained weights of the contributions to their respective reference spectra on the whole spectrum range.

2.1.2. Methodological limitations

Linear combination fitting is a comparative technique, so that its accuracy is highly dependent on the chosen references, the relevance of their choice and the reliability of the experimental samples. Below we list some of these limitations.

2.1.2.1. *References choice*

As previously stated, the edge position is sensitive to the formal charge. But the XANES shape can also be altered by many other factors (atomic distance, symmetry, spin). Consequently, the edge position may differ even within compounds of the same oxidation state. Figure II - 4 illustrates this phenomenon on manganese-based compounds. The LaMn^{III}O₃ pre-edge starts at a lower energy than Mn^{III}₂O₃ and its edge slope is sharper. The SrMn^{IV}O₃ white line (the edge maximum intensity) is higher than Mn^{IV}O₂ while its shoulder around 6550 eV is less intense. At $\mu=0.5$, edge positions vary by 1.2 eV and 1.8 eV for Mn^{III} and Mn^{IV} compounds, respectively. Consequently, references with structures close to the studied compounds should be favored.

New phases are likely to appear during operation of the electrocatalytic materials. They should also be considered in the LCF references. However, while simple compounds like Ni nanoparticles will most likely oxidize into solely nickel oxides or nickel (oxy)hydroxide, it is hard to predict the evolution of complex structures like nickel borides which are uncommon. The variety of phases that could potentially form during the electrochemical reaction is large, including nickel borates, nickel oxide and nickel (oxy)hydroxide. Therefore, anticipating the evolution of nickel borides requires some assumptions as to the nature of the evolved species.

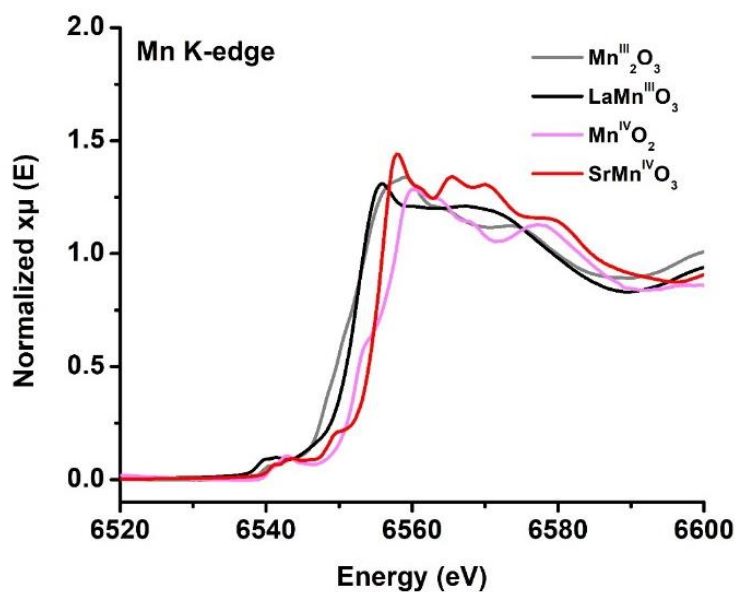


Figure II - 4 XANES of manganese oxides. Oxides with the same Mn oxidation state can display different edge energies.

2.1.2.2. Reference reliability

A wise choice of references can still provide erroneous results if their experimental spectra are not reliable. This usually comes whether from their poor purity or from degradation during sample preparation or during observation conditions. As all compounds are manipulated under ambient atmosphere, air sensitive nanoparticles would likely oxidize. Some materials are also sensitive to X-ray radiations. Finally, the measurement of X-ray absorption spectra of reference materials is performed by diluting these materials and pressing them in boron nitride or cellulose. The latter can degrade under ionizing radiations and form free radicals, further deteriorating the material of interest⁹⁵.

In order to be trusted, references require *in situ* control. One can be provided simultaneously by XAS through a complementary EXAFS analysis.

2.2. EXAFS fits

2.2.1. Principle

A Fourier transform EXAFS spectrum describes the local environment around the analyzed element. It is composed of peaks, which correspond to the presence of neighboring atoms. The position, intensity and width of these peaks find their physical meaning respectively in bond length (R), number of neighbor atoms (N) and crystal disorder (Debye-Waller factor σ^2)⁹⁶ (Figure II - 5). The experimental FT-EXAFS is then compared to a

Chapter II: Electrocatalytic properties of Ni_xB_y nanoparticles for water splitting

theoretical EXAFS constructed from the reference crystal databases to deduce the most plausible composition.

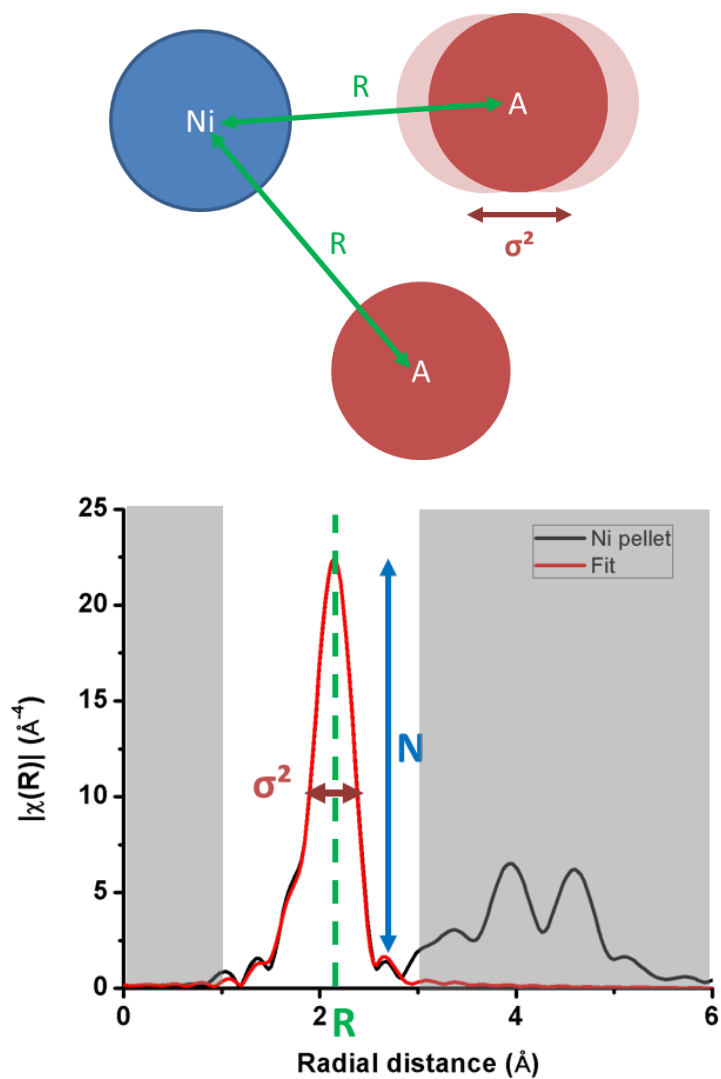


Figure II - 5 Schematic illustration of EXAFS main parameters. Correspondence between atomic local environment (top) and Fourier transform (down). The white domain is the window in which the fit was performed.

Chapter II: Electrocatalytic properties of Ni_xB_y nanoparticles for water splitting

In this chapter, the best fits are determined by the following criteria:

- Firstly, the proposed structure has to be physically relevant. As the fitting software is a mathematical tool, the calculated fits require further analysis from a physical point of view. Due to steric effects, bond length should be higher than 1 Å and the number of atoms on the same path should be limited. The Debye-Waller coefficient should be between 0.003 and 0.015. Those values correspond to perfect crystals and amorphous compounds, respectively. The energy of the edge greatly influences the EXAFS. A variable named ΔE is introduced as a correction between the energy that has been arbitrarily chosen to make the Fourier transform of the EXAFS and the energy employed by the fit. The ΔE of a reliable fit should not be higher than 10 eV.
- Second, the fit quality can be evaluated through several values: uncertainties, reduced χ^2 and R factors (R_f). The fit that displays the lowest values is considered the best.
- Finally, the proposed material should be chemically stable in its environment. For instance, identifying an acidic stable compound in an alkaline medium should raise questions.

In this chapter, the spectra are generally fitted between 1 and 3 Å, where most of the first distances are found. Due to the structural complexity of the studied materials, this range is not expanded to higher distances. Multiple scatterings are not included as they have little influence on the measured distances between Ni and its first neighbors. Finally, due to computational limitations, only 9 variables are usually allowed for a 2 Å range region. Considering that each distance is defined by 3 variables, and after adding ΔE , fits can have up to $3n+1$ variables, where n is the number of paths taken into account. In order to fit more than 2 paths, some variables should be fixed on relevant values that will be discussed each time. In fits of pure compounds spectra, the number of neighbors is fixed to be consistent with the known structure. Calculated Debye-Waller factors are then kept as a phase descriptor and fixed in mixed phase compounds, where the number of neighbors is left fluctuating, as this parameter may vary depending on the amount of the considered phase in the studied material.

Chapter II: Electrocatalytic properties of Ni_xB_y nanoparticles for water splitting

2.2.2. Reference crystal data

Calculated fits are then compared to the structure of the starting materials and to other references in order to identify their possible occurrence in the sample. These reference materials were characterized by Ni-Ni and Ni-O distances, and their respective coordination numbers.

Three nickel oxides have been used as benchmarks: NiO, β -Ni(OH)₂ and γ -NiOOH (Table II - 3). γ -NiOOH is expected to form during OER and is known for its electrocatalytic OER activity⁹⁷. Ni-O and Ni-Ni distances of NiOOH (1.86 and 2.82 Å respectively) are noticeably the shortest among the oxides, which is due to the higher Ni oxidation state. Ni(0)-based materials could oxidize to Ni(II) under the form of NiO or β -Ni(OH)₂. These compounds may be differentiated by comparing Ni-O and Ni-Ni coordination numbers, as the number of neighbors of the Ni-Ni distance is twice the number of neighbors of the Ni-O distance in NiO, while they are the same in Ni(OH)₂.

Phase	Distance	N	R	Ref	ICDD
NiO	Ni-O	6	2.08	98	01-073-1519
	Ni-Ni	12	2.95		
β -Ni(OH) ₂	Ni-O	6	2.13	98	00-057-0907
	Ni-Ni	6	3.12		
γ -NiOOH	Ni-O	6	1.86	99	00-006-0075
	Ni-Ni	6	2.82		

Table II - 3 Theoretical paths of Ni oxides between 1 and 3.2 Å.

3. Results

Spectra are acquired on the SAMBA beamline of SOLEIL between 8200 and 9500 eV. With a velocity of 10 eV sec⁻¹, one spectrum is collected in approximately 2 min 16 sec. Depending on the quality of the signal, between 3 and 20 scans are collected and merged to obtain the displayed spectra (Scan history in Appendix section 3.3.2.). Every composition is expressed as atomic percentage of nickel. For instance, the composition of the material that is 50 % of Ni(OH)₂ and 50 % of Ni₃B means that 50% of the total nickel atoms belong to the Ni(OH)₂ phase and 50 % of the total nickel atoms belong to the Ni₃B phase.

3.1. Solid samples overview

Spectra of reference solid samples were first collected. The EXAFS parts are fitted to assess the purity and reliability of the compounds and obtain the Debye-Waller factor of their crystallographic structure. For recording reference spectra as well as sample spectra, samples are mixed with cellulose (ca. 10% in weight) and then pelletized for analysis. Ni₃B, Ni₄B₃, and Ni nanoparticles were synthesized according to the protocol described in the thesis of Chan Chang⁸⁵. Commercial Ni(OH)₂, NiO and Ni foil are used as references, while we use data from Bediako et al.⁶⁴ for NiOOH and the Ni foil employed as calibration at the beamline for metal Ni⁰. Considering the large diversity of reported nickel borates, they are not considered in the fitting procedures. The analysis of the XANES regions is performed by linear combination. This analysis focuses on determining the Ni oxidation state, which does not change so much in the borates family.

X-ray absorption spectra (XAS) and Fourier Transform EXAFS spectra (FT-EXAFS) of the pure starting compounds are displayed on (Figure II - 6). Nickel oxides XANES spectra feature a sharp edge with an intense white line. Their FT-EXAFS are composed of 2 main peaks. The first one between 1 and 2 Å is attributed to Ni-O distances, while the second one, between 2 and 3 Å belongs to Ni-Ni distances. Differentiating nickel borides and metallic Ni XAS is more delicate. However, Ni₃B and Ni₄B₃ FT-EXAFS display a broader peak that should be a convolution of several peaks, mostly Ni-Ni and Ni-B distances. A slight shift can be observed between Ni-Ni peaks of Ni foil (2.15 Å) and Ni nanoparticles (2.13 Å) and will be investigated later in the chapter.

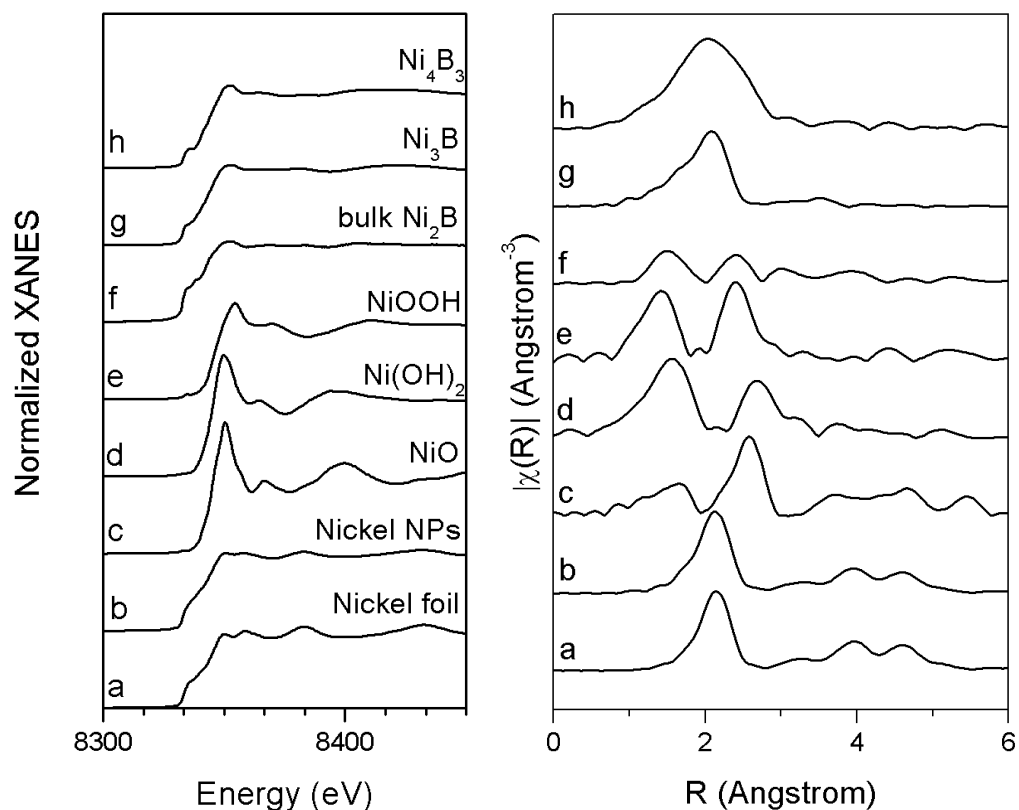


Figure II - 6 XAS spectra (left) and EXAFS Fourier transform (right) of pristine materials: (a) Ni foil, (b) Ni nanoparticles, (c) NiO reference, (d) $\text{Ni}(\text{OH})_2$ reference, (e) NiOOH reference, (f) commercial bulk Ni_2B , (g) Ni_3B nanoparticles, (h) Ni_4B_3 nanoparticles.

3.2. Nickel oxide references

Ni foil and Ni oxide reference FT-EXAFS are fitted to confirm the purity of the materials and to obtain their Debye-Waller factor σ^2 (

Table II - 4) required to analyze XAS of the nickel borides. σ^2 characterizes the crystal structures and will be reused as fixed parameter in fitting spectra of other samples. Only the coordination numbers N are fixed according to the expected tabulated structures. Calculated Ni-Ni and Ni-O distances are compared to crystal data. For NiO and NiOOH, they are consistent with NiO and γ -NiOOH tabulated structure distances. The measured Ni-O distance (2.07 Å) in $\text{Ni}(\text{OH})_2$ from the EXAFS data is shorter than the tabulated one in β - $\text{Ni}(\text{OH})_2$ (2.13 Å). For the Ni foil, the Ni-Ni second path is added to improve fit quality. The Ni-Ni measured distances (2.48 Å and 3.49 Å) are slightly longer than the theoretical values (2.44 Å and 3.45 Å). However, taking into account standard Debye-Waller values, low uncertainties (indicated in brackets) and R_f factors, those fits are considered reliable despite minor discrepancies in the distances. Hence, these Ni oxides are considered of sufficiently high purity to be reliable as references for linear combination analysis.

Chapter II: Electrocatalytic properties of Ni_xB_y nanoparticles for water splitting

The shapes of the Ni K-edges of Ni(OH)₂ and NiO are similar in the XANES range, so that differentiating these two compounds through linear combination is delicate (Figure II - 7). Consequently, only Ni(OH)₂ serves as Ni(II) (hydr)oxide reference for the following linear combination analysis. Ni(OH)₂ and NiO are further discriminated from EXAFS fits, as detailed later. The above-detailed methodology is extended to nickel boride-based electrocatalysts.

Compound	Distance	R	N	10 ³ σ ²	ΔE	Red chi ²	R _f (%)
Ni	Ni-Ni	2.48 (1)	12	6 (1)	7 (1)	1700	0.70
	Ni-Ni	3.49 (2)	6	9 (2)			
NiO	Ni-O	2.07 (2)	6	5 (2)	1 (2)	2100	2.67
	Ni-Ni	2.96 (2)	12	6 (1)			
Ni(OH) ₂	Ni-O	2.07 (1)	6	6 (1)	0 (1)	5500	0.44
	Ni-Ni	3.12 (1)	6	7 (1)			
NiOOH	Ni-O	1.89 (2)	6	10 (2)	3 (2)	8000	2.23
	Ni-Ni	2.83 (2)	6	7 (2)			

Table II - 4 Structural parameters of Ni foil, NiO, Ni(OH)₂ and NiOOH oxide references extracted from Ni K-edge EXAFS fits. In brackets is the uncertainty on the last digit. Fixed parameters are in bold characters. R, N, σ² and ΔE are defined in section 2.2.1.

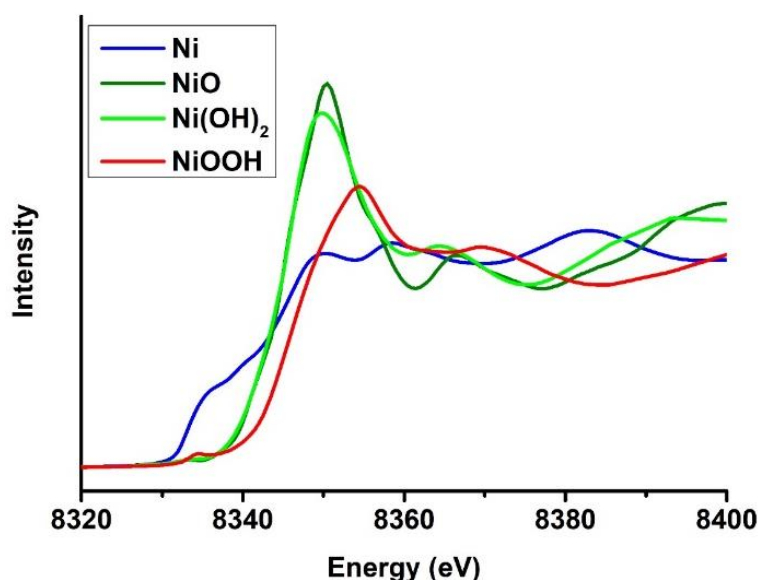


Figure II - 7 XANES of metallic nickel and nickel oxides used as bulk references.

Chapter II: Electrocatalytic properties of Ni_xB_y nanoparticles for water splitting

3.3. Nickel boride-based nanoelectrocatalysts

The electrocatalytic activities of Ni, Ni_3B and Ni_4B_3 nanoparticles are evaluated in HER and OER, respectively in H_2SO_4 0.5 M and KOH 0.5 M. The electrocatalysts (10 mg) are preliminarily dispersed in absolute ethanol (10 mL) with activated acetylene black (10 mg) and Nafion (435 μL) to form an ink. The X-ray absorption spectra were collected in several conditions schematized in Figure II - 8 and defined below:

- Dry state: nanoparticles are deposited as an ink on glassy carbon (GC) substrates and left to dry.
- First resting state: the electrode (the GC plate coated with nanoparticles) is dipped in the electrolyte. This corresponds to the state of the electrode at the open circuit voltage (OCV).
- Under HER/OER conditions: the electrode is subjected to reducing/oxidizing potentials.
- Second resting state: This corresponds to the return at the open circuit voltage.

The LCF is used to analyze every spectrum, but only the FT-EXAFS spectra of activated states are fitted. To test the procedure of EXAFS fitting, we first studied metallic nickel nanoparticles, which will also serve as a reference electrocatalyst to investigate the impact of boron in nickel boride compounds.

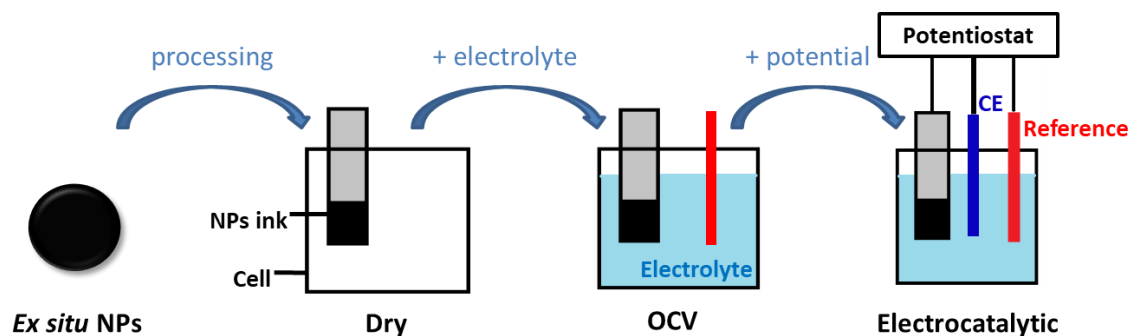


Figure II - 8 Scheme of the successive conditions under which the XAS are collected. The *ex situ* NPs are analyzed as pellets. NPs is nanoparticles. OCV is open circuit voltage. CE is counter-electrode.

3.3.1. Metallic nickel

Before tackling nickel borides, metal Ni nanoparticles are investigated. As a starting reactant of Ni_xB_y synthesis, their morphologies are similar, with particles of *ca.* 20 nm in diameter. Furthermore, the stability and electrocatalytic activity of nickel nanoparticles are

Chapter II: Electrocatalytic properties of Ni_xB_y nanoparticles for water splitting

well referenced^{100–102}. Metallic nickel easily oxidizes under air or in water. Its activity in HER is low, while it is high in OER and has been linked to NiOOH formation. Observing how these phenomena reflect in XAS should facilitate their identification in more complex systems such as nickel borides.

3.3.1.1. Solid sample

In the Ni reported structure $Fm\bar{3}m$, the Ni first path consists of 12 Ni at 2.44 Å (Figure II - 9; Table II - 5). The second path at 3.45 Å is above our established fit range of 1-3 Å. So our first calculation only includes one Ni-Ni distance (Table II - 6, fit 1). According to the fit, the Ni-Ni distance is 2.48 Å with σ^2 of 0.006 and 7.3 neighbors. This low number of neighbor, which the structural model predicted to be 12, raises questions about the fit reliability. A nickel oxide phase is then added to the fit. Indeed, considering the instability of Ni under air, the sample can oxidize during pellet preparation. This phenomenon is expected to be more extended in nanoparticles than in foils because of the higher surface-to-volume ratio. Ni(OH)₂ seems the most realistic choice in ambient air. This new fit (Figure II - 10; Table II - 6, fit 2) displays lower R_f (1200 instead of 1700) and reduced χ^2 (0.39 instead of 0.83). For Ni-O, the low number of neighbors of ca. 0.5 indicates that the nanoparticles are slightly oxidized on the surface. The smaller Ni-O distance compared to the tabulated structure (1.99 Å instead of 2.07 Å) may arise from surface lattice contraction¹⁰³. Still, the number of neighbors for the Ni-Ni distance of metallic nickel remains unchanged (7.3). We conclude that these nanoparticles bear Ni vacancies.

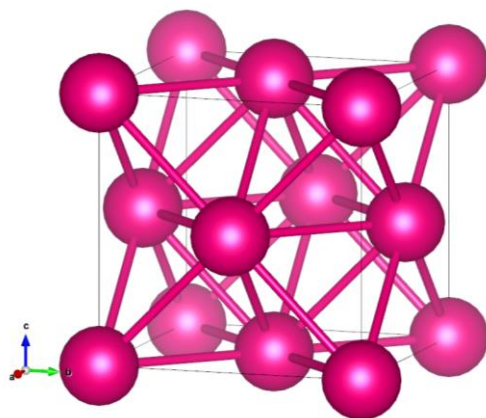


Figure II - 9 Structure of Ni¹⁰⁴.

Phase	Distance	N	R	Ref
Ni	Ni-Ni	12	2.44	104

Table II - 5 Ni theoretical paths of Ni between 1 and 3 Å.

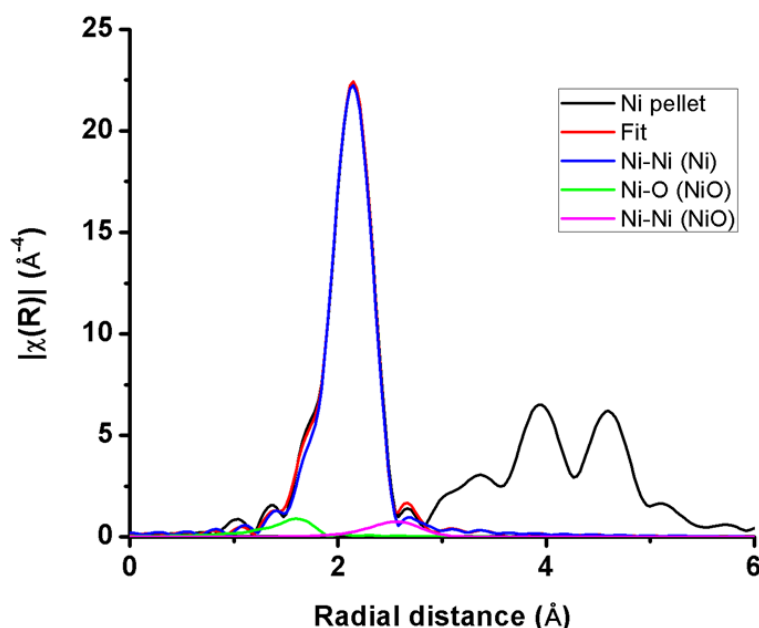


Figure II - 10 Fourier transform of the Ni K-edge EXAFS spectrum for pelletized Ni nanoparticles (black) and its fit between 1 and 3 Å (red). The spectrum is analyzed through 3 distances contributions: Ni-Ni from metal Ni (blue), Ni-O from NiO oxide (green), Ni-Ni from NiO oxide (purple).

Fit	Path	R	N	10 ³ σ ²	ΔE	Red chi ²	Rf (%)
1	Ni-Ni	2.48 (1)	7.3 (5)	6 (1)	-3 (1)	1700	0.83
2	Ni-O	1.99 (4)	0.5 (3)	6	-3 (1)	1200	0.39
	Ni-Ni	2.48 (1)	7.3 (5)	6 (1)			
	Ni-Ni	2.96 (5)	0.5 (4)	7			

Table II - 6 Structural parameters of Ni nanoparticles extracted from Ni K-edge EXAFS refinement. In brackets is the uncertainty on the last digit. R, N, σ² and ΔE are defined in section 2.2.1.

Three possible origins for Ni vacancies are identified:

- Some Ni atoms are oxidized, as shown by the number of Ni-Ni paths decreasing in favor of Ni-O paths. Furthermore, the nickel oxide Ni-Ni distance (2.96 Å) is distinguished from the metal Ni-Ni distance (2.98 Å) with a theoretical coordination number of 6. Therefore, Ni oxidation reduces the number of metal-originated Ni-Ni paths per Ni atoms.
- Downsizing materials results in higher surface to volume ratio. Near the surface, nickel coordination spheres are incomplete. Consequently, nanoscaled compounds usually possess lower average coordination numbers than their bulk counterparts.

Chapter II: Electrocatalytic properties of Ni_xB_y nanoparticles for water splitting

- Previous characterizations by TEM and XRD indicated that these nanoparticles have a polycrystalline structure⁹³. Zones between two crystalline domains should contain Ni defects.

These phenomena could explain the large gap in the coordination numbers measured for Ni nanoparticles and for Ni foil. Ni oxidation also explains why the FT-EXAFS peak in Ni nanoparticles is shifted by 0.02 eV compared to bulk Ni, as the peak is a convolution of Ni-O and Ni-Ni distances.

The Ni(OH)₂ molar content is estimated between 8 and 12 at. % of total Ni, depending on whether its structure is considered perfectly compact or it contains as many vacancies as the metallic nickel phase (detailed calculation in Appendix section 4.1.). From linear combination fitting of XANES for the Ni nanoparticles with Ni foil and Ni(OH)₂ references, this ratio is estimated to be ~ 5 %. This small deviation is attributed to morphological and structural differences between Ni foil and Ni nanoparticles, considering that LCF only takes into account oxide formation and neglects lattice distortion.

As nickel nanoparticles are oxidized during the preparation of the pellets for XAS measurements, their spectrum cannot be used as a reliable reference for LCF. Consequently, the spectra acquired *operando* for Ni nanoparticles are fitted with Ni foil, Ni(OH)₂ and NiOOH spectra.

3.3.1.2. HER

6 “dry state” scans are collected from a Ni nanoparticles-coated glassy carbon (GC) working electrode fixed on a 3-electrodes electrochemical cell. The cell is then filled with H₂SO₄ 0.5 M electrolyte and 6 “resting state” scans are collected. A cyclic voltammogram between 0.24 and -0.56 V/RHE is recorded to verify that the material displayed its usual electroactivity. 20 scans are then collected at -0.36 V/RHE and 16 scans at -0.06 V/RHE, which correspond to the catalytic state and back to the resting state, respectively. The potential profile used in the experiment is displayed in Figure II - 11, top. Another cyclic voltammogram is eventually recorded to check any changes in electroactivity during the experiment.

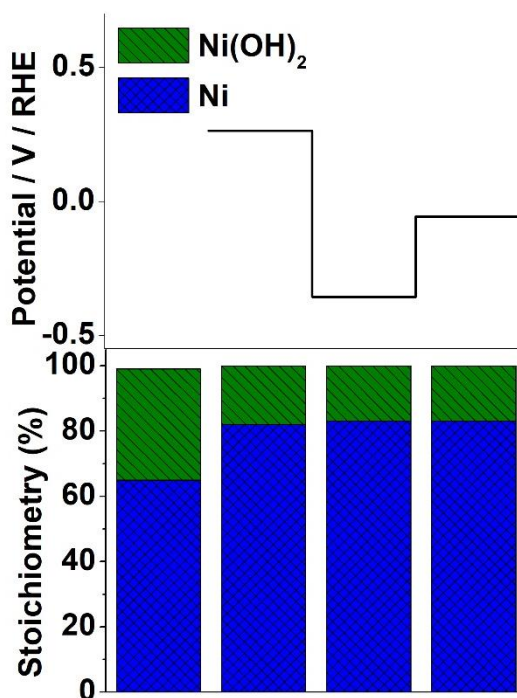


Figure II - 11 Top: Potential applied at each step of the HER experiment of Ni nanoparticles in H_2SO_4 0.5 M. Bottom: Phase compositions (at. %) obtained from linear combination (from left to right) at dried state, resting state, under HER condition, then 0 V/RHE.

The acquired spectra are analyzed with LCF using Ni foil and Ni(OH)₂ as reference samples (Figure II - 11). The dried state is composed of 65 at. % of Ni and 35 at. % Ni(OH)₂. Once the acidic electrolyte is added, the Ni(OH)₂ content drops to 20 %, then remains the same in the reducing conditions of HER. Such an oxidation of the Ni nanoparticles is expected considering that the electrode preparation took place in air at ambient temperature. Indeed, the electrodes are left drying for more than one hour. The decrease of the amount of Ni(OH)₂ when the electrode is in contact with the electrolyte can be explained by its partial dissolution in the acidic medium. Applying a reducing potential does not affect the quantity of dissolved Ni(OH)₂. Reducing potentials have thus no influence on Ni(OH)₂ dissolution.

Given these information, the fit of the FT-EXAFS of HER-active Ni nanoparticles is performed by including Ni and Ni(II) oxide components, resulting in three paths: one Ni-O distance around 2 Å and two Ni-Ni distances around 2.5 Å and 3 Å, hallmarks of Ni⁰ and Ni^{II} respectively. σ^2 values are fixed at their value obtained in section 3.2. We calculate a first fit considering Ni and Ni(OH)₂, then another one where we substitute the Ni(OH)₂ Debye Waller factor by the NiO value. In both fits, the second Ni-Ni path coordination number is half the value of Ni-O coordination number, in agreement with the NiO phase. For this reason, the NiO component is selected instead of Ni(OH)₂ (Figure II - 12; Table II

Chapter II: Electrocatalytic properties of Ni_xB_y nanoparticles for water splitting

- 7). The Ni-Ni number of neighbors is $7.0 \pm 0.4 \text{ \AA}$. Considering the uncertainty range between this value and the Ni-Ni number of neighbors of the starting Ni nanoparticles ($7.3 \pm 0.5 \text{ \AA}$), the FT-EXAFS fit does not enable assessing whether or not more nickel is oxidized in the HER conditions compared to the pristine particles. Ni-O and the first Ni-Ni distances are the same as the solid sample ones (1.99 \AA and 2.48 \AA respectively). The second Ni-Ni distance is in agreement with the Ni-Ni distance in NiO ($3.01 \pm 0.05 \text{ \AA}$).

These results suggest that, under HER conditions, nickel nanoparticles are mainly composed of Ni and NiO, with an oxide molar content between 23 and 29 %. These values are close to the results obtained from linear combination fit of the XANES area (Figure II - 13), which clearly show a decrease in the amount of oxidized nickel under HER conditions. For 20 nm sized nanoparticles, this amount equals to a 2 nm thick layer of oxide at the surface of the nanoparticles. Considering the high content of oxide in the dry state, the NiO oxide layer most likely originate from the exposure to air for approximately an hour during drying of the electrode. This oxide layer partially dissolves when immersed in acidic electrolyte, in agreement with the Pourbaix diagram. The remaining oxide layer stays unchanged afterwards, even during HER. Such a thick HER inactive oxide layer should disable Ni electrocatalytic activity. Consequently, the Ni nanoparticles instability prevents their use in HER electrocatalysis.

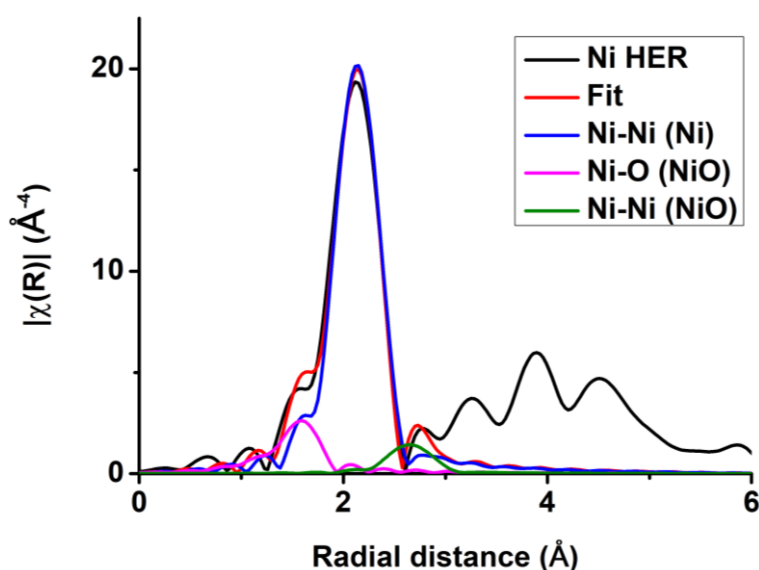


Figure II - 12 Fourier transform of Ni K-edge EXAFS spectrum for Ni nanoparticles under HER conditions (black) and its fit between 1 and 3 Å (red). The latter is split in 3 path contributions: Ni-Ni from metal Ni (blue), Ni-O from NiO oxide (purple), Ni-Ni from NiO oxide (green).

Chapter II: Electrocatalytic properties of Ni_xB_y nanoparticles for water splitting

Path	R	N	$10^3 \sigma^2$	ΔE	Red χ^2	Rf (%)
Ni-O	1.99 (2)	1.4 (3)	5	-2 (2)	66	1.03
Ni-Ni	2.48 (1)	7.0 (4)	6			
Ni-Ni	3.01 (5)	0.7 (5)	6			

Table II - 7 Structural parameters of Ni nanoparticles under HER conditions extracted from Ni K-edge EXAFS refinement. Uncertainties on the last digit are in brackets. Fixed parameters are in bold characters. R, N, σ^2 and ΔE are defined in section 2.2.1.

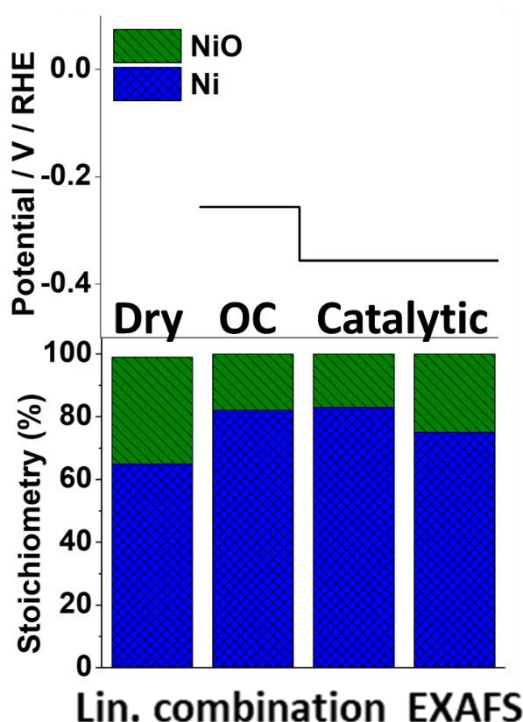


Figure II - 13 Comparison of nanoparticles composition measured by linear combination and EXAFS fitting. Top: Potential applied at each step of the HER experiment for Ni nanoparticles in H_2SO_4 0.5 M. Bottom, from left to right: Phase compositions obtained from linear combination in dried state, resting state (OC) and under HER condition (catalytic), then phase composition obtained from EXAFS fitting under HER conditions.

Chapter II: Electrocatalytic properties of Ni_xB_y nanoparticles for water splitting

3.3.1.3. OER

6 “dry state” scans are collected from the Ni nanoparticles-coated electrode. The 3-electrode electrochemical cell is then filled with the KOH 0.5 M electrolyte and 6 “resting state” (OC) scans are collected. A cyclic voltammogram between 1.07 and 1.56 V/RHE is recorded to assure that the material displayed its usual OER activity. 20 scans are then collected at 1.57 V/RHE and 20 scans at 1.27 V/RHE, which are respectively the catalytic state and open circuit voltage (OCV) (potential behavior is displayed in Figure II - 14, top). Another cyclic voltammogram is eventually recorded to assess any activity modification during the experiment.

The acquired spectra are analyzed by linear combination of Ni foil, Ni(OH)₂ and NiOOH spectra as references (Figure II - 14). As previously, the dried state is composed of 65 at. % of Ni and 35 at. % Ni(OH)₂. Once the alkaline electrolyte is added, the Ni(OH)₂ component increases to 40 at. %. During OER, the material is composed of 40 at. % Ni(0), 15 at. % Ni(II) and 45 at. % Ni(III). When the potential is dropped back to the OCV, the NiOOH component disappears in favor of Ni(OH)₂ (60 %). The alkaline medium then stabilizes Ni(II) species as Ni(OH)₂ with a higher content than under acidic conditions. Under oxidation conditions, Ni(II) species are further oxidized into Ni(III) as NiOOH. The latter is further reduced back to Ni(II) once the potential is lowered to 1.27 V/RHE.

The FT-EXAFS of the Ni-based nanomaterials under OER conditions is fitted by including Ni and NiOOH components, resulting in three distances: one Ni-O distance around 1.9 Å and two Ni-Ni distances around 2.5 Å and 2.8 Å, corresponding to Ni⁰ and Ni^{III} respectively (Figure II - 15; Table II - 8). σ^2 values are fixed at their value obtained above in section 4.2. The Ni-Ni distance number of neighbors of Ni⁰ decreases to 6.2 while Ni-O and Ni-Ni distances in NiOOH show numbers of neighbors of 3.7 and 4.0. Such high values indicate a large oxidation state for nickel and confirm the results obtained from linear combination. The Ni-O distance is measured at 1.88 Å while Ni-Ni distances are 2.50 Å and 2.79 Å. The Ni-O distance is in agreement with the γ -NiOOH structure, but the Ni-Ni longest distance is shorter than expected. This could come from an imprecise deconvolution of the main peak, which overestimates the Ni-Ni contribution in NiOOH at the expense of the Ni-Ni component of Ni⁰. The oxidized component is most likely formed at the surface of the Ni⁰ nanoparticles, which then bear a core-shell morphology.

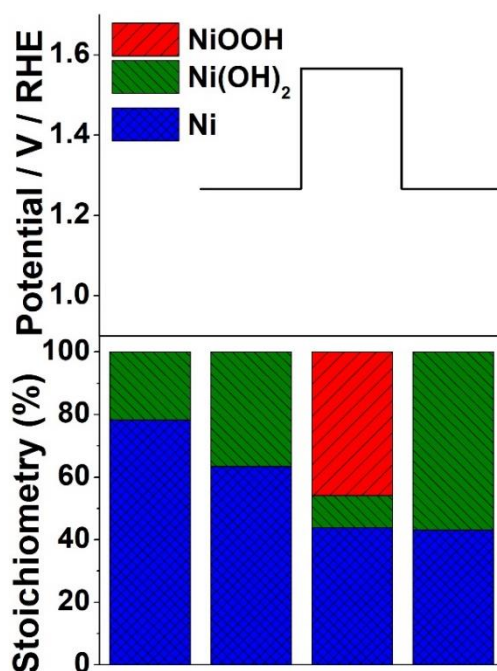


Figure II - 14 Top: Potential applied at each step of OER experiment of Ni nanoparticles in KOH 0.5 M. Bottom: Phase compositions obtained from linear combination (from left to right) at dried state, OCV, under OER condition and then OCV.

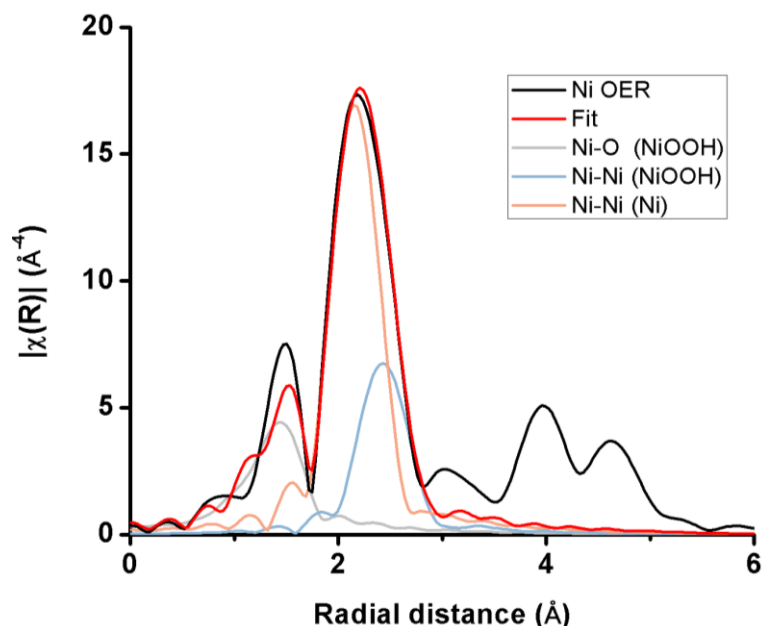


Figure II - 15 Fourier transform of Ni K-edge EXAFS spectrum for Ni nanoparticles under OER conditions (black) and its fit between 1 and 3 Å (red). The latter is split in 3 distance contributions: Ni-O from NiOOH oxide (grey), Ni-Ni from NiOOH oxide (blue), Ni-Ni from metal Ni (purple).

Chapter II: Electrocatalytic properties of Ni_xB_y nanoparticles for water splitting

Path	R	N	$10^3 \sigma^2$	ΔE	Red chi ²	Rf (%)
Ni-O	1.88 (5)	3.7 (6)	10	0 (5)	360	1.88
Ni-Ni	2.50 (2)	6.2 (8)	6			
Ni-Ni	2.79 (2)	4.0 (2)	7			

Table II - 8 Structural parameters of Ni nanoparticles under OER conditions extracted from Ni K-edge EXAFS refinement. Uncertainties on the last digit are in brackets. Fixed parameters are in bold characters. R, N, σ^2 and ΔE are defined in section 2.2.1.

Both FT-EXAFS fit and XANES linear combination show that under OER conditions, Ni nanoparticles are mainly composed of Ni⁰ and Ni^{III} (Figure II - 16). The molar content of the oxidized component is estimated between 54 % and 62 % by FT-EXAFS fit and 45% by linear combination. Such a difference may come from the EXAFS fit taking account only one nickel oxide at once, while XANES enables to consider both NiOOH and Ni(OH)₂ phases. Together, these oxo species account for 60 % of nickel atoms in the material in contact with the alkaline medium. To summarize, in alkaline medium, Ni nanoparticles significantly oxidize to Ni(OH)₂. Then, under OER conditions, they oxidize even more and further to higher oxidation state to form γ -NiOOH. This electrocatalytically active phase only manifests at high potential and is formed reversibly, as NiOOH is reduced back to Ni(II) (hydr)oxide once the system is put back to resting state.

The Ni instability becomes a strength in OER electrocatalysis as it favors the formation of electrocatalytically active γ -NiOOH. This phase, which is only observable under OER conditions, proves that *operando* characterization is essential to unravel electrocatalysis mechanisms. Now that the behavior of simple Ni nanoparticles is described during HER and OER, we can tackle nickel borides and discuss the boron effect on electrocatalytic properties.

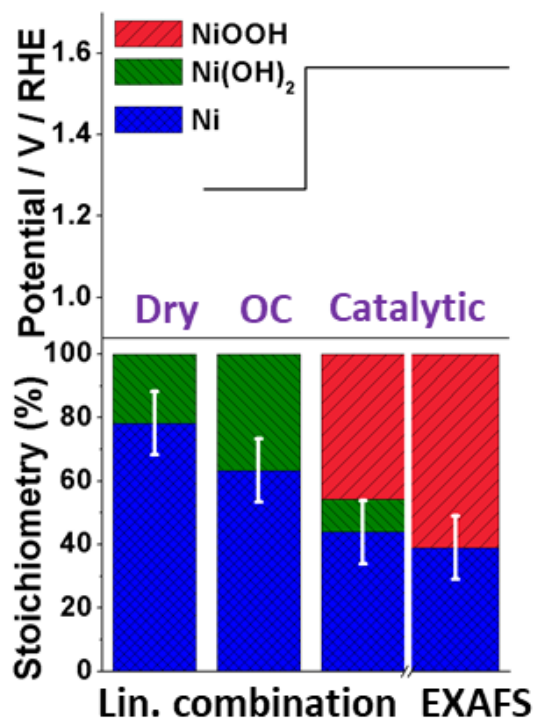


Figure II - 16 Comparison of Ni nanoparticles composition measured by linear combination and EXAFS fitting. Top: Potential applied at each step of the OER experiment in KOH 0.5 M. Bottom, from left to right: Phase compositions obtained from linear combination at dried state, resting state (OC) and under OER condition (catalytic), with the corresponding composition obtained from EXAFS fitting.

Chapter II: Electrocatalytic properties of Ni_xB_y nanoparticles for water splitting

3.3.2. Ni₃B

As showed in Figure II - 1 and Figure II - 2, Ni₃B nanoparticles exhibit high activity both in HER and OER compared to Ni nanoparticles. This questions how boron contributes to enhance electrocatalytic properties compared to bare nickel. To answer this point, Ni₃B is studied in the same *operando* XAS experiments as Ni nanoparticles: its solid state purity is analyzed first, then the composition of the electrode material is studied during HER and OER by interpreting the obtained spectra through LCF. The electrocatalytically active phase is further analyzed through FT-EXAFS.

3.3.2.1. Solid sample

The reported structure of Ni₃B is *Pnma* (Figure II - 17). Its low symmetry limits path degenerescence. Moreover, Ni atoms occupy 2 sites Ni and Ni' with their own paths (Table II - 9). All in all, photoelectrons expelled from the nickel ion can follow 13 different paths between the absorbing nickel and a neighboring atom that is at a distance between 1 and 3 Å. Trying to deconvolute so many paths in such a narrow range would involve too many variables to enable an accurate fit of EXAFS data. A simplified structure is then constructed by merging distances (Table II - 10). Ni-B distances are merged together. 5 out of 6 of them range between 1.95 and 2.33 Å. One Ni'-B distance is 2.60 Å but is still included in this combination to keep all Ni-B paths together. Ni-Ni paths are separated into two groups: the first one includes Ni-Ni distances between 2.46 Å and 2.56 Å, and the second one includes 2.74 Å and 2.81 Å Ni-Ni distances. While the Ni-B number of neighbors is simply fixed to 3, a simple average would have resulted in Ni-Ni distances with degenerescence of 8 for the shortest one and 3.5 for the longest one. Their degenerescences are rounded to 8 and 3, respectively, as longer paths usually exhibit weaker intensities than shorter paths. Simplified reference distances are calculated by averaging distances from the tabulated structure weighted by their degenerescence, thus resulting in 2.12 Å for Ni-B, then 2.50 and 2.76 Å for Ni-Ni. Because of these approximations, Debye-Waller factors are expected to be high.

Chapter II: Electrocatalytic properties of Ni_xB_y nanoparticles for water splitting

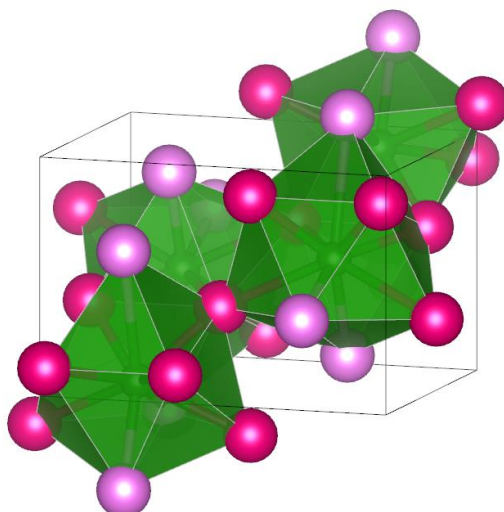


Figure II - 17 Structure of Ni₃B¹⁰⁵. B is green, Ni is pink (Ni sites) and purple (Ni' sites).

Path	Degenerescence	R (Å)	Path	Degenerescence	R (Å)
Ni-B	1	1.97	Ni'-B	1	1.95
Ni-B	1	2.06	Ni'-B	1	2.12
Ni-B	1	2.33	Ni'-Ni	4	2.52
Ni-Ni	3	2.46	Ni'-Ni	4	2.56
Ni-Ni	2	2.50	Ni'-B	1	2.60
Ni-Ni'	1	2.52	Ni'-Ni	2	2.74
Ni-Ni'	2	2.56	Ni'-Ni'	2	2.81
Ni-Ni'	3	2.74			

Table II - 9 Ni theoretical paths in Ni₃B between 1 and 3 Å according to the tabulated crystal structure (PDF card 04-014-0853). In this crystal structure, nickel occupies two different sites Ni and Ni'.

Path	Degenerescence	R
Ni-B	3	2.12
Ni-Ni	8	2.50
Ni-Ni	3	2.76

Table II - 10 Simplified paths of Ni₃B between 1 and 3 Å.

Chapter II: Electrocatalytic properties of Ni_xB_y nanoparticles for water splitting

A first fit of EXAFS data is performed by assuming that the sample is a pure Ni₃B phase (Figure II - 18; Table II - 11, fit 1). The numbers of neighbors are fixed at the previously stated values. As expected, the fit exhibits high σ^2 above 0.010. The longest Ni-Ni path features a Debye-Waller factor of 0.017, which could be considered dubious in a crystalline material. Yet, regarding the amount of approximations used to simplify the structure, this value is expected. Ni-Ni distances (2.49 Å and 2.76 Å) are close to their approximated values. However, the Ni-B distance of 2.04 Å is much shorter than the initial values. This result may arise from the approximations performed when we averaged this distance. We supposed that each peak intensity was equivalent to one another regardless of its distance to Ni, which is rigorously wrong as the further the atom is located, the weaker its contribution is to the EXAFS data. Consequently, the weight of the 2.60 Å Ni'-B path on the averaged distance was overestimated. Indeed, if this path is discarded, an average on the other 5 Ni-B paths gives a distance of 2.09 Å. This value is much closer to the result of the fit, yet still higher than the distance calculated by the fit. Likewise, as the higher distance contribution has been overestimated, the shorter distance contribution might have been conversely underestimated as well.

We then performed a second fit by assuming that Ni₃B was oxidized (Table II - 11, fit 2). Unlike Ni⁰, no pure Ni₃B experimental reference is available, so that the Debye-Waller factors cannot be fixed. Instead, the number of neighbors in the Ni₃B paths are fixed on their approximated values. The Ni-O Debye-Waller factor is set at 0.005, which is the value measured for the NiO phase. The calculated fit shows an energy correction ΔE of -13 eV and gives to Ni₃B originated distances similar lengths and Debye-Waller factors to the first fit, except for Ni-B σ^2 that was 0.008. The coordination number of the Ni-O path is 1.2 ± 1.2 for a distance of 2.19 Å. Such relative uncertainty of 100 % on the number of neighbors of Ni-O path fails to clarify whether or not the compounds are oxidized but the Ni-O long distance does not match with any nickel oxide reference. That, added to the ΔE extremely high value, indicates that this fit is unreliable.

Since the mixed solid Ni₃B/NiO structure fails to fit the FT-EXAFS data, contrary to pure Ni₃B, we conclude that the material is pure Ni₃B. This is unexpected since Ni₃B is supposed to oxidize under air, like Ni metal⁸⁵. Still, the XAS of Ni₃B serves as reference for the XANES linear combination under electrocatalysis conditions, as explained below.

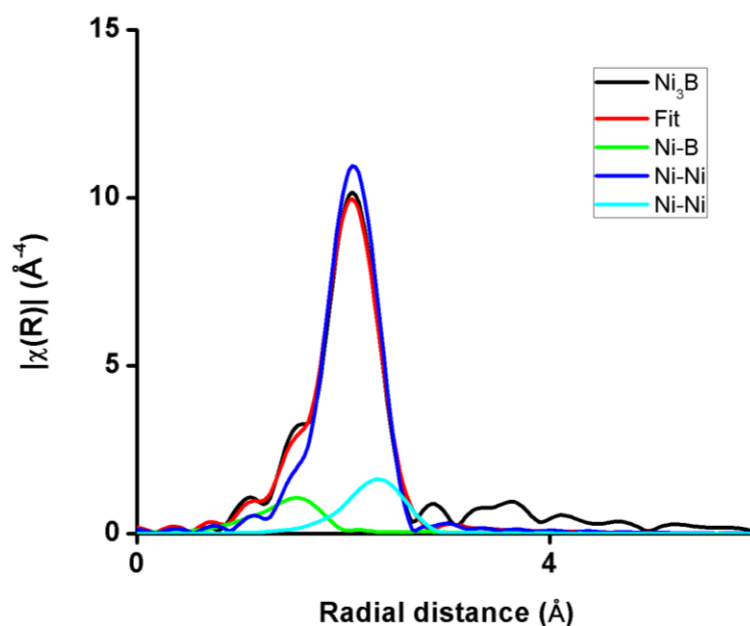


Figure II - 18 FT-EXAFS Ni₃B nanoparticles (black) and its fit between 1 and 3 Å (red). The latter is split in 3 distance contributions: Ni-B (green), and two Ni-Ni (blue and light blue).

Fit	Path	R	N	10 ³ σ ²	ΔE	Red chi ²	Rf (%)
1	Ni-B	2.04 (3)	3.0	13 (5)	-7 (3)	4700	0.63
	Ni-Ni	2.49 (2)	8.0	11 (1)			
	Ni-Ni	2.76 (3)	3.0	17 (4)			
2	Ni-O	2.19 (6)	1.2 (12)	5	-13 (7)	5700	0.41
	Ni-B	2.02 (4)	3.0	8 (6)			
	Ni-Ni	2.47 (3)	8.0	11 (1)			
	Ni-Ni	2.78 (5)	3.0	17 (6)			

Table II - 11 Structural parameters of Ni₃B nanoparticles extracted from Ni K-edge EXAFS refinement. Uncertainties on the last digit are in brackets. Fixed parameters are in bold characters. R, N, σ² and ΔE are defined in section 2.2.1.

3.3.2.2. HER

Nine “dry state” scans are collected from a Ni₃B nanoparticles-coated electrode connected to the electrochemical cell. The cell is then filled with H₂SO₄ 0.5 M electrolyte and nine “resting state” scans are collected. A cyclic voltammogram between 0.24 and -0.56 V/ RHE is recorded to assure that the material displays its usual activity (Figure in Appendix section 3.3.1.). 23 scans are then collected at -0.36 V/RHE and 16 scans at 0.49 V/RHE, which are respectively the activated state and going back to OCV. Another cyclic voltammogram is eventually recorded to assess any activity modification during the experiment.

Chapter II: Electrocatalytic properties of Ni_xB_y nanoparticles for water splitting

The acquired spectra are fitted with linear combination of the spectra of the Ni₃B solid-state and Ni(OH)₂ as reference samples (Figure II - 19). Accordingly, the dried state, resting state and activated state (under electroactivity) are all composed of only Ni₃B. These results attest the stability of the nickel oxidation state in Ni₃B compound under acidic HER conditions.

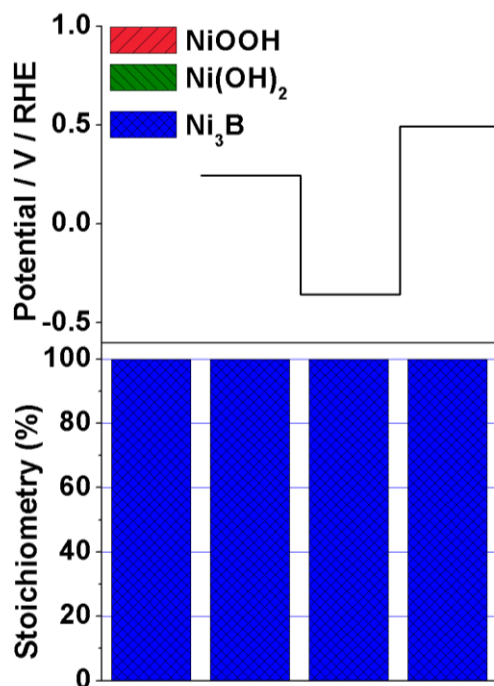


Figure II - 19 Top: Potential applied at each step of the HER experiment with Ni₃B nanoparticles in H₂SO₄ 0.5 M. Bottom: Phase compositions obtained from linear combination (from left to right) in the dried state, resting state, and under HER condition, then OCV.

The FT-EXAFS of HER-active Ni₃B nanoparticles is fitted with Ni₃B and NiO components, resulting in five distances: one Ni-O distance around 2 Å (depending on the oxide taken into account), one Ni-B distance around 2.1 Å and three Ni-Ni distances around 2.5 Å, 2.7 Å and 2.9 Å. σ^2 values are fixed according to the results obtained in sections 3.2 and 3.3.2.1. To reduce the number of variables, Ni₃B based distance lengths are fixed. Ni-O and Ni-Ni distances from nickel oxide are constrained with the relation: $\frac{N(Ni-O)}{N(Ni-Ni)} = 0.5$ or 1, depending on the supposed phase, respectively NiO or Ni(OH)₂. Choosing the NiO phase provides a better fit than with the Ni(OH)₂ phase. The corresponding parameters are displayed in Table II - 12 and the fit is shown on Figure II - 20. The number of neighbors in

Chapter II: Electrocatalytic properties of Ni_xB_y nanoparticles for water splitting

Ni₃B distances is 3.0±0.1 for the Ni-B distance and 8.0±0.1 and 0±2 for the two Ni-Ni distances. The Ni-O number of neighbors is 0.2±0.9, while Ni-O and Ni-Ni distances from NiO are evaluated at 1.9±4 Å and 2.8±7 Å respectively. The relative uncertainty on the Ni-O number of neighbors is 450%. We draw the conclusion that no oxide is formed during the experiment. This conclusion is consistent with the high uncertainties observed on NiO-based distances.

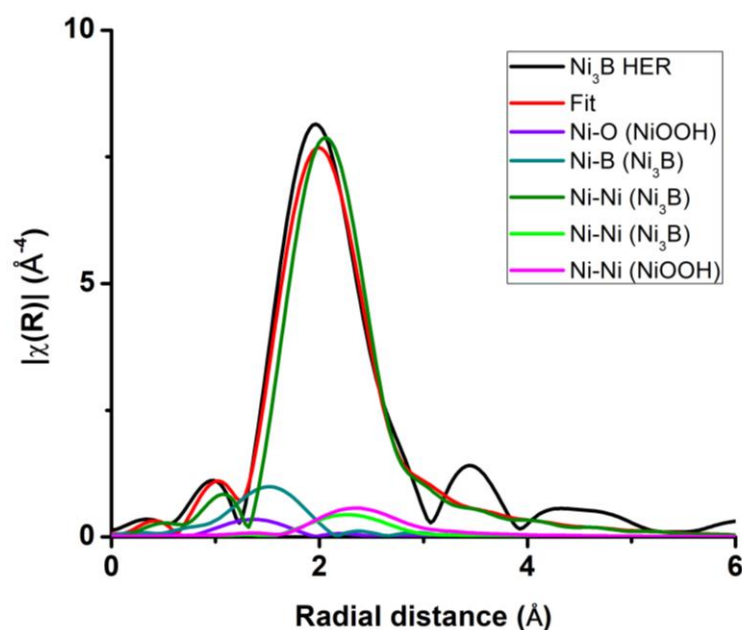


Figure II - 20 Fourier transform of Ni K-edge EXAFS spectrum for Ni₃B nanoparticles under HER conditions (black) and its fit between 1 and 3 Å (red). The latter is split in 5 distance contributions: Ni-O from NiO oxide (purple), Ni-B from Ni₃B (dark cyan), Ni-Ni from Ni₃B (olive), Ni-Ni from Ni₃B (light green), Ni-Ni from NiO oxide (pink).

Path	R	N	10 ³ σ ²	ΔE	Red chi ²	Rf (%)
Ni-O	1.9 (4)	0.2 (9)	5	-5 (7)	723	1.90
Ni-B	2.06	3.0 (1)	13			
Ni-Ni	2.50	8.0 (1)	11			
Ni-Ni	2.73	0 (2)	16			
Ni-Ni	2.8 (7)	0.5	6			

Table II - 12 Structural parameters of Ni₃B nanoparticles under HER conditions extracted from Ni K-edge EXAFS refinement. Uncertainties on the last digit are in brackets. Fixed parameters are in bold characters. Related parameters are colored. In blue: constrained values $N(\text{Ni-Ni}) = 2*N(\text{Ni-O})$. R, N, σ² and ΔE are defined in section 2.2.1.

Chapter II: Electrocatalytic properties of Ni_xB_y nanoparticles for water splitting

Both XANES and FT-EXAFS show no presence of any Ni oxo-species during the whole experiment (Figure II - 21), highlighting the oxidation resistance of Ni_3B . This property explains the Ni_3B high HER electrocatalytic activity compared to Ni. Indeed, Ni atoms are the main electrocatalytic sites in HER³⁹. Preventing the oxidation and deactivation of nickel increases the number of active sites per total number of Ni.

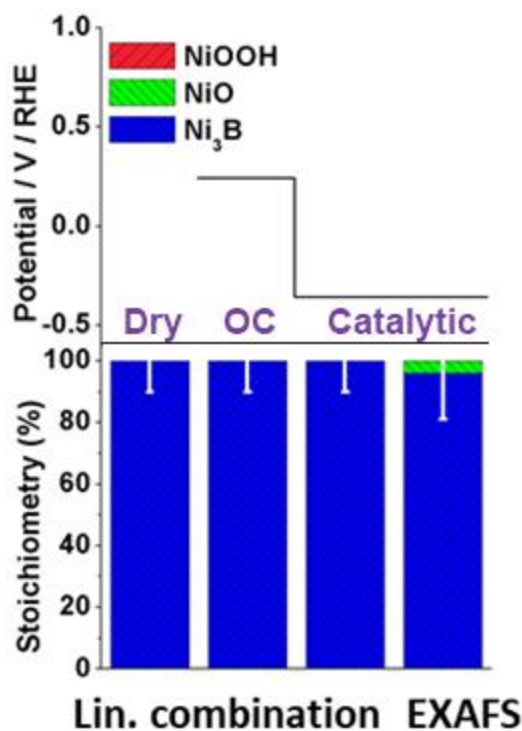


Figure II - 21 Comparison of nanoparticles composition measured by linear combination and EXAFS fitting. Top: Potential applied at each step of HER experiment of Ni_3B nanoparticles in H_2SO_4 0.5 M. Bottom, from left to right: Phase compositions obtained from linear combination at dried state, resting state (OC) and under HER condition (Catalytic), then phase composition obtained from EXAFS fitting under HER conditions.

3.3.2.3. OER

3 “dry state” scans are collected from Ni_3B -coated electrode in an electrochemical cell. Then it is filled with KOH 0.5 M electrolyte and 30 “resting state” scans are collected. Then 30 scans are collected at 1.57 V and 30 scans at 1.22 V, which were respectively activated state and resting state anew. Another cyclic voltammogram is eventually recorded to assess any activity modification during the experiment.

The acquired spectra are fitted by linear combination of reference Ni_3B , $Ni(OH)_2$ and $NiOOH$ spectra (Figure II - 22). Like previously, the dried state is composed only of Ni_3B . Once the alkaline electrolyte is added, the $Ni(OH)_2$ component increases to 10 at. %. During

Chapter II: Electrocatalytic properties of Ni_xB_y nanoparticles for water splitting

OER, the material is composed of 95 % Ni₃B and 5 % NiOOH. When the potential is dropped back to OCV, the NiOOH component disappears in favor of the reappearance of Ni(OH)₂ (10 %). Therefore, the alkaline medium oxidizes the surface of Ni₃B and forms Ni(II) oxide. Then, OER conditions further oxidizes Ni(II) to Ni(III). The decrease in the nickel oxide proportion between the OCV and the following catalytic state can be attributed whether to nickel oxide dissolution, estimated at 0.8 nm for nanoparticles of 20 nm size initially (details in Appendix section 4.1.), or to the uncertainty of the linear combination fit, which is not clearly estimated (Appendix section 4.2.). NiOOH reduces back to Ni(II) oxide once the potential is decreased to 1.27 V/RHE.

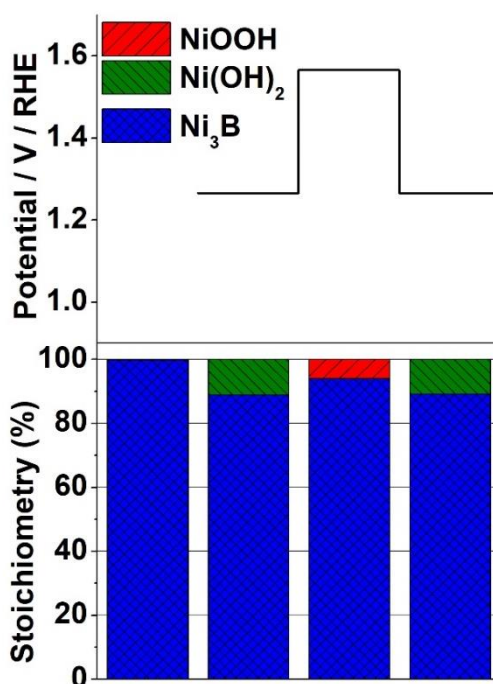


Figure II - 22 Top: Potential applied at each step of OER experiment of Ni₃B nanoparticles in KOH 0.5 M. Bottom: Phase compositions obtained from linear combination (from left to right): at dried state, resting state, under OER condition then resting state again (OC).

The FT-EXAFS of OER-active Ni₃B nanoparticles is fitted by including Ni₃B and NiOOH components with five paths: one Ni-O path around 1.9 Å, one Ni-B path around 2.0 Å and three Ni-Ni paths around 2.5 Å, 2.7 Å and 2.8 Å (Figure II - 23, Table II - 13). σ^2 values are fixed according to the results obtained in section 3.2. and section 3.3.2.1. To reduce the number of variables, Ni₃B-based path distances are fixed. Ni-O and Ni-Ni distances from nickel oxide are correlated with $\frac{N(Ni-O)}{N(Ni-Ni)} = 1$ according to the γ -NiOOH

Chapter II: Electrocatalytic properties of Ni_xB_y nanoparticles for water splitting

structure. The number of neighbors of Ni₃B-based Ni-B and two Ni-Ni paths are 3.0, 6.4 and 3.3 respectively. The number of neighbors for the Ni-O path is 0.6 ± 0.4 . In nickel oxide, the Ni-O and Ni-Ni distances are 1.86 Å and 2.76 Å respectively. These lengths coincide with the γ -NiOOH structure. The decrease in the numbers of neighbors of the shortest Ni-Ni path in Ni₃B, and the positive number of neighbors of the Ni-O distance indicates Ni⁰ partial oxidation to Ni^{III} under OER conditions.

Both FT-EXAFS fit and XANES linear combination show that under OER conditions, NiOOH is formed (Figure II - 24). From EXAFS data, the amount of NiOOH is estimated between 10 % and 12 at. %. This ratio does not match with the nickel oxide content found in the electrocatalytically active state according to the linear combination fit, but it rather fits the nickel oxide content found at the OCV from the LCF. We attribute this discrepancy to the uncertainty of CLF, of at least ± 5 at. %. Under alkaline OER conditions, only 10 % of Ni from the Ni₃B phase oxidizes to electrocatalytically active phase NiOOH, whereas Ni nanoparticles are oxidized at 60 %. Even so, Ni₃B shows higher OER activity than Ni. We hypothesize that the predominant factor here is the nanoparticles core conductivity. While NiOOH contains highly electrocatalytically active sites for OER, it is insulating and less conductive than the nickel boride phase. Electrocatalysts forming an excessive amount of NiOOH, like metal Ni, would show overall performances hindered by the decrease of their electrical conductivity preventing charge transfer. The high oxidation resistance observed for Ni₃B allows only the nanoparticles surface to oxidize with a thickness of ca. 0.7 nm, thus forming an ideal system with electrocatalytically active sites anchored at the surface of the conductive boride core.

Path	R	N	$10^3 \sigma^2$	ΔE	Red χ^2	Rf (%)
Ni-O	1.86 (7)	0.6 (4)	5	-5 (2)	587	0.77
Ni-B	2.04	3.0 (1)	13			
Ni-Ni	2.50	6.4 (6)	11			
Ni-Ni	2.77	3.3 (1)	17			
Ni-Ni	2.76 (6)	0.6	6			

Table II - 13 Structural parameters of Ni₃B nanoparticles under OER conditions extracted from Ni K-edge EXAFS refinement. Uncertainties on the last digit are in brackets. Fixed parameters are in bold characters. Related parameters are colored. In blue: constrained $N(\text{Ni-Ni}) = N(\text{Ni-O})$. R, N, σ^2 and ΔE are defined in section 2.2.1.

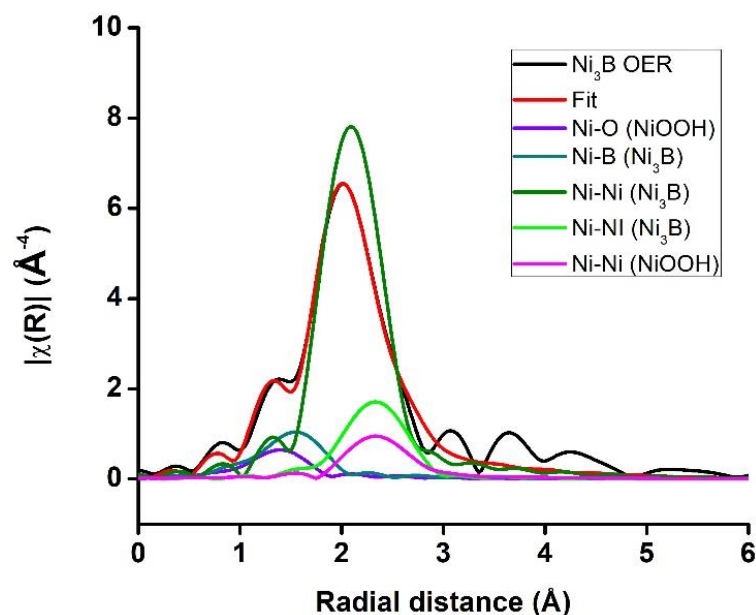


Figure II - 23 Fourier transform of Ni K-edge EXAFS spectrum for Ni_3B nanoparticles under OER conditions (black) and its fit between 1 and 3 Å (red). The latter is split in 5 distance contributions: Ni-O from NiOOH oxide (purple), Ni-B from Ni_3B (dark cyan), Ni-Ni from Ni_3B (olive), Ni-Ni from Ni_3B (light green), Ni-Ni from NiOOH oxide (pink).

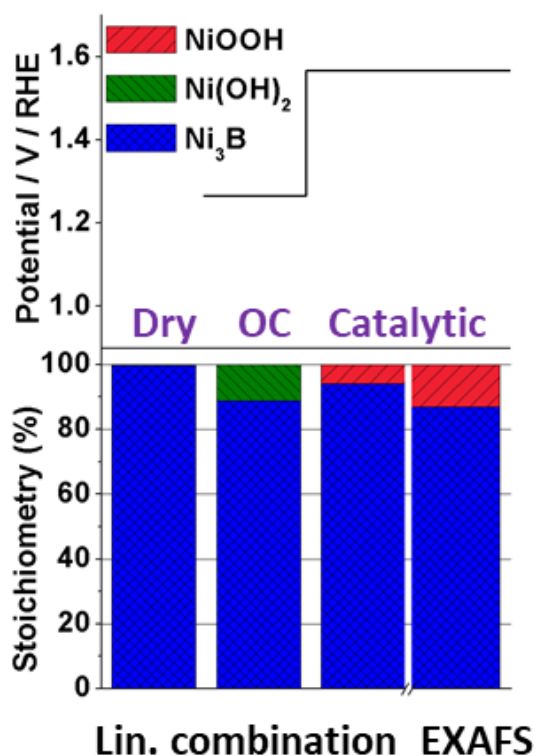


Figure II - 24 Comparison of nanoparticles composition measured by linear combination and EXAFS fitting. Top: Potential applied at each step of OER experiment of Ni_3B nanoparticles in KOH 0.5 M. Bottom, from left to right: Phase compositions obtained from linear combination at dried state, resting state (OC) and under HER condition (Catalytic), then phase composition obtained from EXAFS fitting under OER conditions.

Chapter II: Electrocatalytic properties of Ni_xB_y nanoparticles for water splitting

Overall, the Ni_3B high electrocatalytic activity in HER and OER comes from its stability against oxidation that results in two different phenomena. In acidic and reducing medium, it prevents Ni HER-electrocatalytically active sites to be inhibited. In alkaline and oxidizing medium, it preserves electrical percolation inside and through the nanoparticles. This promising boron effect on Ni-based materials encourages to enrich them with even more boron. We then analyze Ni_4B_3 whose electrocatalytic activity is disappointing.

3.3.3. Ni_4B_3

Ni_4B_3 nanoparticles are obtained by boron insertion in Ni nanoparticles, like Ni_3B . Experimental conditions are optimized to isolate a pure orthorhombic phase of Ni_4B_3 (o- Ni_4B_3). However, TEM-EDX mapping (Figure II - 25) highlights a higher amount of boron on the surface of the nanoparticles. This material exhibits high electrocatalytic activity in HER compared to Ni nanoparticles, but lower than Ni_3B (Figure II – 1). In OER, no activity is observed (Figure II – 2). In order to understand this behavior, we study the evolution of the Ni and boron environment under electrocatalytic condition.

3.3.3.1. *Solid sample*

Like Ni_3B , the orthorhombic Ni_4B_3 reported structure crystallizes in the *Pnma* space group (Figure II - 26). Here, Ni atoms occupy 4 different sites (Table II - 14) resulting in 34 paths between 1 and 3 Å, plus one path at 3.09 Å, which is not so different from the other paths, further impacting the EXAFS fit between 1 and 3 Å. A simpler structure is constructed by merging distances following the same approach than Ni_3B . Ni-B distances are merged together at an estimated distance of 2.1 Å for an average degenerescence of 6. Ni-Ni distances are separated in two groups: the first one includes Ni-Ni distances between 2.2 Å and 2.7 Å, and the second one includes 2.7 Å and 3.0 Å Ni-Ni distances. These groups have an average degenerescence of 7 and 3 respectively.

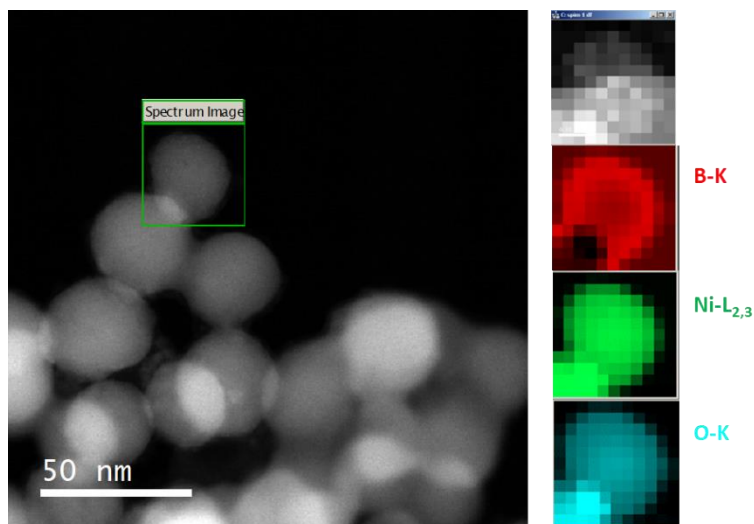


Figure II - 25 TEM image and elemental mapping of a Ni_4B_3 nanoparticle. Boron is in red. Ni is in green. Oxygen is in cyan. A higher concentration of boron can be observed at the surface of the nanoparticle⁸⁵.

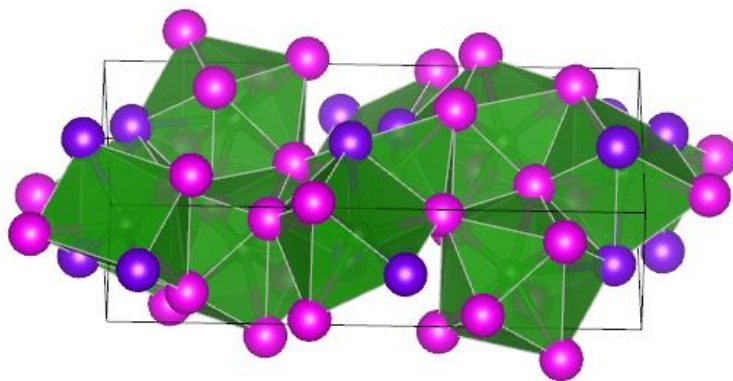


Figure II - 26 Structure of Ni_4B_3 ¹⁰⁵. B is green, Ni is pink and purple.

Chapter II: Electrocatalytic properties of Ni_xB_y nanoparticles for water splitting

Dist.	N	R
Ni-B	2	2.08
Ni-B	1	2.21
Ni-B	2	2.24
Ni-B	1	2.42
Ni-Ni	2	2.46
Ni-Ni	2	2.54
Ni-Ni	3	2.61
Ni-Ni	1	2.85
Ni-Ni	3	2.97
Ni-Ni	4	3.09

Dist.	N	R
Ni-B	1	2.05
Ni-B	1	2.09
Ni-B	4	2.14
Ni-Ni	1	2.35
Ni-Ni	2	2.48
Ni-Ni	2	2.54
Ni-Ni	2	2.62
Ni-Ni	1	2.85
Ni-Ni	1	2.89
Ni-Ni	2	2.98

Dist.	N	R
Ni-B	3	2.06
Ni-B	1	2.08
Ni-Ni	4	2.47
Ni-Ni	1	2.51
Ni-Ni	2	2.58
Ni-Ni	1	2.62
Ni-Ni	2	2.98

Dist.	N	R
Ni-B	1	2.07
Ni-B	3	2.16
Ni-B	2	2.20
Ni-Ni	1	2.51
Ni-Ni	2	2.58
Ni-Ni	4	2.62
Ni-Ni	1	2.89
Ni-Ni	3	2.97

Table II - 14 Ni theoretical paths of Ni₄B₃ between 1 and 3 Å. (PDF card 04-007-0670). Each table correspond to one different Ni site.

Path	Degenerescence	R
Ni-B	6	2.1
Ni-Ni	7	2.5
Ni-Ni	3	2.9

Table II - 15 Simplified paths of Ni₄B₃ between 1 and 3 Å.

Chapter II: Electrocatalytic properties of Ni_xB_y nanoparticles for water splitting

A first fit is performed assuming that the sample is a pure o-Ni₄B₃ phase (Figure II - 27; Table II - 16, fit 1). The numbers of neighbors are fixed at the previously stated values (Table II - 15). The Ni-B distance is 2.11 Å with a Debye-Waller factor of 0.010. Ni-Ni distances are 2.54 and 2.91 Å with Debye-Waller factors of 0.012 and 0.011, respectively. These Ni-Ni distances are shorter than the one expected from the tabulated crystal structure. As it is observed for Ni₃B, this discrepancy may arise from an overestimation of longer paths contribution. The fit exhibits high σ^2 as it is anticipated with excessive distance merges.

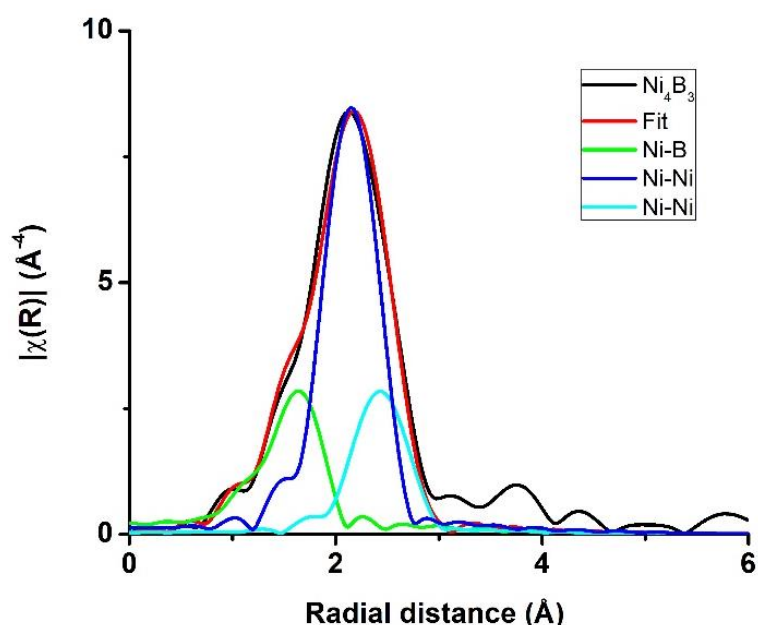


Figure II - 27 FT-EXAFS Ni₄B₃ nanoparticles (black) and its fit between 1 and 3 Å (red). The latter is split in 3 distance contributions: Ni-B (green), and two Ni-Ni (blue and light blue).

Fit	Path	R	N	$10^3 \sigma^2$	ΔE	Red χ^2	Rf (%)
1	Ni-B	2.11 (10)	6.0	10 (6)	-5 (12)	9300	1.95
	Ni-Ni	2.54 (8)	7.0	12 (3)			
	Ni-Ni	2.91 (5)	3.0	11 (10)			
2	Ni-O	2.03 (9)	1.6 (35)	5	-7 (22)	20000	1.87
	Ni-B	2.00 (36)	6.0	17 (10)			
	Ni-Ni	2.53 (12)	7.0	12 (4)			
	Ni-Ni	2.91 (9)	3.0	11 (17)			

Table II - 16 Structural parameters of Ni₄B₃ nanoparticles extracted from Ni K-edge EXAFS refinement. Uncertainties on the last digit are in brackets. Fixed parameters are in bold characters. R, N, σ^2 and ΔE are defined in section 2.2.1.

Chapter II: Electrocatalytic properties of Ni_xB_y nanoparticles for water splitting

We then perform a second fit, considering the hypothesis that o-Ni₄B₃ is partially oxidized (Table II - 16, fit 2). As with the previous nickel boride, Ni₄B₃ path number of neighbors are left on their approximated values. The Ni-O Debye-Waller factor is set at 0.005, the NiO phase value. The calculated fit shows a ΔE of -7 eV and gives to o-Ni₄B₃-originated paths similar distances and Debye-Waller factors than in the first fit, except the Ni-B path whose distance is 2.00 Å and its σ^2 is 0.017. The Ni-O path number of coordination is 1.6 ± 3.5 for a distance of 2.03 Å. Such closeness with Ni-B distance raises concern in the ability of the fit to discriminate these two distances. The Ni-B high Debye-Waller factor is also another clue about an artificial split in two distances: with other parameters constant, if σ^2 increases, the peak intensity decreases. This could be compensated whether by increasing the number of neighbors or by adding a virtual peak. The second option seems to happen here: in order to increase the intensity of the peak of the Ni-B distance, the calculation yields a convolution with a virtually created Ni-O distance instead of decreasing the σ^2 of Ni-B. Therefore, this second fit seems unreliable. The Ni₄B₃ solid sample is then supposed pure and not oxidized, as the first fit suggests.

3.3.3.2. HER

16 “dry state” scans are collected before filling the electrochemical cell with H₂SO₄ 0.5 M electrolyte. 10 “resting state” scans are then collected. 10 scans are then collected at -0.16 V/RHE, under electrocatalytic conditions (Figure II - 28, top). The acquired spectra are fitted by linear combination of reference o-Ni₄B₃ solid-state and Ni(OH)₂ spectra (Figure II - 28). The Ni(OH)₂ content in dry state, resting state and activated state are 5, 10 and 20 at. % respectively. It is hard to conclude on the oxidation of the o-Ni₄B₃ nanoparticles at the dry state. However, the augmentation of percentage of Ni(OH)₂ at the OCV and at the active state (HER) confirm the oxidation of Ni₄B₃ in these conditions.

The FT-EXAFS of Ni₄B₃ nanoparticles in HER conditions is fitted with Ni₄B₃ and NiO components (Figure II - 29; Table II - 17), resulting in four distances: one Ni-O distance around 2 Å, one Ni-B distance around 2.06 Å and two Ni-Ni distances around 2.5 Å and 2.9 Å. σ^2 values are fixed according to the results obtained in sections 3.2 and 3.3.3.1. To reduce the number of variables, the distance lengths in Ni₄B₃ are fixed according to the values obtained from the fit of the solid sample. The number of neighbors for the Ni₄B₃-based Ni-B distance and the two Ni-Ni distance are 6.5 ± 57.1 , 5.8 ± 5.5 and 2.0 ± 81.7 . The Ni-O number of neighbors shows a large uncertainty (0.0 ± 11.6) as well as the Ni-O distance.

Chapter II: Electrocatalytic properties of Ni_xB_y nanoparticles for water splitting

These high uncertainties and questionable values highlight that the EXAFS fit is difficult to exploit in this specific case.

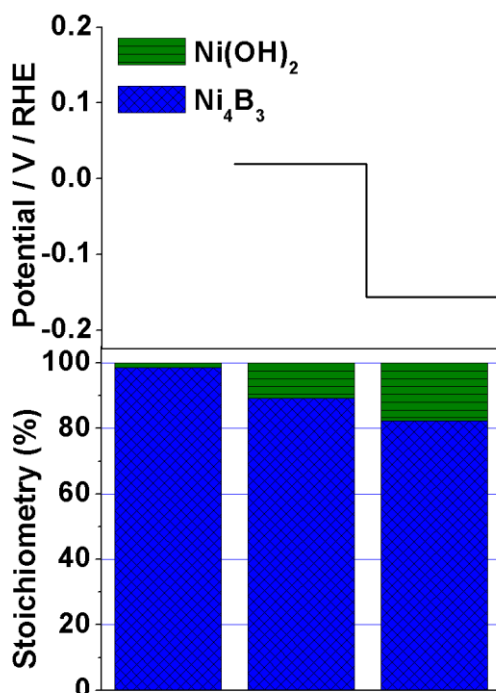


Figure II - 28 Top: Potential applied at each step of HER experiment of Ni_4B_3 nanoparticles in H_2SO_4 0.5 M. Bottom: Phase compositions obtained from linear combination (from left to right) at dried state, resting state, then under HER condition.

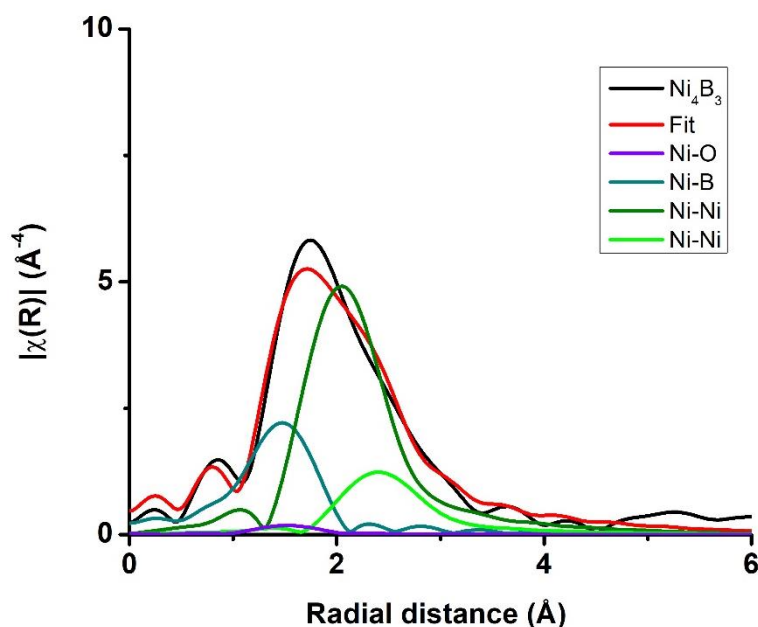


Figure II - 29 Fourier transform of Ni K-edge EXAFS spectrum for Ni_4B_3 nanoparticles under HER conditions (black) and its fit between 1 and 3 Å (red). The latter is split in 5 distance contributions: Ni-O from NiO oxide (purple), Ni-B from Ni_4B_3 (dark cyan), Ni-Ni from Ni_4B_3 (olive), Ni-Ni from Ni_4B_3 (light green).

Chapter II: Electrocatalytic properties of Ni_xB_y nanoparticles for water splitting

Path	R	N	10 ³ σ ²	ΔE	Red chi ²	Rf (%)
Ni-O	2.04 (>1000)	0.0 (116)	5	-10 (2)	7600	3.90
Ni-B	2.11	6.5 (571)	10			
Ni-Ni	2.54	5.8 (55)	12			
Ni-Ni	2.91	2.0 (817)	11			

Table II - 17 Structural parameters of Ni₄B₃ nanoparticles under HER conditions extracted from Ni K-edge EXAFS refinement. Uncertainties on the last digit are in brackets. Fixed parameters are in bold characters. R, N, σ² and ΔE are defined in section 2.2.1.

All in all, XANES fitting with linear combination in HER conditions reveals partially oxidized nickel, at a similar extent than Ni nanoparticles. Yet the oxide has a different origin than in nickel particles: while Ni already oxidizes under ambient atmosphere, Ni₄B₃ is oxidation-resistant in ambient conditions but is oxidized when exposed to the acidic aqueous medium. Its boron-rich layer may have passivated the nanoparticles and then dissolved in H₂SO₄-based electrolyte, thus allowing the underlying o-Ni₄B₃ to get oxidized.

3.3.3.3. OER

6 “dry state” scans are collected from a Ni₄B₃ coated electrode before filling the electrochemical cell with KOH 0.5 M electrolyte. 6 “resting state” scans are then collected. A cyclic voltammogram between 1.07 and 1.67 V/RHE is recorded to assure that the material displayed its usual OER activity. 11 scans are then collected at 1.62 V/RHE, potential at which OER is observed. Another cyclic voltammogram is performed to verify any modification during the electrochemical experiment.

The acquired XANES spectra are fitted by linear combinations of o-Ni₄B₃, Ni(OH)₂ and NiOOH reference spectra (Figure II - 30). Here, the dry state is composed of 70 at. % Ni₄B₃, 25 at. % Ni(OH)₂ and 5 at. % NiOOH. Noteworthy, o-Ni₄B₃ is highly oxidized in the dry state, which is clearly different to what was observed on the electrode used for HER experiment. Since the two electrodes are supposedly identical, this result shows that Ni₄B₃ is eventually highly sensitive to ambient atmosphere. Such differences in composition could then be attributed to the drying time that is not controlled. Once the alkaline electrolyte is added, the material composition was 60 mol. % Ni₄B₃, 35 mol. % Ni(OH)₂ and 5 mol. % NiOOH, showing further oxidation in contact with an alkaline aqueous medium. During OER, the material is composed of 50 % Ni₄B₃, 10 % Ni(OH)₂ and 40 % NiOOH, similar to the behavior of nickel nanoparticles. Most of the oxidized nickel species are Ni(III), suggesting that this state is indeed the active one for OER.

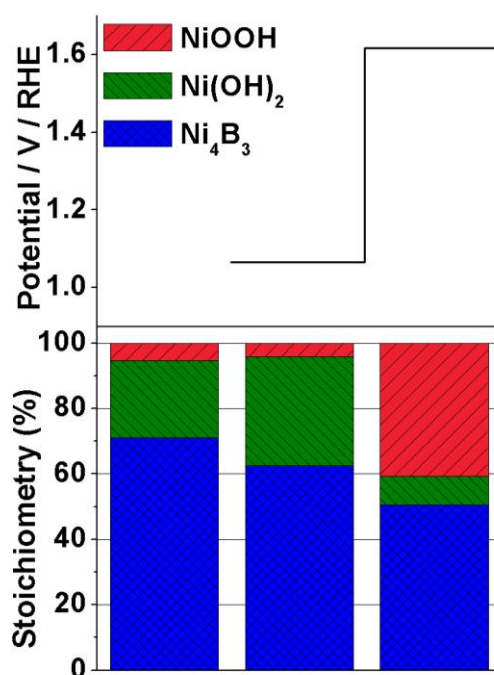


Figure II - 30 Top: Potential applied at each step of OER experiment of Ni₄B₃ nanoparticles in KOH 0.5 M. Bottom: phase compositions obtained from linear combination (from left to right): at dried state, resting state, then under OER condition.

The FT-EXAFS of o-Ni₄B₃ nanoparticles under OER conditions is fitted with Ni₄B₃ and NiOOH components, resulting in five distances: one Ni-O distance around 1.9 Å, one Ni-B path around 2.1 Å and three Ni-Ni paths around 2.5 Å, 2.8 Å and 2.9 Å. σ^2 values are fixed according to the results obtained in sections 3.2. and 3.3.3.1. (Figure II - 31, Table II - 18). To reduce the number of variables, the lengths of Ni₄B₃-based distances are fixed. Ni-O and Ni-Ni distances from nickel oxide are correlated with $\frac{N(Ni-O)}{N(Ni-Ni)} = 1$ according to the γ -NiOOH structure. The number of neighbors in the Ni₄B₃-based Ni-B and two Ni-Ni distances are 5.0 ± 15.3 , 3.4 ± 3.8 and 0.0 ± 7.2 respectively. The number of neighbors for the Ni-O distance was 1.2 ± 1.9 . Nickel oxide-based Ni-O and Ni-Ni distances were 1.91 ± 0.21 Å and 2.89 ± 0.21 Å, respectively. The uncertainty of Ni₄B₃-based distances is large, suggesting that the local structure is strongly different from the structures that can be described by our fits. Still, considering the relatively low uncertainties of nickel oxide-based paths, we could speculate that the material under OER conditions possesses a combination of Ni^{II} and Ni^{III} species, as Ni-O and Ni-Ni distances are intermediate between Ni(OH)₂ and NiOOH phases.

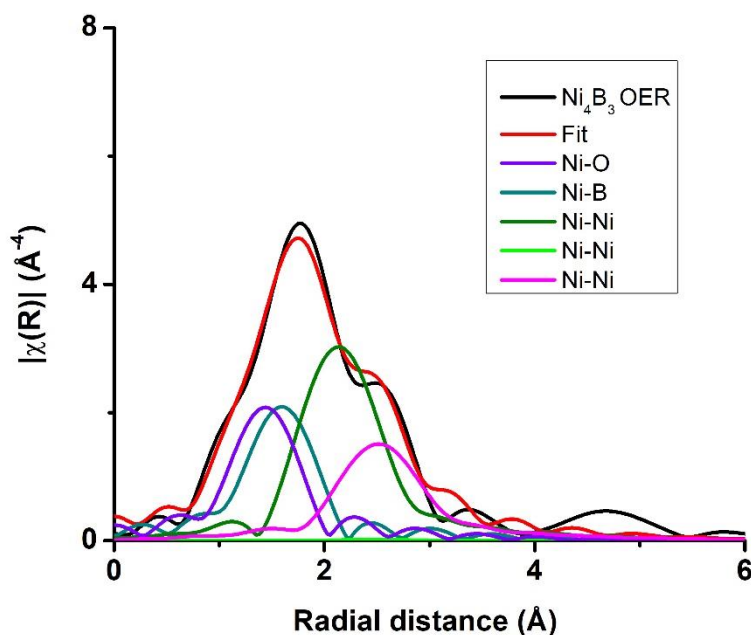


Figure II - 31 Fourier transform of Ni K-edge EXAFS spectrum for Ni₄B₃ nanoparticles under OER conditions (black) and its fit between 1 and 3 Å (red). The latter is split in 5 distance contributions: Ni-O from NiOOH oxide (purple), Ni-B from Ni₄B₃ (dark cyan), Ni-Ni from Ni₄B₃ (olive), Ni-Ni from Ni₄B₃ (light green), Ni-Ni from NiOOH oxide (pink).

Path	R	N	10 ³ σ ²	ΔE	Red chi ²	Rf (%)
Ni-O	1.91 (21)	1.2 (19)	5	0 (11)	3100	1.31
Ni-B	2.11	5.0 (153)	10			
Ni-Ni	2.54	3.4 (38)	12			
Ni-Ni	2.91	0.0 (72)	11			
Ni-Ni	2.89 (21)	1.2	6			

Table II - 18 Structural parameters of Ni₄B₃ nanoparticles under OER conditions extracted from Ni K-edge EXAFS refinement. Uncertainties on the last digit are in brackets. Fixed parameters are in bold characters. Related parameters are colored. In blue: N(Ni-Ni) = N(Ni-O). R, N, σ² and ΔE are defined in section 2.2.1.

XANES linear combination fit reveals that o-Ni₄B₃ follows the same trend than metal Ni for the same experiments: Besides showing that o-Ni₄B₃ is in fact sensitive to oxidation under air, half of the nickel atoms are oxidized during OER and NiOOH is formed. Yet, its OER electrocatalytic activity is low. This surprising behavior may come from the boron-rich layer of the synthesized Ni₄B₃ nanoparticles that does not dissolve in alkaline medium and passivates the metal boride core. Consequently, even if NiOOH is formed at high potential, this passivation layer hinders accessibility of the electrolyte to the catalytic NiOOH layer.

Chapter II: Electrocatalytic properties of Ni_xB_y nanoparticles for water splitting

The o-Ni₄B₃ complex crystal structure, the inhomogeneity of the starting composition caused by a boron-rich layer and the formation of unidentified phases suggested by the inability to obtain a satisfying fit in FT-EXAFS undermines the extraction of any reliable results from FT-EXAFS. XANES linear combination fitting reveal that these nanoparticles exhibit a similar nickel oxide content to Ni nanoparticles. However, their electrocatalytic activities are opposite: while Ni nanoparticles are highly active in OER but inactive in HER, o-Ni₄B₃ nanoparticles show high activity in HER but a poor activity in OER. The passivating boron-rich layer at the surface of these particles could have prevented its electrocatalytic activity in OER. The origin of o-Ni₄B₃ HER performances is still under investigation as inactive nickel oxides Ni(OH)₂ is identified, which is counterintuitive according to the reducing conditions present.

4. Discussion

4.1. Methodology

Nickel borides are challenging materials to study by *operando* XAS because of their low stability under ambient air and their complex crystal and local structure. The random content of oxide that is already found at the dry states of o-Ni₄B₃, and the impact of the electrolyte on the composition of the electrocatalyst highlights the necessity to monitor and to verify the composition at different stages of electrode preparation before studying the *operando* conditions. Besides stating that the composition of the material has already changed before the electrocatalysis, the dissolution of the oxide layer of Ni metal in HER decreases the size of the nanoparticles, and by the same way the surface of the electrocatalytic material.

Nickel boride crystalline structures are hard to analyze through FT-EXAFS. The low symmetry of their lattices added to the short distances results in a FT-EXAFS with the shape of one broad peak on a short range of 1-3 Å that is the convolution of up to 30 paths in the case of Ni₄B₃. By merging these paths, a simplified structure of three paths has been constructed, where each original path is given a weight proportional to its degenerescence. However, this model does not take into account the decrease of intensity of the peaks at higher distances. This oversight is reflected in the number of neighbors obtained for high distances that is lower than expected theoretically.

Chapter II: Electrocatalytic properties of Ni_xB_y nanoparticles for water splitting

After this drastic simplification, we need to fit a broad peak with up to five paths. Usually, the reliability of a fit is verified by the visual shape of the fit compared to the experimental FT-EXAFS. This method, necessary but not sufficient, applies to classical and simple structures, where one peak is attributed to only one distance¹⁰⁶. Most of the FT-EXAFS studies on metal borides are carried out on amorphous materials where the first peak is mainly attributed to the metal-metal distance^{39,67,84}. Rades et al. have analyzed the structure of crystalline FeB by EXAFS but in their article, no detail on their methodology is provided¹⁰⁷. During our work, every calculated fit looks like the experimental FT-EXAFS and we are unable to discriminate one fit from another from a visual criterion. Consequently, the most suitable fit is exclusively determined by the value and the uncertainties of the parameters of the fits.

We verify the oxidation of a compound by comparing the quality of the fits by using a structure without Ni-O distances and a fit where the Ni-O distances are allowed. Indeed, while allowing as many distances as possible to be variables seems to increase the chances to obtain the right phase, the high amount of variables increases the uncertainties on every values, as it was observed on the fit of Ni_3B solid sample.

4.2. Evolution of the electrocatalysts

The metallic nickel nanoparticles contain nickel vacancies. It is then unclear if the nickel oxide phase that is formed afterwards conserves the same amount of vacancies or if the oxygen inserts inside these vacancies. Consequently, only a maximum and a minimum value of the oxide content can be estimated (Appendix section 4.1.). The oversimplification of the FT-EXAFS fitting of Ni_3B and o- Ni_4B_3 structure makes difficult to determine whether these nanoparticles do or do not contain vacancies. However, the high crystallinity of the nanoparticles and the conservation of the nanoparticle size⁸⁵ suggest a boron insertion that may have filled these vacancies.

The formation of NiOOH during OER in alkaline medium is observed with every electrocatalyst, suggesting that NiOOH is the active species for OER. During HER in acidic medium, the metallic nickel nanoparticles are still partially oxidized, while the Ni_3B nanoparticles show no sign of oxidation. The high electroactivity of Ni_3B in HER compared to Ni is then attributed to its higher amount of non-oxidized Ni active sites. These observations on Ni_3B during OER and HER are similar to the reported behavior of metal borides^{39,83}. The stability of Ni_3B to nickel oxidation is attributed to d-electron transfer from

Chapter II: Electrocatalytic properties of Ni_xB_y nanoparticles for water splitting

boron to nickel atoms, thus enriching the d-band of the transition metal¹⁰⁸. During OER, this stability allows Ni₃B nanoparticles to keep a conducting core, while still providing a minimal layer of active phase that is less conducting (Figure II - 32). This core-shell structure-like is favorable to high electroactivity. As XAS on the K-edge does not probe the d-band directly, the enrichment of the d-band is difficult to observe. Investigation on the Ni L-edge could bring more information on the evolution of the d-band of nickel.

o-Ni₄B₃ nanoparticles do not follow the same trend than Ni₃B. While o-Ni₄B₃ is more active than Ni in HER, it is not active in OER, despite the detection of the NiOOH phase under electrocatalytic conditions. The failure of FT-EXAFS fitting to find adequate structure for the catalytic state suggests that the composition of the compound includes a phase that is not taken into account in our fitting methodology, which only includes Ni metal, Ni₃B, o-Ni₄B₃, NiO, β-Ni(OH)₂ and γ-NiOOH. The boron-rich layer on the surface of Ni₄B₃ nanoparticles may have oxidized and formed an insulating boron-rich layer in alkaline electrolyte, impeding then good electroactivity and electron transfer. The dissolution of this boron-rich layer in acidic electrolyte would help recovering electrocatalytic activity comparable to other metal borides as free active nickel sites would appear again. Our FT-EXAFS fitting methodology is not the most practical technique to identify the partial formation of a nickel borate, or more generally a boron-rich, phase from a nickel boride phase. The structure of nickel borates is as complex as the structure of nickel borides. Consequently, trying to fit a material containing both phases would require too many variables on a range too short. Other techniques of analysis should be called into. The investigation of the boron K-edge could assert the presence on borates. However, boron K-edge is difficult to observe under catalytic conditions because of its low energy (around 200 eV). We tried to obtain boron K-edge by inelastic X-ray scattering (IXS) but, because of the presence of a heavy atom such as nickel, which absorbs most of the photons, this technique provides a very low signal to noise ratio. Near ambient pressure X-ray photoelectron spectroscopy could bring insights of the surface of o-Ni₄B₃ nanoparticles under conditions that are close to electrocatalysis. Aside from spectroscopy, local morphology and crystalline modification during OER could be observed by *operando* transmission electron microscopy.

Chapter II: Electrocatalytic properties of Ni_xB_y nanoparticles for water splitting

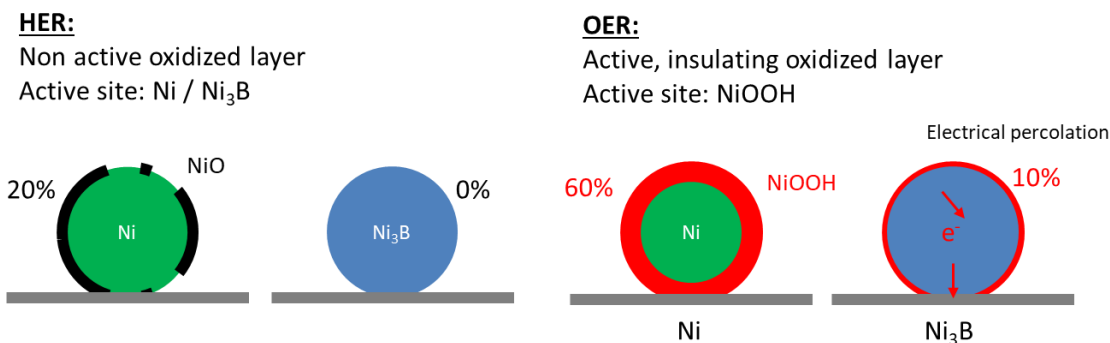


Figure II - 32 Scheme of the activated state of Ni and Ni_3B nanoparticles during HER in acidic electrolyte and during OER in alkaline electrolyte.

5. Conclusion

In this chapter, we introduced two complementary X-ray absorption spectra analysis techniques: XANES linear combination and Fourier transform EXAFS fits. We applied them to Ni_xB_y nanoparticles under HER and OER conditions. Metallic nickel nanoparticles were first studied to set the methodology and then more complex compounds Ni_3B and o- Ni_4B_3 were studied. In the work presented herein, we have followed the materials transformation from the pristine to the electrocatalytically active states.

We explained that the XANES linear combination principle was based on the Beer-Lambert law and could give the composition of the electrodes using a series of references. We then acknowledged its methodological limitations, mostly from the arbitrary choice of said references. We then explained the physical meaning underlying FT-EXAFS parameters and described our approach to find the right fit.

Several phenomena could already be observed from nickel nanoparticles investigations: oxidation of nickel appeared in air and when the electrode is in contact with aqueous electrolytes. Under electrolysis, the quantity of nickel oxide was estimated to be 25 at. % in HER and 60 at. % in OER. The experiment also suggested nickel vacancies inside the nanoparticles and shortened Ni-Ni distances. This may be linked to the nanoscale of the studied materials.

Ni_3B displayed a complex structure that rendered its analysis by FT-EXAFS difficult. A simplification of its structure was necessary. We suspect its high electrocatalytic activity in HER and OER to originate from its high stability towards oxidation. This is linked to the presence of boron in the material. Indeed, previous reports based on XPS and Auger

Chapter II: Electrocatalytic properties of Ni_xB_y nanoparticles for water splitting

spectroscopy have shown that in nickel borides, electron back-donation from boron to nickel enriches nickel in d electrons and increases its “nobility”^{38,109}.

The $\text{o-Ni}_4\text{B}_3$ complex structure needed more simplification than Ni_3B to allow EXAFS fitting and EDX-TEM characterization of the pristine material indicated a boron-rich upper layer. Such very complex structure was too challenging to be described by FT EXAFS *operando*. Still, linear combination methodology indicates a behavior similar to metallic Ni in terms of nickel oxidation state during HER and OER experiments. These results were at first sight contradictory with those we obtained on Ni_3B . Indeed, while our observation on Ni_3B suggested that the presence of boron enhances the HER and OER activity of nickel boride compared to nickel metal, $\text{o-Ni}_4\text{B}_3$ and Ni possessed drastically opposed behavior in HER and OER, with $\text{o-Ni}_4\text{B}_3$ activity being absent in OER. One part of the answer to the discrepancy is linked to the boron-rich upper layer passivating the nanoparticles under OER conditions.

Several points could be reviewed or improved in this work. First, given the uncertainty on the results for $\text{o-Ni}_4\text{B}_3$, other nickel-based phases should be added to linear combination references, especially nickel borates. Nickel sulfate could also be considered as it could be formed in acidic electrolyte. Many qualitative approximations have been made to simplify EXAFS fits, such as merging of paths. It was observed that peaks at different distances did not have similar contributions. Each weight should be estimated more accurately from theoretical calculations. Our interpretations were mostly based on a spherical model with a crystal core and a crystal shell. Our model did not take into account any transient zone nor any amorphous phase. Regarding nickel borides study, more investigations should be performed. Even though preliminary characterization established the stability of these materials, nickel dissolution was not evaluated through *operando* XAS. Eventually, observing Ni_xB_y electrocatalysis from the boron point of view could complete this nickel-based analysis. However, as a light element, boron is difficult to analyze, particularly with *operando* techniques.

Chapter III:

Evolution of manganese and cobalt-based perovskites during the oxygen evolution reaction and the oxygen reduction reaction

1. Introduction

ABO₃ perovskites are a versatile group of materials as their physical properties can be tuned by tailoring A and B cation sites with multiple cationic substitutions (Figure III - 1). In the field of electrocatalysis, they have been widely investigated as cost-effective alternatives to precious metal-based electrocatalysts for OER or ORR¹¹⁰. Their active site is generally placed on the B site as a transition metal cation. The choice of the B site cation(s) influences the bond strength between the surfaces of adsorbed dioxygen. Moreover, the A site cation(s) influences the charge density on the B site transition metal cations, their oxidation state, and the metal-oxygen distance. The A site occupancy also influences the formation of oxide ion vacancies¹¹¹. Overall, the A site cation enables tuning the adsorption energy of reagents and intermediates. Shao-Horn's group has correlated perovskite OER and ORR electrocatalytic activities with the d-block e_g orbitals electronic occupancy of the B site cations (Figure III - 2). These considerations have led to the identification of Ba_{0.5}Sr_{0.5}Co_{0.8}Fe_{0.2}O_{3- δ} (BSCF) as the perovskite with the highest activity in OER.³⁶ However, such high activity comes along with surface instability and amorphization during the reaction, partly due to the lattice oxygen evolution reaction (LOER)^{56,112}. Consequently, there is a need to investigate the structural evolution of perovskite materials during electrocatalysis.

LaMnO₃ is one of the most active bicationic perovskites in ORR^{110,113}. Partial substitution of La³⁺ with Sr²⁺ improves its performances by increasing the material conductivity and providing the optimal amount of e_g electrons (Figure III - 2). The minimum ORR overpotential is observed with 33 at. % Sr¹¹⁴. The same evolution is observed with La_{1-x}Sr_xCoO₃ perovskites for the OER electrocatalytic activity¹¹⁵.

In this chapter, we look into these manganese and cobalt-based perovskites using *operando* XAS. Starting from LaMnO₃, we study the impact of “Sr” substitution in La_{0.67}Sr_{0.33}MnO₃, and “Co” substitution in LaMn_{0.6}Co_{0.4}O₃ onto the OER, the ORR or both. First, we describe LaMnO₃ and La_{0.67}Sr_{0.33}MnO₃ synthesis and their electrocatalytic properties in ORR. Then, we demonstrate the flexibility of our protocol to synthesize La_{0.67}Sr_{0.33}CoO₃ and LaMn_{0.6}Co_{0.4}O₃ perovskites. The electrocatalytic activities in both OER and ORR are then evaluated and discussed according to structural parameters (oxidation state or local environment). Finally, we monitor the evolution of these materials during the electrochemical reaction by *operando* XAS.

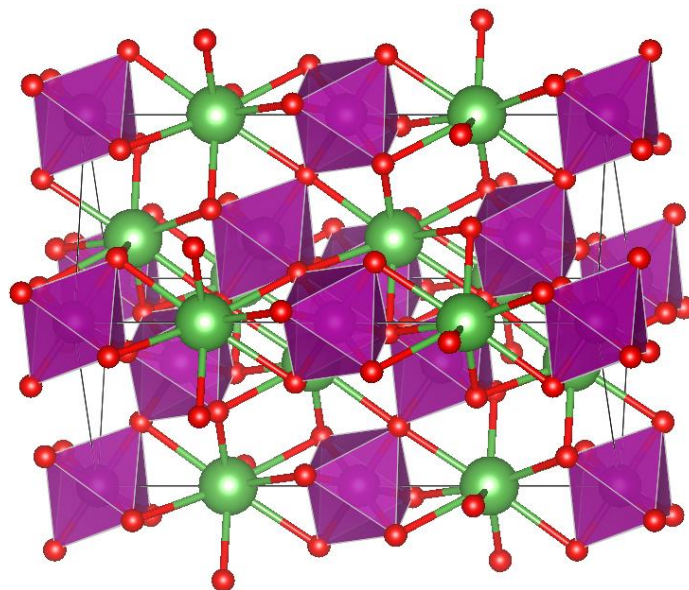


Figure III - 1 Structure of LaMnO_3 perovskite¹¹⁶. La (A site), Mn (B site), and O atoms are in green, purple and red, respectively. While the simple cubic perovskite crystal structure is $P4mm$, the Jahn-Teller effect on Mn^{3+} centers induces a lattice distortion to the $Pbnm$ space group.

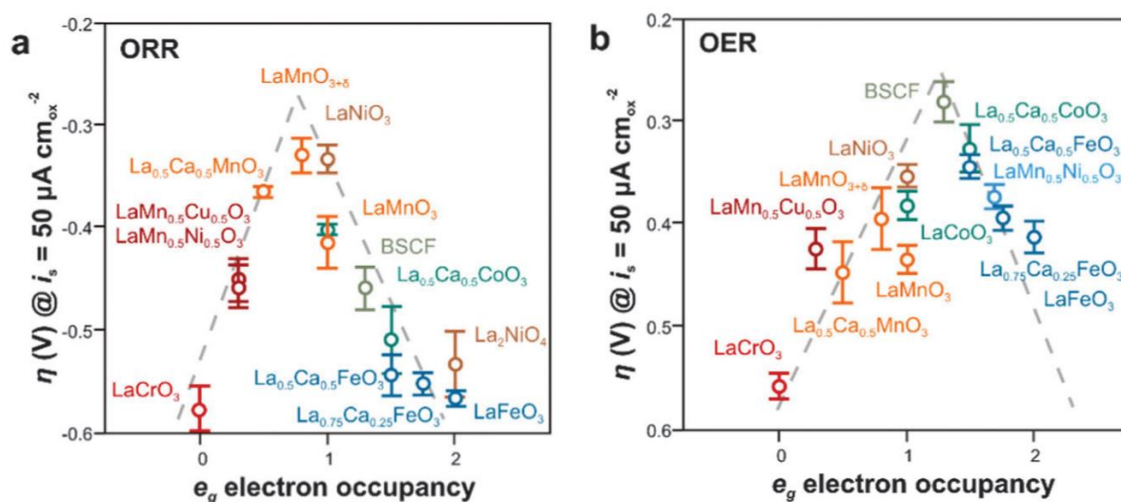


Figure III - 2 ORR and OER electrocatalytic activities of various perovskite oxides in alkaline solution (KOH 0.1 M). (a) Overpotentials for the ORR as a function of e_g electron occupancy. (b) Overpotentials for the OER as a function of e_g electron occupancy. Reproduced from Hong et al. (2015).¹¹⁰

2. Model materials: LaMnO_3 and $\text{La}_{0.67}\text{Sr}_{0.33}\text{MnO}_3$

2.1. An overview of the synthesis of perovskites

Perovskite oxides are multicationic oxides. This simple definition highlights the two main challenges of perovskite synthesis: atomic homogeneity and crystallization. In solid-state synthesis of perovskite oxides, oxide and carbonate precursors are ball-milled together for a long time and then heated up to high temperature, over 1000 °C during several hours¹¹⁷. This step often needs to be repeated several times to achieve pure perovskite phase because the low diffusion coefficient of cations in solids ($10^{-18} \text{ cm}^2 \cdot \text{s}^{-1}$)¹¹⁸ requires long reaction time assisted by vigorous grinding. Other pathways consist in mixing the precursors in a liquid phase, to form an amorphous solid or a mixture of binary oxides, and then crystallize these intermediate mixtures by calcination. This is the strategy of sol-gel synthesis¹¹⁹, co-precipitation^{36,120} and autocombustion synthesis^{121,122}. In nanoscaled perovskites for prospective electrocatalysis, calcination has a negative impact as it tends to trigger a decrease of the surface area by sintering the particles. In some conditions, auto-combustion can bypass this second step of calcination if the combustion temperature is high enough to allow the crystallization of the perovskite. However, organic residues are often observed and, involuntary favor substitution and sintering. Crystallization in liquid phase has been investigated in solvothermal synthesis, where the driving forces are the high solubility and reactivity of the reagents along with the drop of the inorganic material solubility near the critical point of the solvent¹²³. Despite being well crystallized, nanoparticles formed by this pathway exhibit variable sizes and morphologies^{124,125}. Moreover, the limited temperature range accessible with common solvents ($< 300 \text{ °C}$) does not enable crystallization of manganite perovskites. Molten salt synthesis extends the concept as it allows triggering the reaction of soluble precursors at a temperature high enough to crystallize Mn- and Co-based perovskites, above 600 °C. Such an advance is enabled by the use of a salt with melting point much lower than the reaction temperature, thus allowing ions to diffuse much faster than in solid-state synthesis ($10^{-5} - 10^{-8} \text{ cm}^2 \cdot \text{s}^{-1}$)¹¹⁸, even if the process occurs at lower temperature. Moreover, initial grinding of precursors with the molten salts does not need to be as energetic as for solid-state synthesis and the products are also easily recovered by dissolving the salt in a suitable solvent, usually water.

Chapter III: Evolution of Mn and Co-based perovskites during the OER and the ORR

According to Arendt¹¹⁸, and as for other solvents, the reaction in molten salt synthesis proceeds by supersaturation of the molten salt solvent by the constituent reactants, then precipitation of the less soluble products from the solution. The reaction stops when the solution contains only a residual concentration of the reactants, which are then removed with the salt. The choice of a salt is then highly important. It is dictated by its thermal stability and ability (when known) to dissolve reagents, so by its acid-base and coordination properties, for instance. Other critical parameters have been identified to influence the reaction rate, particle size and particle shape¹²⁶. Among them, the concentration of reagents can modify the particle size. Hence, the production of nanomaterials was enabled by diluting reactants in a solvent salt and by thermally quenching the reaction to limit aggregation. Thi N'Goc *et al.* developed this kind of synthesis for $\text{La}_{0.67}\text{Sr}_{0.33}\text{MnO}_3$ nanocrystals in 2017¹²⁷. They used nitrate precursors diluted in molten potassium nitrate. Besides being highly soluble in molten KNO_3 , metal nitrates serve as oxidizing agents, as well as the solvent. Their remnant traces easily decompose upon heating.

2.2. Molten salt synthesis of LaMnO_3 (LMO) and $\text{La}_{0.67}\text{Sr}_{0.33}\text{MnO}_3$ (LSMO)

$\text{La}_{1-x}\text{Sr}_x\text{MnO}_3$ nitrate precursors are $\text{La}(\text{NO}_3)_3 \cdot 6\text{H}_2\text{O}$, $\text{Sr}(\text{NO}_3)_2$ and $\text{Mn}(\text{NO}_3)_2 \cdot 4\text{H}_2\text{O}$. They are purchased hydrated and need preliminary drying before the reaction. A stoichiometric reaction with these precursors would form $\text{La}(\text{OH})_3$ lanthanum hydroxide impurities according to preliminary studies¹²⁷. Indeed, even though the reaction is nearly total, traces of simple oxides remain after heating: lanthanum oxide, strontium oxide and manganese oxide. Among them strontium oxide and manganese oxide are soluble in water and are removed during washing, whereas lanthanum hydroxide is not. Consequently, reactants are mixed with La/Sr/Mn ratio of $0.9-x/x/1$ ($x = 0$ for LaMnO_3 and $x = 0.33$ for $\text{La}_{0.67}\text{Sr}_{0.33}\text{MnO}_3$) and diluted in KNO_3 with a Mn/K molar ratio of 1/10. The powdered mixture is coarsely grinded with a ball miller because no stirring is provided during the heating. The powder is then put in a furnace under air and preheated at 600 °C to increase the heating rate and hence the nucleation rate at a temperature higher than the salt melting point, so in a liquid phase. After one hour, the nanoparticles growth is rapidly stopped by quenching the system at room temperature. The nanoparticles are recovered by dissolving the salt with an adapted liquid solvent. Here, deionized water can be used as it dissolves salt but does not destroy the oxide particles. The purified nanoparticles are obtained after about ten centrifugation-redispersion cycles evaluated from the water conductivity (value under 20 $\mu\text{S}\cdot\text{cm}^{-1}$). Nanoparticles are finally dried under vacuum at 60 °C.

2.3. Material characterization

All peaks on the powder X-ray diffraction (XRD) pattern (Figure III - 3) of the $\text{La}_{0.67}\text{Sr}_{0.33}\text{MnO}_3$ (LSMO) sample are attributed to the perovskite phase. The LaMnO_3 sample includes an additional peak at 15° (2θ $\text{CuK}\alpha$). It could be a potassium compound (i.e. KMnO_2). Aside from this impurity, the X-ray diffractograms indicate only the perovskite phase. We also notice that the angular resolution of these diffractograms is too low to differentiate LaMnO_3 from $\text{La}_{0.67}\text{Sr}_{0.33}\text{MnO}_3$ by the perovskite cell parameters.

According to transmission electron microscopy (TEM) (Figure III - 4), the samples are mainly composed of crystalline nanoparticles with an average diameter of 25 nm. In the LSMO sample, most of the nanoparticles are well-faceted cubes with sharp edges. Whereas in the LMO sample, the nanoparticles appear rounder.

The elemental composition was measured by wavelength diffraction x-ray fluorescence (WDXRF). The LMO sample contains La and Mn in atomic proportion of 1.16/1.00. The La excess confirms the presence of lanthanum oxide impurities that is observed in XRD. This technique is not efficient to quantify the oxygen content. Four elements are detected in the LSMO sample besides oxygen: La, Sr, Mn and K. Their atomic proportions are respectively 0.75/0.31/1.00/0.01. Small amounts of potassium impurities arise from the salt. Considering that the uncertainty of the WDXRF measurements without internal standards is 5 at. %, the sum of La and Sr (1.06) shows that there may be a slight excess of La. Indeed, there is unlikely an excess of strontium oxide in the sample because strontium oxide reacts with water to form strontium hydroxide, which is highly soluble in water ($22.5 \text{ g}\cdot\text{L}^{-1}$ ¹²⁸), and should have been removed during the washing step. Consequently, there may be lanthanum impurities in the LSMO sample, likely hydroxide that is insoluble in water, but such small amounts cannot be detected in XRD. The actual composition of the LSMO sample can then be assumed as $\text{La}_{0.75\pm 0.05}\text{Sr}_{0.31\pm 0.05}\text{MnO}_3 + 0.06 \pm 0.05 \text{La}(\text{OH})_3$.

LMO and LSMO perovskite nanocrystals can be synthesized through molten salt synthesis with an average particle size of 25 nm. Lanthanum hydroxide (about 6 ± 5 mol. % according to WDXRF) can be observed as impurity in LMO. This impurity is insulating and not active in ORR. Consequently, it should not disturb the electrocatalytic measurements.

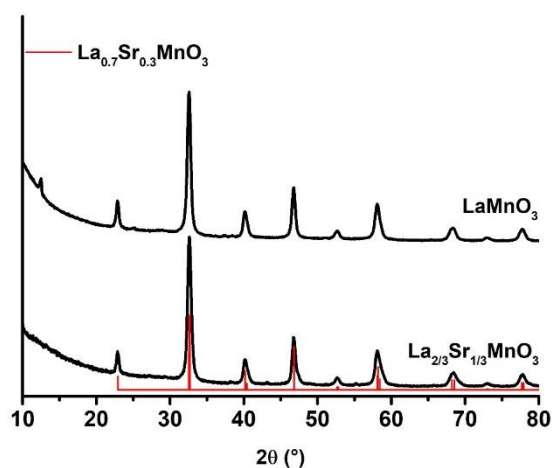


Figure III - 3 Powder XRD patterns of LaMnO_3 (top) and $\text{La}_{0.67}\text{Sr}_{0.33}\text{MnO}_3$ (bottom) synthesized using the molten salts protocol in ref^{127,129}. The reference pattern in red corresponds to $\text{La}_{0.67}\text{Sr}_{0.33}\text{MnO}_3$ (tabulated PDF card 04-014-4312).

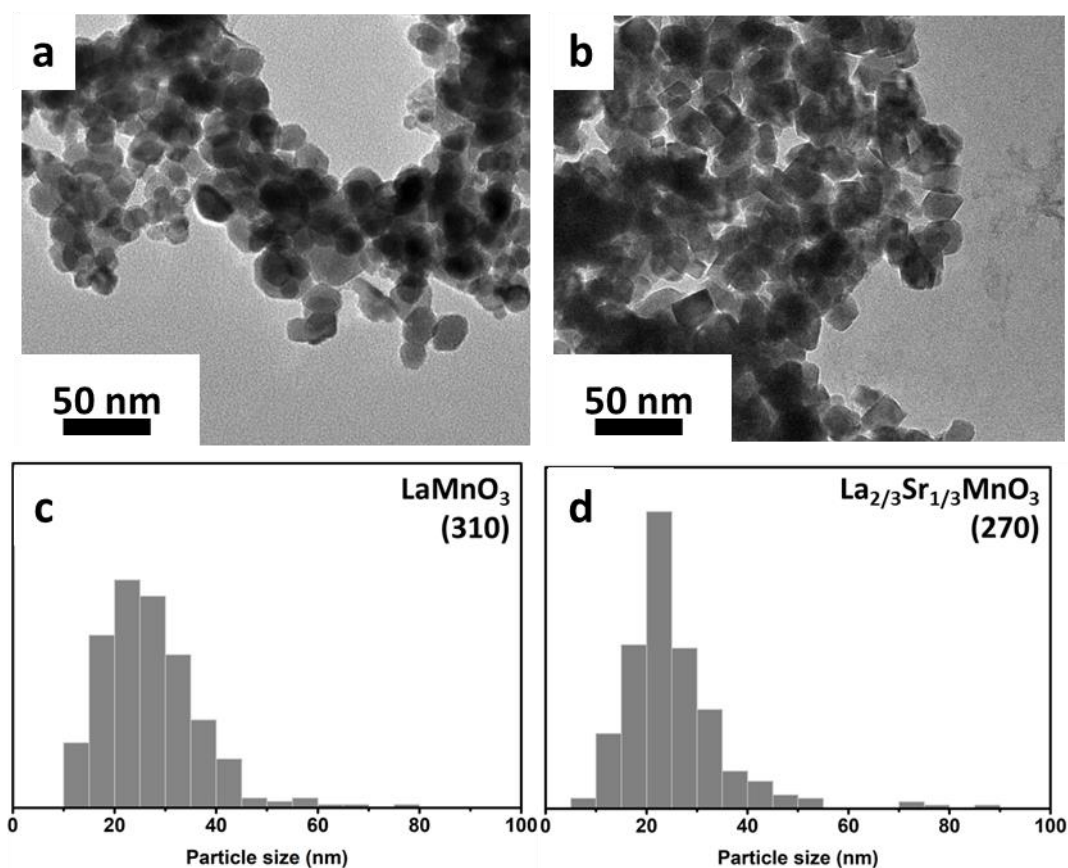
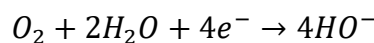


Figure III - 4 Transmission electron microscopy images of pristine nanoparticles and their corresponding particle size distribution of LaMnO_3 (a and c) and $\text{La}_{0.67}\text{Sr}_{0.33}\text{MnO}_3$ (b and d). Number of measured nanoparticles are in brackets.

2.4. Electrocatalytic properties

2.4.1. Electrochemical set-up

Oxide perovskites are stable in alkaline electrolyte¹³⁰. The experiments are therefore run in a KOH 0.1 M electrolyte. In this medium, the oxygen reduction reaction is:



Continuous oxygen bubbling maintains oxygen saturation of the solution to keep the equilibrium potential constant. To avoid dissolution of glass due to the high basicity of the solution, the container used for electrochemistry measurements is a plastic beaker. The three-electrodes setup is composed of an Ag/AgCl reference ($E^0 = 0.197$ V/SHE), a Pt counter electrode in a frit, and a rotating disk working electrode composed of a film of electrocatalyst ink (2 μ L) deposited on a polished glassy carbon substrate (0.07 cm²) (Figure III - 5). The electrocatalyst ink comprises electrocatalyst nanoparticles (10 mg), hydrophilized acetylene black (10 mg), Nafion (435 μ L) and absolute ethanol (10 mL). Acetylene black ensures the electrical conductivity of the composite film, whereas Nafion is an ion-conductive binder that provides the mechanical resistance of the deposit¹³¹. The nanoparticles are homogeneously dispersed through two hours of sonication. The ink is deposited less than 12 h after the start of the preparation to limit any ageing effect. Once the ink is dried, the film is wetted with a drop of electrolyte during 30 min to eliminate air bubbles that could be stuck when first immersed into the electrolyte. Then, the three electrodes are plunged in the electrolyte and connected to the potentiostat. A more detailed protocol of the electrochemical experiment is written in the appendix 1.2. The speed of the rotating disk electrode is set at 1600 rpm. Cyclic voltammograms are recorded from the open circuit voltage (OCV) to 0.4 V / RHE, then back to 1.0 V/RHE with a scan speed of 10 mV·s⁻¹.

2.4.2. Results

At 50 μ A·cm⁻², the potential of both electrocatalysts is around 0.9 V/RHE (Figure III - 6), which is in good agreement with the literature¹¹⁰. For potentials lower than 0.9 V/RHE, LSMO displays higher current density (in absolute value) than LMO. At 0.4 V/RHE, the LSMO and LMO current densities are 3.2 and 2.0 mA·cm⁻², respectively. These experiments confirm that strontium substitution improves LSMO ORR electrocatalytic activity as compared to that of LMO, presumably because of an increase in the electrical conductivity and of an optimal e_g electron filling³⁷. Finally, the perovskite nanocrystals synthesized in molten salts possess electrocatalytic activities comparable to the same compounds formed

Chapter III: Evolution of Mn and Co-based perovskites during the OER and the ORR

by other synthesis methods^{114,132}. This observation validates our synthetic approach. We then synthesized perovskites with different fractions of Mn, Co and Sr in molten salts. First, cobalt-based materials should exhibit high electroactivity toward the oxygen evolution reaction^{67,110}. Second, substituting the manganese perovskites with cobalt should allow the design of bifunctional electrocatalysts (ORR and OER).

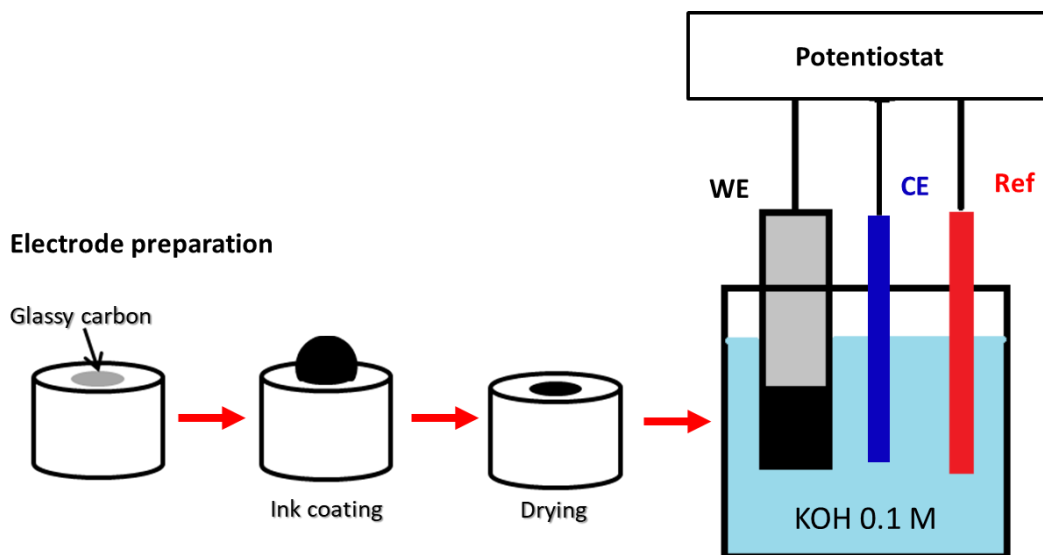


Figure III - 5 Schematic of the working electrode preparation and of the electrochemical set-up.

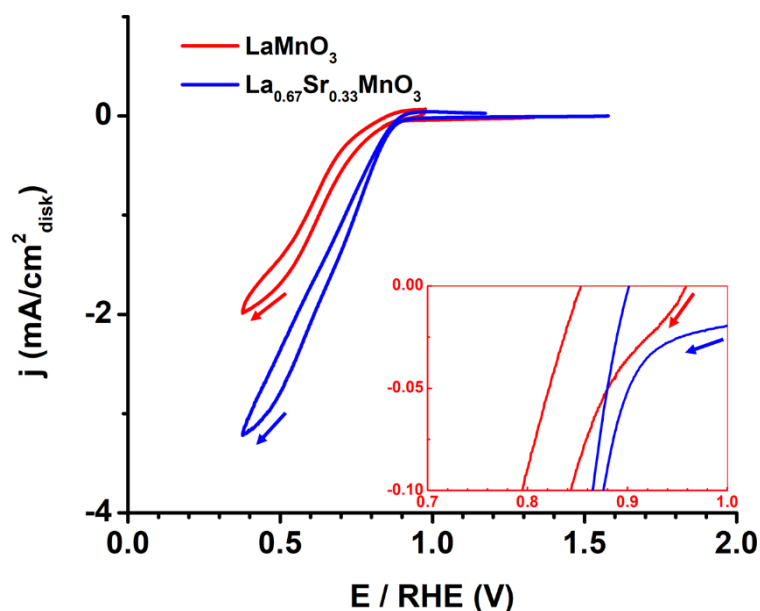


Figure III - 6 Electrocatalytic properties of synthesized perovskites. Cyclic voltammograms (first cycle) of LaMnO_3 (in red) and $\text{La}_{0.67}\text{Sr}_{0.33}\text{MnO}_3$ (in blue) in an O_2 -saturated KOH 0.1 M electrolyte using a rotating disk electrode (1600 rpm) at $10 \text{ mV}\cdot\text{s}^{-1}$. Electrocatalyst loading: $30 \mu\text{g}\cdot\text{cm}^{-2}_{\text{disk}}$. In the red frame is a zoom at the curve around $50 \mu\text{A}\cdot\text{cm}^{-2}_{\text{disk}}$. The arrows indicate the direction of the cycles.

3. Manganese partial substitution in $\text{LaMn}_{1-x}\text{Co}_x\text{O}_3$

Cobalt-doped LaMnO_3 perovskites have shown electrocatalytic activity in both OER and ORR¹³³. However, the evolution of the activity is not linear with the cobalt content. The family $\text{LaMn}_{1-x}\text{Co}_x\text{O}_3$ displays the highest OER activity for $x=0.3$ ¹³³. In the present work, we have attempted the synthesis of these materials at a nanoscale with different levels of substitution in order to understand the role of both Mn and Co and their possible interactions. As for $\text{La}_{1-x}\text{Sr}_x\text{MnO}_3$, the $\text{LaMn}_{1-x}\text{Co}_x\text{O}_3$ ORR activity will be compared to LaMnO_3 , used as reference.

3.1. Synthesis

$\text{LaMn}_{1-x}\text{Co}_x\text{O}_3$ particles are obtained by using a synthesis protocol similar to LaMnO_3 (Appendix section 1.1.1.), by adapting the manganese and cobalt nitrate contents to match the targeted composition. While the LaMnO_3 synthesis only forms electrocatalytically inactive impurities, the presence of cobalt may generate impurities (i.e. CoOOH , Co_3O_4 , $\text{K}_x\text{CoO}_2\dots$) that could be active in OER. The lanthanum precursor is added with equimolar quantity compared to the sum of the manganese and cobalt precursors. Two perovskites are prepared with the La/Mn/Co theoretical ratios of 0.50/0.37/0.13 (sample 1) and 0.50/0.33/0.17 (sample 2).

3.2. Characterization

The elemental compositions of the final powders are determined by WDXRF (Table III - 1). The final compositions of samples 1 and 2 correspond to La/Mn/Co ratios 0.52/0.33/0.15 and 0.51/0.30/0.19, respectively, with an uncertainty of WDXRF measurement of 5 at. %. The lanthanum relative content is higher than the sum of the manganese and cobalt relative contents, suggesting an excess of A site cations. This highlights the presence of a lanthanum phase as a secondary product.

The perovskite and lanthanum trihydroxide phases are detected on the powder X-ray diffractograms (Figure III - 7), thus identifying the lanthanum impurity detected by WDXRF as $\text{La}(\text{OH})_3$. Supposing that all manganese and cobalt are in the perovskite phases, the perovskite compositions are then estimated to be $\text{LaMn}_{0.7}\text{Co}_{0.3}\text{O}_3$ for sample 1 and $\text{LaMn}_{0.6}\text{Co}_{0.4}\text{O}_3$ for sample 2. The $\text{La}(\text{OH})_3$ impurity amounts to *ca.* 2-4 mol. %.

Chapter III: Evolution of Mn and Co-based perovskites during the OER and the ORR

Exp.	Precursors	WDXRF	Composition
1			$\text{LaMn}_{0.7}\text{Co}_{0.3}\text{O}_3$ + 0.03 $\text{La}(\text{OH})_3$
2			$\text{LaMn}_{0.6}\text{Co}_{0.4}\text{O}_3$ + 0.02 $\text{La}(\text{OH})_3$

Table III - 1 Elemental composition of the samples 1 and 2: initial precursor ratio and final composition determined by WDXRF analysis. For the rest of the chapter, the samples are denominated by the composition of the perovskite phase, namely $\text{LaMn}_{0.7}\text{Co}_{0.3}\text{O}_3$ and $\text{LaMn}_{0.6}\text{Co}_{0.4}\text{O}_3$.

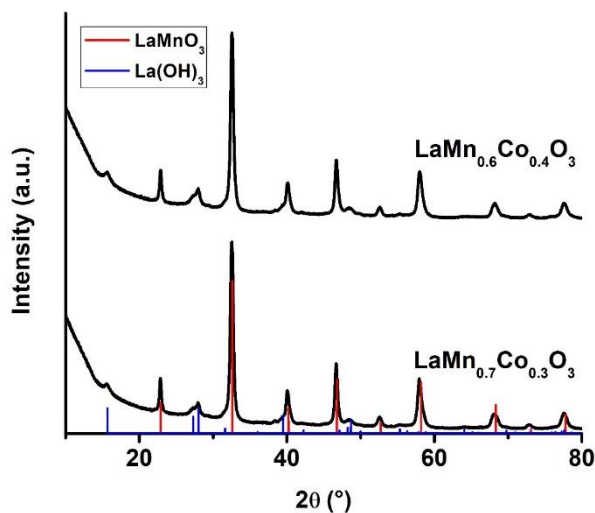


Figure III - 7 XRD patterns of $\text{LaMn}_{0.6}\text{Co}_{0.4}\text{O}_3$ and $\text{LaMn}_{0.7}\text{Co}_{0.3}\text{O}_3$. Red and blue Reference patterns of LaMnO_3 (red, PDF card 00-051-1516) and $\text{La}(\text{OH})_3$ (blue, PDF card 04-005-8587). The LaMnO_3 pattern is used as reference for the perovskite manganite structure independently of its composition.

Chapter III: Evolution of Mn and Co-based perovskites during the OER and the ORR

The nanoscale morphology is observed by transmission electron microscopy (TEM) and scanning transmission electron microscopy (STEM) coupled to X-ray energy dispersive analysis for elemental mapping. TEM images show crystal nanoparticles along with wires and foils of 0.1-1 μm size (Figure III - 8). The nanoparticles shape is smooth and the average size is ca. 30 nm for both perovskites. STEM-EDX elemental mapping of the $\text{LaMn}_{0.7}\text{Co}_{0.3}\text{O}_3$ sample (Figure III - 9) shows that the wires are exclusively composed of lanthanum as heavy element, thus suggesting that these wires are made of the $\text{La}(\text{OH})_3$ phase detected by XRD. The nanoparticles contain lanthanum, manganese and cobalt. Inside the multicationic nanoparticles, the elements seem homogeneously distributed (Appendix 1), as expected for the perovskite phase.

The synthesized compounds are composed of both perovskite nanocrystals and lanthanum hydroxide. The nanoparticles have an average size of around 30 nm and the perovskite compositions are $\text{LaMn}_{0.7}\text{Co}_{0.3}\text{O}_3$ and $\text{LaMn}_{0.6}\text{Co}_{0.4}\text{O}_3$.

4. Synthesis of $\text{La}_{0.67}\text{Sr}_{0.33}\text{CoO}_3$

$\text{La}_{0.67}\text{Sr}_{0.33}\text{CoO}_3$ perovskite is highly active in OER ($1 \text{ A.g}^{-1}_{\text{metals}}$ ⁵⁶) thanks to the presence of Co electrocatalytically active sites and to the pseudo-cubic structure provided by Sr that enhances the conductivity of the material^{56,115}. The first objective is to isolate the cobaltite perovskite phase. To do so, the influence of the temperature on the crystallization was studied. The first synthesis was performed by using the same parameters as $\text{La}_{0.67}\text{Sr}_{0.33}\text{MnO}_3$ and by replacing the manganese nitrate tetrahydrate precursor by cobalt nitrate hexahydrate. Keeping the other parameters fixed, two additional syntheses were then carried out at higher temperature: 700 °C and 800 °C.

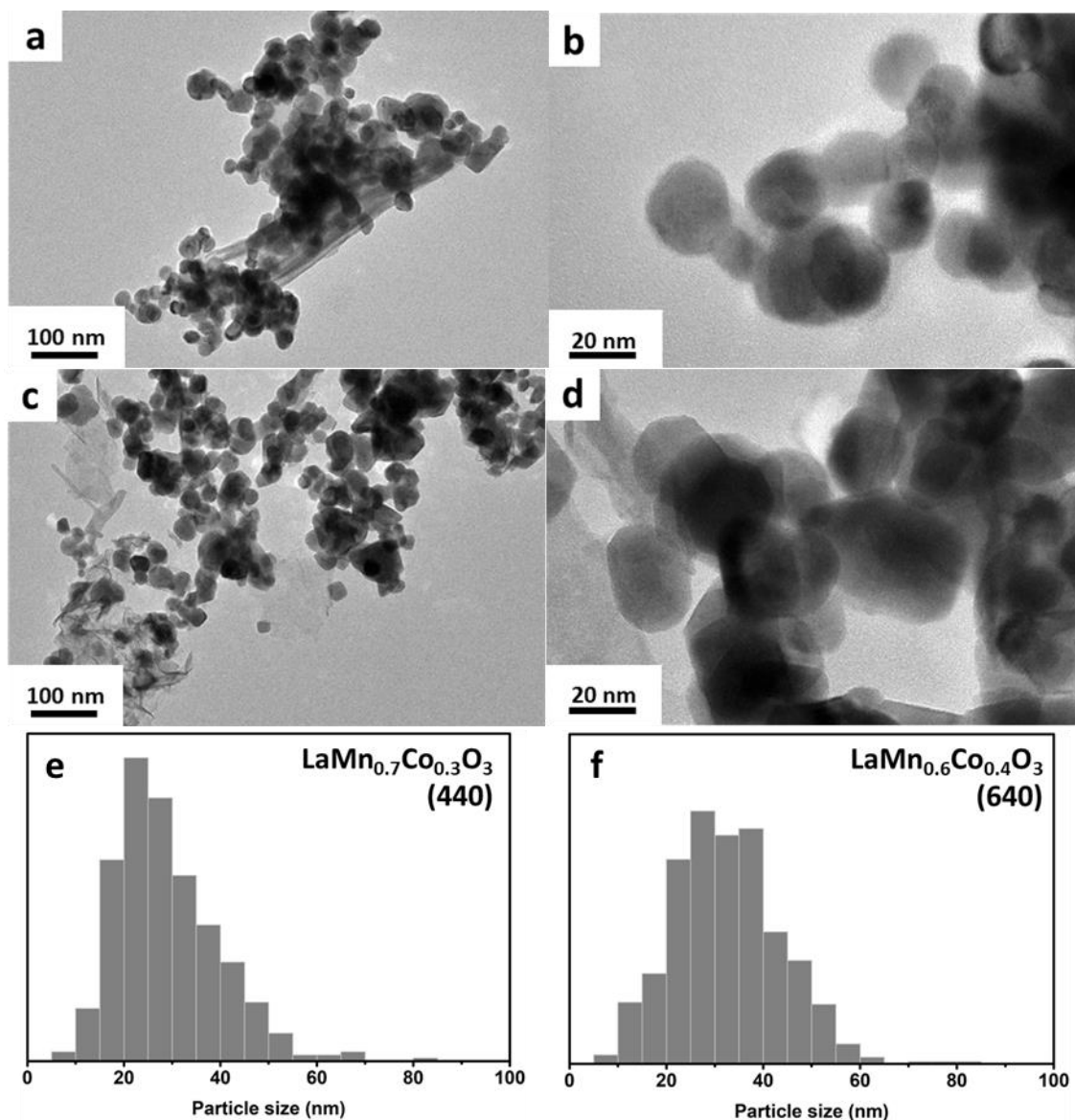


Figure III - 8 Transmission electron microscopy images of $\text{LaMn}_{0.7}\text{Co}_{0.3}\text{O}_3$ (a, b) and $\text{LaMn}_{0.6}\text{Co}_{0.4}\text{O}_3$ (c, d) synthesized at 600 °C during 1 h in KNO_3 . Particle size distributions of $\text{LaMn}_{0.7}\text{Co}_{0.3}\text{O}_3$ (e) and $\text{LaMn}_{0.6}\text{Co}_{0.4}\text{O}_3$ (f). Number of measured particles are in brackets.

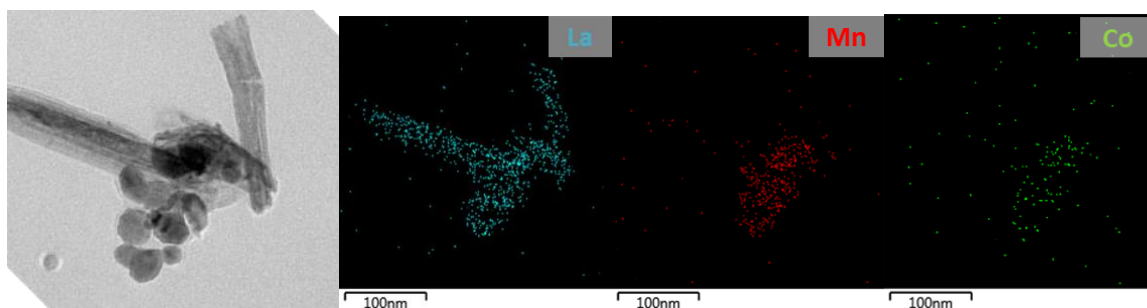


Figure III - 9 scanning TEM (STEM)-EDX mapping of $\text{LaMn}_{0.7}\text{Co}_{0.3}\text{O}_3$ nanoparticles synthesized at 600 °C for 1 h in KNO_3 .

Chapter III: Evolution of Mn and Co-based perovskites during the OER and the ORR

The powder X-ray diffractograms are displayed on Figure III - 10. At 600 °C, only $\text{La}(\text{OH})_3$ and Co_3O_4 phases are detected. At 700 °C, the diffractogram presents peaks from $\text{La}(\text{OH})_3$ and Co_3O_4 phases. The peak at 64.0° from $\text{La}(\text{OH})_3$ is more distinguishable at 700 °C than at 600 °C. Other small peaks (23.1° , 32.8° and 58.8°) are observed and attributed to the $\text{La}_{1-x}\text{Sr}_x\text{CoO}_3$ perovskite. At 800 °C, the diffractogram corresponds to a mixture of both $\text{La}_{1-x}\text{Sr}_x\text{CoO}_3$ and $\text{La}_{1-x}\text{Sr}_{1+x}\text{CoO}_4$ phases. These results show that a synthesis temperature of 600 °C is too low to crystallize the perovskite phase as no multicationic oxide is detected. The perovskite phase starts to appear at 700 °C but in a small amount as single oxides are still predominant. They disappear at 800 °C but besides the pseudo-cubic perovskite, the $\text{La}_{1-x}\text{Sr}_{1+x}\text{CoO}_4$ Ruddlesden-Popper phase is also formed. This lamellar perovskite contains less cobalt than the pseudo-cubic one. At the end of the heating step, blue traces are observed inside the alumina crucible that contains the molten salt crude. These traces remain after the crucible is washed at the end of the reaction (Appendix section 4.3), suggesting that cobalt diffuses in the crucible and is sequestered from the reaction medium. Other types of crucibles were then tested (the study is described in Appendix section 4.3.) but the alumina crucible still seemed the more efficient.

The nature of the molten salt was then modified in order to drive the reaction towards the Co-rich perovskite $\text{La}_{1-x}\text{Sr}_x\text{CoO}_3$. To do so, we increased the oxo-basicity in order to trigger full precipitation of La, Sr and Co cations, in a similar approach as with Brönstedt basicity in water¹³⁴. KNO_3 was therefore changed to NaNO_2 , which bears a dissociation constant 10^{10} times higher than the nitrate¹³⁵. We expected the medium to be more reactive and to provide more oxygen in order to favor the crystallization of multicationic oxides. We run three syntheses in NaNO_2 at different temperatures: 600 °C, 700 °C and 800 °C (Figure III - 11). At 600 °C, the diffractogram shows small and large peaks that do not correspond to any perovskite phase and are not investigated further. At 700 °C, the diffractogram presents only peaks from the pseudo-cubic perovskite phase. At 800 °C, the lamellar Ruddlesden-Popper perovskite is obtained as main product, with some traces of the pseudo-cubic perovskite (23.2° , 40.6° , and 51.8°). The change of salt clearly improves the reactivity of the medium, as much less single cation oxide phases are detected by XRD. From these results, we conclude that $\text{La}_{1-x}\text{Sr}_x\text{CoO}_3$ crystallizes at 700 °C or higher. However, high temperature also favors the $\text{La}_{1-x}\text{Sr}_{1+x}\text{CoO}_4$ formation by activating the O^{2-} -donor behavior of the molten salt. For the rest of this chapter, all syntheses are run at 700 °C in NaNO_2 , which yield the pure pseudo-cubic phase according to XRD.

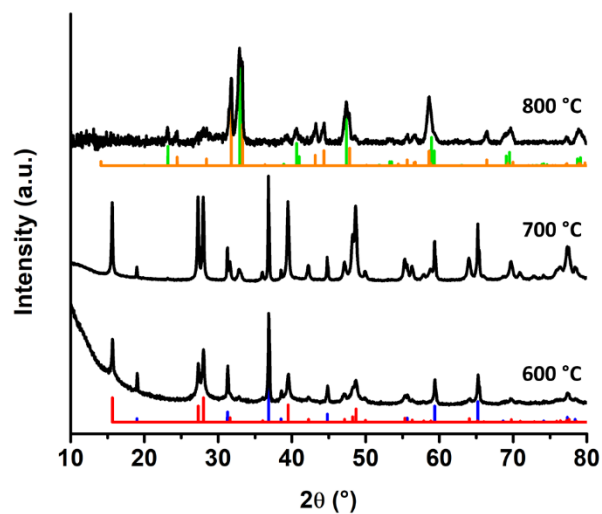


Figure III - 10 XRD patterns of $\text{La}_{0.67}\text{Sr}_{0.33}\text{CoO}_3$ powders synthesized in KNO_3 during 1 h at 600 °C, 700 °C and 800 °C. Reference patterns of $\text{La}_{0.7}\text{Sr}_{0.3}\text{CoO}_3$ (green, PDF card 04-014-1579), $\text{La}_{0.75}\text{Sr}_{1.25}\text{CoO}_4$ (orange, PDF card 04-013-4920), $\text{La}(\text{OH})_3$ (red, PDF card 04-005-8587) and Co_3O_4 (blue, PDF card 04-005-4386).

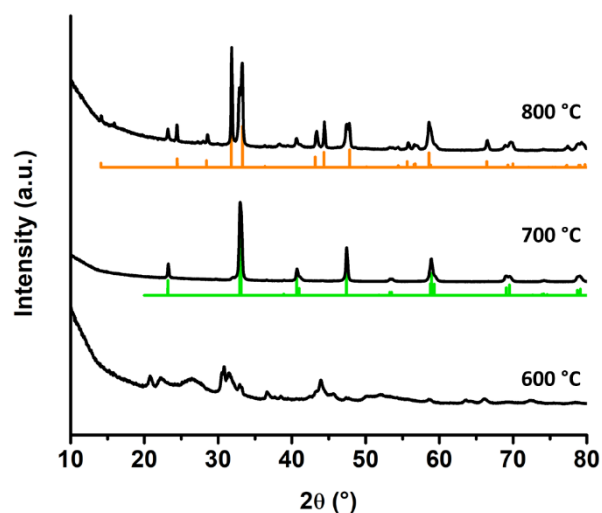


Figure III - 11 XRD patterns of $\text{La}_{0.67}\text{Sr}_{0.33}\text{CoO}_3$ powders synthesized in NaNO_2 during 1 h at 600 °C, 700 °C and 800 °C (top). Reference patterns of $\text{La}_{0.7}\text{Sr}_{0.3}\text{CoO}_3$ (green, PDF card 04-014-1579) and $\text{La}_{0.75}\text{Sr}_{1.25}\text{CoO}_4$ (orange, PDF card 04-013-4920).

Chapter III: Evolution of Mn and Co-based perovskites during the OER and the ORR

TEM shows that the sample synthesized at 700 °C (Figure III - 12, a b) encompasses particles of several morphologies, in contrast to the single-phase XRD patterns. Cuboids of 100-300 nm size are observed. Some of them are fused together. Other crystalline cuboids with intermediate size (100 nm) are also observed. Thin foils can be seen around them. We hypothesize that the cuboids are perovskite crystals and that the foils are lanthanum hydroxides or cobalt (hydr)oxides, which could not be detected by XRD because they are poorly crystalline or because their amounts are too low for the XRD detection threshold. The location of these foils at the surface of the perovskite particles would be compatible with their formation during washing in deionized water, which may have partially ripened the perovskite particles and solubilized the most soluble ion Sr^{2+} , thus leaving lanthanum and cobalt (oxyhydr)oxides on the surface of the material¹¹². In summary, $\text{La}_{1-x}\text{Sr}_x\text{CoO}_3$ nanoparticles are cuboids whose size varies between 50 and 300 nm. They are often fused each other and are covered with (oxyhydr)oxide foils.

In order to increase the O^{2-} concentration of the reaction medium and to obtain less coalesced nanoparticles¹³⁶, Na_2O sodium oxide (3 eq. to Co) was added to the reaction medium as an oxygen source. According to the X-ray diffraction (Figure III - 13, II), the perovskite is the only phase obtained. On the TEM images, more isolated cuboids are observed but many foils remain (Figure III - 12, c and d). Considering the starting ratio of the precursors La/Sr/Co of 0.60/0.33/1.00, the defect in A-site cation, initially used in order to avoid $\text{La}(\text{OH})_3$ impurities in the previous syntheses, can be a cause of the perovskite instability.

Therefore, the same experiment is carried out with La/Sr/Co elemental ratio of 0.67/0.36/1.00 to saturate the A sites. On the diffractogram (Figure III - 13, III)), we see mostly the peaks from the pseudo-cubic phase, but also a peak at 31.8 ° attributed to the lamellar phase with much lower intensity. Indeed, increasing the A-site cations content favors $\text{La}_{1-x}\text{Sr}_{1+x}\text{CoO}_4$ formation. The TEM images (Figure III - 12, e and f) show 50-200 nm cuboids that are partially fused. Foils are less present. However, some nanoparticles seem to present rough surfaces and some porosity that suggest incomplete crystallization.

$\text{La}_{1-x}\text{Sr}_x\text{CoO}_3$ synthesis pathways are clearly different from the original $\text{La}_{1-x}\text{Sr}_x\text{MnO}_3$ molten salt synthesis. For crystallization, the cobaltite perovskite requires a higher temperature and a more oxo-basic solvent. Moreover, cobalt is more sensitive to the surroundings: cobalt species react with most crucibles and cobalt perovskites are poorly

Chapter III: Evolution of Mn and Co-based perovskites during the OER and the ORR

stable in deionized water. In the end, the $\text{La}_{1-x}\text{Sr}_x\text{CoO}_3$ nanoparticles obtained are partially fused and their average size is around 100 nm, which is much larger than the size of $\text{La}_{1-x}\text{Sr}_x\text{MnO}_3$ nanoparticles (see Figure III - 4).

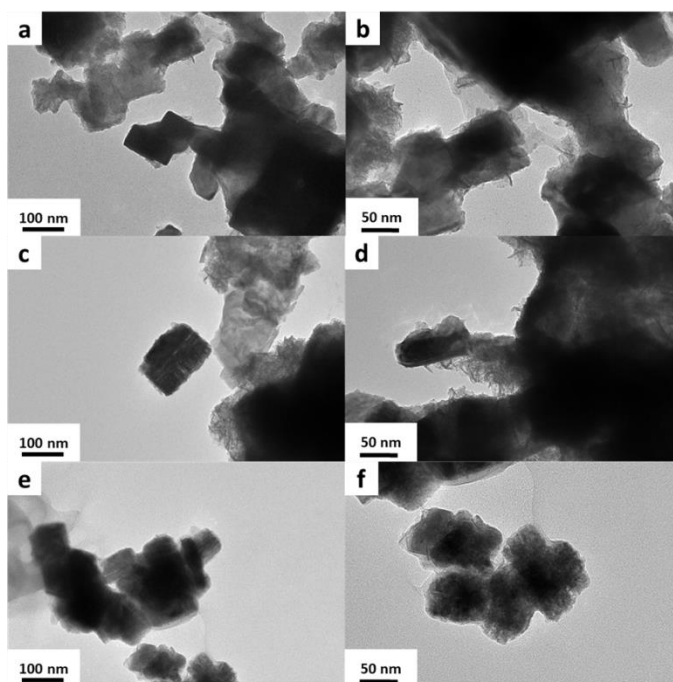


Figure III - 12 TEM images of $\text{La}_{0.67}\text{Sr}_{0.33}\text{CoO}_3$ at 700 °C: with La/Sr/Co/ Na_2O initial ratios 0.60/0.33/1/0 (a and b), 0.60/0.33/1/3 (c and d), and 0.67/0.36/1/3 (e and f).

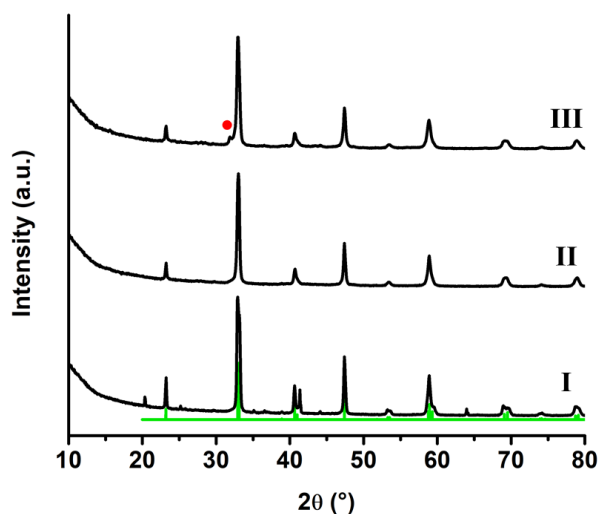


Figure III - 13 X-ray diffractograms of $\text{La}_{0.67}\text{Sr}_{0.33}\text{CoO}_3$ at 700 °C: with La/Sr/Co/ Na_2O initial ratios 0.60/0.33/1/0 (I), 0.60/0.33/0.33 (II), and 0.67/0.36/0.33 (III). The peak indicated with a red dot is attributed to a $\text{La}_{1-x}\text{Sr}_{1+x}\text{CoO}_4$ phase.

5. Electrocatalytic properties of $\text{La}_{1-x}\text{Sr}_x\text{CoO}_3$ and $\text{LaMn}_{1-x}\text{Co}_x\text{O}_3$

The electrocatalytic properties of the newly synthesized perovskites are investigated in OER and ORR. The experimental composition of the studied perovskites are $\text{LaMn}_{0.7}\text{Co}_{0.3}\text{O}_3$ (LMCO30) and $\text{LaMn}_{0.6}\text{Co}_{0.4}\text{O}_3$ (LMCO40). The characterization (DRX, TEM WDXRF) of the $\text{La}_{0.75}\text{Sr}_{0.25}\text{CoO}_3$ perovskite (LSCO) sample tested here is shown in Appendix section 2.2. We use the same experimental set-up as for the LaMnO_3 (LMO) electrochemistry experiments.

First, the electrocatalytic properties of LSCO in OER are verified (Figure III - 14). The cyclic voltammogram is recorded from the open circuit voltage (OCV) at ca. 1.0 V/RHE to 2.2 V/RHE, then back to 1.0 V/RHE with a scan rate of $10 \text{ mV}\cdot\text{s}^{-1}$. Three cycles are recorded. The results are compared to a cyclic voltammogram of a bare glassy carbon substrate in the same conditions. At 2.2 V/RHE, the LSCO current density is consecutively $21 \text{ mA}\cdot\text{cm}^{-2}_{\text{disk}}$, $17 \text{ mA}\cdot\text{cm}^{-2}_{\text{disk}}$ and $15 \text{ mA}\cdot\text{cm}^{-2}_{\text{disk}}$. At the same potential, the bare glassy carbon substrate shows a current density of $0.6 \text{ mA}\cdot\text{cm}^{-2}$. These results prove that LSCO nanoparticles are active in OER electrocatalysis but this activity decreases over the cycles, illustrating the instability of the material at high potential, which has already been reported and attributed to surface amorphization and cobalt leaching^{56,112}. The wave corresponding to the oxidation of Co(III)/Co(IV), which is expected to be around 1.55 V/RHE^{137,138}, is not observed. This let us wonder if the oxidation state of the cobalt is stable all along the reaction, or if the amount of oxidized cobalt is too low to exhibit a noticeable wave on the cyclic voltammogram.

The OER and ORR electrocatalytic activities of LSCO, LMO and both LMCO are investigated (Figure III - 15). The cyclic voltammograms are recorded from the open circuit voltage (OCV) at ca. 1.0 V/RHE to 0.4 V/RHE, then to 1.8 V/RHE and finally back to 1.0 V/RHE with a scan rate of $10 \text{ mV}\cdot\text{s}^{-1}$. The first cycles of each electrocatalysts are displayed on Figure III - 15. At 0.4 V/RHE in the ORR region, the current densities of LSCO, LMO, LMCO30 and LMCO40 are respectively -1.7 , -2.0 , -1.6 and $-1.9 \text{ mA}\cdot\text{cm}^{-2}_{\text{disk}}$. At 1.8 V/RHE in the OER region, they are 3.1 , 0.7 , 0.7 and $1.2 \text{ mA}\cdot\text{cm}^{-2}_{\text{disk}}$. Among these four perovskites, LMO is the electrocatalyst that is the most active in ORR and the less active in OER, while LSCO is the most active in OER and the less active in ORR. The two LMCO have different behaviors. While LMCO40 shows intermediate performances, LMCO30 performances are always close to the material the least active.

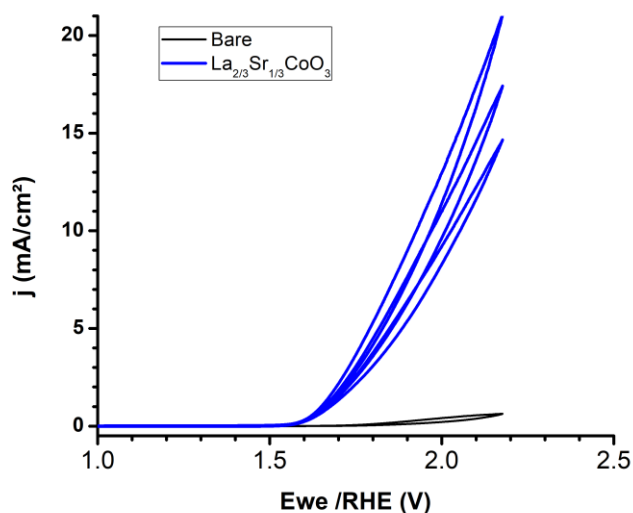


Figure III - 14 Electrocatalytic activity of synthesized $\text{La}_{0.75}\text{Sr}_{0.25}\text{CoO}_3$ perovskite in OER. Cyclic voltammograms of $\text{La}_{0.75}\text{Sr}_{0.25}\text{CoO}_3$ (blue) and the glassy carbon substrate (black) in an O_2 -saturated 0.1 M KOH electrolyte using a rotating disk electrode (1600 rpm) at $10 \text{ mV}\cdot\text{s}^{-1}$. Electrocatalyst loading: $30 \mu\text{g}\cdot\text{cm}^{-2}_{\text{disk}}$.

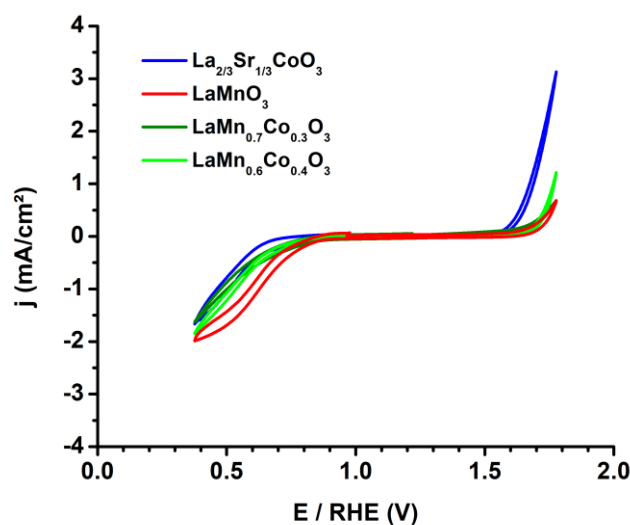


Figure III - 15 Electrocatalytic activity of synthesized perovskites in OER and ORR. Cyclic voltammograms of $\text{La}_{0.75}\text{Sr}_{0.25}\text{CoO}_3$ (blue), LaMnO_3 (red), $\text{LaMn}_{0.7}\text{Co}_{0.3}\text{O}_3$ (dark green) and $\text{LaMn}_{0.6}\text{Co}_{0.4}\text{O}_3$ (light green) in an O_2 -saturated 0.1 M KOH electrolyte using a rotating disk electrode (1600 rpm) at $10 \text{ mV}\cdot\text{s}^{-1}$. Electrocatalyst loading: $30 \mu\text{g}\cdot\text{cm}^{-2}_{\text{disk}}$.

Chapter III: Evolution of Mn and Co-based perovskites during the OER and the ORR

From these results, no clear conclusion can be drawn about the origin of the electrocatalytic activity of LMCO samples. From the LMCO30 electrocatalytic properties, we can even consider that the OER and ORR active sites might be switched, so that OER would occur on Mn sites and ORR on Co sites. To verify this hypothesis, we plotted the cyclic voltammograms of perovskites, where the surface current is normalized to the content of each transition metal inside the perovskite. As the size of LMO, LMCO30 and LMCO40 nanoparticles are similar, their normalized currents are directly comparable. In Figure III - 16, the current is normalized to the manganese content, i.e. the measured currents of the $\text{LaMn}_x\text{Co}_{1-x}\text{O}_3$ perovskites that are displayed in the previous Figure III - 15 are multiplied by $1/x$ with x the cobalt content. In Figure III - 17, the current is multiplied by $1/(1-x)$ to normalize to the Co content inside the perovskite.

The currents of LMCO30 and LMCO40 normalized to the Mn content at 0.4 V/RHE are respectively -2.3 and $-3.1 \text{ mA}\cdot\text{cm}^{-2}$, which are both lower than the current of LMO at the same potential ($-2.0 \text{ mA}\cdot\text{cm}^{-2}$). At 1.8 V/RHE, the normalized currents are $1.0 \text{ mA}\cdot\text{cm}^{-2}$ for LMCO30 and $2.0 \text{ mA}\cdot\text{cm}^{-2}$ for LMCO40, which are higher than the surface current of LMO under the same conditions ($0.9 \text{ mA}\cdot\text{cm}^{-2}$). When normalized to the Co content, the currents of LMCO30 and LMCO40 at 0.4 V/RHE are respectively -5.4 and $-4.6 \text{ mA}\cdot\text{cm}^{-2}$, while the current of LSCO is $-1.7 \text{ mA}\cdot\text{cm}^{-2}$. At 1.8 V/RHE, the normalized current is $2.3 \text{ mA}\cdot\text{cm}^{-2}$ for LMCO30, $3.0 \text{ mA}\cdot\text{cm}^{-2}$ for LMCO40 and $3.1 \text{ mA}\cdot\text{cm}^{-2}$ for LSCO. The mixed transition metal perovskites display a higher activity in ORR than LSCO but all perovskites have similar normalized electroactivities in OER.

These results suggest that if manganese is the active site whether in OER or ORR, it is more active in LMCO materials. If cobalt is the active site, its activity is roughly the same in any perovskite under OER conditions but its ORR activity is enhanced in LMCO compared to LSCO. To summarize, whatever the transition metal site that is active during electrocatalysis, its electroactivity is higher, or similar at worst, in the mixed LMCO phases than in LMO or LSCO. In the following we seek to find the identity of the active site by analyzing these materials with *operando* XAS.

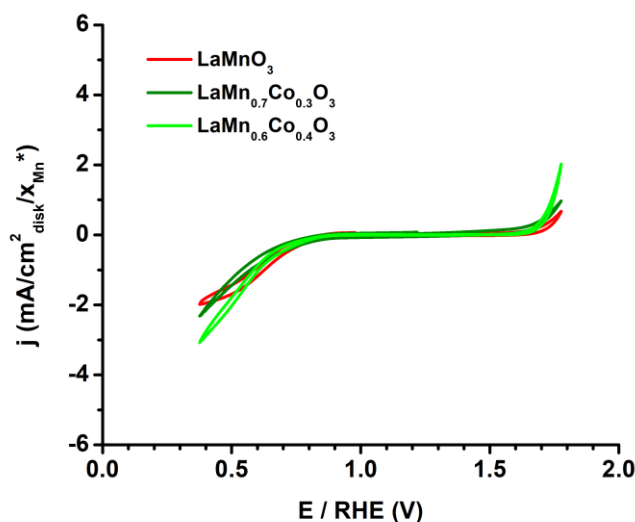


Figure III - 16 Electrocatalytic activity of synthesized perovskites in OER and ORR normalized to the Mn content. Cyclic voltammograms of LaMnO_3 (red), $\text{LaMn}_{0.7}\text{Co}_{0.3}\text{O}_3$ (dark green) and $\text{LaMn}_{0.6}\text{Co}_{0.4}\text{O}_3$ (light green) in an O_2 -saturated 0.1 M KOH electrolyte using a rotating disk electrode (1600 rpm) at $10 \text{ mV}\cdot\text{s}^{-1}$. Electrocatalyst loading: $30 \mu\text{g}\cdot\text{cm}^{-2}_{\text{disk}}$. x_{Mn} is defined in the perovskites as $\text{LaMn}_{x_{\text{Mn}}}\text{Co}_{1-x_{\text{Mn}}}\text{O}_3$. ($x_{\text{Mn}} = 0.7$ in LMCO30 and $x_{\text{Mn}} = 0.6$ in LMCO40)

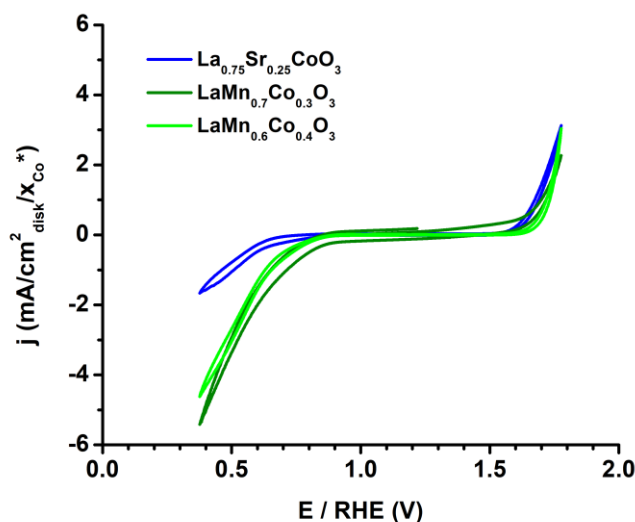


Figure III - 17 Electrocatalytic activity of synthesized perovskites in OER and ORR normalized to the Co content. Cyclic voltammograms of $\text{La}_{0.75}\text{Sr}_{0.25}\text{CoO}_3$ (blue), $\text{LaMn}_{0.7}\text{Co}_{0.3}\text{O}_3$ (dark green) and $\text{LaMn}_{0.6}\text{Co}_{0.4}\text{O}_3$ (light green) in an O_2 -saturated 0.1 M KOH electrolyte using a rotating disk electrode (1600 rpm) at $10 \text{ mV}\cdot\text{s}^{-1}$. Electrocatalyst loading: $30 \mu\text{g}\cdot\text{cm}^{-2}_{\text{disk}}$. x_{Co} is defined in the perovskites as $\text{LaMn}_{1-x_{\text{Co}}}\text{Co}_{x_{\text{Co}}}\text{O}_3$. ($x_{\text{Co}} = 0.3$ in LMCO30 and $x_{\text{Co}} = 0.4$ in LMCO40)

6. XAS analysis

LaMnO₃ (LMO), La_{0.67}Sr_{0.33}MnO₃ (LSMO), La_{0.75}Sr_{0.25}CoO₃ (LSCO), LaMn_{0.70}Co_{0.30}O₃ (LMCO30) and LaMn_{0.60}Co_{0.40}O₃ (LMCO40) were first analyzed by X-ray absorption spectroscopy at the Mn K-edge and Co K-edge. Then, we have followed more specifically the evolution of Mn and Co oxidation states *in situ* during OER and ORR.

6.1. Pristine compounds

As in chapter II, the Mn and Co K-edge spectra of the newly synthesized perovskites are acquired and compared to the spectra of chosen references, whose Mn and Co oxidation states are known.

First, the spectra of Mn⁰, Mn^{III}₂O₃, Mn^{IV}O₂ commercial compounds and LaMn^{III}O₃ synthesized perovskite were recorded. On the same figure, for comparison purpose, the spectrum of SrMn^{IV}O₃ taken from Celorrio et al.¹³⁹ has been plotted (Figure III - 18). At half-edge jump (0.5 absorption intensity), Mn⁰, Mn^{III}₂O₃, LaMn^{III}O₃, Mn^{IV}O₂ and SrMn^{IV}O₃ energies are 6547.3 eV, 6549.8 eV, 6551.0 eV, 6552.8 eV and 6554.1 eV, respectively. As expected, the K-edge energy increases with the oxidation state from Mn⁰ to Mn^{IV}. Structural differences should also explain the energy variation between oxides within the same Mn oxidation state. Consequently, we exclusively used the spectra of LaMn^{III}O₃ and SrMn^{IV}O₃ perovskites as references, as the environment of Mn^{III} is octahedral, as in the studied samples.

LSMO and LMCO spectra are then compared to LaMn^{III}O₃ and SrMn^{IV}O₃ spectra (Figure III - 19). The shape of the edges are very similar. All of them display a pre-edge around 6540 eV and a sharp edge with comparable slope and with little shoulder (SrMn^{IV}O₃ at 6550 eV) or not. LSMO and LMCO energies are between LaMnO₃ and SrMnO₃ energies, suggesting that the partial substitution of Mn by Co in LaMn^{III}O₃ and La by Sr in LSMO modifies the oxidation state of manganese, reaching a value between III and IV. The Mn average oxidation state is estimated by XANES linear combination from LaMn^{III}O₃ and SrMn^{IV}O₃ references (Table III - 2). Accordingly, the manganese average oxidation states in LSMO, LMCO30 and LMCO40 are respectively +3.3, +3.4 and +3.3. While the measured oxidation state of manganese in LSMO concurs with the composition of the perovskite deduced from WDXRF, we observe that the increase in cobalt content in LMCO perovskites decreases slightly the manganese oxidation state. We should then expect that the average oxidation state of cobalt is lower than 3.

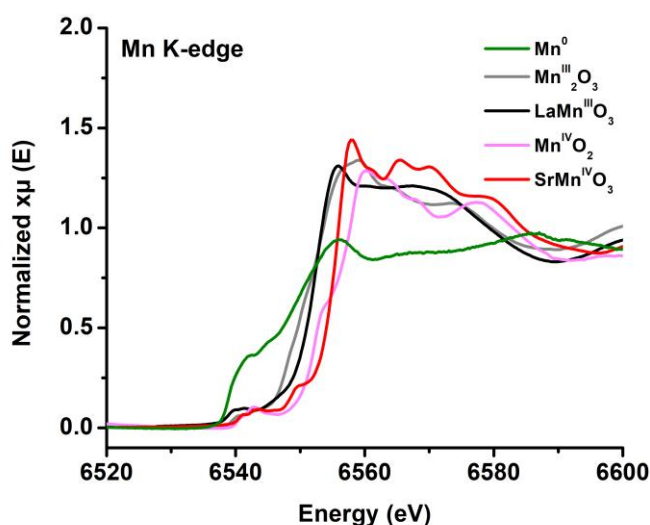


Figure III - 18 XANES spectra of Mn oxides: Mn^0 (green, commercial), $Mn^{III}_2O_3$ (grey, commercial), $LaMn^{III}O_3$ perovskite (black, synthesized), $Mn^{IV}O_2$ (pink, commercial) and $SrMn^{IV}O_3$ perovskite (red, reported¹³⁹).

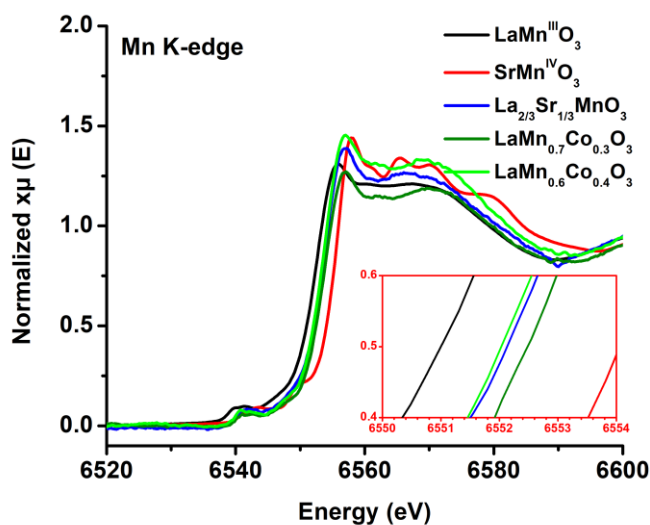


Figure III - 19 XANES spectra of Mn oxide perovskites: $LaMn^{III}O_3$ (black), $SrMn^{IV}O_3$ (red), $La_{0.67}Sr_{0.33}MnO_3$ (blue), $LaMn_{0.7}Co_{0.3}O_3$ (dark green), $LaMn_{0.6}Co_{0.4}O_3$ (light green). In the red frame is a zoom between 6550 and 6554 eV.

Fit composition	$La_{0.67}Sr_{0.33}MnO_3$	$LaMn_{0.7}Co_{0.3}O_3$	$LaMn_{0.6}Co_{0.4}O_3$
$LaMn^{III}O_3$	0.67	0.60	0.70
$SrMn^{IV}O_3$	0.33	0.40	0.30

Table III - 2 Manganese average oxidation states in $La_{0.67}Sr_{0.33}MnO_3$, $LaMn_{0.7}Co_{0.3}O_3$ and $LaMn_{0.6}Co_{0.4}O_3$ calculated by XANES linear combination with $LaMn^{III}O_3$ experimental reference and reported $SrMn^{IV}O_3$ ¹³⁹.

Chapter III: Evolution of Mn and Co-based perovskites during the OER and the ORR

The spectra of $\text{Co}^{\text{II}}(\text{OH})_2$ and $\text{Co}^{\text{III}}\text{OOH}$ commercial compounds and synthesized bulk LaCoO_3 have been recorded and plotted in Figure III - 20. Unfortunately, no pure $\text{Co}(\text{IV})$ oxide material is available and the SrCoO_3 perovskite is not stable enough for a pure phase, containing only $\text{Co}(\text{IV})$, to be characterized¹⁴⁰. At 0.5 intensity, $\text{Co}^{\text{II}}(\text{OH})_2$, $\text{Co}^{\text{III}}\text{OOH}$ and $\text{LaCo}^{\text{III}}\text{O}_3$ energies are 7718.4 eV, 7721.4 eV and 7721.6 eV, respectively. The LaCoO_3 Co K-edge energy is close to that of $\text{Co}^{\text{III}}\text{OOH}$, thus confirming the cobalt oxidation state +3. As the only available perovskite that contains cobalt at a single oxidation state is $\text{LaCo}^{\text{III}}\text{O}_3$, $\text{Co}^{\text{II}}(\text{OH})_2$ XAS is kept as a reference for LCF.

LSCO and LMCO Co K-edge XAS spectra are compared to $\text{Co}^{\text{II}}(\text{OH})_2$ and $\text{LaCo}^{\text{III}}\text{O}_3$ spectra (Figure III - 21). The spectra of every perovskite display a pre-edge at 7710 eV, and the slopes of their edges are very similar. However, only the spectra of LMCO perovskites present a second peak after the white line at 7730 eV. At 0.5 normalized intensity, LSCO, LMCO30 and LMCO40 energies are 7722.1 eV, 7720.4 eV and 7720.4 eV, respectively. By comparing $\text{LaCo}^{\text{III}}\text{O}_3$ and $\text{Co}^{\text{II}}(\text{OH})_2$ energies with the one measured for the synthesized perovskites, the cobalt average oxidation state in LSCO is above +3, while it is between +2 and +3 in LMCO30 and LMCO40. Note that the $\text{Co}^{\text{II}}(\text{OH})_2$ spectrum appears to be too different from the perovskite spectra to be used in a relevant XANES linear combination fitting.

The investigation on pristine perovskites confirms that Mn average oxidation state in $\text{La}^{\text{III}}_{0.67}\text{Sr}^{\text{II}}_{0.33}\text{MnO}_3$ is +3.33, which is in good agreement with the value expected from the WDXRF-derived composition. The Co average oxidation state of $\text{La}_{0.75}\text{Sr}_{0.25}\text{CoO}_3$ cannot be evaluated for lack of $\text{Co}(\text{IV})$ reference. But according to XANES of several references, it appears to be higher than +3, which agrees with the theoretical value of +3.25. The substitution of Mn by Co in LaMnO_3 leads to an increase in the oxidation state of Mn, which rises above +3. Because of charge compensation on the B site, the oxidation state of Co should concomitantly decrease to a value below +3. This charge balancing mechanism needs to be further examined since the Mn oxidation state in $\text{LaMn}_{0.6}\text{Co}_{0.4}\text{O}_3$ is slightly lower than in $\text{LaMn}_{0.7}\text{Co}_{0.3}\text{O}_3$ although this oxide contains more cobalt. Nonetheless, in the following part we study the electrochemical behavior of the perovskite samples described above.

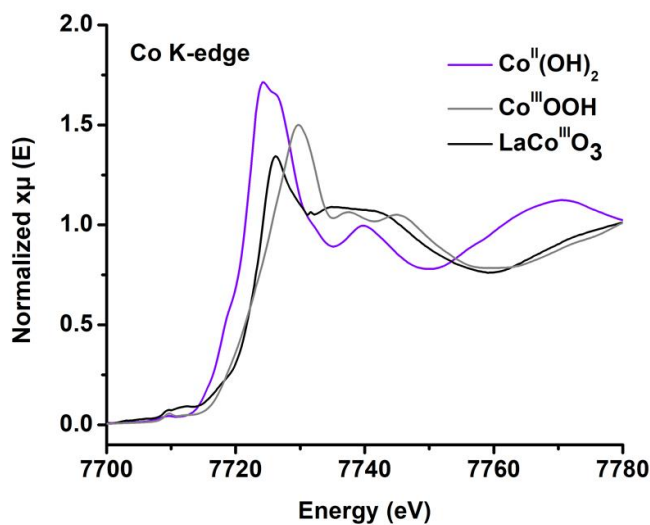


Figure III - 20 XANES of Co oxides: $\text{Co}^{\text{II}}(\text{OH})_2$ (purple, commercial), $\text{Co}^{\text{III}}\text{OOH}$ (grey, commercial) and $\text{LaCo}^{\text{III}}\text{O}_3$ perovskite (black, synthesized bulk).

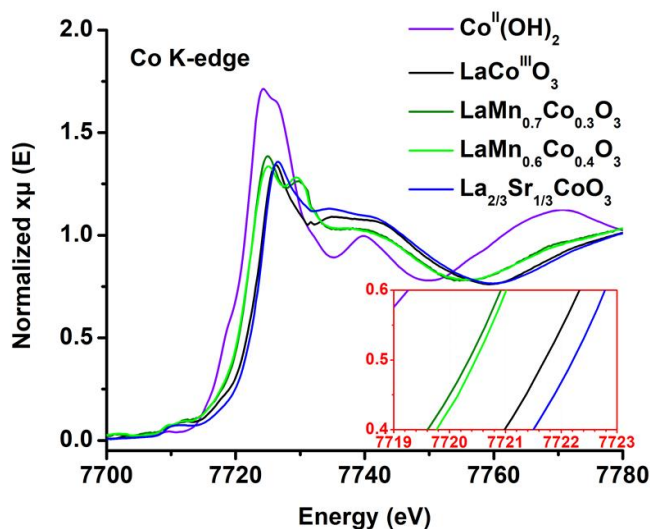


Figure III - 21 XANES spectra of Co oxide perovskites: $\text{LaCo}^{\text{III}}\text{O}_3$ (black), $\text{La}_{0.67}\text{Sr}_{0.33}\text{CoO}_3$ (blue), $\text{LaMn}_{0.7}\text{Co}_{0.3}\text{O}_3$ (dark green), $\text{LaMn}_{0.6}\text{Co}_{0.4}\text{O}_3$ (light green). $\text{Co}^{\text{II}}(\text{OH})_2$ serves as Co(II) oxide reference. In the red frame is a zoom between 7719 and 7723 eV.

Chapter III: Evolution of Mn and Co-based perovskites during the OER and the ORR

6.2. In situ characterization

The protocol used is the same as the one for nickel boride experiments. Some spectra were recorded at the dry state, under open circuit voltage (OCV), under OER/ORR conditions and finally under open circuit voltage (OCV). Because of the long duration of each experiment (around 10 h per material), they were performed onto two beamlines: SAMBA at SOLEIL and B18 at DIAMOND. But as high scan rate implies a lower signal-to-noise ratio, more scans were taken on B18 to compensate their lower quality. As the energy resolution of B18 beamline is lower than the one of SAMBA beamline (Appendix section 3.1.), more scans were taken on B18 to compensate their lower quality.

6.2.1. LaMnO₃

The study of LaMnO₃ (LMO) was performed on the B18 beamline. 16 “dry state” scans are collected from a LMO nanoparticles-coated glassy carbon (GC) electrode connected to an electrochemical cell. The cell was then filled with a KOH 0.1 M electrolyte and 16 “OCV” scans were collected. A cyclic voltammogram between 0.0 and 1.5 V/RHE was recorded to assure that the material displayed its usual activity measured *ex situ* (Appendix 3). Then, several scans were taken at different potentials during a chronoamperometry experiment. The experimental conditions are summarized in Appendix section 3.3.2.

The average spectra are displayed on Figure III - 22. The general shape of the spectra is the same, aside from the slump occurring at 6560 eV on the spectrum taken at 1.8 V/RHE. At the half-edge jump, the energy measured at 0.2 V/RHE is 6549.7 eV while the energies of the other spectra are between 6550.3 eV and 6550.8 eV. This suggests that manganese is reversibly reduced during ORR.

The investigation of the edge evolution is extended to a temporal and a spectral study as shown on Figure III - 23. On the left side, the relative energy at 0.5 normalized intensity of every scan is correlated to the applied potential. The reference energy is the energy of the first scan at OCV. On the right side, the energy of each spectrum is subtracted to the spectrum acquired during the first OCV. The dry differential spectrum shows two positive peaks at 6555 eV and 6570 eV. As they are after the edge, they correspond to a structural modification rather than an oxidation state change. Note that the half-edge jump energy of the scans is shifting to lower energies over the time when the electrode is in its dry state. This shift is not observed once the electrolyte is added. This suggests a manganese reduction possibly

Chapter III: Evolution of Mn and Co-based perovskites during the OER and the ORR

induced by beam degradation when the material is not plunged in an electrolyte. Under progressive reducing conditions (0.6, 0.4 and 0.2 V/RHE), a peak rises on the differential spectra, correlated to the edge energy that decreased by 1 eV.

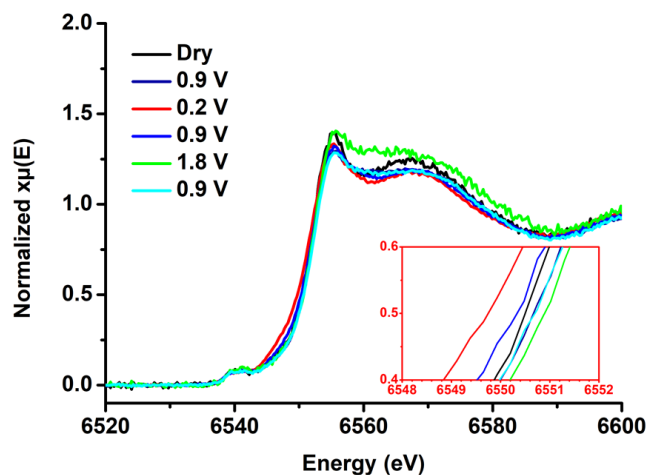


Figure III - 22 XANES spectra of LaMnO_3 during ORR and OER experiment. Dry electrode is in black. Successive potentials are applied: 0.9 (dark blue), 0.2 (red), 0.9 (blue), 1.8 (green), 0.9 V/RHE (cyan). In the red frame is a zoom between 6548 and 6552 eV.

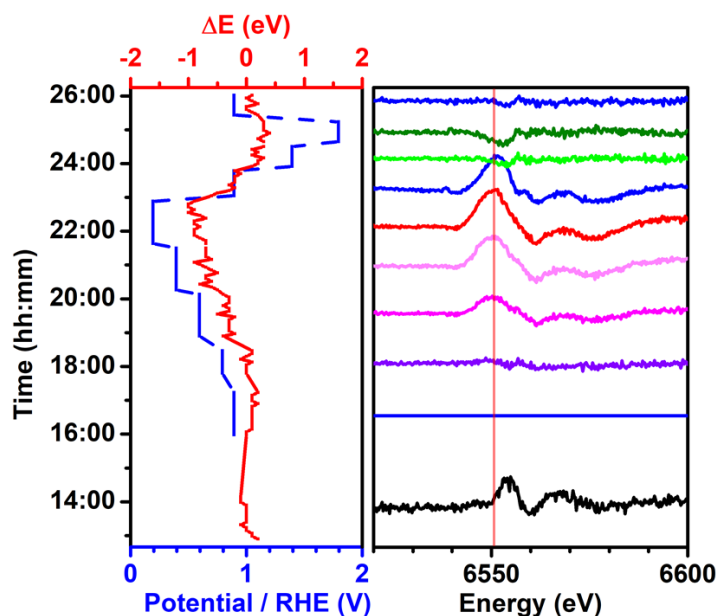


Figure III - 23 LaMnO_3 during in situ XAS ORR and OER experiment. Left: Time evolution of the Mn K-edge energy at the half-edge jump (red) under different potentials (blue). ΔE is the difference between the edge and the edge of the first OCV spectrum. Right: XANES difference spectra of LaMnO_3 at these potentials, from which the first OCV spectrum (0.9 V/RHE) is subtracted. The red vertical line is the half-edge jump energy of the first OCV spectrum.

Chapter III: Evolution of Mn and Co-based perovskites during the OER and the ORR

These modifications of XAS spectra indicate manganese reduction of the perovskite under ORR conditions. This reduction is not totally reversible as the peaks onto the differential spectrum observed at low potential are still present when the electrode is back to OCV at 0.9 V/RHE. However, the scans show that the edge energy rises up to its original value ($\Delta E = 0$ eV) gradually over time when the applied potential is kept at 0.9 V/RHE. Therefore, manganese is oxidized back from ORR conditions but a hysteresis behavior occurs that requires higher potential than the OCV for manganese to recover its initial state. At higher potential of 1.4 V/RHE, the peaks disappear and a small slump can be distinguished at 6555 eV, which gets even larger at 1.8 V/RHE. At these two potentials, the edge position of the scans rises up to 0.4 eV. These results indicate that the oxidation state of manganese increases under strongly oxidizing conditions and that the material recovers a structure close to the one observed during the first OCV. When the electrode is brought back at the OCV of 0.9 V/RHE, the differential spectrum is nearly flat, with the dip at 6555 eV reminiscent from the previous high potential state nearly distinguishable, and the edge energy back to $\Delta E=0$ eV. This suggests that the modifications under oxidizing conditions are reversible.

These results demonstrate that LaMnO_3 perovskite shows reversible manganese oxidation during OER and manganese reduction during ORR. According to the edge energy monitoring, manganese recovers its initial oxidation state when the potential is poised back to OCV. However, according to the overall shape of the XAS, the material requires oxidizing conditions to recover its initial structure after ORR. In the literature, emphasis has been put on the analysis of the bulk and the surface of LaMnO_3 materials to explain the high electroactivity in ORR^{141,142}. EELS and DFT calculations have demonstrated the presence of Mn^{2+} at the surface of the as-prepared perovskite, which promotes the ORR on the material^{127,142}. Yet the possibility that the reduction comes from the vacuum conditions under which the EELS measurement was carried out^{143,144} has not been envisaged. Currently, there is no report on *operando* investigation on LaMnO_3 under ORR or OER conditions.

Chapter III: Evolution of Mn and Co-based perovskites during the OER and the ORR

6.2.2. $\text{La}_{0.67}\text{Sr}_{0.33}\text{MnO}_3$

The $\text{La}_{0.67}\text{Sr}_{0.33}\text{MnO}_3$ experiment was performed on the SAMBA beamline. 3 “dry state” scans were collected from a $\text{La}_{0.67}\text{Sr}_{0.33}\text{MnO}_3$ nanoparticles-coated GC electrode connected to an electrochemical cell. The cell was then filled with KOH 0.1 M electrolyte and 3 “OCV” scans were collected. A cyclic voltammogram was recorded between 1.0 and 0.4 V/RHE to assure that the material displayed the activity measured *ex situ*. Several scans were then taken at different potentials. The experimental conditions are summarized in Appendix section 3.3.2. The merged spectra are displayed on Figure III - 24. The general shape of the spectra is unchanged as a function of the potential applied. The energies at half-edge jump separate in 3 groups. The edges of the spectra measured in the dry state, at 0.4 and 0.2 V/RHE are between 6650.4 eV and 6551.0 eV. At 0.6 V/RHE, the energy is at 6551.5 eV. The energies for 0.8 V/RHE and all the spectra at 1.0 V/RHE are between 6551.8 eV and 6552.3 eV.

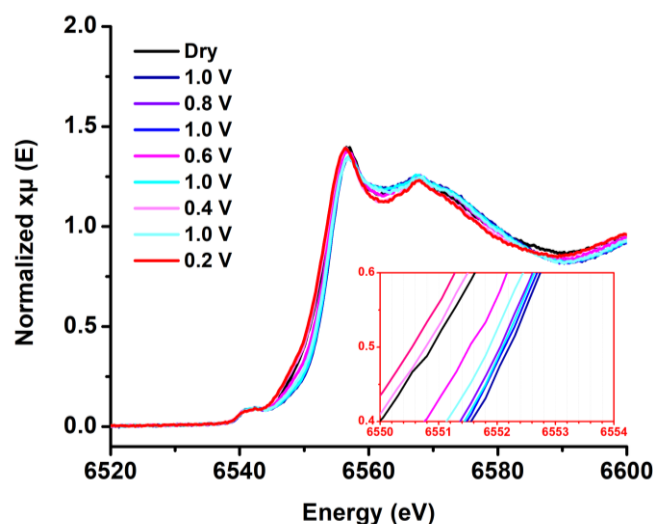


Figure III - 24 XANES spectra of $\text{La}_{0.67}\text{Sr}_{0.33}\text{MnO}_3$ during ORR experiment. Dry electrode is in black. Successive potentials are applied: 1.0 (dark blue), 0.8 (purple), 1.0 (blue), 0.6 (pink), 1.0 (cyan), 0.4 (light pink), 1.0 (light cyan), 0.2 V/RHE (red). In the red frame is a zoom between 6550 and 6554 eV.

Chapter III: Evolution of Mn and Co-based perovskites during the OER and the ORR

Like in LaMnO_3 experiment, we observe a gradual reduction of Mn under reducing conditions. The edge evolution investigation is extended to a temporal and a spectral study as shown on Figure III - 25. The differential spectrum recorded in the dry state shows three bumps at 6552 eV, 6570 eV and 6590 eV. The edge energy of the scans is shifting to lower energies over time, as it was observed on the LaMnO_3 experiment. Under progressive reducing conditions (0.8, 0.6, 0.4 and 0.2 V/RHE), a bump rises on the differential spectra around 6552 eV. The overall shape of the spectra in these ORR conditions is similar to the one of the dry state. This suggests that the perovskite is already reduced in the dry state, which is in accord with the progressive reduction of the gradual reduction observed on the half-edge jump monitoring. The system is brought back to 1.0 V/RHE between each reducing potential. At these resting states, the peak lowers drastically. However, when the electrodes are brought to strongly reducing potentials at 0.4 V/RHE and 0.2 V/RHE, the peak is still distinguishable on the subsequent 1.0 V/RHE spectra, whose energy at half-edge jump remains lower than the first OCV. These modifications indicate reduction of manganese during ORR, which is hardly reversible. At each change of potential, the edge energy shifts progressively. More reducing potentials increase the shift. At 0.6 V/RHE and 0.4 V/RHE, the edge energy reaches a minimum with $\Delta E = -0.5$ and -1.4 eV respectively on the second scan (which equals to around 15 min of steady potential). At 0.8 V/RHE, the minimum is not reached on the third scan. This intermediary state is also observed on the resting state potentials after 0.4 V/RHE and 0.2 V/RHE. Hence, the oxidation state of manganese evolves at the 10 min time scale before reaching a steady value. Still, we must keep in mind that these assumptions are built solely based onto three-point curves, even though they have been distinguished on five different potentials in our experiments.

The $\text{La}_{0.67}\text{Sr}_{0.33}\text{MnO}_3$ ORR investigation shows that, like in LaMnO_3 , manganese reduces under reducing conditions. Yet, the reversibility of this redox change is not complete, especially when very low potentials are applied. Thanks to the higher signal-to-noise ratio provided by the SAMBA beamline, intermediate states during the evolution of the electrocatalysts could be observed.

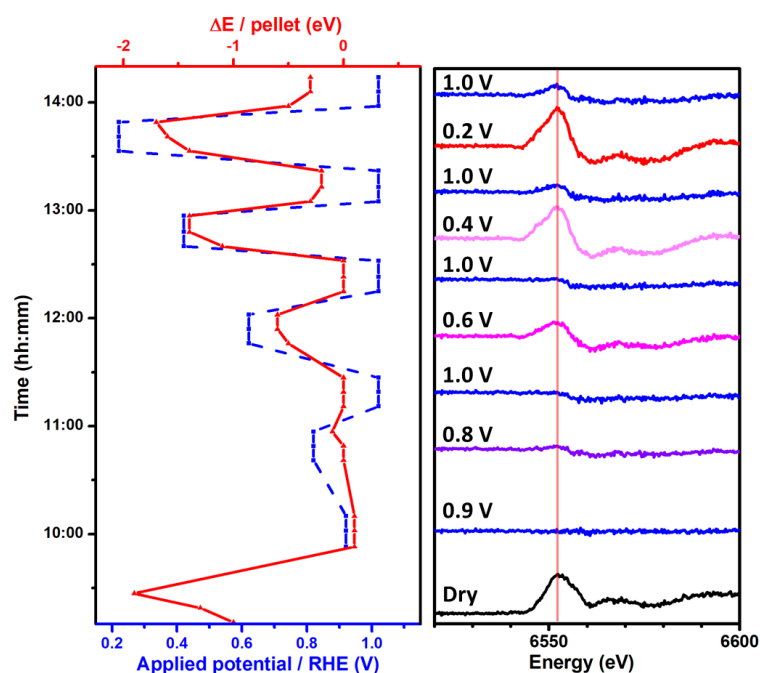


Figure III - 25 $\text{La}_{0.67}\text{Sr}_{0.33}\text{MnO}_3$ during in situ XAS ORR experiment. Left: Time evolution of the Mn K-edge energy (red) at 0.5 normalized intensity under different potentials (blue). ΔE is the difference between the edge and the edge of the first OCV scan. Right: XANES spectra of $\text{La}_{0.67}\text{Sr}_{0.33}\text{MnO}_3$ at these potentials, from which the first OCV spectrum (0.9 V/RHE) is subtracted. The red vertical line is the half-edge jump energy of the first OC spectrum.

6.2.3. $\text{La}_{0.75}\text{Sr}_{0.25}\text{CoO}_3$

The $\text{La}_{0.75}\text{Sr}_{0.25}\text{CoO}_3$ experiment is performed on the B18 beamline. 13 “dry state” scans are collected from a $\text{La}_{0.75}\text{Sr}_{0.25}\text{CoO}_3$ nanoparticles-coated GC electrode connected on an electrochemical cell. The electrochemical cell is then filled with KOH 0.1 M electrolyte and 12 “resting state” scans are collected. A cyclic voltammogram between 0.0 and 1.5 V/RHE is recorded to assure that the material displayed the activity measured *ex situ*. Then, several scans are taken at different potentials. They are summarized in Appendix section 3.3.2. During the first trial at 1.8 V/RHE, the detector had to be displaced for the sake of safety. Hence, another set of spectra at the OCV was taken before reaching the second oxidizing state. We decide to show all the recorded spectra in order to take the whole history of the electrocatalyst into consideration. The merged spectra are displayed on Figure III - 26.

Chapter III: Evolution of Mn and Co-based perovskites during the OER and the ORR

The general shape of the spectra is similar. At half-edge jump, the edge energies separate in 3 groups. The edges of the spectra for 0.4 V/RHE is at 7721.3 eV. The energies recorded in the dry state and at 1.0 V/RHE are 7721.8 eV. The energy at 1.8 V/RHE is 7722.1 eV. Hence, we observe cobalt reduction and oxidation during ORR and OER, respectively.

. The evolution of the spectra on Co K-edge as function of time and the experimental conditions are gathered in Figure III - 27. The second OCV conditions were used as reference as it was recorded on the same location as during the following potentials. The differential spectrum of the second energy scan in OER conditions at 1.8 V/RHE shows a dip at 7725 eV and a flatter one around 7770 eV. The edge energy increases slightly to $\Delta E = 0.4$ eV, indicating cobalt oxidation under OER conditions. The differential spectrum at 0.4 V/RHE displays an intense peak at 7720 eV, a small peak at 7730 eV and a large bump at 7770 eV. The edge energy decreases to $\Delta E = -0.6$ eV. These experiments show that cobalt reduces under reducing conditions and the peaks observed in the EXAFS part of the spectra suggest that the local environment of the cation is modified. On the differential spectrum of the last OCV, the peak at 7720 eV is less intense but the peak at 7730 eV remains. The edge energy is close to the energy of the starting OCV state ($\Delta E = -0.2$ eV). These modifications indicate that the OER electrocatalyst does not recover completely its initial state even after being submitted to ORR conditions and then again to the OCV.

The investigation of $\text{La}_{0.75}\text{Sr}_{0.25}\text{CoO}_3$ under OER and ORR electrocatalysis conditions shows that cobalt follows the same trend as manganese in manganite perovskites described above: cobalt oxidizes during OER and reduces during ORR. The reversibility of these changes is not complete in ORR. The reversibility could not be assessed in OER as no spectrum was acquired at OCV after the perovskite was submitted to OER conditions.

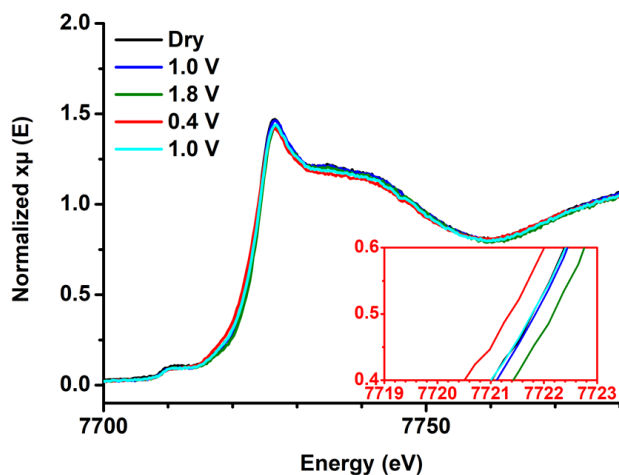


Figure III - 26 XANES spectra of $\text{La}_{0.75}\text{Sr}_{0.25}\text{CoO}_3$ during OER and ORR experiments. Dry electrode is in black. Successive potentials are applied: 1.0 (blue), 1.8 (green), 0.4 (red) and 1.0 V/RHE (cyan). In the red frame is a zoom between 7719 and 7723 eV.

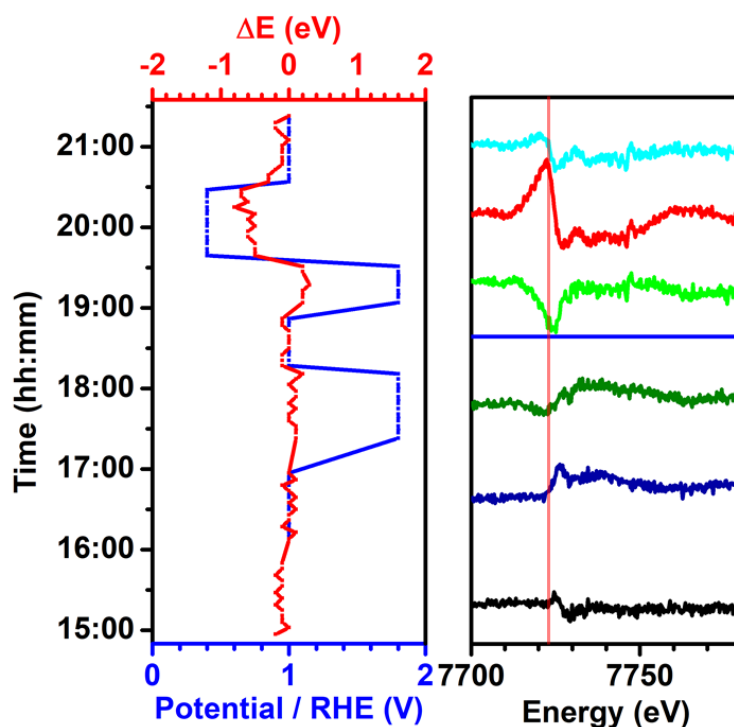


Figure III - 27 $\text{La}_{0.75}\text{Sr}_{0.25}\text{CoO}_3$ during in situ XAS OER and ORR experiment. Left: Time evolution of Co K-edge energy half-edge jump (red) under different potentials (blue). ΔE is the difference between the edge and the edge of the first OCV scan. Right: XANES spectra of $\text{La}_{0.75}\text{Sr}_{0.25}\text{CoO}_3$ at these potentials, from which the second OCV spectrum (0.9 V/RHE) is subtracted. The red vertical line is the half-edge jump energy of the second OCV spectrum.

Chapter III: Evolution of Mn and Co-based perovskites during the OER and the ORR

6.2.4. $\text{LaMn}_{0.6}\text{Co}_{0.4}\text{O}_3$

For *operando* XAS, we have focused on the mixed perovskite with the richest content in cobalt: $\text{LaMn}_{0.6}\text{Co}_{0.4}\text{O}_3$. More scans were required for acquiring Co K-edge spectra than Mn K-edge spectra, because of the lower content of Co than Mn. Manganese and cobalt K-edge spectra are recorded successively on each step during the same experiment. Data collection was performed twice: once on the SAMBA beamline and once on the B18 beamline with the same protocol as the other perovskites. Both experiments provided the same results, thus proving the reproducibility of the experiment. Here, we present the results from the experiment on the SAMBA beamline. Each step is listed in Appendix section 3.3.2. The “control” cyclic voltammogram is recorded between 1.8 and 0.4 V/RHE and shown in Appendix section 3.3.1.

The averaged spectra at the Mn K-edge and Co K-edge are displayed on Figure III - 28 and Figure III - 29, respectively. On each K-edge, no modification in the overall shape, neither on the edge energies, can be observed. At the half-edge jump, the energies of Mn K-edge stay between 6552.0 eV and 6552.2 eV, which is below the energy resolution of 0.2 eV. The energies of the Co K-edge are between 7721.8 and 7722.0 eV. From these observations, no change of oxidation state is detected under OER and ORR electrocatalytic conditions for manganese and cobalt. The evolution of the spectra in function of time and the experimental conditions are gathered in Figure III - 30 for the Mn K-edge and on Figure III - 31 for the Co K-edge.

The differential Mn K-edge spectrum with the OCV state as reference shows in the dry state a peak at 6550 eV with a flat slump centered at 6565 eV. At the same state, the differential spectrum of the Co K-edge features a dip at 7725 eV. These results indicate that the alkaline electrolyte modifies the local structure of manganese but it has little effect on the cobalt local structure, suggesting that the perovskite responds to the new external constraint by adapting the local environment of manganese. The edge energy is shifted to lower energies with time, as observed above with the other perovskites.

Under *operando* conditions, no significant change is observed at any potential on the differential spectra of the Mn K-edge nor the Co K-edge, and the energies at the half-edge jump of both edges stay constant. We conclude that the structure of the $\text{LaMn}_{0.6}\text{Co}_{0.4}\text{O}_3$ perovskite is stable during the electrochemical experiment. Unlike in the previously studied perovskites, the oxidation state of Mn and Co in $\text{LaMn}_{0.6}\text{Co}_{0.4}\text{O}_3$ are hardly sensitive to OER

Chapter III: Evolution of Mn and Co-based perovskites during the OER and the ORR

and ORR conditions. From these results, it is difficult to determine which cation is active during electrocatalytic reactions.

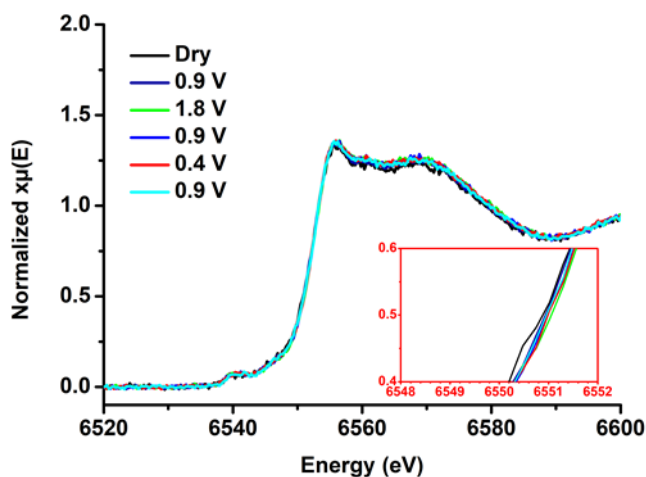


Figure III - 28 XANES spectra of $\text{LaMn}_{0.6}\text{Co}_{0.4}\text{O}_3$ during OER and ORR experiment on Mn K-edge. Dry electrode is in black. Successive potentials are applied: 0.9 (dark blue), 1.8 (green), 0.9 (blue), 0.4 (red) and 0.9 V/RHE (cyan). In the red frame is a zoom between 6548 and 6552 eV.

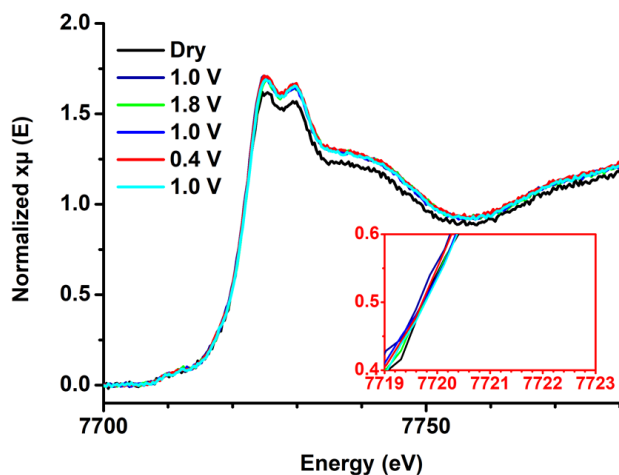


Figure III - 29 XANES spectra of $\text{LaMn}_{0.6}\text{Co}_{0.4}\text{O}_3$ during OER and ORR experiment on Co K-edge. Dry electrode is in black. Successive potentials are applied: 1.0 (blue), 1.8 (green), 0.4 (red) and 1.0 V/RHE (cyan). In the red frame is a zoom between 7719 and 7723 eV.

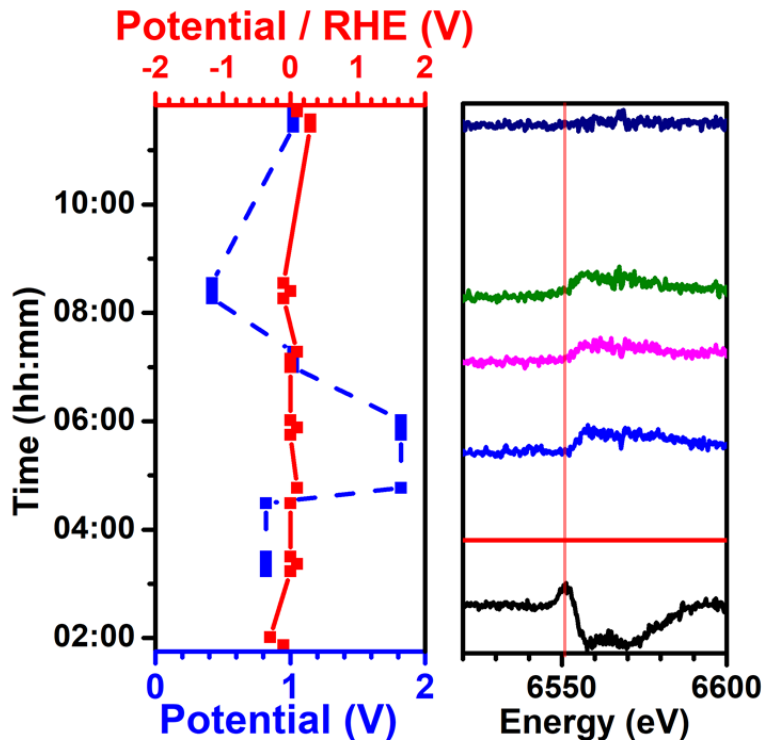


Figure III - 30 $\text{LaMn}_{0.6}\text{Co}_{0.4}\text{O}_3$ during in situ XAS OER and ORR experiment. Left: Time evolution of the Mn K-edge energy (red) at 0.5 normalized intensity at different potentials (blue). ΔE is the difference between the edge and the edge of the first OCV scan. Right: XANES spectra of $\text{LaMn}_{0.6}\text{Co}_{0.4}\text{O}_3$ at these potentials, from which the first OCV spectrum (0.9 V/RHE) is subtracted. The red vertical line is the half-edge jump energy of the first OC spectrum.

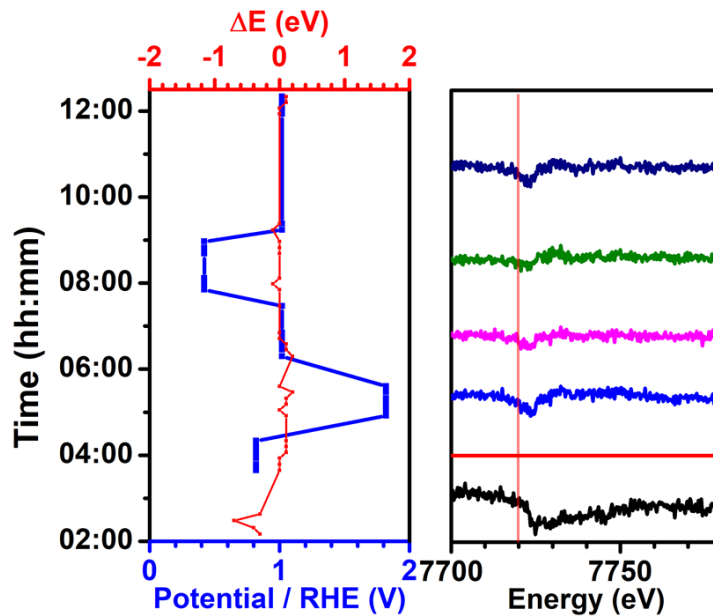


Figure III - 31 $\text{LaMn}_{0.6}\text{Co}_{0.4}\text{O}_3$ during in situ XAS OER and ORR experiment. Left: Time evolution of the Co K-edge energy (red) at 0.5 normalized intensity at different potentials (blue). ΔE is the difference between the edge and the edge of the first OCV scan. Right: XANES spectra of $\text{LaMn}_{0.6}\text{Co}_{0.4}\text{O}_3$ at these potentials, from which the first OCV spectrum (0.9 V/RHE) is subtracted. The red vertical line is the half-edge jump energy of the first OC spectrum.

7. Discussion

7.1. Synthesis and *ex situ* electrochemical characterization

The molten salt synthesis of LaMnO_3 is adaptable to the synthesis of perovskites whose composition are close to the original material to obtain crystalline nanoparticles with a mean size of ca. 20 nm. The obtained $\text{La}_{0.67}\text{Sr}_{0.33}\text{MnO}_3$ are cube-like nanoparticles while the insertion of cobalt in $\text{LaMn}_{1-x}\text{Co}_x\text{O}_3$ gives rounder nanoparticles. While elemental mapping confirms the presence of manganese and cobalt in all the nanoparticles, the resolution of the current images is too low to establish if the repartition of the transition metals is homogeneous inside the nanoparticles. The perovskite phase is accompanied by impurities, mainly $\text{La}(\text{OH})_3$, but whose amount and electroactivity are considered negligible to perturb the future electrochemical experiments of the perovskite phase.

Compared to manganese-based perovskites, the crystallization of $\text{La}_{1-x}\text{Sr}_x\text{CoO}_3$ nanoparticles requires higher temperature and a more oxo-donor solvent. The obtained nanoparticles have a mean size higher than 100 nm and are fused together. A variety of cobalt-based secondary phases can be formed and could interfere with electrocatalysis experiments because these compounds are usually highly active in OER. Aside from the crystallization of $\text{La}_{1-x}\text{Sr}_{1+x}\text{CoO}_4$ perovskite, which appears if the temperature is too high, cobalt reacts with most of the crucibles to produce cobalt silicates in a porcelain crucible or eroded boron nitride in a boron nitride crucible. The washing step is monitored with the water conductivity. If the dissolution of a compound is slow (i.e. $\text{La}(\text{OH})_3$), an early measurement will indicate a low water conductivity that may lead to stop the washing step prematurely. Letting the sample in the water for a longer time would dissolve more impurities, but it could also degrade the surface of the perovskites.

TEM shows foils at the surface of the $\text{La}_{1-x}\text{Sr}_x\text{CoO}_3$ perovskites. The nature and the origin of these foils have not been clearly established but, from the previous comment on the washing step, we may hypothesize that these foils are formed during a too long exposure to liquid solvent, namely water or ethanol from the TEM grid preparation (Appendix section 1.3.2.)

We measured the OER and ORR electrocatalytic properties of $\text{LaMn}_{1-x}\text{Co}_x\text{O}_3$, LaMnO_3 and $\text{La}_{0.75}\text{Sr}_{0.25}\text{CoO}_3$. While the comparison between LMCO and LMO is relevant because they have the same mean size of nanoparticles and they only differ by the B-site composition, comparing LMCO to LSCO is questionable, as LSCO nanoparticles are much

Chapter III: Evolution of Mn and Co-based perovskites during the OER and the ORR

larger and should then provide a lower surface area for the same load of catalyst and the composition of the A-site is also modified. While the materials we have synthesized exhibit OER and ORR activity, comparing their performances to their analogues in the literature requires to normalize their activity to the oxide surface or to the amount of electrocatalytic active sites (either Mn or Co)^{36,37,56,130,132,141}.

7.2. Operando XAS technique

The oxidation state of manganese in LSMO, LMCO30 and LMCO40 is calculated from linear combination fitting with two references: LaMnO₃ and SrMnO₃. While the first one is home-made and has similar size and crystallinity than the samples to be measured, SrMnO₃ XAS is extracted from the publication of Celorrio et al.¹³⁹. The conditions where the data were collected, the size and the crystallinity of the nanoparticles can alter the resulting absorption spectrum. The uncertainty brought by the choice of a reference from the literature is clear by comparing LCF carried out with LaMnO₃ we have synthesized with a LCF done with the XAS of a LaMnO₃ taken from the publication of Celorrio et al.¹³⁹ (Appendix section 4.2). The oxidation state of cobalt cannot be evaluated with the same accuracy by this technique because the only available cobalt perovskite reference is a bulk LaCoO₃. SrCoO₃ is hardly obtainable as a pure perovskite because of the instability of this phase so an experimental sample would likely contain multiple cobalt oxidation states (II, III, IV)¹⁴⁰. Consequently, the evolution of the cobalt oxidation state is qualitatively evaluated by comparing the energy at the half-edge jump of each perovskites to LaCoO₃.

During *operando* experiments, the changes observed on the EXAFS of the perovskites are weak and the energy at the half-edge jump shifts by 2 eV at most. Differential spectra were then plotted to detect when critical changes occur on the XAS during the electrocatalysis. This spectral analysis was completed by a temporal monitoring where, instead of only displaying the average spectrum at each applied potential, we recorded the energy at half-edge jump for every scan recorded consecutively. This allowed us to follow the evolution of the oxidation state under fixed conditions for 30 min to a few hours. In the literature, the *operando* analysis of electrocatalytic experiments on this time-scale is usually dismissed as the emphasis is only put on the applied potential and the equilibrium state is supposed to be reached in less than a minute after setting the new conditions^{56,145}. The kinetics of the materials response to the external stimuli have never been assessed. Theoretically, a time-resolved beamline would be adapted for the changes we seek to observe. However, comparing the scans collected on the B18 beamline (scan rate: 3.5 eV·s⁻¹)

Chapter III: Evolution of Mn and Co-based perovskites during the OER and the ORR

with the scans recorded on the SAMBA beamline (scan rate: $2.0 \text{ eV}\cdot\text{s}^{-1}$) shows that increasing the scan rate degrades the signal-to-noise ratio of the spectrum. A compromise has to be found between a high scan rate to obtain enough points to make a model, and high quality spectra to have exploitable and reliable data.

The temporal evolution of the experiments was monitored by the edge position energy at half-edge jump. Indeed, this energy is an indicator of the oxidation state of the probed element. However, the accuracy of this method based on one point of the spectrum is very low compared to LCF which takes into account a wide range of the spectra, which is why this method is completed by the study of differential spectra to support the observations of the shift of energy. To sum up, monitoring the energy at half-edge jump without LCF cannot bring more than a qualitative evolution of the oxidation state of the transition metal, but the detection of any evolution of the oxidation state helps to identify the phenomena that are worth to be further investigated, such as the impact (or not) of an oxidizing/reducing potential on the perovskite or the transition metal reduction on the dry electrode.

Recording the *operando* experiment of LMCO40 took 10 hours because the Mn K-edge and the Co K-edge were recorded successively and the low amount of each element diminished the scans quality. Collecting the K-edge of both elements at the same time would shorten the duration of the experiment and ensure that both spectra describe the same state of the material. The simultaneous detection of two edges can be performed by X-ray emission spectroscopy but the signal-to-noise ratio of this technique may be lower than XAS⁵⁸.

Our *operando* experiments were rarely carried out under the same conditions: Aside from the use of two different beamlines that has already been discussed, the potentials that we have successively applied may differ from one perovskite to another. The evolution of LSMO under OER conditions was not studied. Instead, we deeply investigated the oxidation state of manganese in this perovskite during ORR. As for the LSCO perovskite, it was investigated twice under OER conditions. The various experimental conditions used gave us different insights on every perovskites. Experiments on LMO and LSCO enabled examining the oxidation state of the transition metal in a single B-site perovskite during OER and ORR. Furthermore, our focus on studying LSMO under ORR conditions highlighted the effect of the strength of the reducing condition on the perovskite. Still, one phenomenon is observed on every perovskites: at the dry state, the energy at the half-edge jump shifts to a lower

Chapter III: Evolution of Mn and Co-based perovskites during the OER and the ORR

energy, indicating a reduction of the transition metal upon processing of the electrode. This shift is not observed anymore when the electrolyte is added. We suggest that the dry electrode overheats under the X-rays and reduces in the presence of the carbon-rich environment provided by the formulation of the electrode¹⁴⁶. The aqueous electrolyte, by cooling down the electrode, prevents the overheating-induced reduction. This hypothesis could be proved by collecting the spectra of the dry electrode at two moments distant in time to see if the phenomenon still happens without a beam exposure, or by analyzing the nanoparticles on a carbon-free electrode to test the impact of the presence of carbon on the reduction of the transition metals.

7.3. Observations on the electrocatalysts

According to linear combination fittings (Table III - 2), the oxidation state of manganese in $\text{La}_{0.67}\text{Sr}_{0.33}\text{MnO}_3$ is +3.3 is in agreement with the theoretical value. Cobalt substitution in LaMnO_3 increases the oxidation state of manganese. At the same time, the oxidation state of cobalt is estimated to be lower than +III in the mixed Mn/Co perovskites. An average oxidation state of +3 on the B-site cation of the perovskite is then still possible, with the presence of Mn^{3+} , Mn^{4+} , Co^{2+} and Co^{3+} in these sites.

Under reducing conditions, the perovskites containing one transition metal see a reversible reduction of this transition metal. A similar phenomenon is observed under oxidizing conditions, where the transition metal is oxidized. The oxidation of cobalt during OER in LSCO has already been observed and the OER activity of the cobalt perovskite has been attributed to the presence of Co^{4+} in the activated phase at high potential⁵⁶. Conversely, the LSCO ORR activity is attributed to the reduction of cobalt to Co^{2+} , which has a high ORR activity³². In the same way, highly oxidized manganese cations are active sites in OER^{14,147}. At 0.2 V/RHE, the shift of the energy at half-edge jump of LSMO is more than 1.5 eV while the shift of LMO is less than 1 eV, suggesting a higher reduction of manganese in the LSMO perovskite. Considering that the oxidation state of the manganese is higher in LSMO, this higher shift is interpreted as a compensating reduction of Mn^{4+} . The average oxidation state of the manganese during ORR is then lower than +3. Risch *et al.* drew similar conclusion from *operando* XAS of electrodeposited $\delta\text{-K}_x\text{MnO}_{2-y}\cdot z\text{H}_2\text{O}$ at the Mn $L_{2,3}$ -edge, where they observed that the ORR active phase of manganese oxide contains mixed Mn^{2+} and Mn^{3+} ¹⁴⁸.

Chapter III: Evolution of Mn and Co-based perovskites during the OER and the ORR

In a mixed Mn/Co LMCO perovskite, no reduction or oxidation of the transition metal cations is detected as the energy at half-edge jump stays constant along the experiment. According to the evaluation of the oxidation states on the as-prepared compounds, during both OER and ORR, LMCO perovskites contain manganese with an average oxidation state higher than +3 and cobalt with an average oxidation state lower than +3. By referring to the reported electrocatalytic activities of Mn^{4+} ¹⁴⁸ and Co^{2+} ³², we conclude that manganese should be the active site in OER and cobalt should be the active site in ORR. When the electroactivities of the perovskites are normalized to the manganese content (Figure III - 16), LMCO perovskites are more active than LMO in OER. This indicates that cobalt-substitution in LMO increases the activity of the manganese sites. Under reducing conditions, when the current is normalized to cobalt content, LMCO perovskites exhibit higher ORR activity than LSCO (Figure III - 17). Since the electrocatalytic activity does not only depend on the content of transition metal, but also on the surface composition and the specific surface area, we cannot directly conclude on any enhanced performance brought by the mixed transition metal composition because the LSCO sample is too different from the LMCO perovskites. The larger size of the LSCO nanoparticles reduces the number of active sites per disk area. Moreover, the presence of strontium increases the average oxidation state of cobalt, which may have reduced the content of ORR active Co^{2+} .

The variation of manganese oxidation state in LSMO is progressive under reducing conditions or under OCV and may last more than 15 min. This effect cannot be unambiguously observed on the other perovskites because the signal-to-noise ratio and the number of scans recorded on LMO and LSCO experiments are too low. Besides, the oxidation state evolution of the transition metal in LMCO is too weak to be exploited. This slow reduction could be explained by a progressive reduction of the manganese at the surface of the electrocatalyst or by the modification of the bulk composition of the materials. A time-resolved surface analysis of the material should bring answer to the first question and orient the research for the second question.

8. Conclusion

In this chapter, we have described the synthesis of LaMnO_3 and $\text{La}_{0.67}\text{Sr}_{0.33}\text{MnO}_3$ perovskite nanoparticles in molten salt and adapted the protocol to the synthesis of both $\text{LaMn}_{1-x}\text{Co}_x\text{O}_3$ and $\text{La}_{1-x}\text{Sr}_x\text{CoO}_3$ perovskites. We have studied the electrocatalytic properties of all synthesized perovskites in OER and ORR and analyzed the evolution of the transition metals during these reactions by *operando* XAS on Mn and Co K-edge.

The synthesis of $\text{La}_{1-x}\text{Sr}_x\text{CoO}_3$ perovskite nanoparticles was more difficult because of the specific cobalt chemistry: the cobaltite required a reaction medium richer in oxygen to form, while it also exhibited instability in contact with water. Still, this material showed an OER electrocatalytic activity in the same order of magnitude than the reported LSCO^{56,115}. The compositions of $\text{LaMn}_{1-x}\text{Co}_x\text{O}_3$ perovskites were close to LaMnO_3 so the minor amount of cobalt did not affect the synthesis that is based on the manganite perovskite synthesis. A slight increase of the nanoparticle size was observed and correlated to the concentration of Co in the material. $\text{LaMn}_{1-x}\text{Co}_x\text{O}_3$ displayed electrocatalytic activity in both OER and ORR, as it was reported by Liu et al.¹³³, though these activities were lower than the perovskites that contain only one transition metal, namely LaMnO_3 (in ORR) and $\text{La}_{0.75}\text{Sr}_{0.25}\text{CoO}_3$ (in OER). The normalization of the current by one of the transition metal content shows that if we suppose that only one transition metal is active during the electrocatalysis, then the activity per active site is higher in the $\text{LaMn}_{1-x}\text{Co}_x\text{O}_3$ than in LaMnO_3 or $\text{La}_{0.75}\text{Sr}_{0.25}\text{CoO}_3$. This suggests that both transition metals contribute to the electrocatalysis, whether by being an active site, or by increasing the intrinsic activity of the other transition metal.

XAS analysis on the as-prepared materials allowed us to estimate the manganese average oxidation state in $\text{La}_{0.67}\text{Sr}_{0.33}\text{MnO}_3$, $\text{LaMn}_{0.7}\text{Co}_{0.3}\text{O}_3$ and $\text{LaMn}_{0.6}\text{Co}_{0.4}\text{O}_3$ of +3.33, +3.40 and +3.30, respectively. The Co average oxidation state could not be calculated for lack of perovskite reference containing Co^{II} or Co^{IV} . Still, the average oxidation state of cobalt in $\text{La}_{0.75}\text{Sr}_{0.25}\text{CoO}_3$ was confirmed to be higher than +3. In $\text{LaMn}_{1-x}\text{Co}_x\text{O}_3$, cobalt showed an average oxidation state between +2 and +3. This feature indicates charge transfer from manganese to cobalt in $\text{LaMn}_{1-x}\text{Co}_x\text{O}_3$ perovskites. *Operando* XAS experiments showed that in perovskites with a single cation (manganites and cobaltites) in the B-site, the average oxidation state of the transition metal varied with the electrochemical conditions, *i.e.* the cation oxidizes under OER and reduces under ORR. For manganites, we suspect

Chapter III: Evolution of Mn and Co-based perovskites during the OER and the ORR

structural changes to occur during ORR and that oxidizing conditions were required to reach again the initial state. Intermediate states were observed for the $\text{La}_{0.67}\text{Sr}_{0.33}\text{MnO}_3$ perovskite at each modification of potential. The origin and the nature of this slow redox reaction is still unclear. The evolution of manganese and cobalt in LMCO were surprisingly different than their pure transition metal counterparts as manganese and cobalt K-edge were invariant during the electrochemical experiment.

The $\text{La}_{0.75}\text{Sr}_{0.25}\text{CoO}_3$ perovskite nanoparticles were much larger than the other materials and they could not be obtained without impurities. Improving the synthesis of $\text{La}_{1-x}\text{Sr}_x\text{CoO}_3$ would provide more accurate comparisons. Achieving this goal would also allow the synthesis of $\text{LaMn}_x\text{Co}_{1-x}\text{O}_3$ perovskites where cobalt would be the major transition metal cation. $\text{La}_{1-x}\text{Sr}_x\text{Mn}_{1-y}\text{Co}_y\text{O}_3$ quaternary perovskites could also be investigated. Manganese average oxidation state was calculated by XANES linear combination from reference perovskites. Obtaining these kind of references for cobalt perovskites would enable the estimation of cobalt average oxidation state more accurately. Still, the results from this technique should be double-checked by another type of analysis. Chemical titration would help to confirm manganese average oxidation state in perovskites without cobalt, as in $\text{La}_{1-x}\text{Sr}_x\text{MnO}_3$ ¹²⁷.

To summarize, we confirmed the oxidation/reduction of the transition metal during OER/ORR respectively in the perovskites that contain a single transition metal, while the average oxidation states of both transition metals seem stable in the $\text{LaMn}_{1-x}\text{Co}_x\text{O}_3$ perovskites. Investigating this stability requires more sensitive *in situ* techniques to detect any possible weak evolution. For instance, we could consider analyzing the transition metal L-edge, which should be more sensitive to oxidation variation than the K-edge. On the other hand, electrocatalysis mostly impacts the surface of the perovskite. A surface analyzing technique, such as near-ambient pressure X-ray photoelectron spectroscopy, would probe the nanoparticles surface exclusively, where the changes should occur the most. The second intriguing observation is the identification of the intermediate states that were observed in the LMO experiment. However, none of the beamlines were optimized enough to draw conclusions on the origin of this slow transformation in the $\text{LaMn}_x\text{Co}_{1-x}\text{O}_3$ perovskites. While the slow scan rate of the SAMBA beamline allowed only a few scans to be taken, the low signal-to-noise ratio of the B18 beamline did not allow the phenomenon to be detected. Compromises between the set-ups of the two beamlines needed to be found. As for the origin of the intermediate state, it was still not clear if the slow reduction/oxidation occurs on the

Chapter III: Evolution of Mn and Co-based perovskites during the OER and the ORR

surface or in the bulk of the material. This intermediate state, as well as the evolutions of Mn and Co average oxidation state, were determined from a single point per spectrum, at half-edge jump. This choice, although commonly used, was arbitrary. Taking more points into account would provide more reliable results. For Mn K-edge, XANES linear combination could be considered, as the spectra of relevant references are available.

While the data collection of nickel borides and manganite cobaltite perovskites were carried out the same way, data treatment of the perovskites was more qualitative and emphasized the evolution of the electrocatalyst during the whole experiment, rather than a clear description of the electroactive phase. Yet, in both studies, the need to couple XAS with other *operando* techniques has been highlighted.

Chapter IV:
An *in situ* XAS and TEM study of Co_3O_4 ,
a model system for the OER

1. Introduction

X-ray absorption spectroscopy at the K-edge of transition metals is a powerful technique that gives information on the average electronic and local environment of an element, which does not take into account materials heterogeneity. The high penetration depth of hard X-rays makes this technique easily adaptable to *in situ* analysis. However, its efficiency may be questioned when it comes to its sensitivity, since the concentration of electroactive species in the whole material can be very low.

To overcome these limitations, two complementary techniques are addressed in this chapter: L-edge XAS and transmission electron microscopy (TEM). XAS at the transition metal L-edge provides information on the electronic environment of the metal, like K-edge XAS, but it can show a higher sensitivity in terms of chemical speciation. Indeed, L₂ and L₃ edges probe the 2p → 3d transitions that directly indicate the occupation of 3d orbitals and consequently the metal oxidation state (Figure IV - 1). On the other side, TEM provides local nano- or atom-scale information on nanoparticle morphology and structure. New developments in the field of TEM have been reported during the last years to adapt this technique to *in situ* experiments⁷³. *In situ* electrochemical TEM in liquid electrolyte starts to emerge^{149,150}.

Because of the short travel length of soft X-ray photons and of electrons in a gas (such as air, for instance), L-edge XAS of transition metals and TEM both require vacuum environment to enable radiations to probe the materials. Consequently, airtight electrochemical cells have been developed for these techniques. These cells have been developed independently until now, because of the different technical constraints that are imposed by the two techniques.

Herein, we compare the evolution of a model OER electrocatalyst using *in situ* XAS at the metal K-edge, *ex situ* XAS at the corresponding L-edge and *in situ* TEM. We use Co₃O₄ spinel nanoparticles as a model material (Figure IV - 2) for the OER electrocatalysis. We will first characterize the Co₃O₄ nanoparticles that will be studied throughout this chapter and we will verify that their behavior in OER electrocatalysis is similar to those reported in the literature from *in situ* XAS at the Co K-edge. We will then present a XAS preliminary *ex situ* study at the Co L-edge on various supports in view of future *in situ* XAS experiments

Chapter IV: An *in situ* XAS and TEM study of Co_3O_4 , a model system for the OER

at the Co L-edge. We will finally present and investigate the OER experiments by *in situ* TEM and *in situ* XAS and compare the results.

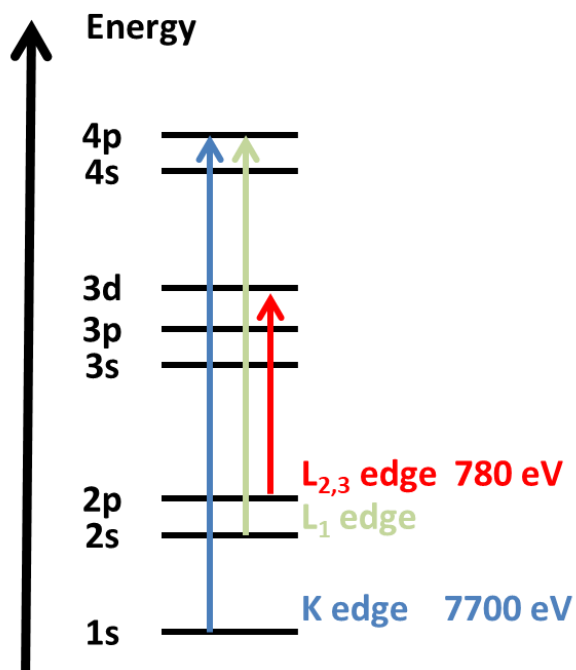


Figure IV - 1 Scheme of cobalt K-edge and L-edge transitions

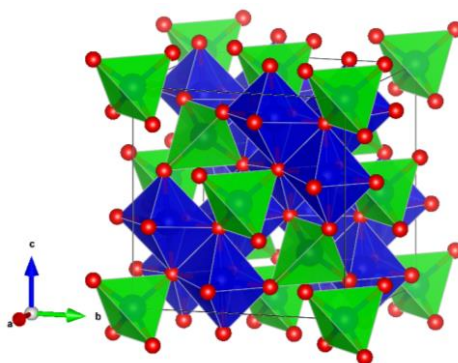


Figure IV - 2 Structure of Co_3O_4 . Oxygen are in red. Co^{II} are in blue at the center of the octahedral sites. Co^{III} are in green at the center of tetrahedral sites.

2. Co₃O₄ nanoparticles synthesis and characterization

Co₃O₄ is the most ubiquitous OER electrocatalyst in alkaline media and demonstrates large activity (10 mA cm⁻² at an overpotential of 0.5 V¹⁴⁷). Its synthesis is simple through several synthesis pathways¹⁵¹⁻¹⁵⁴ and commercial precursors are available¹⁵⁵, thus making it an affordable materials for fundamental study on electrocatalysis.^{156,157} The Co₃O₄ OER electrocatalytic activity is generally attributed to the Co⁴⁺ species that are only stable under oxidizing conditions¹⁵⁸⁻¹⁶⁰. The reversibility of cobalt oxidation examined through XAS at the Co K-edge, coupled with the reversible amorphization observed by X-ray diffraction suggests that the Co₃O₄ modification during OER is reversible in neutral medium.⁶⁰ Similar reversible changes have been observed by XRD in alkaline medium⁷⁷.

We synthesized Co₃O₄ nanoparticles by microwave-assisted hydrothermal synthesis from cobalt (II) nitrate hexahydrate (2 10⁻² mol·L⁻¹)¹⁶¹. The pH is raised above 11.3 with ammonia to precipitate cobalt (II) dihydroxide that readily oxidizes into Co^{III} species by reaction with O₂ dissolved in the solution¹⁵⁸. The solution is then heated by microwaves (850 W) to 100 °C for 10 min. The high temperature ramp and homogeneous heating provided by microwaves favor the formation of small and crystalline nanoparticles with a narrow size distribution (see Figure IV-3 and Figure IV-4)). The final mixture is cooled down to room temperature. The nanoparticles are washed 5 times with deionized water and dried under vacuum. A detailed protocol is described in appendix 1.1.2.

The powder X-ray diffractogram of the sample displays peaks that are all attributed to Co₃O₄ (Figure IV - 3). The noisy signal is due to the low amount of powder analyzed (40 mg) and to the fluorescence of cobalt under the Cu K α radiation. TEM indicates crystalline nanoparticles with an average size of 5 nm (Figure IV - 4). Cyclic voltammetry was then performed in KOH 0.1 M between 0.4 and 1.8 V/RHE with a scan rate of 10 mV·s⁻¹. The results are plotted in Figure IV - 5. The electrode exhibits a high electrocatalytic activity in OER as the current at 1.8 V/RHE (11 mA·cm⁻²_{disk}) is at least ten times higher than the current of an electrode without electrocatalyst (< 1 mA·cm⁻²_{disk}). This OER activity is comparable to the reported performances of Co₃O₄^{162,163}. The reversible redox wave at ~1.55 V/RHE corresponds to the Co^{III}/Co^{IV} redox peak^{137,138}.

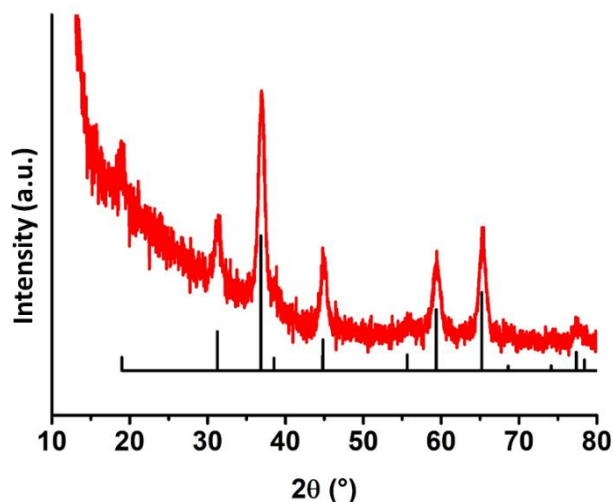


Figure IV - 3 Powder XRD pattern of Co_3O_4 nanoparticles formed by microwave-assisted hydrothermal synthesis at $100\text{ }^\circ\text{C}$ for 10 min (in red). The reference pattern in black corresponds to Co_3O_4 (PDF 00-042-1467).

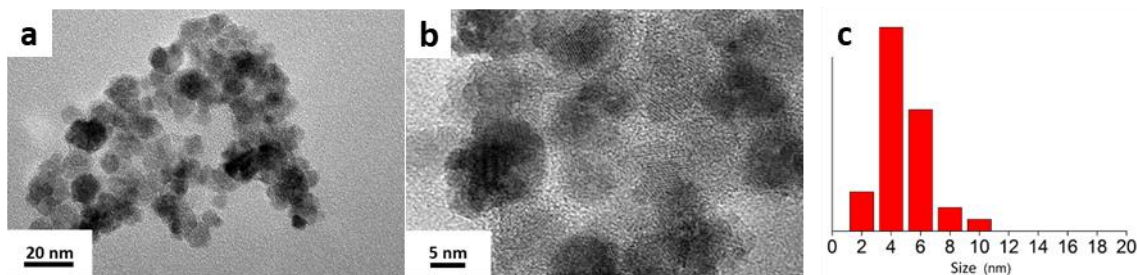


Figure IV - 4 Transmission electron microscopy images (left and middle) and size distribution (right) of Co_3O_4 nanoparticles synthesized in alkaline water ($\text{pH}=11.3$) at $100\text{ }^\circ\text{C}$.

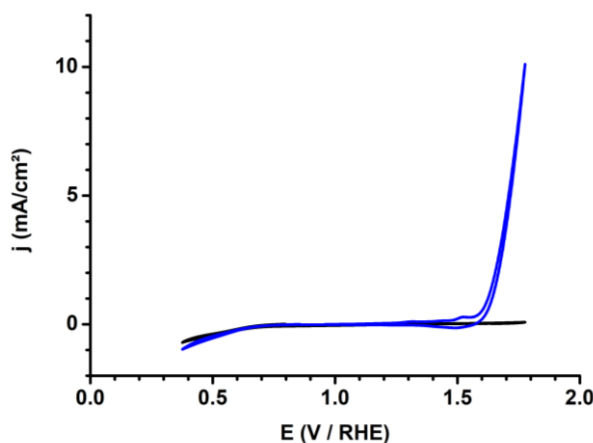


Figure IV - 5 Electrocatalytic activity (without correction) of synthesized Co_3O_4 spinels (in blue) and a blank electrode (in black) in KOH 0.1 M solution ($\text{pH} = 13$) using a rotating disk electrode (1600 rpm). The peak at 1.5 V/RHE is attributed to the $\text{Co}^{\text{III}}/\text{Co}^{\text{IV}}$ oxidation.

Chapter IV: An *in situ* XAS and TEM study of Co₃O₄, a model system for the OER

In situ XAS experiments in different electrolytes (KOH 0.1 M or KPi 0.1 M (pH=7)) were then performed to further study the nature of the electroactive species. To reproduce conditions used in *in situ* TEM electrochemical experiment, the electrocatalyst ink was only composed of Co₃O₄ nanoparticles (10 mg) dispersed in absolute ethanol (10 mL), without any carbon black or Nafion®. Preliminary experiments in KPi 0.1 M with a classical Co₃O₄ ink (Appendix section 1.2.1.) indicated that the formulation's modification has little impact on the cobalt oxidation state evolution in Co₃O₄ during OER (See Appendix section 3.3.4.).

First, experiments in KOH 0.1 M were performed and three Co K-edge XAS spectra were recorded which correspond to the dry state, the open circuit voltage (0.8 V/RHE) and OER conditions (2.2 V vs. RHE) (Figure IV - 6). The energies at half-edge jump for the dry electrode, at 0.8 and 2.2 V vs. RHE are 7719.7, 7719.7 and 7719.8 eV respectively, suggesting that there is no evolution of the oxidation state when the electrode is immersed in the basic electrolyte but a small oxidation under OER conditions in this condition (confirmed by reproducing the experiment). A second set of experiments were performed in KPi 0.1 M (pH = 7) with acquisition of five spectra, at the dry state and at 4 successive potentials: 1.0 (OCV), 2.0, 1.0 and 2.0 V vs. RHE (Figure IV - 7). At half-edge jump, the energy of the dry electrode is 7719.9 eV. The energies of the successive potentials 1.0, 2.0, 1.0 and 2.0 V vs. RHE are respectively 7719.8, 7720.2, 7720.0 and 7720.2 eV. Again, there is no significant change of the oxidation state when the electrode is immersed. The increase of the edge position energy with the potential confirms cobalt oxidation under OER conditions. However, the difference of edge position energy between the two OCV (7719.8 and 7720.0 eV) at 1.0 V/RHE indicates that the material remains partly oxidized after the first stage in OER conditions.

TEM and XRD indicate that the synthesized spinel cobalt oxides are 5 nm size nanoparticles. The measured electrocatalytic activity in OER is comparable to what has been reported^{162,163}. The results of the *in situ* XAS experiments in KPi are comparable to those obtained by Bergmann et al.⁶⁰ who also observed cobalt oxidation of Co₃O₄ during OER. However, their study suggests that this oxidation is reversible, while our results indicate that cobalt stays partly oxidized after OER in our experiment.

Now that we have verified that the Co₃O₄ nanoparticles synthesized display their reported OER activity, our next goal is to investigate the evolution of the Co L-edge during

Chapter IV: An *in situ* XAS and TEM study of Co_3O_4 , a model system for the OER

OER electrocatalysis for the purposes of observing more significant and convincing signs of cobalt oxidation or structural change during OER.

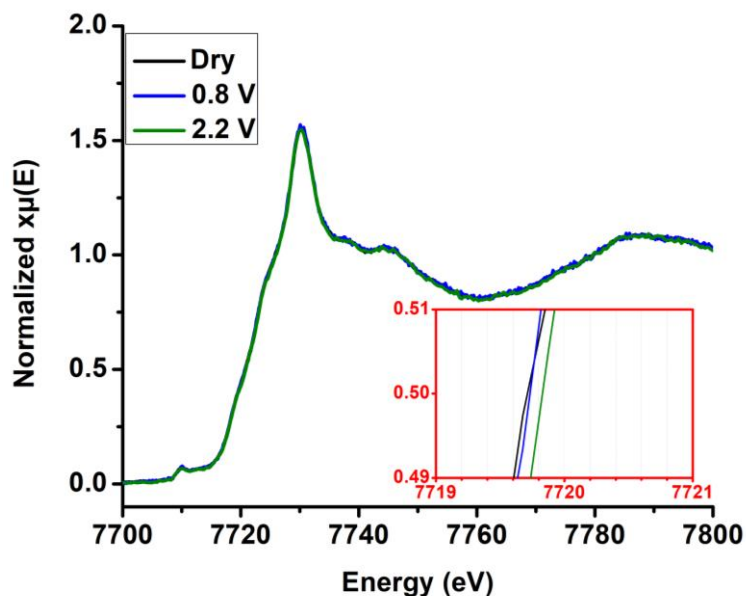


Figure IV - 6 XANES spectra of Co_3O_4 recorded during OER in KOH 0.1 M on Co K-edge. The spectrum corresponding to the dry electrode is in black. Successive potentials are applied: 0.8 (blue) and 2.2 V/RHE (green). In the red frame is a zoom between 7719 and 7721 eV.

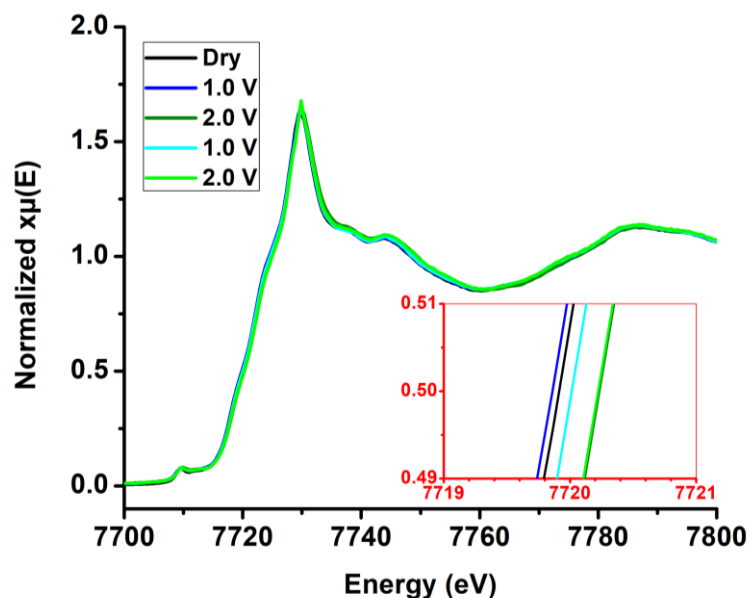


Figure IV - 7 XANES of Co_3O_4 during OER in KPi 0.1 M on Co K-edge. The spectrum corresponding to the dry electrode is in black. Successive potentials are applied: 1.0 (blue), 2.0 (dark green), 1.0 (cyan) and 2.0 V/RHE (light green). In the red frame is a zoom between 7719 and 7721 eV.

3. XAS at the Co L-edge

The K-edge of transition metals describes the $1s \rightarrow 4p$ transition. The oxidation of the transition metal is then mostly observed by the stabilization of the $1s$ states that increases the energy of the $1s \rightarrow 4p$ transition. More accurate and sensitive information on the oxidation state can be obtained by directly probing the $3d$ valence band of the transition metal. The L_2 and L_3 edges of transition metal describe the $2p \rightarrow 3d$ transition and the associated spin-orbit coupling ($J=1/2$ for L_2 and $J=3/2$ for L_3). The occupancy of the transition metal $3d$ states is obtained by comparing the intensities of the L_2 and L_3 edges. XAS at the Co L-edge has been performed on the LUCIA beamline, where spectra can be collected from two detectors: a fluorescence yield detector and a total electron yield current collector, which measures the photoelectrons created by the absorbed X-rays (Figure IV - 8). *Ex situ* experiments have been conducted. For these experiments, the samples were pressed as pellets ($\varnothing = 8$ mm) and contacted to a conductive substrate *via* a carbon adhesive or a silver glue.

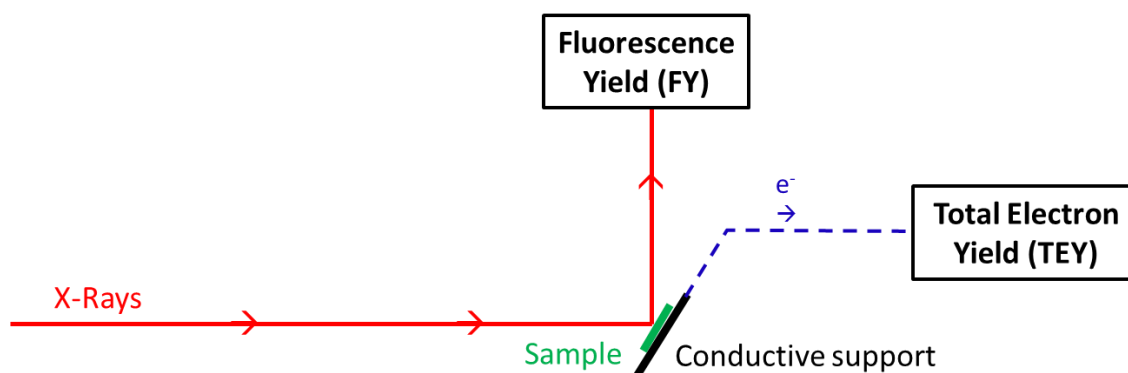


Figure IV - 8 Scheme of LUCIA beamline. The electrode (green) is fixed on a conductive support that measures the total electron yield (TEY). The photons emitted from the fluorescence of the material are collected at the fluorescence detector (FEY).

3.1. *Ex situ* analysis of reference compounds

L-edge X-ray absorption spectra of cobalt-based oxide pellets were first recorded from both detection modes: the fluorescence yield and the total electron yield (Figure IV - 9). Each spectrum is a merge of four to six scans. The baseline is removed from the collected spectra and the spectra are normalized to the intensity of the L_2 -edge peak. The fluorescence yield (FY) spectra are noisier than the total electron yield (TEY) spectra. This is due to the low amount of photons that are collected by the fluorescence detector at 700 eV. The normalized intensity of the L_3 peak of the FY spectra are between 1 and 1.5, while they are between 2.1 and 2.7 for the TEY spectra. Such a difference can be attributed to self-

Chapter IV: An *in situ* XAS and TEM study of Co_3O_4 , a model system for the OER

absorption phenomena that can alter the FY spectra¹⁶⁴. It can also be attributed to the TEY that collects electrons at the surface because of the low mean free path of the electrons (chapter I section 3.1.3.). The L_3 -edge TEY spectrum of reference $\text{Co}^{\text{II}}(\text{OH})_2$ bears one peak at 780 eV whose normalized intensity is 2.7, with a shoulder at 782 eV. The L_3 edge of reference $\text{Co}^{\text{III}}\text{OOH}$ is at 782 eV with a relative intensity of 2.1. The shift to higher energy compared to $\text{Co}^{\text{II}}(\text{OH})_2$ is in agreement with the higher oxidation state of cobalt in $\text{Co}^{\text{III}}\text{OOH}$ ¹⁶⁵. Moreover, the L_3 edge of $\text{Co}^{\text{III}}\text{OOH}$ is less intense than $\text{Co}^{\text{II}}(\text{OH})_2$, in agreement with lower occupancy of 3d levels in $\text{Co}^{\text{III}}\text{OOH}$. The TEY spectrum of $\text{LaCo}^{\text{III}}\text{O}_3$ is identical to the spectrum of $\text{Co}^{\text{III}}\text{OOH}$, which is expected as cobalt has the same electronic structure and octahedral environment in both compounds. The L_3 edge spectrum of $\text{LaMn}_{0.7}\text{Co}_{0.3}\text{O}_3$ displays two peaks: one at 779 eV and another at 782 eV. These peaks suggest the presence of both Co^{II} and Co^{III} in the compound.

Overall, these experiments show that Co L-edge spectra can be collected by fluorescence yield and total electron yield. The spectra given by these two detectors differ by the signal-to-noise ratio and the relative intensity of the peaks. The TEY spectra, which have a higher signal-to-noise ratio, show a shift of L_3 -edge to higher energy and a drop of the normalized intensity of L_3 -edge when the oxidation state of cobalt increases, as expected.

Because of the low energy of the Co L-edge (around 780 eV), XAS experiments must be run under vacuum. Consequently, *in situ* or *operando* experiments at the Co L-edge require a closed and pressure resistant electrochemical cell.

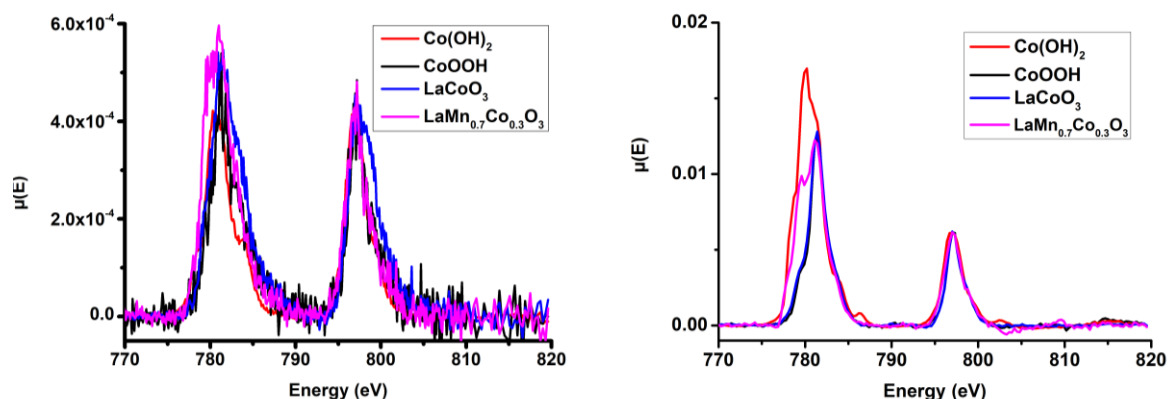


Figure IV - 9 Fluorescence yield (left) and total electron yield (right) spectra of Co L-edge of references $\text{Co}(\text{OH})_2$ (red), CoOOH (black), LaCoO_3 (blue) and $\text{LaMn}_{0.7}\text{Co}_{0.3}\text{O}_3$ (purple).

Chapter IV: An *in situ* XAS and TEM study of Co₃O₄, a model system for the OER

3.2. Co L-edge XAS spectra of Co₃O₄ electrodes before and after OER

The *operando* cell for used for XAS at the Co L-edge is described in the Appendix section 3.2.2. As the setup to record *in situ* XAS on Co L-edge could not be finalized before the end of this PhD work, the Co₃O₄ electrocatalyst deposited on the electrode was analyzed out of the cell before and after the electrochemical reaction. Disconnecting the electrode from the cell facilitates the measurement. We can expose the front of the electrode to the beam and thus improve the signal-to-noise ratio. Even if *operando* XAS on Co L-edge will require the use of an optically transparent Si₃N₄ substrate instead of the glassy carbon one (Appendix section 3.2.2.), we use a glassy carbon substrate for this *ex situ* study because it is much more mechanically resistant compared to Si₃N₄ and provides spectra with a higher signal to noise ratio (Appendix section 4.5.).

An ink of Co₃O₄ is prepared in absolute ethanol (1 mg·mL⁻¹). 10 μL are deposited on a 1 cm² glassy carbon substrate. The “Dry” spectrum is collected once the ink is dried. The substrate is then dipped in the electrolyte. After 30 min, it is removed and the spectrum called “OCV” is recorded. The substrate is then placed in the cell as working electrode and a current density of 10 mA·cm⁻²_{substrate} is applied for two hours. The substrate is then removed and left to dry before the “OER” spectrum is recorded. The experiment is carried out in KOH 0.1 M (Figure IV - 10) and KPi 0.1 M (pH=7) (Figure IV - 11).

In KOH 0.1 M, the FY spectra (Figure IV - 10 left) display L₃ edges with normalized intensities between 1.0 and 1.2. This edge seems less intense on the “OER” spectrum. In TEY (Figure IV - 10 right), the L₃ edge normalized intensities of the Dry, OCV and OER spectra are respectively 1.7, 1.9 and 1.6, suggesting a reduction from the “Dry” state to the “OCV” state, then an oxidation from the “OCV” state to the “OER” state. Comparable results to the ones measured on the Co-K edge are then observed regarding the reminiscent oxidation of the material after OER.

In KPi 0.1 M, the FY spectra (Figure IV - 11 left) display L₃ edges whose relative intensities are all 1.1. In the TEY, the L₃ edge relative intensities of the Dry, OC and OER spectra are respectively 1.7, 1.6 and 1.9, suggesting that cobalt is reduced after OER, which is contradictory with our observations on Co K-edge. Such a difference can be attributed to the difference of environment of the electrode during spectrum recording. The Co K-edge spectrum was acquired *in situ*, where a potential of 1.0 V/RHE was applied. The Co L-edge spectrum is recorded on the electrode after being removed from the cell and dried. The

Chapter IV: An *in situ* XAS and TEM study of Co_3O_4 , a model system for the OER

electrocatalyst may have reduced during the drying or under the vacuum it was exposed during the XAS collection¹⁴³.

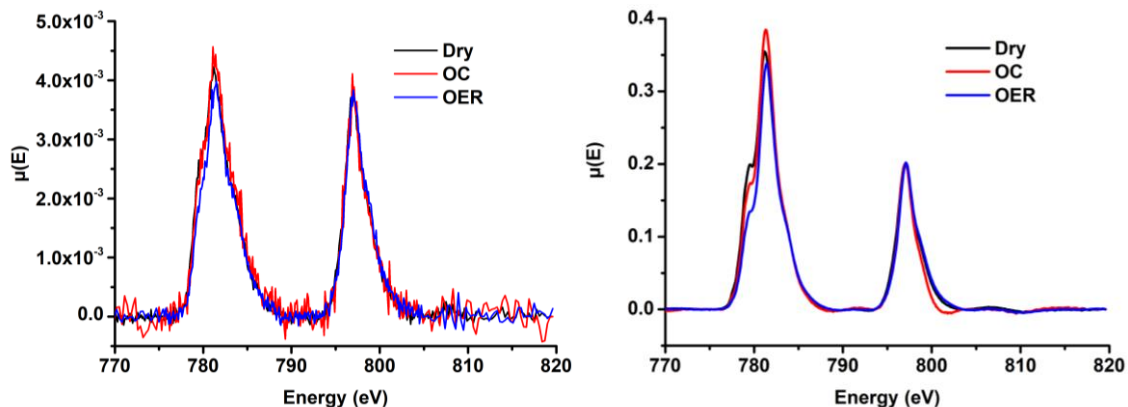


Figure IV - 10 Fluorescence yield (left) and total electron yield (right) spectra of Co L-edge of Co_3O_4 nanoparticles deposited on a glassy carbon (black), after 30 min of immersion in KOH 0.1 M (red), after 2 h at a current density of $10 \text{ mA}\cdot\text{cm}^{-2}_{\text{substrate}}$ in KOH 0.1 M (blue).

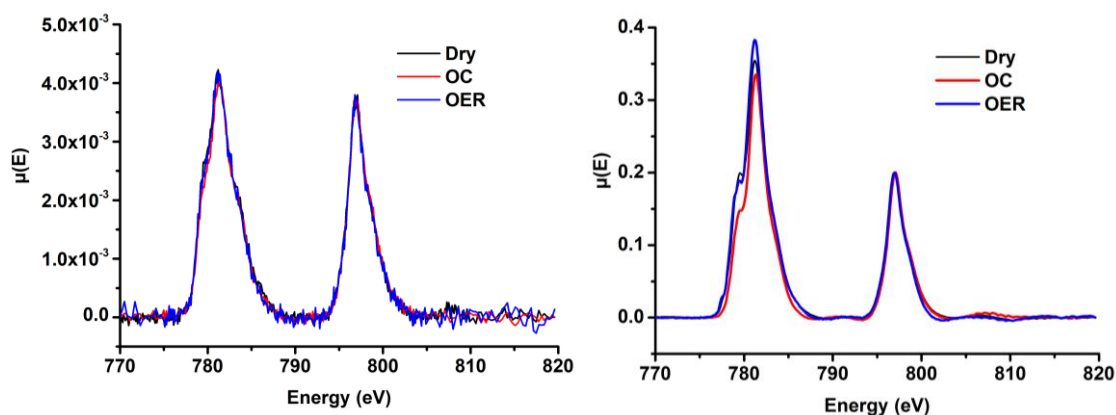


Figure IV - 11 Fluorescence yield (left) and total electron yield (right) spectra of Co L-edge of Co_3O_4 nanoparticles deposited on a glassy carbon (black), after 30 min immersed in KPi 0.1 M (red), after 2 h under at a current density of $10 \text{ mA}\cdot\text{cm}^{-2}_{\text{substrate}}$ in KPi 0.1 M (blue).

Chapter IV: An *in situ* XAS and TEM study of Co₃O₄, a model system for the OER

Overall, X-ray absorption spectroscopy at the transition metal L-edge provides information exclusively on the electronic environment of the metal through the edge energies and L₂ and L₃ relative intensities. However, the signal-to-noise ratio of the acquired spectrum is detector dependent. Even if the total electron yield detector provides the most reliable spectrum, it cannot be used on an *operando* electrochemical setup. The TEY detector collects the electrons emitted from the sample as a result of X-ray absorption. However, during a chronoamperometry measurement, the current is governed by the applied potential. Consequently, only the fluorescence yield detector is useable in conditions close to the *in situ* experiments, but at the cost of long acquisition times. The analysis of *post mortem* electrodes confirms cobalt partial oxidation in alkaline electrolyte, but suggests cobalt reduction in neutral electrolyte, which is in contradiction with our observations on *operando* XAS on the Co K-edge (Figure IV - 7).

4. *In situ* TEM experiment

In order to assess morphological and structural changes, the Co₃O₄ nanoparticles were then studied by transmission electron microscopy *ex situ* and *in situ*. This study, led by Ovidiu Ersen and Nathaly Ortiz from IPCMS, has been published in a dedicated article⁸¹. The particles were analyzed by TEM through a commercially available *in situ* electrochemical TEM cell composed of a working electrode made of glassy carbon (Figure IV - 12). The OER electrocatalytic activity was studied in KOH 0.1 M and KPi 0.1 M (pH=7), by cyclic voltammetry and chronopotentiometry⁸¹. Nanoparticles amorphization was observed and proved to be irreversible after two hours under a current of 10 mA·cm⁻²_{substrate}. An electron energy loss (EEL) spectrum recorded *post mortem* after the electrocatalyst was removed from the electrolyte after chronopotentiometry in KOH 0.1 M indicates significant cobalt reduction (Figure IV - 13). Such observations are different from those obtained through XAS at the K-edge but they are in accord with the results from XAS at the L-edge. Such a discrepancy still requires additional efforts to be understood. We have therefore performed *ex situ* and *in situ* XAS experiments using the TEM electrochemical electrodes or cell to understand this behavior.

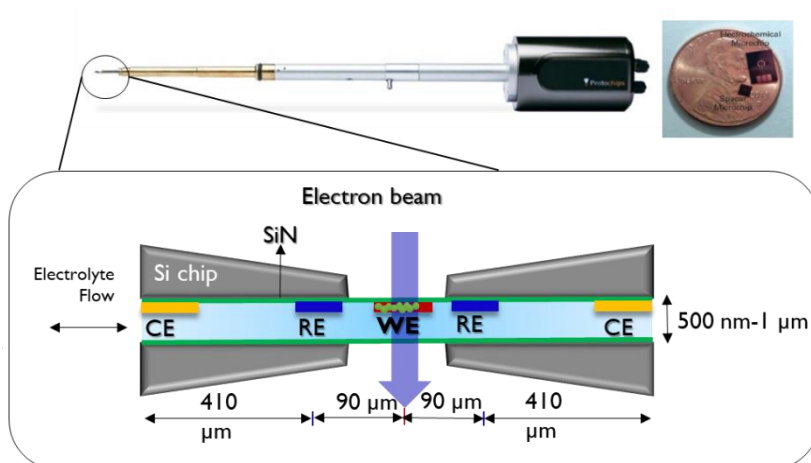


Figure IV - 12 Top left: image of the *in situ* TEM sample holder. Top right: image of the electrochemical microchip on a 1 cent coin for scale. Bottom: side view scheme of the electrochemical *in situ* TEM cell. The working electrode (WE) is glassy carbon. Reference (RE) and counter electrodes (CE) are made of platinum.

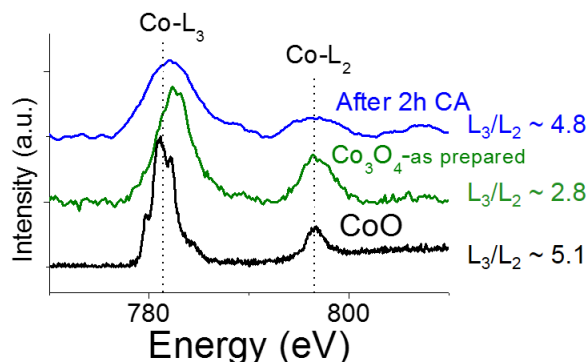


Figure IV - 13 Co L-edge EEL spectra of CoO (black), Co_3O_4 as prepared (green) and after 2h of chronopotentiometry measurements (blue) at 10 mA cm^{-2} substrate in aqueous 0.1 M KOH (Post-mortem). Reproduced from Ortiz Peña et al., ACS Nano (2019)⁸¹

4.1. Post mortem Co K-edge XAS spectra of Co_3O_4 in the TEM electrochemical cell

First, an XAS spectrum at the Co K-edge has been collected on dry Co_3O_4 nanoparticles still in the TEM electrochemical cell after OER electrocatalysis (2 h at $10 \text{ mA} \cdot \text{cm}^{-2}$ substrate in KOH 0.1 M). We have selected these conditions corresponding to a reduced cobalt state according to EELS. The spectra are collected on two areas of the chip (Figure IV - 14, left). The first spectrum (*post mortem*) is taken on nanoparticles localized on the glassy carbon electrode that were active during OER. The second spectrum (OCV) is taken on nanoparticles that are far from the working electrode, and should not have been affected by any electrochemical reaction. This set of data is considered as a control sample. The spectra are collected on the LUCIA beamline by TEY (Figure IV - 14, right). The global shape of both spectra corresponds to the one expected for Co_3O_4 (see spectra above). Yet the

Chapter IV: An *in situ* XAS and TEM study of Co_3O_4 , a model system for the OER

half-edge jump for the OCV and *post mortem* spectra are respectively 7720.0 and 7719.4 eV, thus indicating that the nanoparticles localized on the electrode (*post mortem*) are more reduced than the nanoparticles far from the electrode. This result supports the observations made by EELS.

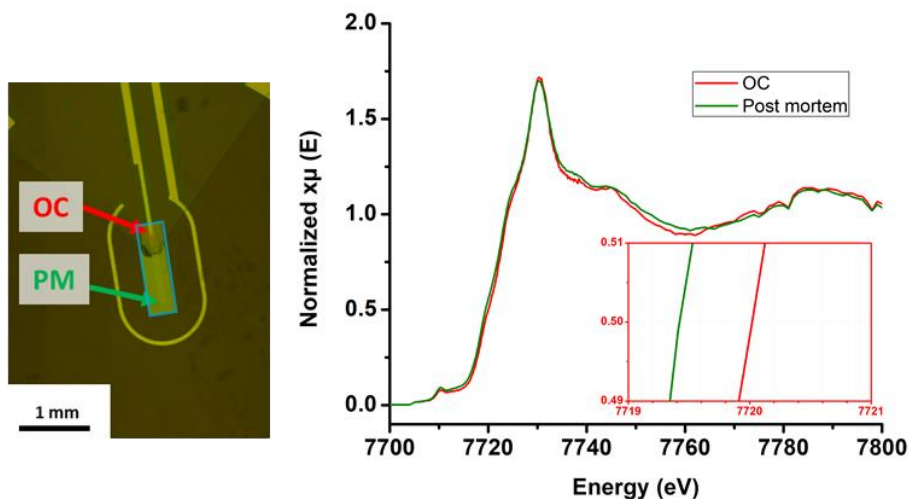


Figure IV - 14 Co K-edge XAS of the electrochemical chip after the *in situ* TEM OER experiment. Left: Top view image of the *in situ* electrochemical TEM cell. The window of the cell is framed in blue. The location where the open-circuit (OC) and post-mortem (PM) spectra are taken are arrowed in red and green respectively. Right: XANES of the two locations on Co K-edge. OC is in red. Post-mortem is in green. In the red frame is a zoom between 7719 and 7721 eV.

Both post mortem K-edge XAS and EELS show the reduction of Co_3O_4 after 2 hours under OER conditions in 0.1M KOH followed by exposure to vacuum in the TEM electrochemical cell. The reduction of cobalt in the TEM cell is therefore confirmed. This reduction comes either from the exposure of the cell to vacuum during the EELS analysis¹⁴³ or to the electron beam irradiation of the TEM.

4.2. *In situ* Co K-edge XAS spectra of Co_3O_4 in the TEM electrochemical cell

During *in situ* TEM, the cell is exposed to electron beam irradiation⁸¹, that can damage the sample. Likewise, compounds can be damaged by synchrotron X-ray radiation during XAS experiments. To evaluate the extent of these damages, we have attempted recording *in situ* Co K-edge XAS spectra of the electrocatalyst inside the TEM electrochemical cell. The experiment was performed at the SAMBA beamline (Figure IV - 15). The Co_3O_4 nanoparticles were deposited on the chip from an ink composed of nanoparticles dispersed in absolute ethanol ($1 \text{ mg}\cdot\text{mL}^{-1}$) following the same procedure employed for the *in situ* TEM experiment⁸¹. Because of the small size of the window of the

Chapter IV: An *in situ* XAS and TEM study of Co_3O_4 , a model system for the OER

TEM cell ($400 \times 50 \mu\text{m}$), the beam is reduced to a minimum size of $300 \times 200 \mu\text{m}$ (Figure IV - 16, left). The spectrum displayed on Figure IV - 16, right is obtained by merging 13 scans collected while the nanoparticles are still dry and not in contact with the electrolyte. The total acquisition time is 2 h. It is compared to the spectrum of Co_3O_4 nanoparticles deposited alone on a glassy carbon plate and used as working electrode in the conventional cell for *in situ* XAS (Figure IV - 16, right). The overall shapes of the two spectra are the same. However, the signal-to-noise ratio of the spectrum from the TEM cell is too low for more in depth analysis. This ratio could be improved by increasing the photon flux, which has been dramatically diminished with the reduction of the beam size.

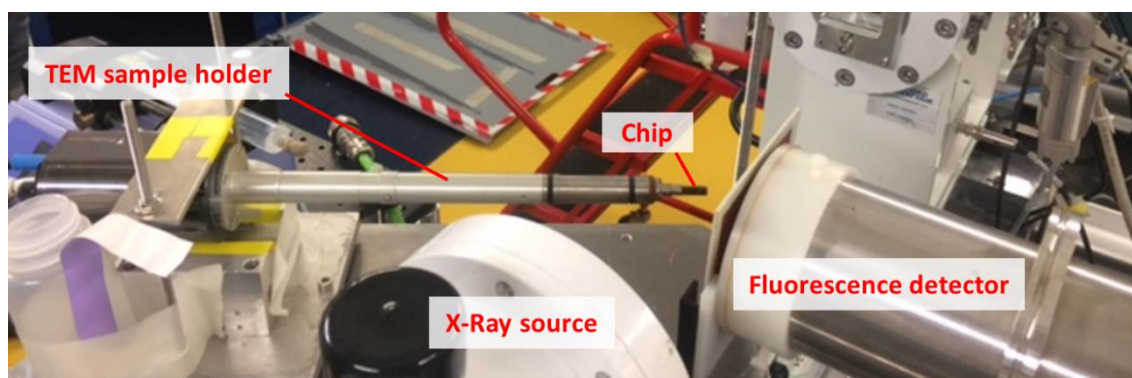


Figure IV - 15 Image of the setup of XAS on the TEM electrochemical chip/cell on the SAMBA beamline.

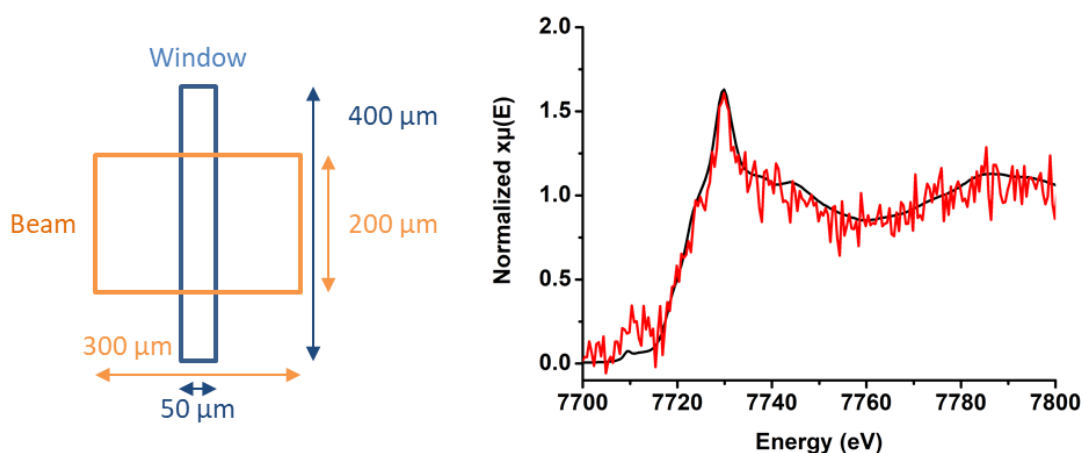


Figure IV - 16 Left: scheme of the size of the beam (in orange) and the window of the chip (in blue). Right: Co K-edge XANES of Co_3O_4 nanoparticles in XAS (black) and TEM (red) electrochemical cells at the dry state.

In situ TEM observation of Co_3O_4 electrocatalysts under OER conditions demonstrated irreversible nanoparticles amorphization⁸¹ along with unexpected cobalt reduction, especially in alkaline medium. The oxidation state of the materials on the *post*

Chapter IV: An *in situ* XAS and TEM study of Co₃O₄, a model system for the OER

mortem TEM electrochemical cell is confirmed by EELS and XAS at the Co K-edge. XAS measurement on a TEM chip is considered to evaluate the role of electrochemical setup on the evolution of the cobalt oxidation state. Even though a spectrum of Co₃O₄ is recorded, the setup needs improvement in terms of signal-to-noise ratio and rate of acquisition in order to obtain useful data from prospective *in situ* measurements.

5. Discussion

5.1. In situ techniques

X-ray absorption spectroscopy at the Co L-edge and transmission electron microscopy are techniques that use short length photons and electrons and therefore require a vacuum environment. Electrochemical cells have been designed separately for these techniques to carry out *in situ/operando* experiments. Their small size requires adapted settings to circulate the electrolyte and the species on the electrodes¹⁶⁶. Optical transparency becomes a determining criterion for the choice of the components that are placed on the path of the beam, especially the working electrode. Following the aim to reduce the path of the beam through the system and to detect by fluorescence, a cell whose working electrode is in a back scattering geometry is used for L-edge XAS.

In this chapter, the XAS spectra were collected by two detection modes: fluorescence yield and total electron yield. Even if the spectra collected from the TEY are of high quality, this detection mode is not adapted to electrochemical experiment because it measures the variation of the electron current, which is a fixed parameter during electrocatalysis. Consequently, the FY is the only detection mode useable during an *in situ* electrochemical experiment. However, the signal to noise ratio in FY mode is very low and self-absorption of the transition metal alters the shape of the L-edges, preventing them to be directly interpreted by comparing the intensities of L₂ and L₃ edges. More advanced techniques such as partial fluorescence yield (PFY) or inverse partial fluorescence yield (IPFY) could overcome the self-absorption phenomenon⁵⁰.

The oxidation state of a transition metal is usually calculated from the ratio of the integrated intensities of L₃/L₂⁴⁷. However, our study is limited to a quick qualitative comparison of the two edges because of the low quality of the spectra and/or the small differences between the compared spectra.

Chapter IV: An *in situ* XAS and TEM study of Co₃O₄, a model system for the OER

An XAS spectrum of Co₃O₄ was acquired at the Co K-edge in the environmental TEM cell. However, even after two hours of scan collection, the quality of the spectrum is not high enough to extract any accurate information on the oxidation state. The settings of this experiment need more optimization, especially on the beam size and the intensity of the beam. Still, this proof of concept is promising to extend the coupling of TEM and XAS to the *operando* analysis of electrocatalysts¹⁶⁷.

5.2. Insights on Co₃O₄ behavior during OER

All the employed techniques confirm the oxidation of cobalt during OER, although the changes are surprisingly weak. The shift of energy at half-edge jump at the Co K-edge between the spectra of the OCV and the active state is between 0.1 and 0.2 eV, which is the same value as the shift that is observed in the previous chapter with La_{0.75}Sr_{0.25}CoO₃ in OER, even though the perovskite contains cobalt whose oxidation state is already high (+III/+IV), while cobalt in Co₃O₄ is expected to oxidize from Co^{+II} to Co^{+III} and eventually Co^{+IV}⁶⁰.

The oxidation state of the electrocatalyst after electrocatalysis and after drying is unclear. In alkaline medium, the oxidation of cobalt is supported by XAS at the Co L-edge, while the Co₃O₄ nanoparticles are reduced after the same experiment inside the TEM cell. In neutral medium, the analysis of the Co K-edge shows an oxidation of Co₃O₄ at the first OCV and a partial oxidation is kept after OER going back to the OCV, while the Co L-edge spectra suggest a reduction. We can then wonder if retrieving the electrode from the electrolyte alters the electrode. Following this question, we summarize the previous observations on cobalt redox evolution during OER in Figure IV - 17 and Figure IV - 18 where, after OER, the states before the electrolyte removal (OCV back) and after the electrolyte removal (P-M) are discriminated. While we do not have enough data to conclude on the evolution of Co₃O₄ in KPi, we still have contradictory results in KOH: XAS at the Co L-edge suggests a slight cobalt oxidation between dry and *post mortem*, but TEM shows cobalt reduction between the same states and it is supported by XAS at the Co K-edge in the TEM cell. These inconclusive results raise the question of the transferability between the *in situ* cells for XAS and TEM. The design of an electrochemical cell adapted for XAS and TEM should ease the concordance of the results from both *operando* techniques.

Chapter IV: An *in situ* XAS and TEM study of Co_3O_4 , a model system for the OER

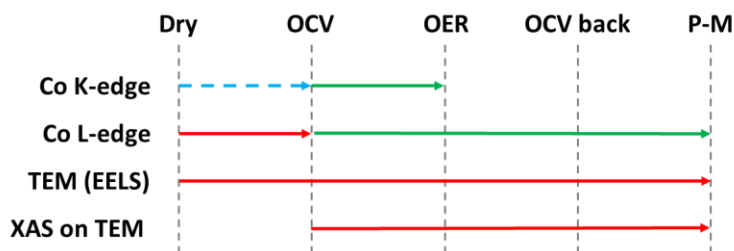


Figure IV - 17 Summary of the observations on cobalt redox evolution during OER in KOH 0.1 M through the different techniques. The color of the arrow indicates the evolution between the two considered states: oxidation (in green), reduction (in red) and unchanged (in blue). A dotted arrow means that the change can be considered negligible. OCV: Open Circuit Voltage. P-M: Post-mortem.

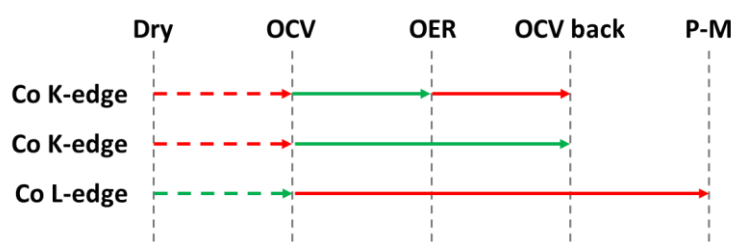


Figure IV - 18 Summary of the observations on cobalt redox evolution during OER in KPi 0.1 M ($\text{pH} = 7$) through the different techniques. The color of the arrow indicates the evolution between the two considered states: oxidation (in green), reduction (in red). A dotted arrow means that the change can be considered negligible. OCV: Open Circuit Voltage. P-M: Post-mortem. The observations on the Co K-edge experiment are divided in two lines for a better readability.

6. Conclusion

In this chapter, we study the evolution of cobalt oxidation state of Co_3O_4 during OER reaction by *operando* XAS at the Co K-edge and *ex situ* XAS at the Co L-edge and *operando* TEM.

While the setup for *in situ* XAS on Co L-edge is still under development, the oxidation of cobalt under OER conditions is observed by *ex situ* electrochemical measurement, *operando* TEM and *operando* XAS.

Post mortem analysis do not allow to draw any clear conclusion on the evolution of cobalt oxidation state after electrocatalysis, compared to its oxidation state before electrocatalysis. In neutral medium, XAS at the Co K-edge sustains the oxidation of cobalt, whereas XAS on Co L-edge suggests cobalt reduction. In alkaline medium, XAS on Co L-

Chapter IV: An *in situ* XAS and TEM study of Co₃O₄, a model system for the OER

edge indicates cobalt oxidation and EELS indicates cobalt reduction. XAS at the Co K-edge of the *post mortem* TEM electrochemical cell confirms the EELS observation that cobalt reduces between before and after the electrocatalysis. We then tried to reproduce an *in situ* XAS experiment whose setup is as close as possible to the setup employed during the *in situ* TEM electrochemical experiment. The settings still have to be optimized. The inconclusive results on the becoming of the electrocatalyst after electrocatalysis are based on small variations of the oxidation state. By differentiating the resting state inside the electrolyte after the electrocatalysis from the *post mortem* state when the electrode is dried, we propose two non-exclusive hypotheses to explain these results. First, the vacuum environment to which the electrode is exposed during the *post mortem* analysis by EELS and XAS on the L-edge triggers a reduction of cobalt (III). Second, the electron beam of the TEM damages the nanoparticles and reduces cobalt.

These diverging results show the necessity to couple multiple *in situ* techniques in order to describe the electrocatalyst the most faithfully and to watch over any phenomenon that may interfere with the electrochemical system. Transmission electron microscopy and X-ray absorption spectroscopy at low energy are run under particularly drastic conditions such as low pressure environment and on a small scale that require specific adaptations of the whole electrochemical experiment. Understanding how such changes influence the electrocatalytic system is an indispensable prerequisite for extracting relevant information from *in situ* techniques.

General conclusion

General conclusion

This thesis was focused on the study of the electrocatalytic activity of nickel borides (in HER and OER), manganite cobaltite perovskites (in OER and ORR) and cobalt oxide spinels (in OER) by *operando* X-ray absorption spectroscopies. Through this investigation, this work contributes to both the understanding of the electrocatalytic activity of the studied materials and a reflection on what information *operando* XAS can provide to the understanding of such electrocatalysts.

The nickel borides are compounds whose EXAFS are complex to analyze because of their complex and unique structures, yielding excessive amounts of short interatomic distances. Even though strong approximations were done, the obtained results are supported by two methods: linear combination fitting and EXAFS fitting. The electroactive phase for Ni₃B is the same as the one observed in metallic Ni: Ni^{III}OOH during the OER, and the non-oxidized phase in HER. However, we demonstrate that Ni₃B contains a lower amount of active phase in OER, while it is also more active than metal Ni. By using a core-shell model, we attribute the high activity of Ni₃B to its resistance to oxidation, which allows the nanoparticles to form a thin electroactive NiOOH shell at the interface with the electrolyte, while keeping a highly conductive Ni₃B core. Consequently, we postulate that the presence of boron limits the nickel oxidation. Nevertheless, EXAFS fitting and LCF do not give concluding results on the study of Ni₄B₃, indicating that our model is not suitable to describe the electroactivity of this compound. In this case, the formation of an additional phase such as a nickel borate has been suggested, although further investigation is required to confirm this hypothesis.

To investigate nickel boride nanoparticles, we have used data treatment methods that are commonly used in the characterization of pristine compound, but have been scarcely employed to follow electrocatalysts during *operando* XAS experiments. We use linear combination fitting to estimate the nickel oxide content inside the nickel (boride) nanoparticles. Such a quantification has been rarely done previously in *operando* experiments⁶⁴, as most of them merely follow the oxidation state of the transition metal by the shift of the half-edge jump. By coupling linear combination fitting and EXAFS fitting, we were able to provide a quantitative estimation of the thickness of the nickel oxide layer that is formed around the nickel boride nanoparticles during electrocatalysis.

General conclusion

Manganite cobaltite perovskites have been studied as they are expected to display a bifunctional activity due to the presence of both Mn and Co, which have been demonstrated to be active transition metals in ORR and OER, respectively. Yet the non-linearity of the relationship between the ORR/OER activity of the perovskites and their Mn/Co content raises questions about a synergy effect between these two transition metals. While *operando* XAS show that in single B-site perovskites such as LaMnO_3 or $\text{La}_{0.67}\text{Sr}_{0.33}\text{CoO}_3$ the oxidation state of the transition metal increases during OER and decreases during ORR, the oxidation states of these same transition metals are remarkably stable in the mixed B-site perovskites. The energy at half-edge jump indicates that the mixed perovskites contain Mn^{4+} and Co^{2+} , suggesting that the predominant roles of Mn and Co in ORR and OER are switched, with Mn^{4+} being the active site of OER and Co^{2+} the active site for ORR.

Co_3O_4 spinel is a model OER electrocatalyst that is reported to reversibly oxidize during OER. While we observe the oxidation of Co_3O_4 by XAS, the measurements are not precise enough to enable a clear measurement of the oxidation state of Co during electrocatalysis, as the results from different techniques are either not concluding (Co L-edge) or contradictory (Co K-edge and TEM). We also observe a divergence between the behaviors observed by probing the Co L-edge and the Co-K-edge. Such divergence may originate from the difference between the resting state after electrocatalysis, which is a state that is still inside the electrolyte (i.e. *operando* XAS on Co K-edge), and the *post mortem* state, where the material is completely removed from the electrochemical cell and may have been analyzed several hours to several days after the experiment (i.e. XAS on Co L-edge and EELS). We also question the influence of the environment of the analysis on the sample, as the vacuum environment where Co L-edge XAS and EELS are collected can reduce the transition metals in the nanoparticles. At the moment, the discording results indicate that we do not look at the same state of the electrocatalyst through these techniques of analysis. We can even wonder if we follow the same electrocatalytic mechanism during all these electrochemical experiments. For instance, does the X-ray beam or the electron beam have any impact on the electrocatalysis? This leads to the question of which of these techniques reproduces the most faithfully the electrocatalytic mechanism that occurs *ex situ*.

Operando XAS also provides access to data treatment methods that are not relevant for the XAS characterization of *ex situ* materials, bringing then new insights on the investigation of electrocatalysts. Firstly, the time monitoring of XAS experiments highlights the inertia of the electrochemical response of the $\text{La}_{0.67}\text{Sr}_{0.33}\text{MnO}_3$ electrocatalyst to the

General conclusion

applied potential as the oxidation state of the manganese reaches a steady state after more than 15 min. The time monitoring has also brought to light the progressive reduction of the transition metal by the X-ray beam on the dry electrodes specifically, due to the simultaneous presence of a carbon rich environment and a heating source. Secondly, the comparison of the XAS spectra from different samples is usually assured by the normalization of the XAS, which corrects the variation of concentration from each sample as well as the flux of the beam. However, during an *operando* experiment, we analyze the same area of the material on the same beamline with a steady flux. Consequently, by bypassing the normalization of the spectra, we could get information on the evolution of the concentration of the electrocatalyst during the electrocatalysis, and therefore its stability. An example of this analysis is described in Appendix section 4.4.

All these observations highlight a weakness of the current development of *operando* techniques: the process of adaptation has focused on dealing with the anticipated obstacles for the analysis of an electrochemical experiment (liquid environment, application of a potential...). However, aside from the recording of *in situ* cyclic voltammograms, the reproducibility of the electrocatalytic process during an *operando* analysis is rarely questioned. In this thesis, we have proved that the electrocatalyst often evolves during electrocatalysis. But the material can also be altered by unexpected parameters such as the preparation of the electrode, the beam effect, or the duration of the experiment, despite the control cyclic voltammograms still ensuring a regular electrocatalytic activity. The verification of the agreement of the *operando* experiments with the *ex situ* electrochemical experiments is necessary but not trivial, of course. Cross checking the results between several *operando* techniques, as we have done with TEM and XAS, is a safeguard to hasty and mistaken conclusions.

Appendix

Appendix

Appendix

1. Methods

1.1. Material synthesis

1.1.1. Synthesis of perovskites in molten salts

1.1.1.1. *Manganite cobaltite perovskites*

The manganite perovskites are synthesized from the nitrate precursors $\text{La}(\text{NO}_3)_3 \cdot 6\text{H}_2\text{O}$ (Sigma-Aldrich, > 99 %), $\text{Sr}(\text{NO}_3)_2$ (Aldrich, 99 %), $\text{Mn}(\text{NO}_3)_2 \cdot 4\text{H}_2\text{O}$ (Aldrich, 98 %), $\text{Co}(\text{NO}_3)_2 \cdot 6\text{H}_2\text{O}$ (Alfa Aesar, > 98 %) and KNO_3 (Sigma-Aldrich, > 99%) whose weights (in grams) are summed up in the Appendix Table 1. The solid mixture is coarsely grinded with a ball miller (20 Hz, 2 min) and dried in a vacuum oven (60 °C) for at least 24 hours. 2.5 g of the powder is put into an alumina crucible and placed for one hour in a muffle furnace under air and preheated at 600 °C. The crucible is then removed from the oven and cooled down at room temperature, under air. The recovered black solid is dissolved in deionized water (c.a. 60 mL). The dispersion is centrifuged (20 000 rpm) then the transparent supernatant is removed. The remaining black solid is redispersed in deionized water and washed by ten centrifugation-redispersion cycles monitored by measuring the supernatant conductance which must reach the value for deionized water (20 $\mu\text{S cm}^{-1}$). Nanoparticles are finally dried under vacuum oven at 60 °C overnight.

	La(NO₃)₃	Sr(NO₃)₂	Mn(NO₃)₂	Co(NO₃)₂	KNO₃
LaMnO₃	2.77		2.04		7.22
La_{0.67}Sr_{0.33}MnO₃	1.67	0.44	1.65		6.50
LaMn_{0.7}Co_{0.3}O₃	3.70		1.60	0.60	8.60
LaMn_{0.6}Co_{0.4}O₃	3.50		1.35	0.75	8.10

Appendix Table 1 Synthesis of manganite cobaltite perovskites. Weight of the precursors (in grams) for each perovskite.

1.1.1.2. *Cobaltite perovskites*

The cobaltite perovskites are synthesized from the nitrate precursors $\text{La}(\text{NO}_3)_3 \cdot 6\text{H}_2\text{O}$ (Sigma-Aldrich, > 99 %, 2.04 g), $\text{Sr}(\text{NO}_3)_2$ (Aldrich, 99 %, 0.50 g), $\text{Co}(\text{NO}_3)_2 \cdot 6\text{H}_2\text{O}$ (Alfa Aesar, > 98 %, 2.00 g) and NaNO_2 (Sigma-Aldrich, > 99%, 4.90 g). The solid mixture is coarsely grinded with a ball miller (20 Hz, 2 min) and dried in a vacuum oven (60 °C) for 3 hours and grinded again with a mortar. It is then dried again in the vacuum oven for more than 24 hours to avoid extra-hydration of precursors. 2.5 g of the powder is put into an

Appendix

alumina crucible and placed in a muffle furnace under air and preheated at 700 °C for one hour. The crucible is then removed from the oven and cooled down at room temperature. The recovered black solid is dissolved in deionized water (c.a. 100 mL). The dispersion is centrifuged (20 000 rpm) then the transparent supernatant is removed. The remaining black powder is redispersed in deionized water, washed and dried as the manganese perovskites described above.

The synthesis parameters for the LSCO perovskite samples presented in this thesis are summarized in the tables below.

Theoretical molar ratio La/Sr/Co	Crucible	Temperature (°C)	Heating time (min)
0.60/0.33/1	Alumina	600	60
		700	
		800	
	Porcelain	600	
		700	
		800	
	Boron Nitride	800	

Appendix Table 2 Parameters of the syntheses of $La_{1-x}Sr_xCoO_3$ carried out in KNO_3 molten salts with a Co/ KNO_3 molar ratio of 1/10.

Theoretical molar ratio La/Sr/Co	Na₂O molar ratio to Co	Temperature (°C)	Heating time (min)
0.60/0.33/1	0	600	60
0.60/0.33/1	0	700	60
0.60/0.33/1	0	800	60
0.60/0.33/1	0	700	30
0.60/0.33/1	3	700	30
0.67/0.36/1	3	700	30

Appendix Table 3 Parameters of the syntheses of $La_{1-x}Sr_xCoO_3$ carried out in $NaNO_2$ molten salts with a Co/ $NaNO_2$ molar ratio of 1/10.

Appendix

1.1.2. Synthesis of spinel nanoparticles by microwave-assisted heating

Cobalt (II) nitrate hexahydrate (Sigma Aldrich, 98%) is dissolved in water ($2 \cdot 10^{-2} \text{ mol} \cdot \text{L}^{-1}$)¹⁶¹ for a total solution volume of ca. 40 mL. The pH is raised above 11.3 with ammonium hydroxide (Carlo Erba, 30 %) and the solution is stirred for an hour. The solution is separated into two glass tubes of 30 mL and then heated by microwave heating in an Anton Paar Monowave 300 oven (850 W power input) to 100 °C for 10 min. The final mixture is cooled down to room temperature. The nanoparticles are washed 5 times with deionized water and dried under vacuum.

1.2. Ex situ electrochemical measurements

1.2.1. Setup preparation

Usual ink: A composite ink is prepared from the electrocatalyst (10 mg), activated acetylene black (Alfa Aesar, 99.9 %, 10 mg) and absolute ethanol (VWR, 10 mL). It is sonicated for 2 hours and Nafion dispersed in ethanol (Sigma Aldrich, 5 % dispersion, 435 μL) is added. The suspension is sonicated again for 30 min. The electrochemical experiment is carried out less than 12 hours after the start of the ink preparation.

Sole nanoparticle ink: It is the same preparation than the classical ink, but without Nafion and activated acetylene black.

The glassy carbon substrate ($\varnothing = 3 \text{ mm}$) is previously polished on a 1 μm paper (Buehler TexMet C, 5 min) and a 0.05 μm paper (Buehler ChemoMet, 5 min). 2 μL of the ink is dropped on the substrate. The deposit is dried for 30 min in air. A few microliter of electrolyte is then dropped on the substrate to wet the electrode. After 30 min, the substrate is installed on the working electrode. The KOH (Alfa Aesar, 85 %) 0.1 M electrolyte is prepared the day of the electrochemical experiment.

The electrochemical measurements are carried out in a plastic beaker to prevent any glass dissolution from a glass beaker in an alkaline medium. The electrolyte is saturated with oxygen by bubbling for 30 min before the beginning of the experiment and all along the measurement during both OER and ORR experiments. The reference electrode is a saturated Ag/AgCl electrode ($E^0 = 0.197 \text{ V/SHE}$). The counter electrode is a platinum wire separated from the electrolyte with a frit. The working electrode is composed of the nanoparticle ink

Appendix

deposited onto the glassy carbon substrate that is placed on a rotating disk electrode (1600 rpm).

1.2.2. Cyclic voltammetry

The cyclic voltammograms are recorded with a scan sweep rate of $10 \text{ mV} \cdot \text{s}^{-1}$ over 5 cycles. For the OER/ORR experiments (LMO, LSCO and LMCO), the cyclic voltammograms are recorded from the OCV to 1.8 V/RHE, then 0.4 V/RHE, then back to OCV. For the OER experiment (Co_3O_4), the cyclic voltammogram is recorded from OCV to 1.8 V/RHE. For the ORR experiments (LMO and LSMO), the cyclic voltammograms are recorded from the OCV to 0.4 V/RHE.

1.3. Techniques of characterization

1.3.1. X-ray diffraction

Powder X-ray diffraction (XRD) was performed on a Bruker D8 advance diffractometer equipped with a Cu K_α source ($K_{\alpha 1} = 1.5406 \text{ \AA}$, $K_{\alpha 2} = 1.5443 \text{ \AA}$) in reflection mode, with an accelerating voltage of 40 kV and a current of 40 mA. The intensity of the diffracted X-rays is measured on a 2θ range between 10° and 80° with a step of 0.06 for a total acquisition time of 30 min. Because of X-ray fluorescence of cobalt, the slit, which is usually fixed at [0.11 V, 0.25 V], is reduced to [0.20 V, 0.25 V].

1.3.2. Transmission electron microscopy

Transmission electron microscopy (TEM) was performed on a FEI 120 kV. The samples are prepared from the evaporation of a drop of a nanoparticle suspended in absolute ethanol onto a copper grid on which a carbon film was previously deposited.

1.3.3. Elemental mapping

Elemental mapping was performed on a JEOL JEM 2100 Plus LaB₆ working at an accelerating voltage of 200 kV.

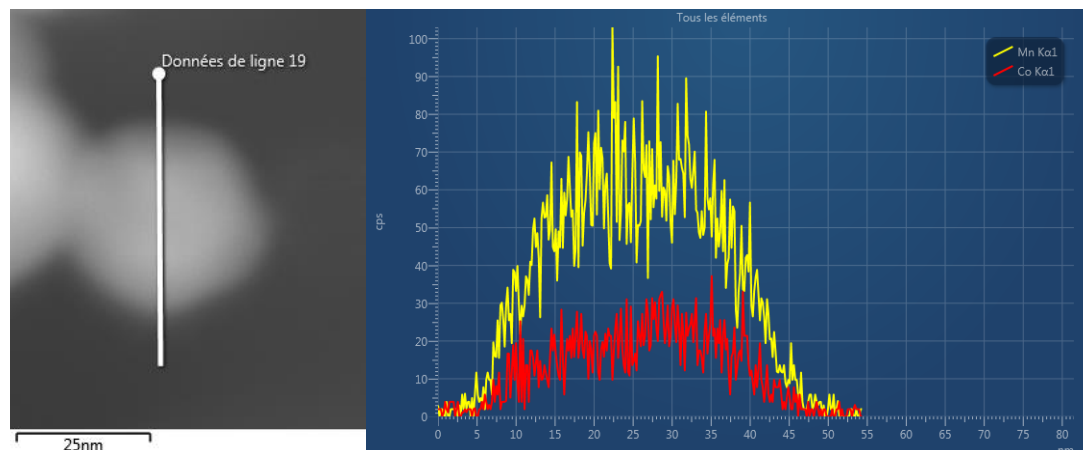
1.3.4. Wavelength-dispersive X-ray fluorescence

The atomic composition was measured by wavelength-dispersive X-ray fluorescence (WDXRF) on a Bruker S8 Tiger spectrometer on pelletized powders.

Appendix

2. Material characterization

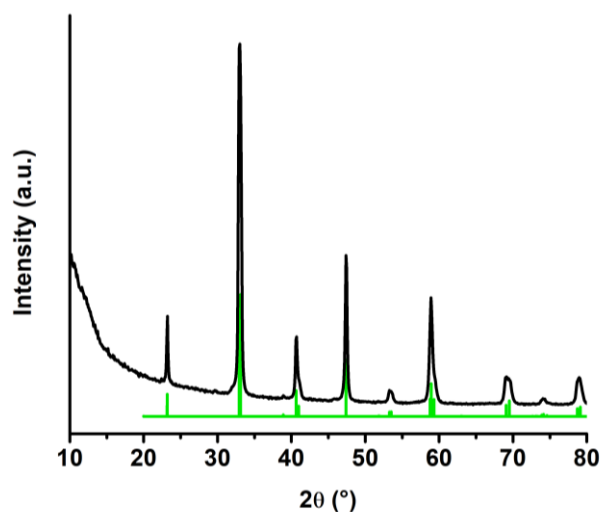
2.1. Elemental distribution inside $\text{LaMn}_{0.70}\text{Co}_{0.30}\text{O}_3$ nanoparticles



Appendix Figure 1 TEM image of LMC030 and Co (in red) and Mn (in yellow) repartition along the white line.

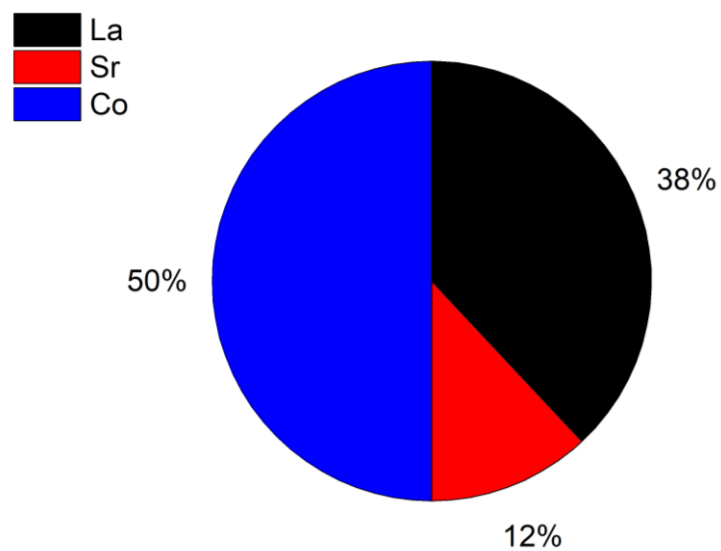
2.2. Characterization of the $\text{La}_{1-x}\text{Sr}_x\text{CoO}_3$ perovskite

The protocol of synthesis is described in Appendix section 1.1.1.2.

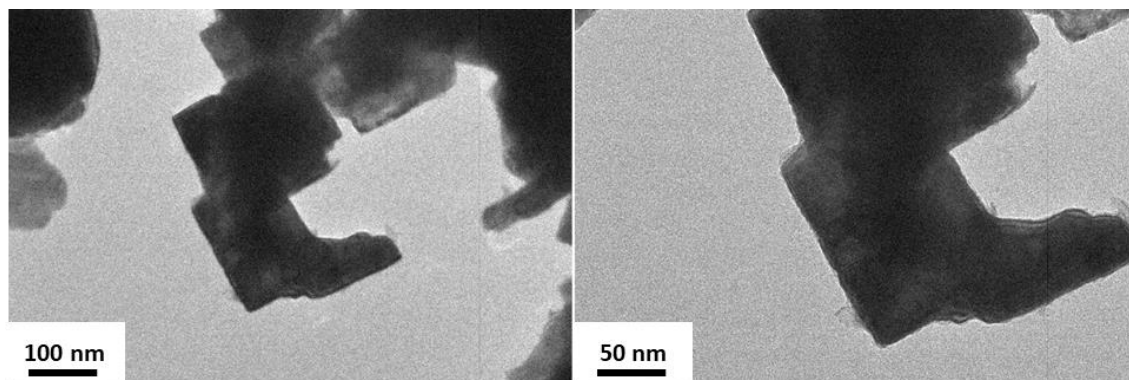


Appendix Figure 2 XRD patterns of $\text{La}_{1-x}\text{Sr}_x\text{CoO}_3$ synthesized at 700 °C in NaNO_2 from La/Sr/Co ratio of 0.60/0.33/1.00. Green peaks account for tabulated $\text{La}_{0.7}\text{Sr}_{0.3}\text{CoO}_3$ (PDF card 04-014-1579).

Appendix



Appendix Figure 3 Elemental composition of the LSCO perovskite determined by WDXRF analysis. The estimated composition of the perovskite is $\text{La}_{0.76}\text{Sr}_{0.24}\text{CoO}_3$.



Appendix Figure 4 Transmission electron microscopy images of $\text{La}_{0.75}\text{Sr}_{0.25}\text{CoO}_3$

Appendix

3. XAS measurements

3.1. Beamline settings

3.1.1. SAMBA beamline

XAS spectra at the Mn, Co and Ni K-edges were collected on the SAMBA beamline at the SOLEIL synchrotron with a Si(220) monochromator with an energy resolution of $\Delta E/E = 6 \times 10^{-5}$. The Ni K-edge spectra were collected between 8200 and 9500 eV with a scan rate of $10 \text{ eV}\cdot\text{s}^{-1}$ and an integration time of 0.5 s per point for a recording time of 3 min per scan. The Co K-edge spectra were collected between 7550 and 8300 eV with a scan rate of $2.5 \text{ eV}\cdot\text{s}^{-1}$ with an integration time of 0.1 s per point for a recording time between 6 and 7 min. The Mn K-edge spectra were collected between 6400 and 7400 eV with a scan rate of $2.5 \text{ eV}\cdot\text{s}^{-1}$ with an integration time of 0.1 s per point for a recording time of 8 min per scan.

3.1.2. B18 beamline

XAS spectra at the Mn and Co K-edges were collected on the B18 beamline at the DIAMOND synchrotron with a Si(111) monochromator with an energy resolution of $\Delta E/E = 1.4 \times 10^{-4}$. The Co K-edge spectra were collected between 7510 and 8560 eV with a scan rate of $3.5 \text{ eV}\cdot\text{s}^{-1}$ and an integration time of 0.07 s per point for a recording time between 6 and 7 min. The Mn K-edge spectra were collected between 6340 and 7390 eV with a scan rate of $3.5 \text{ eV}\cdot\text{s}^{-1}$ with an integration time of 0.07 s per point for a recording time of 5 min per scan.

The security procedure of the beamline specifies that the detector must be removed anytime the analyzed sample (here the experimental setup) is manipulated. Hence, the detector is removed between the collection of the dry and the OCV scans to fill the cell with the electrolyte.

3.1.3. LUCIA beamline

XAS spectra at the Co K- and $L_{2,3}$ -edges were collected on the LUCIA beamline at the SOLEIL synchrotron with a monochromator Si(111) with an energy resolution of $\Delta E/E = 1.4 \times 10^{-4}$ for the K-edge and a Multilayer Grating Monochromator (MGM) for the $L_{2,3}$ -edge.

Appendix

The Co K-edge spectra were collected between 7600 and 8000 eV with a scan rate varying depending on the energy and summarized in Appendix Table 4. The total recording time of a scan is 19-20 min. The Co L_{2,3}-edge spectra were collected between 760 and 820 eV with a scan rate varying depending on the energy and summarized in Appendix Table 5. The total recording time of a scan is 17-18 min.

From (eV)	To (eV)	Step (eV)	Time (sec)
7600	7700	2	1
7700.3	7760	0.3	2
7761	7850	1	1
7852	7800	2	1

Appendix Table 4 Settings for the acquisition of XAS on Co K-edge on LUCIA beamline. Variation of the step size and the integration time as a function of the energy range.

From (eV)	To (eV)	Step (eV)	Time (sec)
760	770	0.3	1
770.1	810	0.1	2
810.3	820	0.3	1

Appendix Table 5 Settings of the acquisition of XAS on Co L_{2,3}-edge on LUCIA beamline. Variation of the step size and the integration time as a function of the energy range.

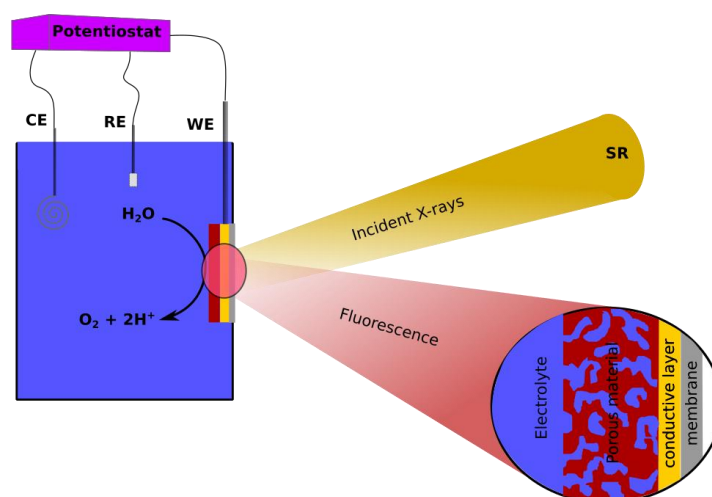
Appendix

3.2. Cell description

3.2.1. In situ cell for K-edge

The *in situ* electrochemical cell for hard X-rays is appropriate for use in fluorescence mode in order to allow a large volume of electrolyte (around 10 mL). A simplified scheme of the cell is displayed on Appendix Figure 5. An image of the experimental setup used on B18 beamline is on Appendix Figure 6. The reference is a saturated calomel electrode (0.244 V/NHE). The counter electrode is a platinum wire in a frit. The working electrode is a glassy carbon plate covered with an electrocatalyst ink. The plate is glued on a hole on the side of the cell so that one side is in contact with the electrolyte, and the other side is directly exposed to the incident X-rays. In this configuration, X-rays are only absorbed by the components of the working electrode, namely the electrocatalyst ink and the glassy carbon plate whose thickness is 60 μm , which is transparent enough for K-edge XAS of transition metals (Appendix Figure 7). The vertical position of the working electrode allows oxygen bubbles that are formed during OER to escape to the surface of the aqueous electrolyte, and thus refresh the species near the electrocatalysts. The cell is large enough to add an oxygen bubbling inlet for ORR/OER experiments. The preparation of the ink containing the electrocatalyst is described in Appendix Section 1.2.1. The ink is dropped onto the glassy carbon plate. Once the ink is dried, the concentration of the electrocatalyst on the plate is not homogeneous. Usually, there are more electrocatalysts deposited on the edges than on the center of the deposit. The beam is centered on an area with a high amount of electrocatalyst and far enough from the edges to ensure that the area corresponds to operating electrocatalysts.

Appendix



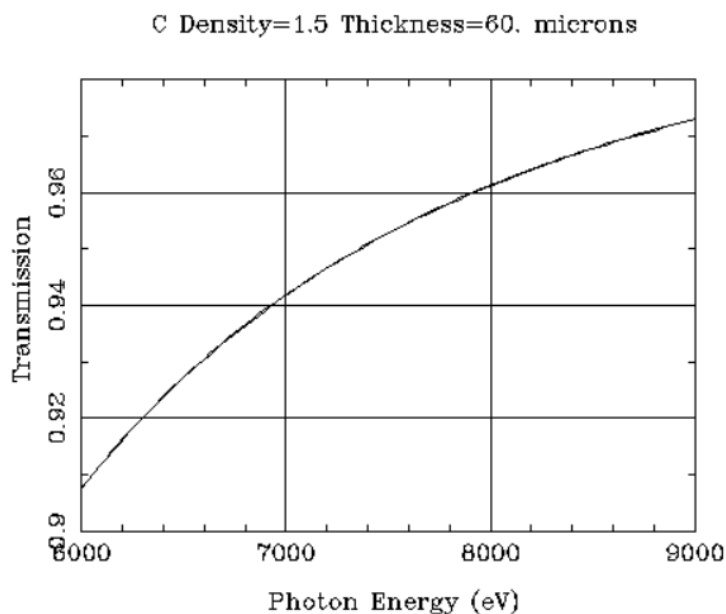
Appendix Figure 5 Simplified scheme of the side view of the in situ electrochemical cell.



Appendix Figure 6 Experimental setup of operando XAS measurement on B18 beamline. Ref is the reference electrode. CE is the counter electrode. WE is the working electrode. O₂ indicates the oxygen bubbling inlet.

Appendix

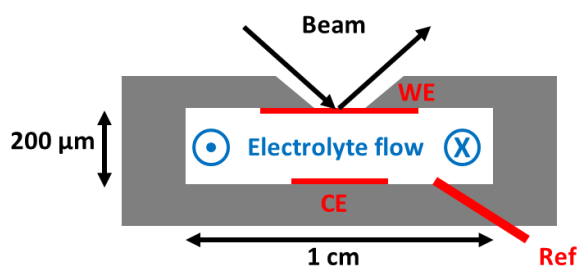
Filter Transmission



Appendix Figure 7 Transmission coefficient of a 60 μm glassy carbon foil between 6000 and 9000 eV.

3.2.2. In situ cell for L-edge

In order to function properly, the electrochemical cell requires several criteria. Because the cobalt L-edge is measured under vacuum, the cell must be resistant to pressure and to the corrosive electrolytes, such as alkaline or acidic aqueous solutions or organic solvents. Moreover, in order to reduce photon loss, the beam path to the material should cross a layer as thin as possible (Appendix Figure 8).

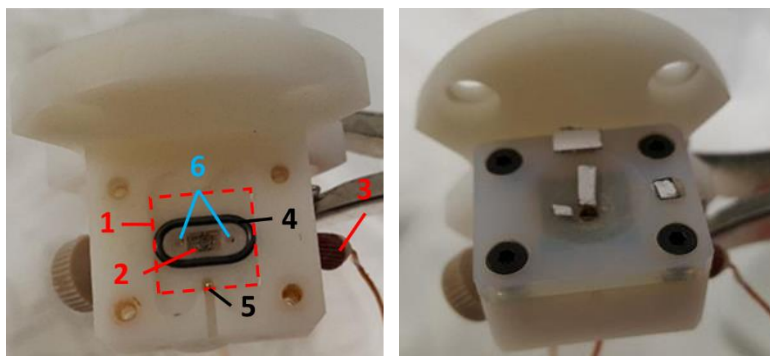


Appendix Figure 8 Side view scheme of the electrochemical cell. Electrodes are in red. Reference electrode is a silver wire. The counter electrode is a platinum plate or platinum foil. The working electrode is a nanoparticle ink deposited on conductive plate (glassy carbon or Si_3N_4).

Appendix

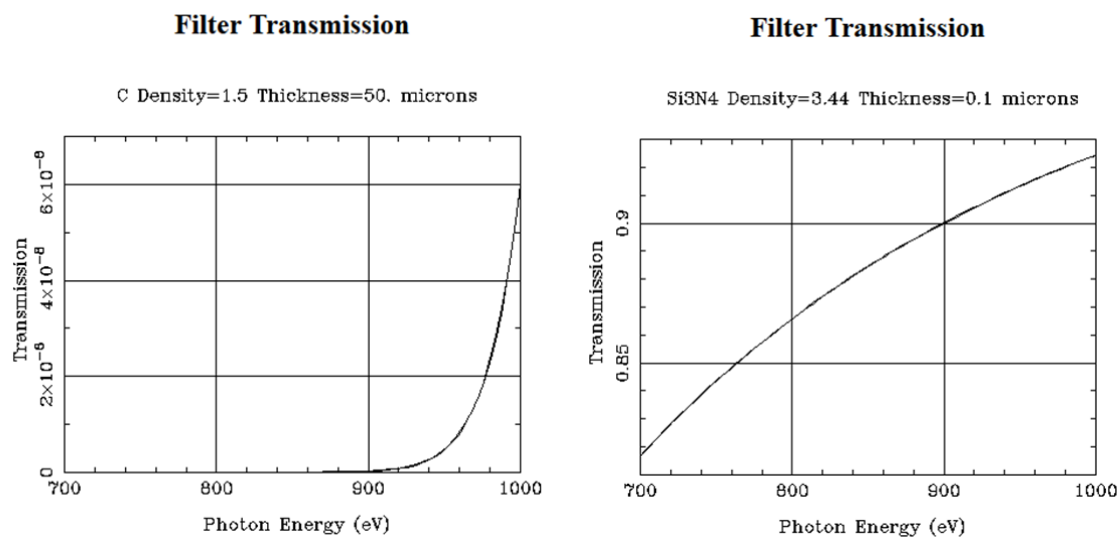
The electrochemical cell is made of PEEK polymer (Appendix Figure 9). It is composed of a 1 cm² working electrode (1) placed in front of a platinum counter electrode (2) with a spacing of 200 μm . The pseudo-reference electrode is a silver wire (3) inserted from the side and in contact with the cell through one of the electrolyte inlet (6). A waterproof rubber O-ring (4) surrounds the counter electrode and the inlets and delimits the electrochemical system in an area of 45 mm². The gold spring (5) connects the working electrode plate to the potentiostat. All in all, the electrochemical reaction occurs in a volume of 9 mm³. In such small volume, oxygen accumulation quickly creates an overpressure. To avoid such pressure build up, the gas is evacuated through the electrolyte circulation (6). The electrode is analyzed in a back scattering geometry, where the beam goes through the electrode to analyze the part that is in contact with the electrolyte. The electrolyte flow is regulated by a peristaltic pump outside the vacuum chamber.

In our previous *in situ* experiments on transition metal K-edges, the working electrode consisted on nanoparticles deposited on a glassy carbon plate. However, this substrate is non-transparent at 700 eV (Appendix Figure 10). Instead, a Si₃N₄ plate is used to transmit 70 % of the photons and to resist to pressure. It is coated with 10 nm of Au/Ti beforehand to assure the conductivity of the electrode.



Appendix Figure 9 Top view image of the cell open (left) and closed (right). 1: location of the working electrode plate. 2: platinum foil as counter electrode. 3: reference electrode input. 4: waterproof O-ring. 5: golden spring. 6: electrolyte inlet/outlet. The fluorescent white papers enables a visual tracking of the beam to align the cell.

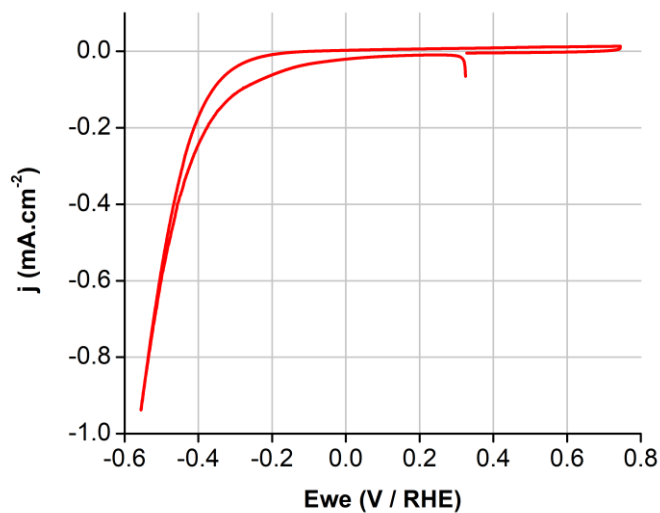
Appendix



Appendix Figure 10 Transmission coefficient of 50 μm of carbon (left) and 0.1 μm of Si_3N_4 (right) between 700 and 1000 eV.

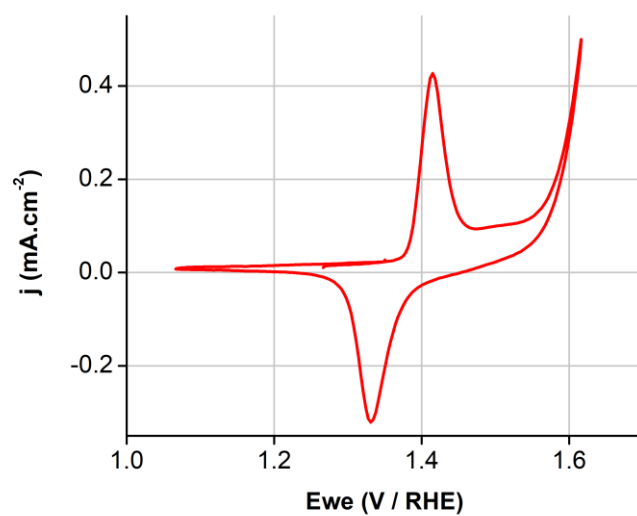
3.3. Operando experiments

3.3.1. Cyclic voltammograms of in situ experiments

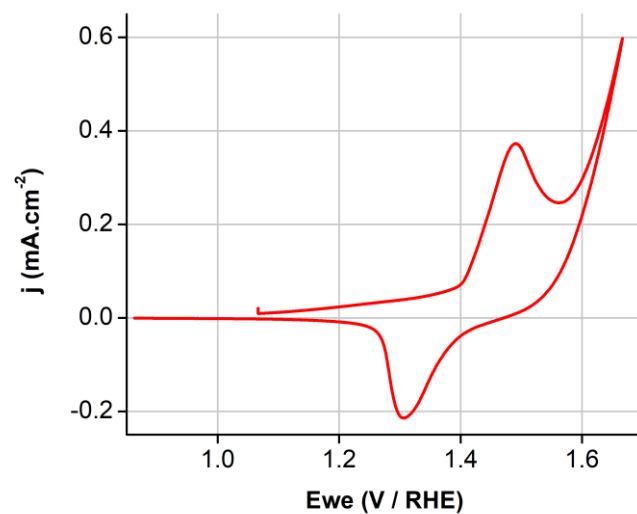


Appendix Figure 11 Control cyclic voltammograms of Ni_3B in H_2SO_4 0.5 M solution during the operando experiment of HER. Scan rate: 50 mV s^{-1} .

Appendix

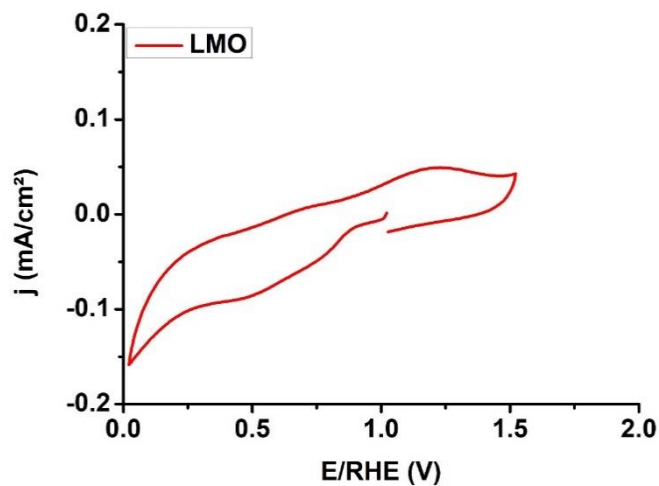


Appendix Figure 12 Control cyclic voltammograms of Ni_3B in KOH 0.5 M solution during the operando experiment of OER. Scan rate: 50 mV s^{-1} .

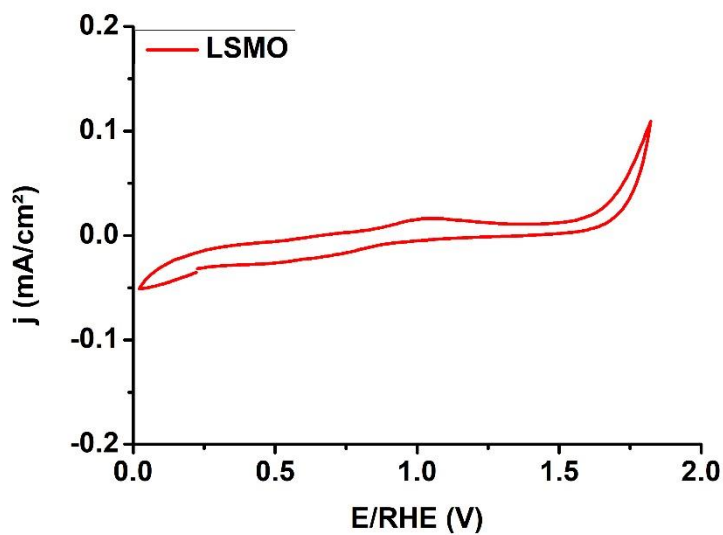


Appendix Figure 13 Control cyclic voltammograms of Ni_4B_3 in KOH 0.5 M solution during the operando experiment of OER. Scan rate; 50 mV s^{-1} .

Appendix

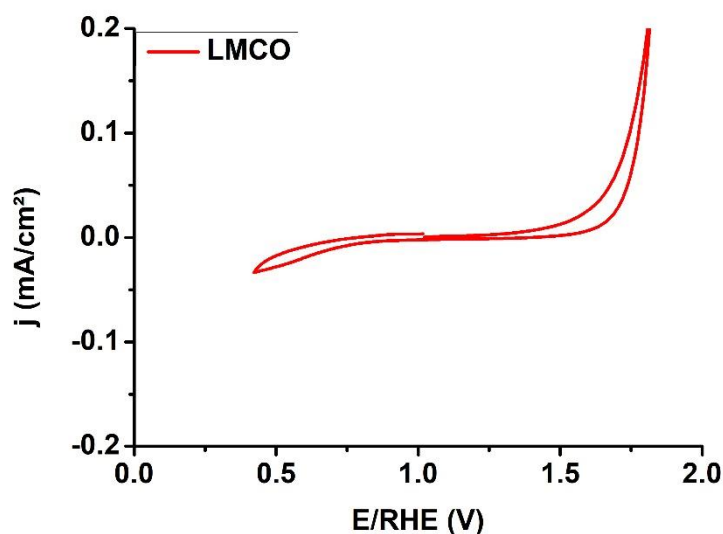


Appendix Figure 14 Control cyclic voltammograms of LaMnO_3 in O_2 -saturated KOH 0.1 M solution during the operando experiment.



Appendix Figure 15 Control cyclic voltammograms of $\text{La}_{0.67}\text{Sr}_{0.33}\text{MnO}_3$ in O_2 -saturated KOH 0.1 M solution during the operando experiment.

Appendix



Appendix Figure 16 Control cyclic voltammograms of $\text{LaMn}_{0.6}\text{Co}_{0.4}\text{O}_3$ in O_2 -saturated KOH 0.1 M solution during the operando experiment.

3.3.2. Scan history of the operando experiments

Potential (V/RHE)	Dry	OCV	-0.56	-0.36
Scans	6	6	20	16

Appendix Table 6 Operando study of Ni during HER. Potential of each steps and the number of scans acquired. No potential was applied during the steps in blue.

Potential (V/RHE)	Dry	OCV	1.57	1.27
Scans	6	6	20	20

Appendix Table 7 Operando study of Ni during OER. Potential of each steps and the number of scans acquired. No potential was applied during the steps in blue.

Potential (V/RHE)	Dry	OCV	-0.56	-0.36
Scans	9	9	23	16

Appendix Table 8 Operando study of Ni_3B during HER. Potential of each steps and the number of scans acquired. No potential was applied during the steps in blue.

Appendix

Potential (V/RHE)	Dry	OCV	1.57	1.22
Scans	3	30	30	30

Appendix Table 9 Operando study of Ni₃B during OER. Potential of each steps and the number of scans acquired. No potential was applied during the steps in blue.

Potential (V/RHE)	Dry	OCV	-0.16
Scans	16	10	10

Appendix Table 10 Operando study of Ni₄B₃ during HER. Potential of each steps and the number of scans acquired. No potential was applied during the steps in blue.

Potential (V/RHE)	Dry	OCV	1.62
Scans	6	6	11

Appendix Table 11 Operando study of Ni₄B₃ during OER. Potential of each steps and the number of scans acquired. No potential was applied during the steps in blue.

Potential (V/RHE)	Dry	OCV	0.8	0.6	0.4	0.2	0.9	1.4	1.8	0.9
Scans	16	16	9	16	16	16	16	8	8	8

Appendix Table 12 Operando study of LaMnO₃. Potential of each steps and the number of scans acquired. No potential was applied during the steps in blue.

Potential (V/RHE)	Dry	OCV	0.8	1.0	0.6	1.0	0.4	1.0	0.2	1.0
Scans	3	3	3	3	3	3	3	3	3	3

Appendix Table 13 Operando study of La_{2/3}Sr_{1/3}MnO₃. Potential of each steps and the number of scans acquired. No potential was applied during the steps in blue.

Potential (V/RHE)	Dry	OC	1.8	1.0	1.8	0.4	1.0
Scans	13	12	12	9	6	12	12

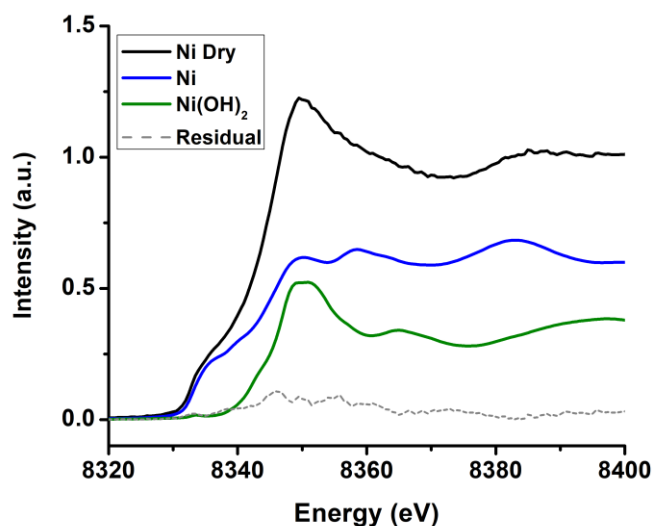
Appendix Table 14 Operando study of La_{0.75}Sr_{0.25}CoO₃. Potential of each steps and the number of scans acquired.

Appendix

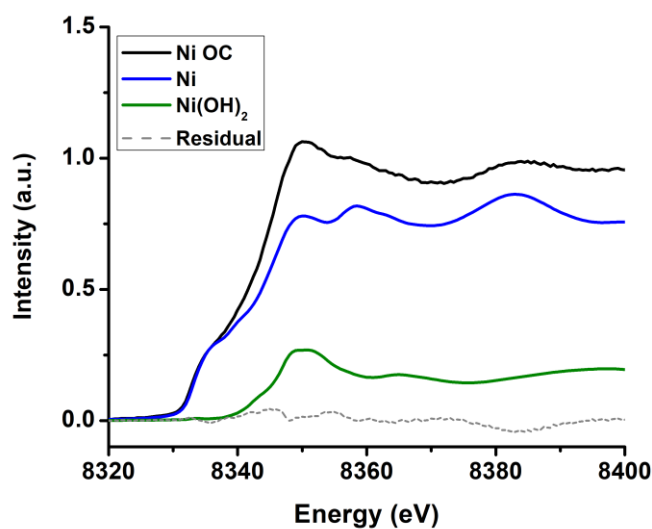
V / RHE	Dry	Dry	OC	OC	1.8	1.8	1.0	1.0	0.4	0.4	1.0	1.0
K-Edge	Mn	Co	Mn	Co	Mn	Co	Mn	Co	Mn	Co	Mn	Co
Scans	2	4	3	6	3	6	3	6	3	6	3	6

Appendix Table 15 Operando study of $\text{LaMn}_{0.6}\text{Co}_{0.4}\text{O}_3$. Potential of each steps and the number of scans acquired.

3.3.3. XANES corresponding to the linear combination fitting

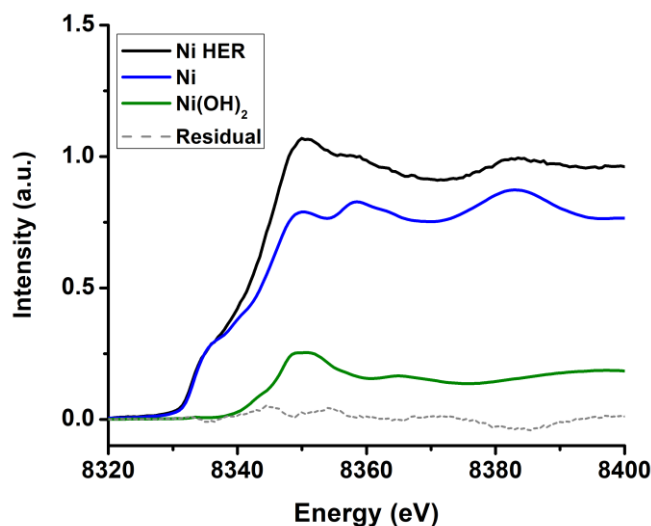


Appendix Figure 17 Linear combination applied to Ni nanoparticles under dry state during the HER experiment. The experimental spectrum is in black. The calculated contribution by LCF of pristine Ni and $\text{Ni}(\text{OH})_2$ are in blue and green respectively. The residual difference between the experimental spectrum and the fit constructed from the sum of all contributions is plotted in dotted grey.

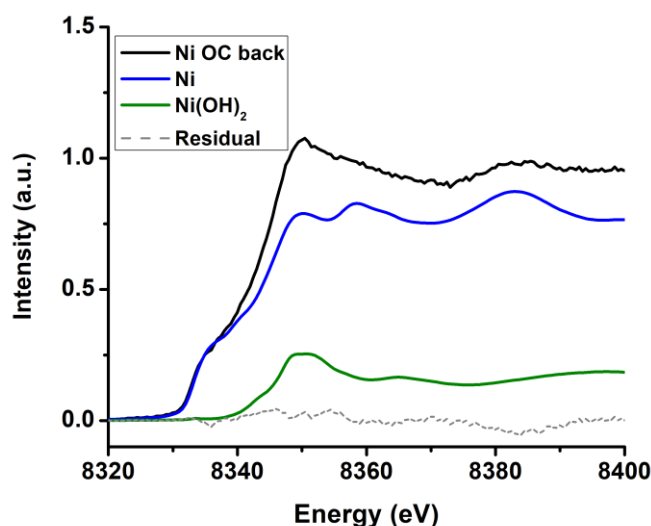


Appendix

Appendix Figure 18 Linear combination applied to Ni nanoparticles under resting state during the HER experiment. The experimental spectrum is in black. The calculated contribution by LCF of pristine Ni and Ni(OH)₂ are in blue and green respectively. The residual difference between the experimental spectrum and the fit constructed from the sum of all contributions is plotted in dotted grey.



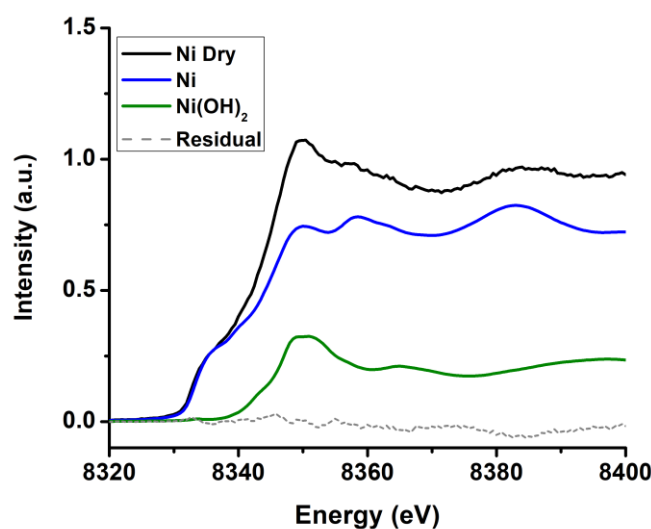
Appendix Figure 19 Linear combination applied to Ni nanoparticles under electrocatalytic conditions during the HER experiment. The experimental spectrum is in black. The calculated contribution by LCF of pristine Ni and Ni(OH)₂ are in blue and green respectively. The residual difference between the experimental spectrum and the fit constructed from the sum of all contributions is plotted in dotted grey.



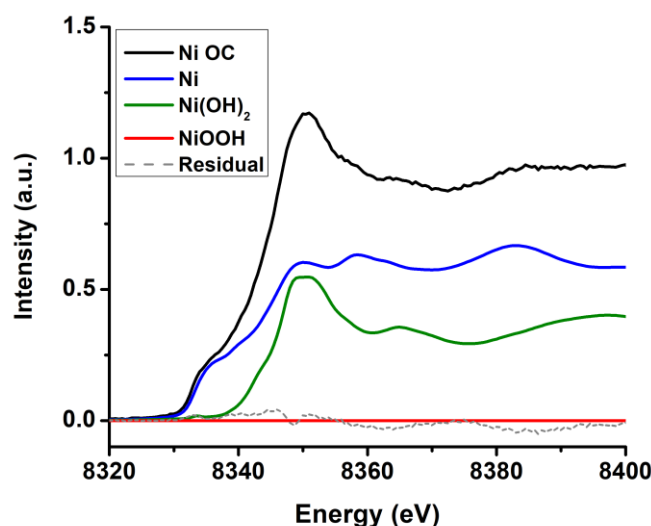
Appendix Figure 20 Linear combination applied to Ni nanoparticles under resting state after the electrocatalysis during the HER experiment. The experimental spectrum is in black. The calculated contribution by LCF of pristine Ni and Ni(OH)₂ are in blue and green

Appendix

respectively. The residual difference between the experimental spectrum and the fit constructed from the sum of all contributions is plotted in dotted grey.

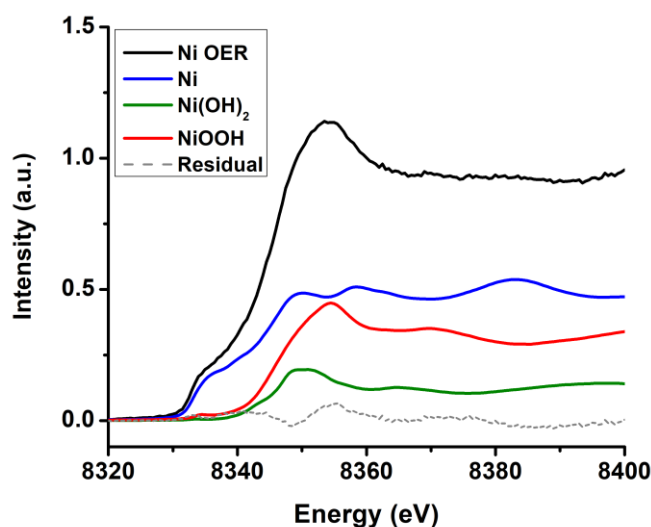


Appendix Figure 21 Linear combination applied to Ni nanoparticles under dry state during the OER experiment. The experimental spectrum is in black. The calculated contribution by LCF of pristine Ni and Ni(OH)₂ are in blue and green respectively. The residual difference between the experimental spectrum and the fit constructed from the sum of all contributions is plotted in dotted grey.

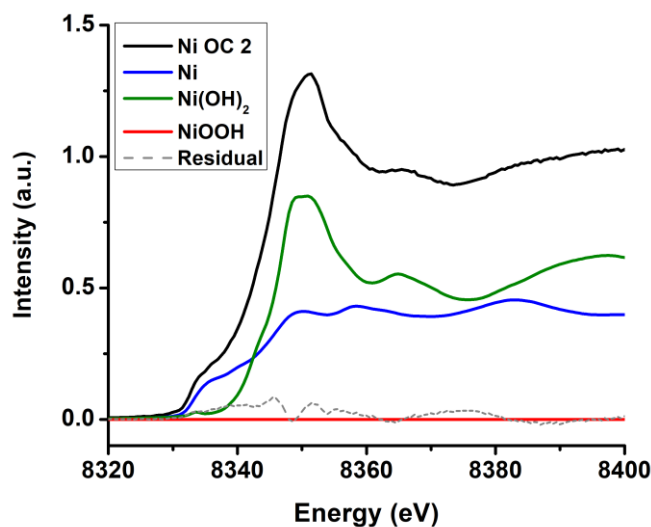


Appendix Figure 22 Linear combination applied to Ni nanoparticles under resting state during the OER experiment. The experimental spectrum is in black. The calculated contribution by LCF of pristine Ni, Ni(OH)₂ and NiOOH are in blue, green and red respectively. The residual difference between the experimental spectrum and the fit constructed from the sum of all contributions is plotted in dotted grey.

Appendix

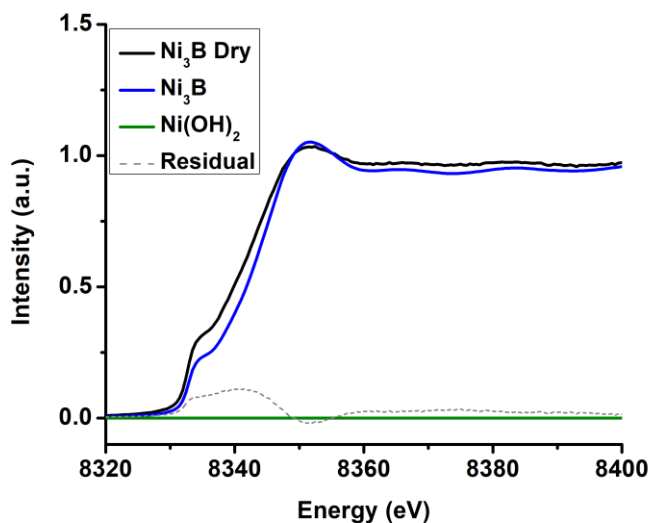


Appendix Figure 23 Linear combination applied to Ni nanoparticles under electrocatalytic state during the OER experiment. The experimental spectrum is in black. The calculated contribution by LCF of pristine Ni, Ni(OH)₂ and NiOOH are in blue, green and red respectively. The residual difference between the experimental spectrum and the fit constructed from the sum of all contributions is plotted in dotted grey.

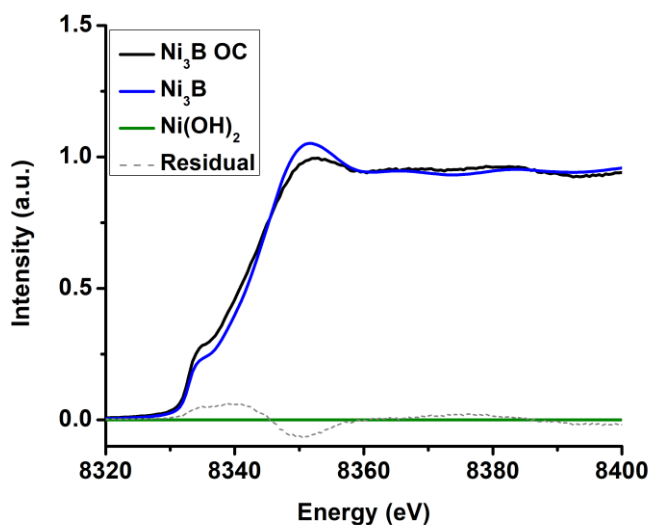


Appendix Figure 24 Linear combination applied to Ni nanoparticles under resting state after the electrocatalysis during the OER experiment. The experimental spectrum is in black. The calculated contribution by LCF of pristine Ni, Ni(OH)₂ and NiOOH are in blue, green and red respectively. The residual difference between the experimental spectrum and the fit constructed from the sum of all contributions is plotted in dotted grey.

Appendix

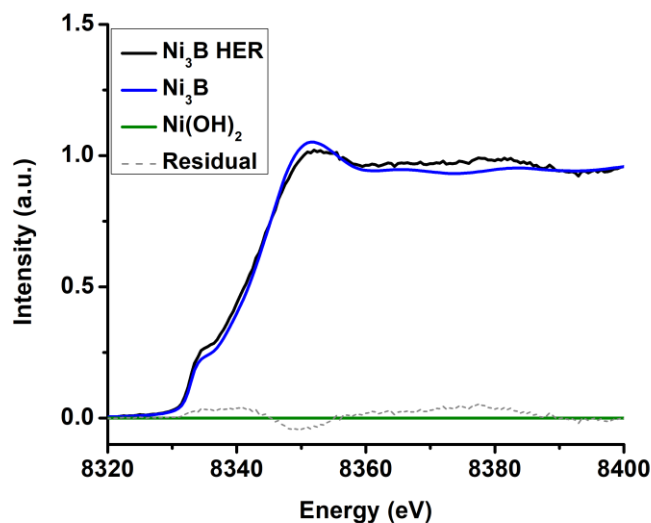


Appendix Figure 25 Linear combination applied to Ni₃B nanoparticles under dry state during the HER experiment. The experimental spectrum is in black. The calculated contribution by LCF of pristine Ni₃B and Ni(OH)₂ are in blue and green respectively. The residual difference between the experimental spectrum and the fit constructed from the sum of all contributions is plotted in dotted grey.

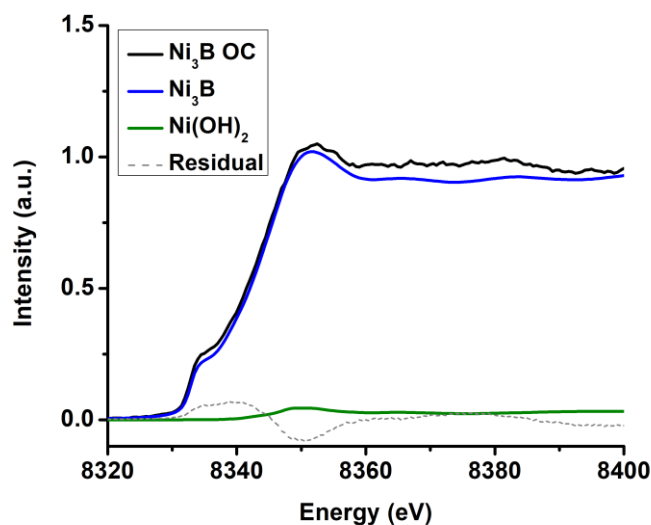


Appendix Figure 26 Linear combination applied to Ni₃B nanoparticles under resting state during the HER experiment. The experimental spectrum is in black. The calculated contribution by LCF of pristine Ni₃B and Ni(OH)₂ are in blue and green respectively. The residual difference between the experimental spectrum and the fit constructed from the sum of all contributions is plotted in dotted grey.

Appendix

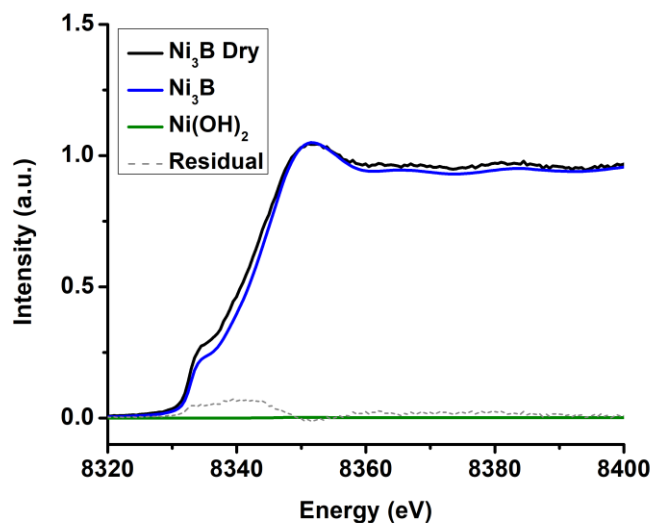


Appendix Figure 27 Linear combination applied to Ni_3B nanoparticles under electrocatalytic state during the HER experiment. The experimental spectrum is in black. The calculated contribution by LCF of pristine Ni_3B and $\text{Ni}(\text{OH})_2$ are in blue and green respectively. The residual difference between the experimental spectrum and the fit constructed from the sum of all contributions is plotted in dotted grey.

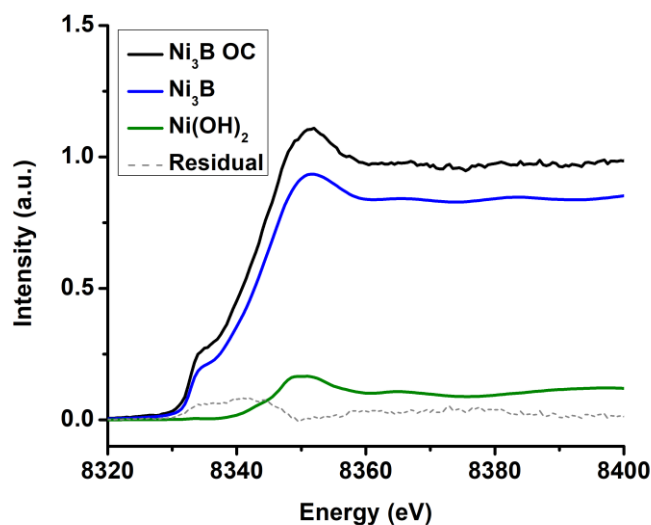


Appendix Figure 28 Linear combination applied to Ni_3B nanoparticles under resting state after the electrocatalysis during the HER experiment. The experimental spectrum is in black. The calculated contribution by LCF of pristine Ni_3B and $\text{Ni}(\text{OH})_2$ are in blue and green respectively. The residual difference between the experimental spectrum and the fit constructed from the sum of all contributions is plotted in dotted grey.

Appendix

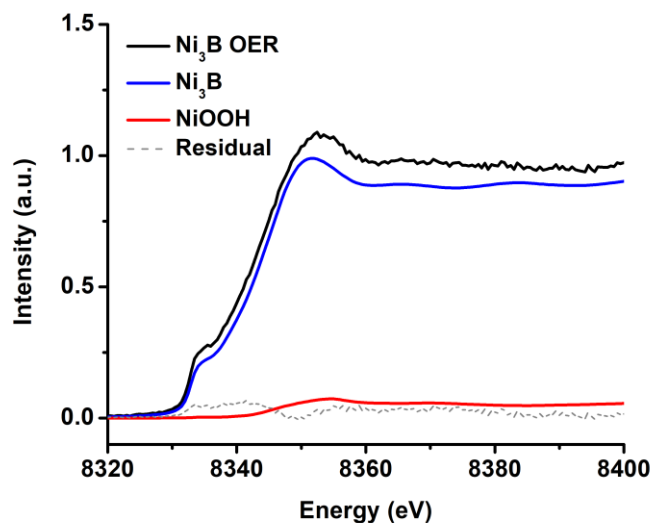


Appendix Figure 29 Linear combination applied to Ni_3B nanoparticles under dry state during the OER experiment. The experimental spectrum is in black. The calculated contribution by LCF of pristine Ni_3B and $\text{Ni}(\text{OH})_2$ are in blue and green respectively. The residual difference between the experimental spectrum and the fit constructed from the sum of all contributions is plotted in dotted grey.

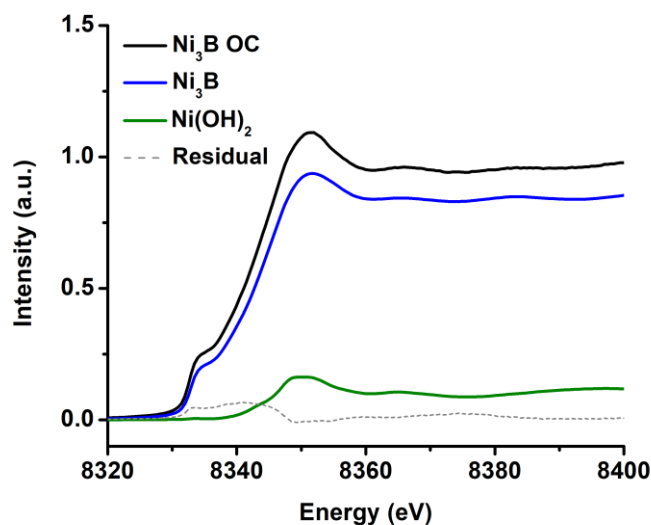


Appendix Figure 30 Linear combination applied to Ni_3B nanoparticles under resting state during the OER experiment. The experimental spectrum is in black. The calculated contribution by LCF of pristine Ni_3B and $\text{Ni}(\text{OH})_2$ are in blue and green respectively. The residual difference between the experimental spectrum and the fit constructed from the sum of all contributions is plotted in dotted grey.

Appendix

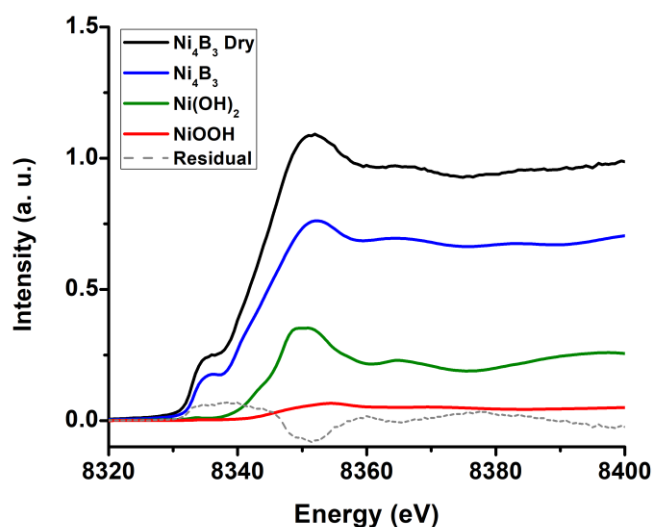


Appendix Figure 31 Linear combination applied to Ni_3B nanoparticles under electrocatalytic state during the OER experiment. The experimental spectrum is in black. The calculated contribution by LCF of pristine Ni_3B and NiOOH are in blue and red respectively. The residual difference between the experimental spectrum and the fit constructed from the sum of all contributions is plotted in dotted grey.

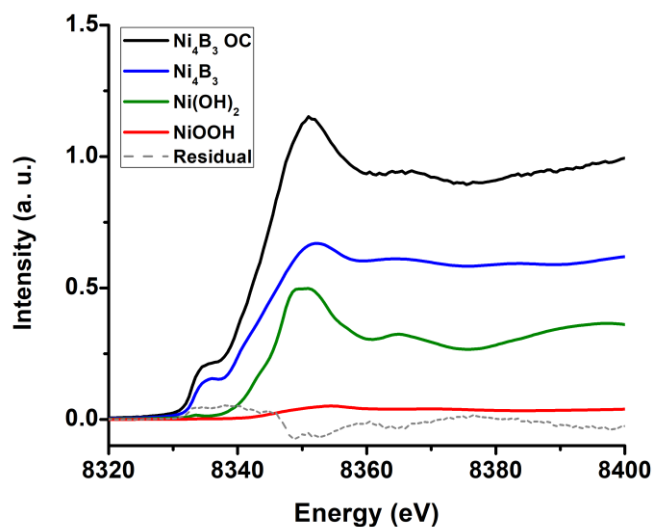


Appendix Figure 32 Linear combination applied to Ni_3B nanoparticles under resting state after the electrocatalysis during the OER experiment. The experimental spectrum is in black. The calculated contribution by LCF of pristine Ni_3B and $\text{Ni}(\text{OH})_2$ are in blue and green respectively. The residual difference between the experimental spectrum and the fit constructed from the sum of all contributions is plotted in dotted grey.

Appendix

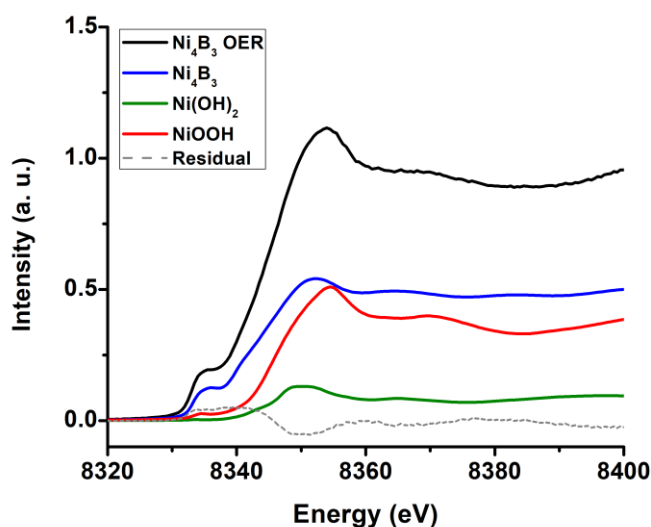


Appendix Figure 33 Linear combination applied to Ni_4B_3 nanoparticles under dry state during the OER experiment. The experimental spectrum is in black. The calculated contribution by LCF of pristine Ni_3B , $Ni(OH)_2$ and $NiOOH$ are in blue, green and red respectively. The residual difference between the experimental spectrum and the fit constructed from the sum of all contributions is plotted in dotted grey.



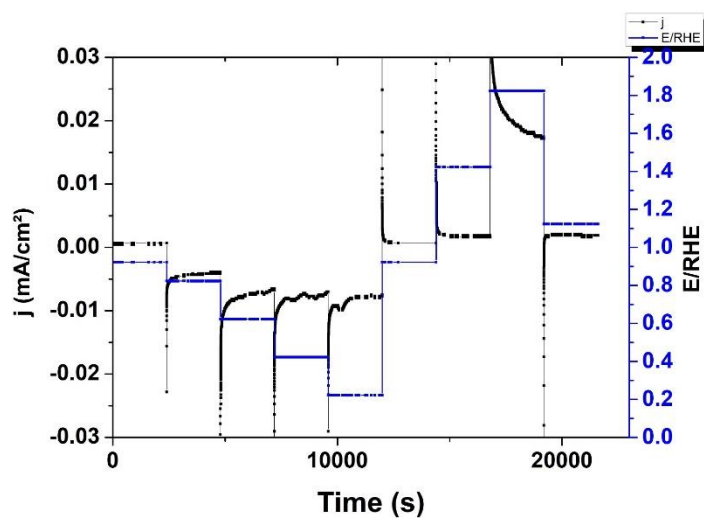
Appendix Figure 34 Linear combination applied to Ni_4B_3 nanoparticles under resting state during the OER experiment. The experimental spectrum is in black. The calculated contribution by LCF of pristine Ni_3B , $Ni(OH)_2$ and $NiOOH$ are in blue, green and red respectively. The residual difference between the experimental spectrum and the fit constructed from the sum of all contributions is plotted in dotted grey.

Appendix



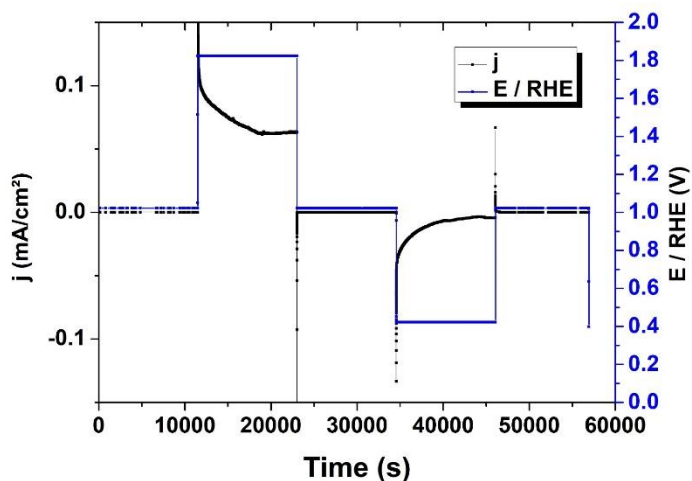
Appendix Figure 35 Linear combination applied to Ni_4B_3 nanoparticles under electrocatalytic state during the OER experiment. The experimental spectrum is in black. The calculated contribution by LCF of pristine Ni_3B , $\text{Ni}(\text{OH})_2$ and NiOOH are in blue, green and red respectively. The residual difference between the experimental spectrum and the fit constructed from the sum of all contributions is plotted in dotted grey.

3.3.4. Chronoamperometry of some *operando* experiments



Appendix Figure 36 Chronoamperogram of $\text{La}_{0.67}\text{Sr}_{0.33}\text{MnO}_3$ in O_2 -saturated KOH 0.1 M solution during the *operando* experiment.

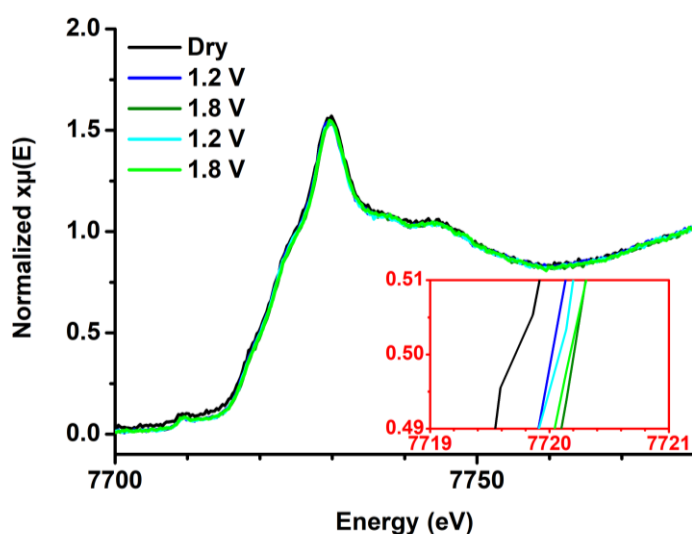
Appendix



Appendix Figure 37 Chronoamperogram of $\text{LaMn}_{0.6}\text{Co}_{0.4}\text{O}_3$ in O_2 -saturated KOH 0.1 M solution during the operando experiment.

3.3.5. Operando XAS of Co_3O_4 from a classical ink

The ink composition is described in section 1.2.1.



Appendix Figure 38 XANES of Co_3O_4 during OER in KPi 0.1 M on Co K-edge. The spectrum corresponding to the dry electrode is in black. Successive potentials are applied: 1.2 (blue), 1.8 (dark green), 1.2 (cyan) and 1.8 V (light green). In the red frame is a zoom between 7719 and 7721 eV.

Appendix

3.3.6. Supplementary FT-EXAFS fits without paths from nickel oxides

Path	R	N	$10^3 \sigma^2$	ΔE	Red χ^2	Rf (%)
Ni-B	2.06	3.0 (1)	13	-5 (2)	137	2.33
Ni-Ni	2.50	8.0 (1)	11			
Ni-Ni	2.73	1 (2)	16			

Appendix Table 16 Structural parameters of Ni_3B nanoparticles under HER conditions extracted from Ni K-edge EXAFS refinement. Uncertainties on the last digit are in brackets. Fixed parameters are in bold characters. R, N, σ^2 and ΔE are defined in chapter II section 2.2.1.

Path	R	N	$10^3 \sigma^2$	ΔE	Red χ^2	Rf (%)
Ni-B	2.04	3.0 (1)	13	-5 (2)	773	2.97
Ni-Ni	2.50	6.1 (6)	11			
Ni-Ni	2.77	3.3 (1)	17			

Appendix Table 17 Structural parameters of Ni_3B nanoparticles under OER conditions extracted from Ni K-edge EXAFS refinement. Uncertainties on the last digit are in brackets. Fixed parameters are in bold characters. R, N, σ^2 and ΔE are defined in chapter II section 2.2.1.

Path	R	N	$10^3 \sigma^2$	ΔE	Red χ^2	Rf (%)
Ni-B	2.11	6.7 (23)	10	-10 (3)	385	3.90
Ni-Ni	2.54	5.8 (12)	12			
Ni-Ni	2.91	2.1 (20)	11			

Appendix Table 18 Structural parameters of Ni_4B_3 nanoparticles under HER conditions extracted from Ni K-edge EXAFS refinement. Uncertainties on the last digit are in brackets. Fixed parameters are in bold characters. R, N, σ^2 and ΔE are defined in chapter II section 2.2.1.

Path	R	N	$10^3 \sigma^2$	ΔE	Red χ^2	Rf (%)
Ni-B	2.11	9.0 (10)	10	4 (2)	360	2.27
Ni-Ni	2.54	2.7 (7)	12			
Ni-Ni	2.91	1.4(10)	11			

Appendix Table 19 Structural parameters of Ni_4B_3 nanoparticles under OER conditions extracted from Ni K-edge EXAFS refinement. Uncertainties on the last digit are in brackets. Fixed parameters are in bold characters. R, N, σ^2 and ΔE are defined in chapter II section 2.2.1.

Appendix

4. Discussion

4.1. Calculation of the nickel oxide content and layer thickness

According to the EXAFS fits in Table II – 6, the average number of O neighbors around a Ni is 0.5, while the theoretical value is 6 neighbors in the Ni(OH)₂ crystalline structure. If we suppose that the nickel oxide phase formed in our nanoparticles is indeed the crystalline structure, then the percentage of oxidized nickel is calculated from:

$$0.5/6 = 8 \%$$

However, the average number of Ni neighbors around a Ni (i.e. Ni-Ni distances) is 7.6, which, compared to the theoretical value of 12 neighbors of the crystalline structure, corresponds to a vacancy content of 37 % (the effect of the size of the nanoparticles is neglected). Consequently, if we consider that the nickel oxide phase contains the same percentage of vacancies than the metallic nickel phase, the percentage of oxidized nickel is then:

$$\frac{0.5}{6} * \frac{12}{7.6} = 13 \%$$

In conclusion, the percentage of nickel oxide in the synthesized nickel nanoparticles is between 8 and 13 %, depending on the percentage of vacancies inside the nickel oxide phase.

Supposing that the nickel oxide phase is a layer on the surface of the nanoparticles forming a core-shell structure and that all the phases have the same densities, the relation between the nickel oxide layer thickness e , the nickel oxide content x and the nanoparticle size R is:

$$x = 1 - \left(1 - \frac{e}{R}\right)^3$$

From this relation, we calculate that a nickel oxide content of 13 % in Ni nanoparticles of 20 nm corresponds to a nickel oxide layer of less than 1 nm.

4.2. Evaluation of the uncertainty of linear combination fitting

In chapter II section 2.1.2.1., we stated that the choice of the reference for the linear combination fitting can highly impact the results of this technique. Here, we demonstrate

Appendix

this statement with LCF of manganese-based perovskites with manganite perovskite references from different origins.

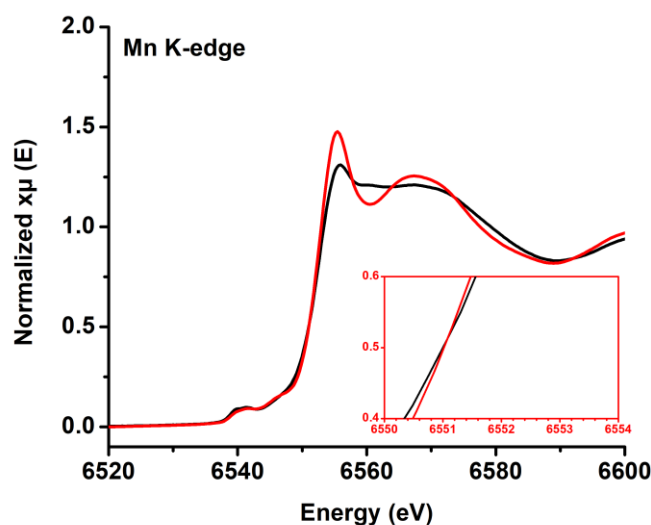
In chapter III, we synthesized LaMnO_3 , $\text{La}_{0.67}\text{Sr}_{0.33}\text{MnO}_3$, $\text{LaMn}_{0.7}\text{Co}_{0.3}\text{O}_3$ and $\text{LaMn}_{0.6}\text{Co}_{0.4}\text{O}_3$ nanoparticles. To evaluate the oxidation state of the manganese, we did a LCF with the XAS of our synthesized $\text{LaMn}^{\text{III}}\text{O}_3$ and a $\text{SrMn}^{\text{IV}}\text{O}_3$ perovskite taken from Celorrio et al.¹³⁹. (Appendix Table 20, column 2) We then did the LCF with the XAS of $\text{LaMn}^{\text{III}}\text{O}_3$ and $\text{SrMn}^{\text{IV}}\text{O}_3$ perovskites that have both been taken from Celorrio et al. to compare the impact of the origin of LaMnO_3 on the oxidation state calculated from XANES LCF (Appendix Table 20, column 3). With the LaMnO_3 from the literature, the content of Mn^{III} (LaMnO_3 contribution) is overvalued by up to 0.09 in $\text{LaMn}_{0.7}\text{Co}_{0.3}\text{O}_3$, which is higher than the uncertainties calculated from the LCF that are lower than 0.03. Consequently, the impact of the choice of the reference is more important than the uncertainty of the LCF calculation on the LCF result.

Even though $\text{LaMnO}_{3(\text{nanoparticles})}$ and $\text{LaMnO}_{3(\text{literature})}$ are the same phase, the LaMnO_3 from the literature are larger nanoparticles (50 nm compared to 20 nm for our synthesized perovskites) and such a small detail has an effect on the shape of the XAS¹⁶⁸. Moreover, the difference in synthesis method (sol-gel in the literature, molten salts in our work) could also alter the purity of the perovskite.

	$\text{LaMnO}_{3(\text{nanoparticles})}/\text{SrMnO}_3$	$\text{LaMnO}_{3(\text{literature})}/\text{SrMnO}_3$
$\text{La}_{0.67}\text{Sr}_{0.33}\text{MnO}_3$	0.67 / 0.33 (2)	0.74 / 0.26 (2)
$\text{LaMn}_{0.7}\text{Co}_{0.3}\text{O}_3$	0.60 / 0.40 (2)	0.69 / 0.31 (1)
$\text{LaMn}_{0.6}\text{Co}_{0.4}\text{O}_3$	0.70 / 0.30 (3)	0.75 / 0.25 (2)

Appendix Table 20 Mn^{III} and Mn^{IV} molar content in $\text{La}_{0.67}\text{Sr}_{0.33}\text{MnO}_3$, $\text{LaMn}_{0.7}\text{Co}_{0.3}\text{O}_3$ and $\text{LaMn}_{0.6}\text{Co}_{0.4}\text{O}_3$ perovskites calculated from XANES linear combination fitting with two sets of references: our synthesized $\text{LaMnO}_{3(\text{nanoparticles})}$ and SrMnO_3 taken from Celorrio et al.¹³⁹ (second column) and $\text{LaMnO}_{3(\text{literature})}$ and SrMnO_3 both taken from Celorrio et al.¹³⁹ (third column). The uncertainty on the last digit calculated from LCF is under brackets.

Appendix



Appendix Figure 39 XANES of as-prepared LaMnO_3 by our molten salt synthesis (in black) and reported by Celorrio et al.¹³⁹ (in red). In the red frame is a zoom between 6550 and 6554 eV.

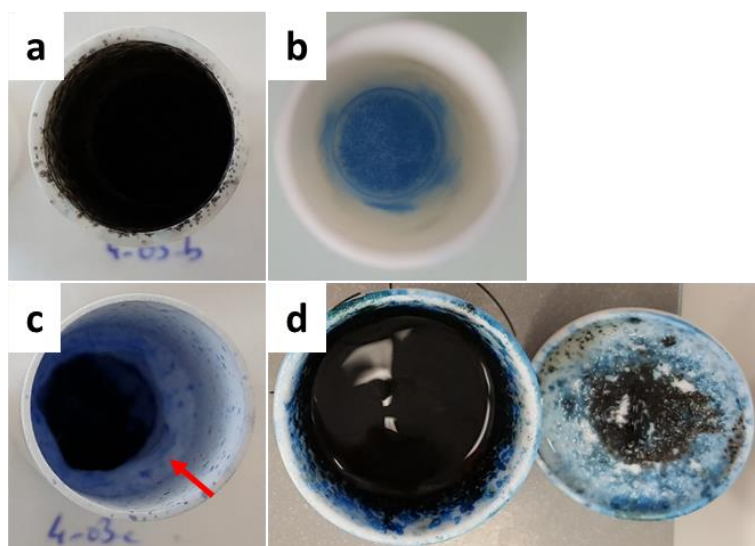
In this LCF applied to manganite perovskites, we have demonstrated that even two different references with the same phase can give quite diverging LCF results. We can then wonder about the uncertainty of this method when the references chosen are much more different from the studied phase as it is the case in chapter II, where nickel boride nanoparticles are fitted with (bulk) commercial nickel oxides. As the uncertainty on the choice of the references cannot be estimated and the uncertainty on the LCF calculation is negligible, no uncertainty range is given on the LCF combination in chapter II.

4.3. Impact of the nature of the crucible on the synthesis of $\text{La}_{1-x}\text{Sr}_x\text{CoO}_3$

Porcelain and boron nitride crucibles were considered for the synthesis of $\text{La}_{1-x}\text{Sr}_x\text{CoO}_3$. The boron nitride crucible is a cylinder with the same dimensions as the alumina crucible. The porcelain crucible is a flat-bottomed bowl that is shorter than the other crucibles but slightly wider. We reproduce the perovskite synthesis at 800 °C in these crucibles. After heating, their visual aspects are compared to the aspect of the alumina crucible at the same step (Appendix Figure 40). In the alumina crucible, most of the solid is black, which is the color of the nanoparticles, and it also covers the sides of the container. In the boron nitride crucible, the black solid is only in the bottom of the crucible, under a white ring cohesive to the crucible wall. This white wall is covered with blue spots, suggesting

Appendix

sequestration of cobalt species and possible reaction due to the reducing properties of boron nitride. In the porcelain crucible, the black crude is present in the bottom and the wall is covered by black and blue stains. The porcelain is no more covered with glaze. The crude clearly reacts also with porcelain.

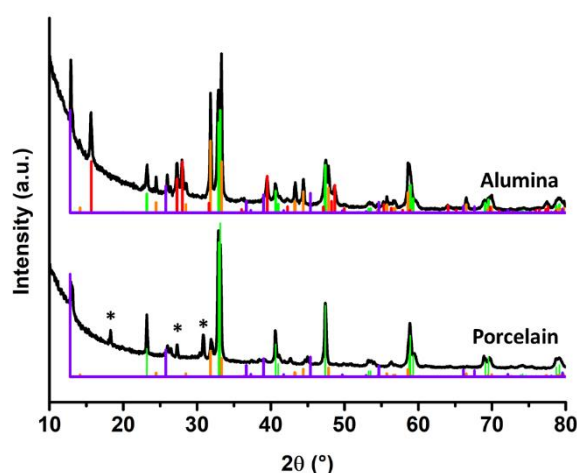


Appendix Figure 40 Crucible aspect after $\text{La}_{2/3}\text{Sr}_{1/3}\text{CoO}_3$ synthesis in molten salts. The alumina crucible (a) contains only a black mixture composed of the nanoparticles embedded in the salt. After the mixture is removed (b), blue traces still remain on the crucible. The boron nitride crucible (c) contains a mixture of white and blue powders (indicated by the red arrow), which are respectively eroded boron nitride and the products of cobalt reacting with boron nitride. The porcelain crucible (d) contains a mixture of black and blue powders. The black component is the nanoparticles in salts. The blue component is cobalt reacting with the porcelain silica to form cobalt silicates.

The sample synthesized in the porcelain crucible is mainly black and is further investigated by X-ray diffraction. Its diffractogram is compared to the one obtained with an alumina crucible under the same conditions, i.e. at 800 °C under air. We also note that the synthesis carried out in the alumina crucible is theoretically done under the same conditions than the first synthesis presented at 800 ° in the alumina crucible. However, their diffractograms are not similar. An unidentified critical parameter of the synthesis may not have been taken into account. One possible origin is the ageing of the precursors. Consequently, the diffractogram displayed on each figure is the diffractogram whose synthesis was carried out at the same time as the other synthesis compared on the same figure. The diffractogram of the sample from the alumina crucible displays peaks from $\text{La}_{1-x}\text{Sr}_x\text{CoO}_3$ pseudo-cubic perovskite, $\text{La}_{1-x}\text{Sr}_{1+x}\text{CoO}_4$ lamellar perovskite, $\text{La}(\text{OH})_3$ and hydrated potassium cobalt oxide phases. The diffractogram of the sample from the porcelain

Appendix

crucible exhibits peaks from both $\text{La}_{1-x}\text{Sr}_x\text{CoO}_3$ and $\text{La}_{1-x}\text{Sr}_{1+x}\text{CoO}_4$ phases and of a potassium cobalt oxide phase. Three peaks are not identified at 18.3° , 27.3° and 30.8° . The powder synthesized in the alumina crucible contains many oxides, including both perovskites with comparable amounts. The powder synthesized in porcelain crucible is mainly $\text{La}_{1-x}\text{Sr}_x\text{CoO}_3$ perovskite with a small amount of impurities. Considering the aspect of the porcelain crucible at the end of the reaction, we hypothesize that unidentified peaks indicate the presence of silicate-based species. To avoid these additional impurities, we choose to further investigate reactions in alumina crucibles, where the pseudo-cubic phase is far not pure, but where the secondary products originate only from the reaction precursors and are not due to the reaction between our precursors and the chemical component in the crucible.



Appendix Figure 41 XRD patterns of $\text{La}_{2/3}\text{Sr}_{1/3}\text{CoO}_3$ powders synthesized in KNO_3 during 1 h at 800°C in alumina and porcelain crucibles. Reference patterns of $\text{La}_{0.7}\text{Sr}_{0.3}\text{CoO}_3$ (green, PDF card 04-014-1579), $\text{La}_{0.75}\text{Sr}_{1.25}\text{CoO}_4$ (orange, PDF card 04-013-4920), $\text{La}(\text{OH})_3$ (red, PDF card 04-005-8587) and $\text{K}_{0.3}\text{CoO}_2 \cdot 0.4\text{H}_2\text{O}$ (purple, PDF card 04-012-5548). Unattributed peaks are identified with a star.

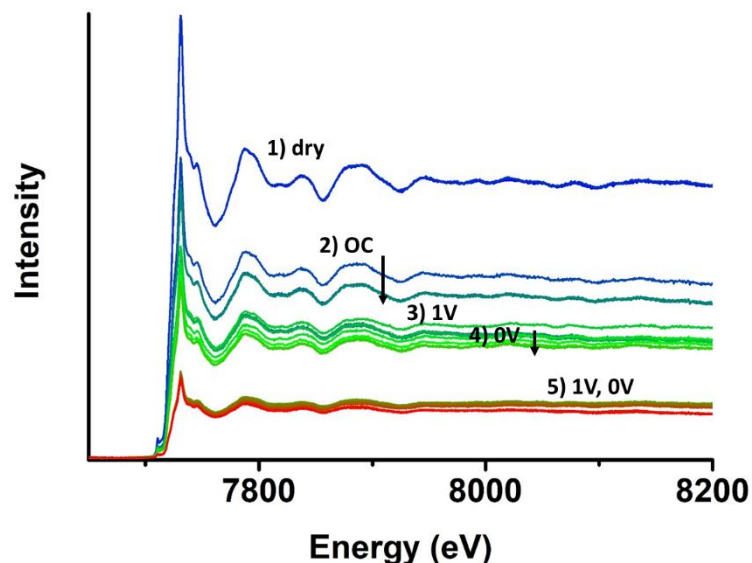
4.4. Monitoring the stability of the electrocatalyst by the intensity of the raw XAS

An *operando* XAS experiment on Co_3O_4 during OER in KPi 0.1 M was carried out on the SAMBA beamline, where the ink contained only the Co_3O_4 nanoparticles dispersed in absolute ethanol. 3 “dry” scans are collected then 4-5 scans are collected at each applied potential (OCV, 1.0 V/Ag/AgCl, 0.0 V/Ag/AgCl, 1.0 V/Ag/AgCl, 0.0 V/Ag/AgCl). The

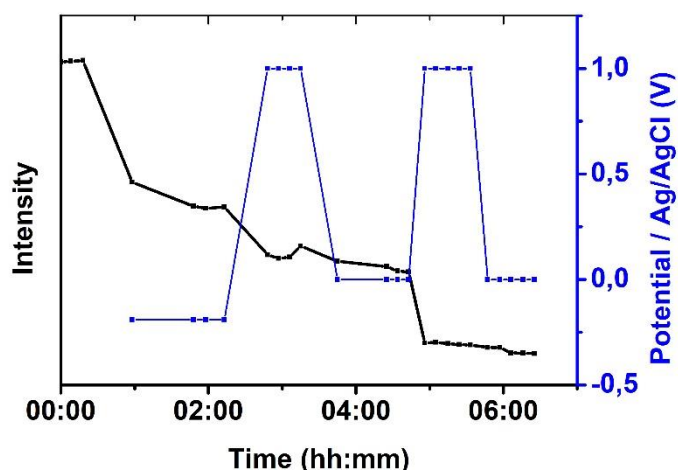
Appendix

scans without normalization are displayed on Appendix Figure 42. We observe that the intensities of the scans are decreasing during the experiment. When we correlate with the state of the electrode/the applied potential, we observe that the first drop of intensity (around 40 % loss) occurs between the dry and the first resting state, suggesting either that the concentration of cobalt decreased or that the electrolyte partially absorbs the X-ray beam. The second drop occurs while the system is still under resting state. This clearly implies that the concentration of cobalt is decreasing, whether through the dissolution of the nanoparticles or through the detachment of the nanoparticles from the working electrode into the electrolyte. Another drop of intensity is observed when a potential of 1.0 V/Ag/AgCl is applied, then the intensity stays stable under the oxidizing conditions. The reduction of the potential to 0.0 V/Ag/AgCl re-engages the progressive loss of intensity overtime at a resting state, although this second loss is less important than the loss during the first OCV, because the loss is proportional to the present concentration of cobalt. Raising the potential back to 1.0 V/Ag/AgCl halves the remaining intensity, which then stays relatively stable under the oxidizing potential and slightly decreases once the potential is reduced back to 0 V/Ag/AgCl. The temporal monitoring of the experiment displayed on Appendix Figure 43 (the relative intensity is chosen as the difference between the intensity of the scan after the edge at 8000 eV and the intensity at the scan before the edge at 7600 eV) clearly shows that the loss of intensity overtime cannot be modelled by a regular (exponential or linear) plot. Instead, the plot exhibits three significant drops around 1h, 2h30, and 4h45 which correspond respectively to the transition from dry to OCV and the two transitions from 1.0 to 0.0 V/Ag/AgCl. While the loss of intensity from dry to OCV could be attributed to the absorption of the electrolyte, the drop of intensities when the potential is reduced from 1.0 to 0.0 V/Ag/AgCl clearly reflects a decrease of cobalt concentration, hence a dissolution of the nanoparticles or a detachment of the nanoparticles from the working electrode. This potential-driven decrease of cobalt concentration is not observed when a classical ink (section 1.2.1.), which contains Nafion, activated acetylene black and nanoparticles inside absolute ethanol is employed instead of the sole dispersion of nanoparticles that is used, here. We then attribute the loss of cobalt to the detachment of Co_3O_4 nanoparticles from the working electrode, which is prevented by the mechanical stabilization provided by Nafion in the classical ink.

Appendix



Appendix Figure 42 Raw scans of Co_3O_4 in KPi 0.1 M on Co K-edge during operando experiment. The prepared ink only contains Co_3O_4 nanoparticles in absolute ethanol. The potentials are plotted against Ag/AgCl reference. The potentials applied are indicated above the scans and numbered in the chronological order. When necessary, the arrows indicate the direction of the change during a constant applied potential.



Appendix Figure 43 Co_3O_4 during in situ XAS OER experiment. Time evolution of the relative intensity of the scans on Co K-edge under different potentials. The relative intensity is the difference between the intensities at 8000 eV and 7600 eV .

Appendix

Abstract

References

1. de Miranda, P. E. V. Hydrogen Energy. in *Science and Engineering of Hydrogen-Based Energy Technologies* 1–38 (Elsevier, 2019). doi:10.1016/B978-0-12-814251-6.00001-0
2. Commission, E. Communication from the commission to the European parliament, the council, the European economic and social committee and the committee of the regions. *A hydrogen strategy for a climate-neutral Europe* (2020). Available at: https://ec.europa.eu/energy/sites/ener/files/hydrogen_strategy.pdf.
3. IEA. Hydrogen production costs by production source. (2018). Available at: <https://www.iea.org/data-and-statistics/charts/hydrogen-production-costs-by-production-source-2018>.
4. Seh, Z. W. *et al.* Combining theory and experiment in electrocatalysis: Insights into materials design. *Science* (80-.). **355**, eaad4998 (2017).
5. Minguzzi, A. *et al.* Observing the oxidation state turnover in heterogeneous iridium-based water oxidation catalysts. *Chem. Sci.* **5**, 3591 (2014).
6. Minguzzi, A. *et al.* Easy Accommodation of Different Oxidation States in Iridium Oxide Nanoparticles with Different Hydration Degree as Water Oxidation Electrocatalysts. *ACS Catal.* **5**, 5104–5115 (2015).
7. IEA. *Global electricity demand by region in the New Policies Scenario, 2000-2040.*, IEA, Paris (2019).
8. Younesi, R., Veith, G. M., Johansson, P., Edström, K. & Vegge, T. Lithium salts for advanced lithium batteries: Li-metal, Li-O₂, and Li-S. *Energy and Environmental Science* **8**, 1905–1922 (2015).
9. Lu, Y.-C. *et al.* Lithium–oxygen batteries: bridging mechanistic understanding and battery performance. *Energy Environ. Sci.* **6**, 750 (2013).
10. Gul, T., Pales, A. F. & Paoli, L. *Batteries and hydrogen technology: keys for a clean energy future.* Iea (2020).
11. Bockris, J. O. & Otagawa, T. Mechanism of oxygen evolution on perovskites. *J. Phys. Chem.* **87**, 2960–2971 (1983).

Abstract

12. Kobussen, A. G. C., Willems, H., De Wit, J. H. W. & Broers, G. H. J. The oxygen evolution reaction on cobalt Part I. Reaction order experiments and impedance measurements. *J. Electroanal. Chem.* **170**, 227–242 (1984).
13. Song, F. *et al.* An Unconventional Iron Nickel Catalyst for the Oxygen Evolution Reaction. *ACS Cent. Sci.* **5**, 558–568 (2019).
14. Zhang, B. & Sun, L. Across the Board: Licheng Sun on the Mechanism of O–O Bond Formation in Photosystem II. *ChemSusChem* **12**, 3401–3404 (2019).
15. Moysiadou, A., Lee, S., Hsu, C.-S., Chen, H. M. & Hu, X. Mechanism of Oxygen Evolution Catalyzed by Cobalt Oxyhydroxide: Cobalt Superoxide Species as a Key Intermediate and Dioxygen Release as a Rate-Determining Step. *J. Am. Chem. Soc.* **142**, 11901–11914 (2020).
16. Rossmeisl, J., Qu, Z. W., Zhu, H., Kroes, G. J. & Nørskov, J. K. Electrolysis of water on oxide surfaces. *J. Electroanal. Chem.* **607**, 83–89 (2007).
17. Dau, H. *et al.* The Mechanism of Water Oxidation: From Electrolysis via Homogeneous to Biological Catalysis. *ChemCatChem* **2**, 724–761 (2010).
18. Nørskov, J. K. *et al.* Origin of the Overpotential for Oxygen Reduction at a Fuel-Cell Cathode. *J. Phys. Chem. B* **108**, 17886–17892 (2004).
19. Bockris, J. O. & Potter, E. C. The Mechanism of the Cathodic Hydrogen Evolution Reaction. *J. Electrochem. Soc.* **99**, 169 (1952).
20. Thomas, J. G. N. Kinetics of electrolytic hydrogen evolution and the adsorption of hydrogen by metals. *Trans. Faraday Soc.* **57**, 1603 (1961).
21. McCrory, C. C. L. *et al.* Benchmarking Hydrogen Evolving Reaction and Oxygen Evolving Reaction Electrocatalysts for Solar Water Splitting Devices. *J. Am. Chem. Soc.* **137**, 4347–4357 (2015).
22. Marković, N. M., Adžić, R. R., Cahan, B. D. & Yeager, E. B. Structural effects in electrocatalysis: oxygen reduction on platinum low index single-crystal surfaces in perchloric acid solutions. *J. Electroanal. Chem.* **377**, 249–259 (1994).
23. Gasteiger, H. A., Kocha, S. S., Sompalli, B. & Wagner, F. T. Activity benchmarks and requirements for Pt, Pt-alloy, and non-Pt oxygen reduction catalysts for PEMFCs.

Abstract

- Appl. Catal. B Environ.* **56**, 9–35 (2005).
24. Iwakura, C., Fukuda, K. & Tamura, H. The anodic evolution of oxygen on platinum oxide electrode in alkaline solutions. *Electrochim. Acta* **21**, 501–508 (1976).
 25. Zhuo, S. & Sohlberg, K. Platinum dioxide phases: Relative thermodynamic stability and kinetics of inter-conversion from first-principles. *Phys. B Condens. Matter* **381**, 12–19 (2006).
 26. Lee, Y., Suntivich, J., May, K. J., Perry, E. E. & Shao-Horn, Y. Synthesis and Activities of Rutile IrO₂ and RuO₂ Nanoparticles for Oxygen Evolution in Acid and Alkaline Solutions. *J. Phys. Chem. Lett.* **3**, 399–404 (2012).
 27. Guan, J. *et al.* Synthesis and Demonstration of Subnanometric Iridium Oxide as Highly Efficient and Robust Water Oxidation Catalyst. *ACS Catal.* **7**, 5983–5986 (2017).
 28. Mccrory, C. C. L., Jung, S., Peters, J. C. & Jaramillo, T. F. Benchmarking Heterogeneous Electrocatalysts for the Oxygen Evolution Reaction. *J. Am. Chem. Soc.* **135**, 16977–16987 (2013).
 29. Frydendal, R. *et al.* Benchmarking the Stability of Oxygen Evolution Reaction Catalysts: The Importance of Monitoring Mass Losses. *ChemElectroChem* **1**, 2075–2081 (2014).
 30. Stephens, I. E. L., Bondarenko, A. S., Grønbjerg, U., Rossmeisl, J. & Chorkendorff, I. Understanding the electrocatalysis of oxygen reduction on platinum and its alloys. *Energy Environ. Sci.* **5**, 6744 (2012).
 31. Sun, Y., Delucchi, M. & Ogden, J. The impact of widespread deployment of fuel cell vehicles on platinum demand and price. *Int. J. Hydrogen Energy* **36**, 11116–11127 (2011).
 32. He, X., Yin, F. & Li, G. A Co/metal–organic-framework bifunctional electrocatalyst: The effect of the surface cobalt oxidation state on oxygen evolution/reduction reactions in an alkaline electrolyte. *Int. J. Hydrogen Energy* **40**, 9713–9722 (2015).
 33. Gorlin, Y. & Jaramillo, T. F. A bifunctional nonprecious metal catalyst for oxygen reduction and water oxidation. *J. Am. Chem. Soc.* **132**, 13612–13614 (2010).

Abstract

34. Proietti, E. *et al.* Iron-based cathode catalyst with enhanced power density in polymer electrolyte membrane fuel cells. *Nat. Commun.* **2**, 416 (2011).
35. Anselmi-Tamburini, U. *et al.* Enhanced low-temperature protonic conductivity in fully dense nanometric cubic zirconia. *Appl. Phys. Lett.* **89**, 163116 (2006).
36. Suntivich, J., May, K. J., Gasteiger, H. A., Goodenough, J. B. & Shao-Horn, Y. A Perovskite Oxide Optimized for Oxygen Evolution Catalysis from Molecular Orbital Principles. *Science (80-.)*. **334**, 1383–1385 (2011).
37. Suntivich, J. *et al.* Design principles for oxygen-reduction activity on perovskite oxide catalysts for fuel cells and metal–air batteries. *Nat. Chem.* **3**, 546–550 (2011).
38. Carenco, S., Portehault, D., Boissière, C., Mézailles, N. & Sanchez, C. Nanoscaled metal borides and phosphides: Recent developments and perspectives. *Chem. Rev.* **113**, 7981–8065 (2013).
39. Gupta, S., Patel, M. K., Miotello, A. & Patel, N. Metal Boride-Based Catalysts for Electrochemical Water-Splitting: A Review. *Adv. Funct. Mater.* **30**, 1906481 (2020).
40. Wang, T., Chen, H., Yang, Z., Liang, J. & Dai, S. High-Entropy Perovskite Fluorides: A New Platform for Oxygen Evolution Catalysis. *J. Am. Chem. Soc.* **142**, 4550–4554 (2020).
41. Meng, Y. *et al.* Structure–Property Relationship of Bifunctional MnO₂ Nanostructures: Highly Efficient, Ultra-Stable Electrochemical Water Oxidation and Oxygen Reduction Reaction Catalysts Identified in Alkaline Media. *J. Am. Chem. Soc.* **136**, 11452–11464 (2014).
42. Marković, N. M., Adžić, R. R., Cahan, B. D. & Yeager, E. B. Structural effects in electrocatalysis: oxygen reduction on platinum low index single-crystal surfaces in perchloric acid solutions. *J. Electroanal. Chem.* **377**, 249–259 (1994).
43. Kibler, L. A. Hydrogen electrocatalysis. *ChemPhysChem* **7**, 985–991 (2006).
44. Frydendal, R., Paoli, E. A., Chorkendorff, I., Rossmeisl, J. & Stephens, I. E. L. Toward an Active and Stable Catalyst for Oxygen Evolution in Acidic Media: Ti-Stabilized MnO₂. *Adv. Energy Mater.* **5**, 1500991 (2015).
45. Roe, A. L. *et al.* X-ray Absorption Spectroscopy of Iron-Tyrosinate Proteins. *J. Am.*

Abstract

- Chem. Soc.* **106**, 1676–1681 (1984).
46. Hannay, C. *et al.* X-ray Absorption Spectroscopic Study of the Structure and Bonding in $M[B(3\text{-isopropylpyrazol-1-yl})_4]_2$, where M is Fe, Co, Ni, Cu, and Zn. *Inorg. Chem.* **33**, 5983–5987 (1994).
 47. George, S. J., Lowery, M. D., Solomon, E. I. & Cramer, S. P. Copper L-edge spectral studies: a direct experimental probe of the ground-state covalency in the blue copper site in plastocyanin. *J. Am. Chem. Soc.* **115**, 2968–2969 (1993).
 48. Ravel, B. Introduction to X-ray Absorption Spectroscopy. in (2015).
 49. Merritt, E. A. X-ray Absorption Edges. Available at: http://skuld.bmsc.washington.edu/scatter/AS_periodic.html.
 50. Asakura, D. *et al.* Material/element-dependent fluorescence-yield modes on soft X-ray absorption spectroscopy of cathode materials for Li-ion batteries. *AIP Adv.* **6**, 035105 (2016).
 51. Harks, P. P. R. M. L., Mulder, F. M. & Notten, P. H. L. In situ methods for Li-ion battery research: A review of recent developments. *J. Power Sources* **288**, 92–105 (2015).
 52. Gu, Q., Kimpton, J. A., Brand, H. E. A., Wang, Z. & Chou, S. Solving Key Challenges in Battery Research Using In Situ Synchrotron and Neutron Techniques. *Adv. Energy Mater.* **7**, 1–7 (2017).
 53. Liu, X. *et al.* Distinct charge dynamics in battery electrodes revealed by in situ and operando soft X-ray spectroscopy. *Nat. Commun.* **4**, 2568 (2013).
 54. Nam, K. W. *et al.* Combining in situ synchrotron X-Ray diffraction and absorption techniques with transmission electron microscopy to study the origin of thermal instability in overcharged cathode materials for lithium-ion batteries. *Adv. Funct. Mater.* **23**, 1047–1063 (2013).
 55. Yamamoto, K. *et al.* Improved Cyclic Performance of Lithium-Ion Batteries: An Investigation of Cathode/Electrolyte Interface via In Situ Total-Reflection Fluorescence X-ray Absorption Spectroscopy. *J. Phys. Chem. C* **118**, 9538–9543 (2014).

Abstract

56. Fabbri, E. *et al.* Dynamic surface self-reconstruction is the key of highly active perovskite nano-electrocatalysts for water splitting. *Nat. Mater.* **16**, 925–931 (2017).
57. Lassalle-Kaiser, B., Zitolo, A., Fonda, E., Robert, M. & Anxolabéhère-Mallart, E. In Situ Observation of the Formation and Structure of Hydrogen-Evolving Amorphous Cobalt Electrocatalysts. *ACS Energy Lett.* **2**, 2545–2551 (2017).
58. Gul, S. *et al.* Simultaneous detection of electronic structure changes from two elements of a bifunctional catalyst using wavelength-dispersive X-ray emission spectroscopy and in situ electrochemistry. *Phys. Chem. Chem. Phys.* **17**, 8901–8912 (2015).
59. Friebel, D., Miller, D. J., Nordlund, D., Ogasawara, H. & Nilsson, A. Degradation of bimetallic model electrocatalysts: An in situ x-ray absorption spectroscopy study. *Angew. Chemie - Int. Ed.* **50**, 10190–10192 (2011).
60. Bergmann, A. *et al.* Reversible amorphization and the catalytically active state of crystalline Co₃O₄ during oxygen evolution. *Nat. Commun.* **6**, 8625 (2015).
61. Hinnemann, B. *et al.* Biomimetic hydrogen evolution: MoS₂ nanoparticles as catalyst for hydrogen evolution. *J. Am. Chem. Soc.* **127**, 5308–5309 (2005).
62. Bergmann, A. *et al.* Reversible amorphization and the catalytically active state of crystalline Co₃O₄ during oxygen evolution. *Nat. Commun.* **6**, 8625 (2015).
63. Kwon, G. *et al.* Resolution of Electronic and Structural Factors Underlying Oxygen-Evolving Performance in Amorphous Cobalt Oxide Catalysts. *J. Am. Chem. Soc.* **140**, 10710–10720 (2018).
64. Bediako, D. K. *et al.* Structure-activity correlations in a nickel-borate oxygen evolution catalyst. *J. Am. Chem. Soc.* **134**, 6801–6809 (2012).
65. Kanan, M. W. *et al.* Structure and valency of a cobalt-phosphate water oxidation catalyst determined by in situ X-ray spectroscopy. *J. Am. Chem. Soc.* **132**, 13692–13701 (2010).
66. Choi, Y.-W., Mistry, H. & Roldan Cuenya, B. New insights into working nanostructured electrocatalysts through operando spectroscopy and microscopy. *Curr. Opin. Electrochem.* **1**, 95–103 (2017).

Abstract

67. Masa, J. *et al.* Amorphous Cobalt Boride (Co₂B) as a Highly Efficient Nonprecious Catalyst for Electrochemical Water Splitting: Oxygen and Hydrogen Evolution. *Adv. Energy Mater.* **6**, 1502313 (2016).
68. Menezes, P. W. *et al.* High-Performance Oxygen Redox Catalysis with Multifunctional Cobalt Oxide Nanochains: Morphology-Dependent Activity. *ACS Catal.* **5**, 2017–2027 (2015).
69. Masa, J. *et al.* Ultrathin High Surface Area Nickel Boride (Ni₃B) Nanosheets as Highly Efficient Electrocatalyst for Oxygen Evolution. *Adv. Energy Mater.* **7**, 1–8 (2017).
70. Enman, L. J., Burke, M. S., Batchellor, A. S. & Boettcher, S. W. Effects of Intentionally Incorporated Metal Cations on the Oxygen Evolution Electrocatalytic Activity of Nickel (Oxy)hydroxide in Alkaline Media. *ACS Catal.* **6**, 2416–2423 (2016).
71. Wang, J. & Zeng, H. C. CoHPi Nanoflakes for Enhanced Oxygen Evolution Reaction. *ACS Appl. Mater. Interfaces* **10**, 628–6298 (2018).
72. Smith, A. M., Trotochaud, L., Burke, M. S. & Boettcher, S. W. Contributions to activity enhancement via Fe incorporation in Ni-(oxy)hydroxide/borate catalysts for near-neutral pH oxygen evolution. *Chem. Commun. Chem. Commun* **51**, 5261–5263 (2015).
73. Li, X. *et al.* In Situ/Operando Characterization Techniques to Probe the Electrochemical Reactions for Energy Conversion. *Small Methods* **2**, 1700395 (2018).
74. Paloukis, F. *et al.* In situ X-ray photoelectron spectroscopy study of complex oxides under gas and vacuum environments. *Appl. Surf. Sci.* **423**, 1176–1181 (2017).
75. Han, Y. *et al.* Observing the Electrochemical Oxidation of Co Metal at the Solid/Liquid Interface Using Ambient Pressure X-ray Photoelectron Spectroscopy. *J. Phys. Chem. B* **122**, 666–671 (2017).
76. Wang, J. *et al.* Boosting the Electrocatalytic Activity of Co₃O₄ Nanosheets for a Li-O₂ Battery through Modulating Inner Oxygen Vacancy and Exterior Co³⁺ /Co²⁺ Ratio. *ACS Catal.* **7**, 6533–6541 (2017).

Abstract

77. Reikowski, F. *et al.* Operando Surface X-ray Diffraction Studies of Structurally Defined Co₃O₄ and CoOOH Thin Films during Oxygen Evolution. *ACS Catal.* **9**, 3811–3821 (2019).
78. Khalakhan, I. *et al.* In-situ electrochemical atomic force microscopy study of aging of magnetron sputtered Pt-Co nanoalloy thin films during accelerated degradation test. *Electrochim. Acta* **211**, 52–58 (2016).
79. Kim, Y.-G., Baricuatro, J. H., Javier, A., Gregoire, J. M. & Soriaga, M. P. The Evolution of the Polycrystalline Copper Surface, First to Cu(111) and Then to Cu(100), at a Fixed CO₂RR Potential: A Study by Operando EC-STM. *Langmuir* **30**, 15053–15056 (2014).
80. Han, B. *et al.* Nanoscale structural oscillations in perovskite oxides induced by oxygen evolution. *Nat. Mater.* **16**, 121–126 (2017).
81. Ortiz Peña, N. *et al.* Morphological and Structural Evolution of Co₃O₄ Nanoparticles Revealed by in Situ Electrochemical Transmission Electron Microscopy during Electrocatalytic Water Oxidation. *ACS Nano* **13**, 11372–11381 (2019).
82. Gupta, S., Patel, N., Miotello, A. & Kothari, D. C. Cobalt-Boride: An efficient and robust electrocatalyst for Hydrogen Evolution Reaction. *J. Power Sources* **279**, 620–625 (2015).
83. Li, H. *et al.* Earth-Abundant Iron Diboride (FeB₂) Nanoparticles as Highly Active Bifunctional Electrocatalysts for Overall Water Splitting. *Adv. Energy Mater.* **7**, 1–12 (2017).
84. Masa, J. *et al.* Ultrathin High Surface Area Nickel Boride (Ni_xB) Nanosheets as Highly Efficient Electrocatalyst for Oxygen Evolution. *Adv. Energy Mater.* **7**, 1700381 (2017).
85. Chan Chang, T.-H.-C. Elaboration de borures et phosphures métalliques : synthèse de nanomatériaux en sels fondus et réactivité de surface. (2017).
86. Jiang, W. J. *et al.* Crystallinity-Modulated Electrocatalytic Activity of a Nickel(II) Borate Thin Layer on Ni₃B for Efficient Water Oxidation. *Angew. Chemie - Int. Ed.* **56**, 6572–6577 (2017).

Abstract

87. Gupta, S. *et al.* Co-Ni-B nanocatalyst for efficient hydrogen evolution reaction in wide pH range. *Appl. Catal. B Environ.* **192**, 126–133 (2016).
88. Gupta, S. *et al.* Co-Mo-B Nanoparticles as a non-precious and efficient Bifunctional Electrocatalyst for Hydrogen and Oxygen Evolution. *Electrochim. Acta* **232**, 64–71 (2017).
89. Jiang, J. *et al.* Highly active and durable electrocatalytic water oxidation by a NiB 0.45 /NiO x core-shell heterostructured nanoparticulate film. *Nano Energy* **38**, 175–184 (2017).
90. Arivu, M., Masud, J., Umapathi, S. & Nath, M. Facile synthesis of Ni₃B/rGO nanocomposite as an efficient electrocatalyst for the oxygen evolution reaction in alkaline media. *Electrochem. commun.* **86**, 121–125 (2018).
91. Zeng, M. *et al.* Nanostructured Amorphous Nickel Boride for High-Efficiency Electrocatalytic Hydrogen Evolution over a Broad pH Range. *ChemCatChem* **8**, 708–712 (2016).
92. Park, H., Encinas, A., Scheifers, J. P., Zhang, Y. & Fokwa, B. P. T. Boron-Dependency of Molybdenum Boride Electrocatalysts for the Hydrogen Evolution Reaction. *Angew. Chemie - Int. Ed.* **56**, 5575–5578 (2017).
93. Carenco, S. *et al.* Controlled design of Size-tunable monodisperse nickel nanoparticles. *Chem. Mater.* **22**, 1340–1349 (2010).
94. Carenco, S. *et al.* Revisiting the Molecular Roots of a Ubiquitously Successful Synthesis: Nickel(0) Nanoparticles by Reduction of [Ni(acetylacetonate)₂]. *Chem. - A Eur. J.* **18**, 14165–14173 (2012).
95. Nakamura, Y., Ogiwara, Y. & Phillips, G. O. Free radical formation and degradation of cellulose by ionizing radiations. *Polym. Photochem.* **6**, 135–159 (1985).
96. Teo, B. K. *EXAFS: Basic Principles and Data Analysis.* **9**, (Springer Berlin Heidelberg, 1986).
97. Conell, R. S., Corrigan, D. A. & Powell, B. R. The electrochromic properties of sputtered nickel oxide films. *Sol. Energy Mater. Sol. Cells* **25**, 301–313 (1992).
98. Cairns, R. W. & Ott, E. X-Ray Studies of the System Nickel—Oxygen—Water. I.

Abstract

- Nickelous Oxide and Hydroxide. *J. Am. Chem. Soc.* **376**, 527–533 (1933).
99. Glemser, O. & Einerhand, J. Die Struktur höherer Nickelhydroxyde. *Zeitschrift für Anorg. Chemie* **261**, 43–51 (1950).
100. Beverskog, B. & Puigdomenech, I. Revised Pourbaix diagrams for nickel at 25–300°C. *Corros. Sci.* **39**, 969–980 (1997).
101. Chen, S., Duan, J., Ran, J., Jaroniec, M. & Qiao, S. Z. N-doped graphene film-confined nickel nanoparticles as a highly efficient three-dimensional oxygen evolution electrocatalyst. *Energy Environ. Sci.* **6**, 3693 (2013).
102. Subbaraman, R. *et al.* Trends in activity for the water electrolyser reactions on 3d M(Ni,Co,Fe,Mn) hydr(oxy)oxide catalysts. *Nat. Mater.* **11**, 550–557 (2012).
103. Apai, G., Hamilton, J. F., Stohr, J. & Thompson, A. Extended x-ray absorption fine structure of small Cu and Ni clusters: Binding-energy and bond-length changes with cluster size. *Phys. Rev. Lett.* **43**, 165–169 (1979).
104. Häglund, J., Fernández Guillermet, A., Grimvall, G. & Körling, M. Theory of bonding in transition-metal carbides and nitrides. *Phys. Rev. B* **48**, 11685–11691 (1993).
105. Gumeniuk, R., Borrmann, H. & Leithe-Jasper, A. Refinement of the crystal structures of trinickel boron, Ni₃B, and tripalladium boron, Pd₃B. *Zeitschrift für Krist. - New Cryst. Struct.* **221**, 425–426 (2006).
106. Risch, M. *et al.* Structural changes of cobalt-based perovskites upon water oxidation investigated by EXAFS. *J. Phys. Chem. C* **117**, 8628–8635 (2013).
107. Rades, S., Kornowski, A., Weller, H. & Albert, B. Wet-chemical synthesis of nanoscale iron boride, XAFS analysis and crystallisation to α -FeB. *ChemPhysChem* **12**, 1756–1760 (2011).
108. Carenco, S., Portehault, D., Boissière, C., Mézailles, N. & Sanchez, C. Nanoscaled metal borides and phosphides: Recent developments and perspectives. *Chem. Rev.* **113**, 7981–8065 (2013).
109. Diplas, S. & Løvvik, O. M. Electronic structure studies of Ni-X (X: B, S, P) alloys using x-ray photoelectron spectroscopy, x-ray induced Auger electron spectroscopy and density functional theory calculations. *J. Phys. Condens. Matter* **21**, (2009).

Abstract

110. Hong, W. T. *et al.* Toward the rational design of non-precious transition metal oxides for oxygen electrocatalysis. *Energy Environ. Sci.* **8**, 1404–1427 (2015).
111. Zhang, H. M., Shimizu, Y., Teraoka, Y., Miura, N. & Yamazoe, N. Oxygen sorption and catalytic properties of $\text{La}_{1-x}\text{Sr}_x\text{Co}_{1-y}\text{Fe}_y\text{O}_3$ Perovskite-type oxides. *J. Catal.* **121**, 432–440 (1990).
112. Han, B. *et al.* Activity and stability trends of perovskite oxides for oxygen evolution catalysis at neutral pH. *Phys. Chem. Chem. Phys.* **17**, 22576–22580 (2015).
113. Wang, Y. & Cheng, H. P. Oxygen reduction activity on perovskite oxide surfaces: A comparative first-principles study of LaMnO_3 , LaFeO_3 , and LaCrO_3 . *J. Phys. Chem. C* **117**, 2106–2112 (2013).
114. Stoerzinger, K. A. *et al.* Highly Active Epitaxial $\text{La}_{(1-x)}\text{Sr}_x\text{MnO}_3$ Surfaces for the Oxygen Reduction Reaction: Role of Charge Transfer. *J. Phys. Chem. Lett.* **6**, 1435–1440 (2015).
115. Cheng, X. *et al.* Oxygen Evolution Reaction on $\text{La}_{1-x}\text{Sr}_x\text{CoO}_3$ Perovskites: A Combined Experimental and Theoretical Study of Their Structural, Electronic, and Electrochemical Properties. *Chem. Mater.* **27**, 7662–7672 (2015).
116. Guo, Y., Zhang, X. & Wäppling, R. Crystal structure of $\text{La}_{1-x}\text{Sr}_x\text{MnO}_{3-2x+\delta}\text{F}_{2x}$. *J. Alloys Compd.* **306**, 133–140 (2000).
117. Grimaud, A. *et al.* Double perovskites as a family of highly active catalysts for oxygen evolution in alkaline solution. *Nat. Commun.* **4**, 1–7 (2013).
118. Arendt, R. H., Rosolowski, J. H. & Szymaszek, J. W. Lead zirconate titanate ceramics from molten salt solvent synthesized powders. *Mater. Res. Bull.* **14**, 703–709 (1979).
119. Pradhan, A. K. *et al.* Synthesis and magnetic characterizations of manganite-based composite nanoparticles for biomedical applications. in *Journal of Applied Physics* **103**, (2008).
120. Patel, F. & Patel, S. $\text{La}_{1-x}\text{Sr}_x\text{CoO}_3$ ($x=0, 0.2$) perovskites type catalyst for carbon monoxide emission control from auto-exhaust. in *Procedia Engineering* **51**, 324–329 (2013).
121. Epherre, R. *et al.* Manganite perovskite nanoparticles for self-controlled magnetic

Abstract

- fluid hyperthermia: about the suitability of an aqueous combustion synthesis route. *J. Mater. Chem.* **21**, 4393 (2011).
122. Thorat, N. D. *et al.* Polyvinyl alcohol: an efficient fuel for synthesis of superparamagnetic LSMO nanoparticles for biomedical application. *Dalt. Trans.* **41**, 3060 (2012).
123. Lai, J., Niu, W., Luque, R. & Xu, G. Solvothermal synthesis of metal nanocrystals and their applications. *Nano Today* **10**, 240–267 (2015).
124. Urban, J. J., Ouyang, L., Jo, M. H., Wang, D. S. & Park, H. Synthesis of single-crystalline $\text{La}_{1-x}\text{Ba}_x\text{MnO}_3$ nanocubes with adjustable doping levels. *Nano Lett.* **4**, 1547–1550 (2004).
125. Zhu, D., Zhu, H. & Zhang, Y. Hydrothermal synthesis of $\text{La}_{0.5}\text{Ba}_{0.5}\text{MnO}_3$ nanowires. *Appl. Phys. Lett.* **80**, 1634–1636 (2002).
126. Yoon, K. H., Cho, Y. S. & Kang, D. H. Molten salt synthesis of lead-based relaxors. *J. Mater. Sci.* **33**, 2977–2984 (1998).
127. Thi N’Goc, H. Le *et al.* Surface-Driven Magnetotransport in Perovskite Nanocrystals. *Adv. Mater.* **29**, 1604745 (2017).
128. Lide, D. R. Physical constants of inorganic Compounds. in *CRC Handbook of Chemistry and Physics* 43–401 (2007).
129. Gonell, F. *et al.* Versatile Molten Salt Synthesis of Manganite Perovskite Oxide Nanocrystals and Their Magnetic Properties. *ChemNanoMat* **5**, 358–363 (2019).
130. Risch, M. Perovskite Electrocatalysts for the Oxygen Reduction Reaction in Alkaline Media. *Catalysts* **7**, 154 (2017).
131. Gonell, F. *et al.* Structure–Activity Relationship in Manganese Perovskite Oxide Nanocrystals from Molten Salts for Efficient Oxygen Reduction Reaction Electrocatalysis. *Chem. Mater.* **32**, 4241–4247 (2020).
132. Celorrio, V. *et al.* Mean Intrinsic Activity of Single Mn Sites at LaMnO_3 Nanoparticles Towards the Oxygen Reduction Reaction. *ChemElectroChem* **5**, 3044–3051 (2018).

Abstract

133. Liu, X. *et al.* Cobalt-Doped Perovskite-Type Oxide LaMnO₃ as Bifunctional Oxygen Catalysts for Hybrid Lithium–Oxygen Batteries. *Chem. - An Asian J.* **13**, 528–535 (2018).
134. Jolivet, J., Henry, M. & Livage, J. *Metal oxide chemistry and synthesis: from solution to solid state.* (2000).
135. Al Raihani, H., Durand, B., Chassagneux, F., Kerridge, D. H. & Inman, D. Zirconia formation by reaction of zirconium sulfate in molten alkali-metal nitrates or nitrites. *J. Mater. Chem.* **4**, 1331 (1994).
136. Epherre, R. Perovskites de manganèse nanométriques : vers des applications biomédicales. (2010).
137. Risch, M. *et al.* Water oxidation by amorphous cobalt-based oxides: in situ tracking of redox transitions and mode of catalysis. *Energy Environ. Sci.* **8**, 661–674 (2015).
138. Chivot, J., Mendoza, L., Mansour, C., Pauporté, T. & Cassir, M. New insight in the behaviour of Co–H₂O system at 25–150 °C, based on revised Pourbaix diagrams. *Corros. Sci.* **50**, 62–69 (2008).
139. Celorrio, V., Calvillo, L., Granozzi, G., Russell, A. E. & Fermin, D. J. AMnO₃ (A = Sr, La, Ca, Y) Perovskite Oxides as Oxygen Reduction Electrocatalysts. *Top. Catal.* **61**, 154–161 (2018).
140. Melinescu, A., Velciu, G., Marinescu, V., Hornoiu, C. & Preda, M. Synthesis and stability of the strontium cobaltite thermally treated in air. *Rev. Chim.* **70**, 3330–3334 (2019).
141. Stoerzinger, K. A. *et al.* Oxygen electrocatalysis on (001)-oriented manganese perovskite films: Mn valency and charge transfer at the nanoscale. *Energy Environ. Sci.* **6**, 1582–1588 (2013).
142. Ignatans, R. *et al.* The Effect of Surface Reconstruction on the Oxygen Reduction Reaction Properties of LaMnO₃. *J. Phys. Chem. C* **123**, 11621–11627 (2019).
143. Deibert, M. C. & Kahraman, R. An Auger spectroscopic investigation of the high temperature reduction of zirconium dioxide surfaces in vacuum. *Appl. Surf. Sci.* **37**, 327–336 (1989).

Abstract

144. Zhou, G. & Yang, J. C. Reduction of Cu₂O Islands Grown on a Cu(100) Surface through Vacuum Annealing. *Phys. Rev. Lett.* **93**, 226101 (2004).
145. Li, J. *et al.* Structural and mechanistic basis for the high activity of Fe–N–C catalysts toward oxygen reduction. *Energy Environ. Sci.* **9**, 2418–2432 (2016).
146. Cochran, S. J. & Larkins, F. P. Surface reduction of some transition-metal oxides. An X-ray photoelectron spectroscopic study of iron, cobalt, nickel and zinc oxides. *J. Chem. Soc. Faraday Trans. 1 Phys. Chem. Condens. Phases* **81**, 2179 (1985).
147. Jung, S., McCrory, C. C. L., Ferrer, I. M., Peters, J. C. & Jaramillo, T. F. Benchmarking nanoparticulate metal oxide electrocatalysts for the alkaline water oxidation reaction. *J. Mater. Chem. A* **4**, 3068–3076 (2016).
148. Risch, M. *et al.* Redox Processes of Manganese Oxide in Catalyzing Oxygen Evolution and Reduction: An in Situ Soft X-ray Absorption Spectroscopy Study. *J. Phys. Chem. C* **121**, 17682–17692 (2017).
149. Beermann, V. *et al.* Real-time imaging of activation and degradation of carbon supported octahedral Pt-Ni alloy fuel cell catalysts at the nanoscale using: In situ electrochemical liquid cell STEM. *Energy Environ. Sci.* **12**, 2476–2485 (2019).
150. Zhu, G. Z. *et al.* In situ liquid cell TEM study of morphological evolution and degradation of Pt-Fe nanocatalysts during potential cycling. *J. Phys. Chem. C* **118**, 22111–22119 (2014).
151. Xiao, Z. *et al.* Green Fabrication of Ultrathin Co₃O₄ Nanosheets from Metal–Organic Framework for Robust High-Rate Supercapacitors. *ACS Appl. Mater. Interfaces* **9**, 41827–41836 (2017).
152. Koza, J. A., He, Z., Miller, A. S. & Switzer, J. A. Electrodeposition of crystalline Co₃O₄ - A catalyst for the oxygen evolution reaction. *Chem. Mater.* **24**, 3567–3573 (2012).
153. Wang, K. *et al.* Solvent-Free Chemical Approach to Synthesize Various Morphological Co₃O₄ for CO Oxidation. *ACS Appl. Mater. Interfaces* **9**, 16128–16137 (2017).
154. Nkeng, P., Koenig, J. F., Gautier, J. L., Chartier, P. & Poillierat, G. Enhancement of

Abstract

- surface areas of Co₃O₄ and NiCo₂O₄ electrocatalysts prepared by spray pyrolysis. *J. Electroanal. Chem.* **402**, 81–89 (1996).
155. Lukashuk, L. *et al.* Operando Insights into CO Oxidation on Cobalt Oxide Catalysts by NAP-XPS, FTIR, and XRD. *ACS Catal.* **8**, 8630–8641 (2018).
 156. Davidson, C., Kissel, G. & Srinivasan, S. Electrode Kinetics of the Oxygen Evolution Reaction at NiCo₂O₄ from 30% KOH. *J. Electroanal. Chem.* **132**, 129–135 (1982).
 157. Wang, Y. *et al.* Synergistic Mn-Co catalyst outperforms Pt on high-rate oxygen reduction for alkaline polymer electrolyte fuel cells. *Nat. Commun.* **10**, 1506 (2019).
 158. Bajdich, M., García-Mota, M., Vojvodic, A., Nørskov, J. K. & Bell, A. T. Theoretical investigation of the activity of cobalt oxides for the electrochemical oxidation of water. *J. Am. Chem. Soc.* **135**, 13521–13530 (2013).
 159. McAlpin, J. G. *et al.* EPR Evidence for Co(IV) Species Produced During Water Oxidation at Neutral pH. *J. Am. Chem. Soc.* **132**, 6882–6883 (2010).
 160. Singh, R. N. *et al.* Thin films of Co₃O₄ and NiCo₂O₄ obtained by the method of chemical spray pyrolysis for electrocatalysis III. The electrocatalysis of oxygen evolution. *J. Appl. Electrochem.* **20**, 442–446 (1990).
 161. Abidat, I. *et al.* Co₃O₄/rGO Catalysts for Oxygen Electrocatalysis: On the Role of the Oxide/Carbon Interaction. *J. Electrochem. Soc.* **166**, H94–H102 (2019).
 162. Zhang, Y. *et al.* Crystal plane-dependent electrocatalytic activity of Co₃O₄ toward oxygen evolution reaction. *Catal. Commun.* **67**, 78–82 (2015).
 163. Wang, H. Y. *et al.* In Operando Identification of Geometrical-Site-Dependent Water Oxidation Activity of Spinel Co₃O₄. *J. Am. Chem. Soc.* **138**, 36–39 (2016).
 164. Trevorah, R. M., Chantler, C. T. & Schalken, M. J. Solving self-absorption in fluorescence. *IUCrJ* **6**, 586–602 (2019).
 165. Cressey, G., Henderson, C. M. B. & van der Laan, G. Use of L-edge X-ray absorption spectroscopy to characterize multiple valence states of 3 d transition metals; a new probe for mineralogical and geochemical research. *Phys. Chem. Miner.* **20**, 111–119 (1993).

Abstract

166. Tillier, J. *et al.* Electrochemical Flow-Cell Setup for In Situ X-ray Investigations. *J. Electrochem. Soc.* **163**, H913–H920 (2016).
167. Li, Y. *et al.* Complex structural dynamics of nanocatalysts revealed in Operando conditions by correlated imaging and spectroscopy probes. *Nat. Commun.* **6**, 1–6 (2015).
168. Nordhei, C., Ramstad, A. L. & Nicholson, D. G. Nanophase cobalt, nickel and zinc ferrites: synchrotron XAS study on the crystallite size dependence of metal distribution. *Phys. Chem. Chem. Phys.* **10**, 1053–1066 (2008).

Abstract

Résumé:

Pour satisfaire la demande énergétique mondiale, les batteries métal-air et les électrolyseurs sont envisagés pour le stockage et la conversion énergétique. La lenteur des réactions de formation de l'oxygène (OER), de réduction de l'oxygène (ORR) et de formation du dihydrogène (HER) impliquées dans ces dispositifs nécessite des électrocatalyseurs pour atteindre les performances requises. Ce travail est focalisé sur des électrocatalyseurs sous forme de nanoparticules et à base de métaux de transition, à bas coût, avec des activités électrocatalytiques élevées mais dont l'évolution lors des réactions nécessite une compréhension approfondie dans le but d'améliorer les performances. L'objectif a été de mieux comprendre l'évolution des catalyseurs en conditions opératoires en mobilisant une technique de choix : la spectroscopie d'absorption des rayons X (XAS) *in situ*. Nous avons ainsi pu d'abord d'expliquer la très grande activité électrocatalytique de borures de nickel pour l'HER et l'OER, avec une grande stabilité du borure dans le premier cas et la formation *in situ* d'un oxyde en surface des nanoparticules de borure dans le deuxième cas. Nous avons ensuite cherché synthétiser puis à comprendre la réactivité des pérovskites oxydes manganites et cobaltites pour l'ORR et l'OER en étudiant *in situ* les variations de degré d'oxydation des métaux de transition. Enfin, la possibilité de coupler les analyses *operando* XAS et en microscopie électronique à transmission a été évaluée pour le cas modèle de Co_3O_4 .

Abstract:

To meet the global energy needs, metal-air batteries and water splitting devices are foreseen as potential energy conversion and storage devices. The sluggishness of the Oxygen Evolution Reaction (OER), the Oxygen Reduction Reaction (ORR) and the Hydrogen Evolution Reaction (HER) that are involved in these devices calls for the use of electrocatalysts to achieve the required performances. This work focuses on cost-effective, transition metal-based electrocatalyst nanoparticles with high electrocatalytic activities, but whose evolution during the reactions requires thorough understanding in order to improve activity and stability. The goal is to better understand the electrocatalyst evolution under operating conditions by using *in situ* X-ray absorption spectroscopy (XAS). We were able to explain the high HER and OER activities of nickel borides, which are due to the high stability of borides in the former case, and to the *in situ* formation of an oxide layer around the boride nanoparticles in the latter case. We then synthesized and studied the reactivity of manganite cobaltite perovskite oxides during ORR and OER by studying *in situ* the evolution of the oxidation state of the transition metals. Finally, we evaluated the possibility to couple *operando* XAS analysis and transmission electron microscopy imaging on the model OER electrocatalyst Co_3O_4 .